

Montanuniversität Leoben

Dissertation

**Structural instabilities in  
nanostructured metals**

Marlene Kapp

Leoben, August 2017

This work was financially supported by the FWF Austrian Science fund under grant 24429-N20 and the European Research Council under ERC Grant No. 340185 USMS.

Copyright © 2017 by Marlene Kapp. All rights reserved.

Erich Schmid Institute of Materials Science  
Austrian Academy of Sciences  
Jahnstrasse 12  
A-8700 Leoben

This thesis was typeset by the use of KOMA-Script and L<sup>A</sup>T<sub>E</sub>X 2<sub>ε</sub>.

# Affidavit

I declare in lieu of oath, that I wrote this thesis and performed the associated research myself, using only literature cited in this volume.

Marlene Kapp

Leoben, August 2017



# Danksagung

Nachdem meine Zeit am ESI nun schon viele Jahre andauert, begonnen als studentische Mitarbeiterin, über meine Diplomarbeit bis hin zur Dissertation, möchte ich einen großen Dank den fixen “Größen“ am ESI aussprechen. So sind die langgedienten Gruppenleiter und wissenschaftlichen Mitarbeiter, das technische Personal, die Sekretärinnen und Reinigungskräfte jene, die mich und so viele andere Diplomanden und Dissertanten unterstützten und für den am ESI so maßgeblichen Zusammenhalt verantwortlich sind. Auf diese Weise kann dieses Institut so viel mehr als nur ein Arbeitsplatz sein!

Bei meinem Betreuer Prof. Reinhard Pippan möchte ich mich bedanken, dass er mir mit dieser Arbeit die Möglichkeit gab meine wissenschaftlichen Fähigkeiten weiterzuentwickeln. Ich danke ihm für seine Geduld, sein Vertrauen und seine maßlos sprießenden Ideen. Seine aufmunternde Art ist nicht nur bei komplexen Experimenten hilfreich, sondern lässt einen auch in schwierigen Kletterpassagen über sich hinauswachsen. So wurde in den letzten Jahren nicht nur an meinen fachlichen Qualitäten gefeilt, sondern auch an meinen persönlichen - nicht zuletzt durch die vielen Konferenzen, an denen ich Vorträge halten durfte. Vielen Dank!

Anfangs mit Mikromechanik in der Hochverformungsgruppe noch ein Exot möchte ich mich bei Daniel Kiener für die vielen Diskussionen über Pillar & co. bedanken. Sein Einsatz beschränkt sich am ESI nicht nur auf miniaturisierte Welten, sondern gilt auch dem feierabendlichen Zusammensein als erster Grillmeister und institutseigener Sommelier. Schön, dass er nun dabei von Verena Maier-Kiener unterstützt wird, die mir in allen Lebenslagen mit Rat und Tat zur Seite steht. Danke euch zwei!

Der Mikromechanikgruppe bestehend aus Ruth Konetschnik, Reinhard Fritz und Markus Alfreider bin ich genauso zu Dank verpflichtet wie Stefan Wurster, der mir all seine Tricks und - wenn es sein musste - magischen Hände zur Verfügung gestellt hat. ASMEC lässt grüßen!

## *Danksagung*

Besonderer Dank gilt auch den Werkstatt-Jungs Franz Hubner und Robin Neubauer für viele Spezialanfertigungen, Herwig Felber für seinen Einsatz zum Erhalt von FIB und REM, Silke Modritsch für die unzähligen Proben und Peter Kutleša für die Unterstützung bei allen HPT Anliegen.

Tief in der Schuld stehe ich bei Martin Bärnthaler für seine Geduld bei zyklischen HPT Versuchen und bei Thomas Leitner für die nachfolgende Revolution des Elektro-Martin. Ich danke all meinen Kollegen in der Hochverformungsgruppe und dem restlichen ESI für die schöne Zeit, die ich hier verbringen konnte.

Meinen Eltern, Schwestern und Schwiegereltern danke ich für ihre allseitige Unterstützung und dem Ausgleich abseits der Arbeit. Meine tiefe Dankbarkeit gilt Oliver, ohne den diese Arbeit nicht möglich gewesen wäre. Er avancierte in den letzten Jahren zu einem zweiten Betreuer, der auch in scheinbar aussichtslosen Situationen einen Weg fand, daraus gestärkt und klüger hervorzugehen. Es war einmalig mit ihm die Begeisterung für diese Arbeit teilen zu dürfen. Ich weiß sein Verständnis für unzählige Stunden am FIB trotz schönstem Kletterwetter, seine positive und lösungsorientierte Art und die geniale Zeit abseits des Instituts sehr zu schätzen!

# Abstract

Nanocrystalline (NC) and ultrafine-grained (UFG) materials have attracted extensive attention due to their superior strength under monotonic loading but also during high cycle fatigue. Such high strength materials allow for constructions requiring less material volume and can therefore promote light-weight efforts for the automotive or aviation industry. Still some difficulties have to be overcome to make this material class reliable aspirants for technical applications. Firstly, their propensity to deform via shear bands during monotonic or cyclic loading causes the initial structure to locally collapse what deteriorates the material's ductility or lifetime. Secondly, during cyclic loading the initial NC or UFG structure tends to coarsen what degrades the strength. The knowledge about the underlying driving forces and mechanisms for such instabilities is still at its infancy, but its understanding the key to overcome them. By using different experimental methodologies, involving static and cyclic loading conditions, intriguing insights into both phenomena have been gained.

Cyclic micro bending experiments have been performed on UFG copper revealing structural modifications by a growth of larger grains at the expense of adjacent smaller ones. Thereby the continuous migration of high angle grain boundaries was identified as the basic mechanisms of cyclic grain growth. This migration procedure is not just thermally assisted, proven by cyclic high pressure torsion experiments performed under cryogenic conditions on UFG nickel where a distinct coarsening of the structure took place. Irrespective of the deformation temperature grain coarsening was amplified within shear bands, thus, regions of strain concentration. This emphasizes the crucial role of the cyclic strain in triggering the migration of a grain boundary. Because the hydrostatic pressure prevents failure of the sample the cyclic softening portion stemming exclusively from grain growth could be quantified for the first time. Additionally, grain coarsening as well as the propagation of shear bands could be studied up to large cyclic strains, which allow the conclusion that cyclically induced growing of grains is not an “everlasting“ process as it levels off at a certain grain size. This final, coarsened grain size is determined by the nominal strain amplitude.

Strain localizations affecting the mechanical behaviour occur also under static loading conditions, which was investigated on a pearlitic nanocomposite exhibiting a lamellar arrangement of ferrite and carbon rich cementite. Micro compression experiments revealed different types of strain localization, depending on the loading

## *Abstract*

direction with respect to the lamellar orientation of the harder cementite. Perpendicular loading leads to shearing of the cementite into the shear band direction, parallel loading to buckling within a kink band and inclined loading localizes the strain by confined layer slip parallel to the cementite lamellae, without deforming it. Not only the lamellar orientation but also the strain path has an influence on the deformation behavior, as for instance during bending the strain gradient prohibits the formation of catastrophic shear bands. Also during cyclic bending homogeneous deformation occurs and in addition pronounced grain growth is prevented by the layered architecture. Thus, for cyclically loaded nanolamellar architectures structural instabilities can be avoided, which enhances the reliability for their in-service use.

# Contents

<b>Affidavit</b>	<b>III</b>
<b>Danksagung</b>	<b>V</b>
<b>Abstract</b>	<b>VII</b>
<b>1 Motivation</b>	<b>1</b>
<b>2 Introduction</b>	<b>5</b>
2.1 Processing nanostructured materials by high pressure torsion . . . . .	5
2.1.1 High pressure torsion setup . . . . .	5
2.1.2 Investigated materials . . . . .	6
2.2 Deformation induced instabilities in nanostructured metals . . . . .	7
2.2.1 Plastic deformation mechanisms in nanostructured metals . . . . .	7
2.2.2 Shear bands in nanostructured metals . . . . .	10
2.2.3 Grain growth . . . . .	13
2.3 Experimental methodology . . . . .	14
2.3.1 Microsample testing . . . . .	16
2.3.2 Cyclic high pressure torsion . . . . .	20
<b>3 Experimental observations and summary of publications</b>	<b>21</b>
3.1 List of Publications . . . . .	21
3.2 Microstructural instabilities during static loading conditions . . . . .	23
3.3 Microstructural instabilities during cyclic loading conditions . . . . .	26
3.3.1 High purity model materials . . . . .	26
3.3.2 Pearlitic steel . . . . .	32
<b>4 Conclusions</b>	<b>35</b>
<b>5 List of appended papers</b>	<b>45</b>
<b>A Importance of dislocation pile-ups on the mechanical properties and the Bauschinger effect in microcantilevers</b>	<b>49</b>
A.1 Introduction . . . . .	50
A.2 Experimental details . . . . .	51
A.3 Results . . . . .	53

A.4	Discussion . . . . .	56
A.5	Conclusion . . . . .	58
<b>B</b>	<b>Anisotropic deformation characteristics of an ultrafine- and nanolamellar pearlitic steel</b>	<b>61</b>
B.1	Introduction . . . . .	62
B.2	Experimental . . . . .	63
B.3	Results . . . . .	66
B.3.1	Microhardness measurements . . . . .	66
B.3.2	Micro pillar testing . . . . .	66
B.3.3	SEM characterization of the deformed microstructure after testing . . . . .	68
B.4	Discussion . . . . .	71
B.4.1	Onset of yielding . . . . .	71
B.4.2	Strain hardening . . . . .	73
B.4.3	The stress-strain behavior at larger strains . . . . .	76
B.4.4	The deformation behavior at larger strains . . . . .	77
B.4.5	Remarks to the macro behavior of a pearlitic steel . . . . .	78
B.5	Conclusion . . . . .	78
<b>C</b>	<b>Ultra-strong and damage tolerant metallic bulk materials: A lesson from nanostructured pearlitic steel wires</b>	<b>83</b>
C.1	Introduction . . . . .	84
C.2	Material and Experimental Approach . . . . .	85
C.3	Results and Discussion . . . . .	87
C.3.1	Parallel testing orientation . . . . .	87
C.3.2	Perpendicular testing orientation . . . . .	90
C.3.3	Fractography . . . . .	90
C.4	Conclusions . . . . .	94
C.5	Methods . . . . .	95
<b>D</b>	<b>Structural instabilities during cyclic loading of ultrafine-grained copper studied with micro bending experiments</b>	<b>101</b>
D.1	Introduction . . . . .	102
D.2	Experimental . . . . .	103
D.3	Results . . . . .	105
D.3.1	Cyclic hysteresis loops . . . . .	105
D.3.2	Changes in the surface morphology . . . . .	105
D.3.3	Changes in microstructure . . . . .	106
D.4	Discussion . . . . .	109
D.5	Conclusion . . . . .	114
<b>E</b>	<b>Cyclically induced grain growth within shear bands investigated in UFG nickel by cyclic high pressure torsion</b>	<b>119</b>

E.1	Introduction . . . . .	120
E.2	Experimental . . . . .	122
E.3	Results . . . . .	124
	E.3.1 Shear band formation . . . . .	124
	E.3.2 Microhardness . . . . .	124
	E.3.3 Microstructural evolution . . . . .	125
	E.3.4 Crystallographic orientation . . . . .	127
E.4	Discussion . . . . .	129
E.5	Conclusion and outlook . . . . .	132
<b>F</b>	<b>Strength and ductility of heavily deformed pearlitic microstructures</b>	<b>137</b>
F.1	Introduction . . . . .	137
F.2	Fracture toughness as a function of cold working . . . . .	138
F.3	Effect of the lamellar arrangement during compression loading . . . . .	142
F.4	Concluding remarks with respect to processing and applications . . . . .	144
<b>G</b>	<b>Fatigue induced instabilities studied by inexhaustible ultrafine-grained samples</b>	<b>149</b>
G.1	Introduction . . . . .	150
G.2	Experimental . . . . .	151
G.3	Results . . . . .	154
	G.3.1 Shear band evolution in UFG structures with increasing strain	154
	G.3.2 Microhardness and structural evolution with accumulated strain for different strain amplitudes . . . . .	154
	G.3.3 Cyclic high pressure torsion of UFG structures at cryogenic conditions . . . . .	160
	G.3.4 Effect of different starting grain sizes . . . . .	160
G.4	Discussion . . . . .	163
	G.4.1 Accumulated strain vs. strain amplitude . . . . .	163
	G.4.2 Evolution of structural parameters and its effect on cyclic soft- ening . . . . .	165
	G.4.3 Driving forces for cyclically induced grain growth in UFG structures . . . . .	166
	G.4.4 Growth of cyclically induced shear bands . . . . .	167
	G.4.5 Effect of the starting grain size on cyclically induced strain localization . . . . .	168
G.5	Conclusion . . . . .	169



# 1

## Motivation

In the last decades strong efforts have been made to increase strength and ductility of metals, both are essential design parameters for structural components. Among various strategies, which have been developed to increase the strength of materials, the refinement of the microstructure has the potential to increase the strength by retaining moderate ductility [1] [2] [3]. It is applicable to any materials system as it is not restricted by phenomena like precipitation hardening. The fundamental work of Hall and Petch already showed a clear correlation of strength increase with grain refinement in 1951 [4]. Since then methods apart from classical thermomechanical processing routes and alloying have been developed which can realize structures well below 1  $\mu\text{m}$  or even 100 nm in size, referred to as ultrafine-grained (UFG) or nanocrystalline (NC) materials [1]. Two different strategies, bottom-up and top-down processes, can be applied for microstructural design. The difference between these processes lies in the starting configuration of the material and the following synthesis procedure [2]. In bottom-up processes, like inert gas condensation which was invented by Gleiter [5], the NC or UFG structured materials are synthesized on a plain substrate. However, in top-down processes an initially bulk and coarse grained material is refined into a fine scaled microstructure by applying large degrees of deformation at low temperatures, known as severe plastic deformation (SPD) methods [1]. The most common SPD techniques are equal-channel angular pressing (ECAP) [6], accumulative roll bonding (ARB) [7] or high pressure torsion (HPT) [8]. The main advantage of HPT lies in the possibility to deform any kind of material, for instance even relatively brittle systems such as chromium [9] or tungsten [10], due to the applied high hydrostatic pressure. With this procedure single phase pure or alloyed metals can be refined to grain sizes between 700 nm and 50 nm, but also complex multiphase materials with structural sizes below 50 nm can be achieved [1] [2]. The potential of SPD to process the strongest structural materials

## 1 Motivation

has already been demonstrated for pearlitic steels. By wire drawing it was possible to produce pearlitic wires with a tensile strength of almost 7 GPa [11] corresponding to one third of the theoretical strength limit. This achievement is outstanding and encouraging for HPT processing, which follows a very similar processing principal but additionally allows to fabricate bulk-like materials instead of the 20  $\mu\text{m}$  thick wires. The underlying grain or phase architecture of such nanostructured composites offer superior strength and toughness combinations [12]. However, these fine scaled structures also induce difficulties. Nanostructured materials possess enhanced grain boundary fractions, which are believed to facilitate mechanical or thermal induced structural instabilities which deteriorate the materials strength, ductility or life time. Strain localization in shear bands and grain coarsening are the two main issues leading to structural instability.

In principal both phenomena can occur as a consequence of plastic deformation during static and cyclic loading, although their characteristics can vary depending on the deformation mode, as will be described later in more detail. In any case, microstructural changes will alter the mechanical response and can deteriorate the mechanical performance and ductility substantially. For instance, grain coarsening may enhance ductility at the expense of a softening, while shear banding can cause inhomogeneous plastic deformation and thereby further shorten the ductility of the samples during tensile tests (Fig. 1.1a) [3]. On the other hand, during low cycle fatigue testing, when large strain amplitudes are applied, both mechanisms lead to cyclic softening thereby shortening the life-time dramatically (Fig. 1.1b) [13] [14].

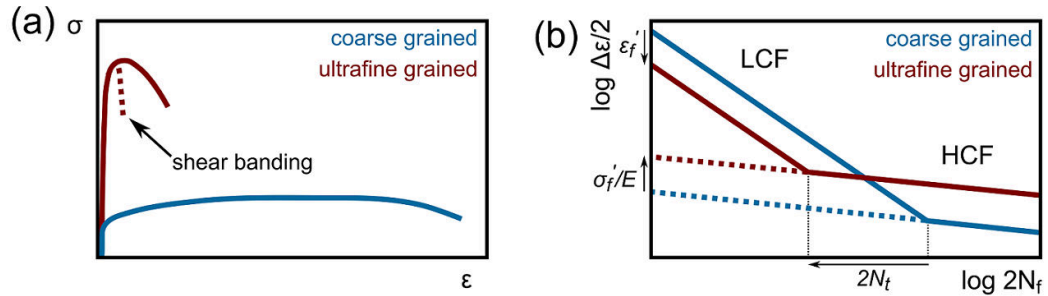


**Figure 1.1** Schematics according to [3] and [13] comparing the mechanical response of coarse grained and ultrafine grained structures during a) tensile testing and b) fatigue testing.

As mechanical properties are essential design parameters for structural components, their modification during plastic deformation seriously alters their sustainability and could therefore be responsible for fatal structural design failures. Thus, to make these high strength materials suitable for technical applications, an understanding of instability initiation and development is of utmost importance. Therefore the ba-

sic mechanisms of shear band formation and grain coarsening need to be identified, as it may offer strategies to subdue or avoid them. As these instabilities have been observed under various experimental conditions systematic studies are required to prove the influence of deformation mode, loading parameters, crystallography, grain boundary type, grain architecture and their impact on the mechanical properties. Only the knowledge about the driving forces or fundamental processes triggering the collapse of the ultrafine- or nanocrystalline structure will allow to design stable and reliable ultra-strong materials.

The following chapters will summarize the current knowledge on mechanically induced grain growth and shear band formation. Further, the used experimental techniques will be described shortly before the main findings of the thesis are presented.



# 2

## Introduction

### 2.1 Processing nanostructured materials by high pressure torsion

#### 2.1.1 High pressure torsion setup

The first high pressure torsion setup was invented by Bridgeman [15] for a completely different objective than grain refinement of metallic materials, which is the main purpose of HPT nowadays. However, the setup of current HPT tools is very similar to the first hand driven setup from 1935. It consists of two anvils, where the upper one is fixed and the lower one rotates. However, in contrast to the initial setup of Bridgeman, nowadays so called quasi-constrained HPT is utilized, which uses anvils with a cavity rather than a flat surface. This setup ensures application of high hydrostatic pressures which prevents cracking of the sample [16]. A disc-shaped sample is placed between the two anvils. Both, the sample and the anvil are sand-blasted to ensure sufficient friction in order to avoid slipping of the sample between the anvils. The lower anvil rotates monotonically under the hydrostatic pressure and thereby severe amounts of shear strain,  $\gamma$ , can be imposed to the sample, which can be calculated according to Eq. 2.1

$$\gamma = \frac{2\pi rn}{t} \quad (2.1)$$

with the HPT disc radius,  $r$ , the number of rotations,  $n$ , and the HPT disc thickness,  $t$ .

## 2 Introduction

The equivalent v. Mises strain,  $\epsilon_{vM}$ , can be calculated with Eq. 2.2

$$\epsilon_{vM} = \frac{\gamma}{\sqrt{3}} = \frac{2\pi rn}{\sqrt{3}t} \quad (2.2)$$

In addition to monotonic deformation, the lower anvil can also be rotated cyclically for a certain twist angle,  $\Theta$ , thus simulating fatigue loading conditions. As the strain depends on the disc radius and thickness, different cyclic strains can be applied by adapting the sample geometry and the number of cycles.

### 2.1.2 Investigated materials

High pressure torsion induces a breakdown of initially coarse grains down to sizes of 200-700 nm for pure metals, 50-100 nm for single phase alloyed metals and even below 50 nm for multiphase materials and composites. In the initial stage of the refinement process dislocations are generated which accumulate and form into cell boundaries. With ongoing deformation and further increase of the dislocation density cells become smaller and the misorientation between them increases resulting in high angle grain boundaries (HAGB). At sufficiently large strains the grain size distribution is not changed anymore and a dynamic steady state or saturation regime is attained. The ultrafine-grained structure at this stage consists of about 20 % low angle grain boundaries (LAGB) and 80 % HAGB. For further details to the fragmentation process see also [17] [18].

In this thesis the structural stability of pure metals, e.g. of high-purity model materials such as 99.95 % copper and 99.99 % nickel and of a high strength nanolamellar pearlitic steel is investigated by different methodologies. The shape of the grains depends on the viewing direction of the HPT disc. For UFG copper and nickel the grains get elongated in the shearing direction, while in the radial and torsional direction remain relatively equiaxed with 500 nm and 300 nm grain size (calculated from electron back scatter diffraction (EBSD) data, area weighted), respectively (Fig. 2.1a-b). The pearlitic nanocomposite is characterized by a lamellar arrangement of the softer ferrite and harder intermetallic cementite phase with 15-20 nm and 3 nm lamellae thickness, respectively (Fig. 2.1c). The significant reduction of grain size and lamellae thickness leads to important implications compared to coarse grained materials, such as i) larger grain boundary or interface fraction; ii) less ordered or distorted grain boundaries or interfaces are far from their equilibrium structure [1] and iii) fewer dislocations can be stored within the grains [3]. Additional variations related to the multiphase pearlitic nanocomposite are iv) stoichiometric changes of the cementite due to dissolution of carbon atoms in the ferritic phase [19] [20] [21] and v) replacement of the colony structure with various lamellae orientations by

a single lamellar orientation parallel to the shearing direction [20] [22] [23]. These peculiarities may in turn provoke the mentioned instabilities, which will be briefly summarized in the following chapters.

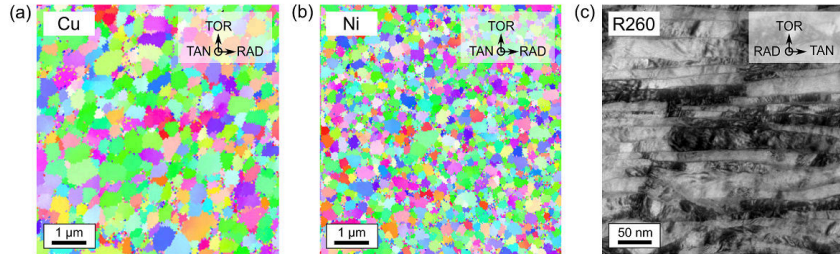


**Figure 2.1** Microstructures for a) UFG Cu, b) UFG Ni (viewing direction parallel to the tangential (TAN) direction of the HPT disc), and c) the nanolamellar pearlitic steel (R260, viewing direction parallel to the radial (RAD) direction of the HPT disc) [22].

## 2.2 Deformation induced instabilities in nanostructured metals

As described in chapter 2.1 NC and UFG structures possess specific peculiarities which can affect physical or mechanical properties and may lead to structural changes during plastic deformation. Although the current understanding of plasticity in nanostructured materials is still at its infancy and mostly based on MD simulations, the most important findings will be shortly summarized, as they are essential for understanding the plastic deformation and the evolution of structural instabilities.

### 2.2.1 Plastic deformation mechanisms in nanostructured metals

#### *Single phase materials*

In coarse grained materials of medium to high stacking fault energy plastic deformation at low homologous temperatures is realized by the activation of intragranular dislocation sources and the subsequent glide of emitted dislocations. As the grain volume available in UFG or NC grains becomes sufficiently small the generation of dislocations by classic intragranular dislocation sources, such as Frank-Read sources, becomes increasingly difficult. Although recent studies have shown that dislocation

## 2 Introduction

mediated plasticity is still possible at grain scales down to 10-20 nm [24] [25], the nucleation sites for dislocations are transferred to the grain boundaries. Molecular dynamic (MD) simulations on NC Ni showed the emission of partial dislocations from grain boundaries and their absorption within opposite grain boundaries. Upon their movement in the grain interior they leave behind a stacking fault if not followed by a trailing partial [26]. Below 10-20 nm many studies have claimed that dislocation based deformation mechanisms are replaced by deformation processes being related to grain boundaries. For instance MD simulations have revealed the accommodation of plastic strain by the relative movement of adjacent grains along their boundaries in NC materials [27], which is schematically shown in figure 2.2a. This process is called grain boundary sliding and could be realized by atomic shuffling near grain boundaries and local diffusion processes [26]. In addition, grain rotation has also been reported to accommodate plastic deformation at the nanoscale [28] [24]. Such processes might become dominant for grain sizes below 10 nm.

For grain sizes in the ultrafine-grained regime ( $> 100$  nm), TEM investigations have not only evidenced the prevalence of dislocation mediated plasticity [29] but also the operation of dislocation sources located in the grain boundary [30]. This alternative nucleation sites for dislocations are also related to the complex and disordered nature of SPD grain boundaries consisting of dislocations within the boundary. These “non-equilibrium dislocations“ can move under an applied load [30]. However, if the movement of the dislocations gets disturbed, for instance by grain boundary ledges or triple junctions, they can be emitted into the grain interior. Upon further straining the mobile dislocation will glide through the grain interior until absorbed again in the opposite grain boundary [29] [31] as schematically shown in figure 2.2b.

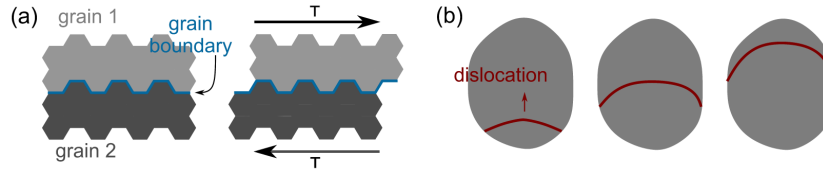


**Figure 2.2** Possible deformation mechanisms for NC and UFG materials are a) grain boundary sliding [2] and b) dislocation mediated plasticity by nucleation of dislocations from grain boundaries, subsequent movement through the grain interior and absorption in the opposite grain boundary.

### *Nanolaminates*

For nanocomposites, such as lamellar pearlitic structures, the deformation processes are somewhat different. Unlike the single phase NC materials, diffusion based processes like grain boundary sliding are not feasible in layered structures simply from

geometrical considerations. Thus, it is assumed that the main carriers of plasticity are dislocations. The thickness of the layers between interfaces corresponds to the smallest free glide path for dislocations. The interlamellar distance will therefore affect the dislocation movement significantly [32] [33] and govern the exact deformation mechanism [34]. Nucleation sites for the dislocations are located at the interfaces [37]. Once a dislocation half loop is emitted into the layer it moves by progressive bowing through the layer interior towards the opposite interface, where it could be partly inserted [35] [36] [37]. For a layer thickness in the micron and sub-micron regime pile-up formation at interfaces is assumed, however, below an interlamellar spacing of 50 nm dislocations do not have enough space to pile up anymore and confined layer slip will become important. Thereby, dislocation segments spanning between the adjacent interfaces will bow out under an applied load parallel to the layers as shown in Fig. 2.3a, unless they are restricted at grain or subgrain boundaries, which also span between the interfaces. This procedure is in principal similar to bowing a dislocation segment between two pinning points, i.e. Orowan mechanism, where the required stress to continue bowing the dislocation scales with the inverse of the distance between the pinning points. A similar correlation between the stress to bow dislocation half loops and the interlamellar spacing does apply to these layered structures.

For very fine layers below a few nanometers the curvature of such a dislocation would increase tremendously and therefore also the required stresses. As a consequence confined layer slip becomes unfeasible. The exact deformation mechanism at such fine length scales is still under investigation, however, two explanations exist. First, when the shear stress exceeds the interface strength, the dislocation will cross the interface and continue its movement in the adjacent layer as outlined in figure 2.3b. Nevertheless, this idea is yet to be proven experimentally. On the other hand, simulations have suggested that the nucleation of dislocations from interfaces becomes dominant over confined layer slip for the finest lamellar spacings [38].

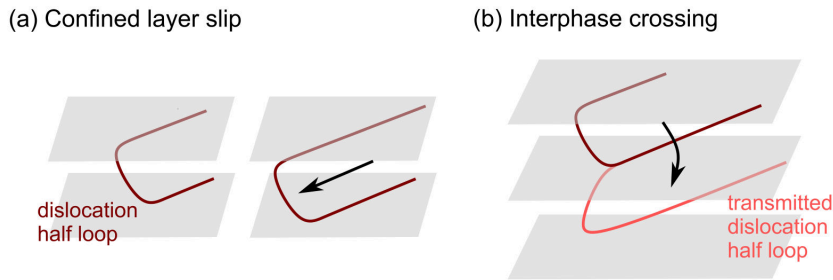


**Figure 2.3** Plastic deformation in multilayers a) in the range of about 3-50 nm lamellar spacing is realized by confined layer slip and b) below 3 nm crossing of dislocation through interfaces is suggested similar to [32].

### 2.2.2 Shear bands in nanostructured metals

The localization of strain within shear bands can occur under various loading conditions, such as for static, cyclic, tensile, compressive, shear or torsional strainig.

#### Static loading conditions

##### *Single phase alloys*

Although dislocation slip is an inhomogeneous event at the mesoscale, generally most metallic materials deform homogeneous at the global scale, at least at moderate strains. However, at large strains deformation can become inhomogeneous as observed for the first time during heavy cold rolling of an initially coarse grained copper alloy in 1922 [39]. It was suggested by Sevillano [40] that heavily cold worked structures are prone to form such shear bands due to the difficulty to maintain strain hardening in very fine-grained structures. Subsequently the material is not able to counteract a local collapse of the structure and allows for strain concentration in this softer region [41] [42]. Unfortunately, UFG and NC metals lack of sufficient strain hardening capacity due to the limited number of dislocations that can be stored within small grains [3]. They are therefore prone to form shear bands during deformation shortly after the yield stress is exceeded [43] [44] [45] [46]. An example of a shear band developed during compressive loading is shown for a Fe-Cu alloy in Fig. 2.4a [43]. Once the instability has formed it can grow in length and in some cases also in width [43] [44], which seems to correlate with the materials grain size [43]. For initially coarse grained materials, a refinement of the structure was reported due to the severe strains present within the shear band [47]. Nanocrystalline structures on the other hand do not necessarily show further refinement within the shear band [44]. However, a general feature seems to be the elongation of grains along the shear direction [43] [44] [47] and the formation of texture [44] [47].

Descriptions of the structure of shear bands are experimentally readily available, however, insights into the formation process of shear bands are limited. Strain mapping obtained from digital image correlation during in-situ TEM testing of NC Ni samples revealed a continuous localization of strain in several localized bands until one of them becomes dominant resulting in a continuous softening [46]. Further, MD simulations revealed strain localization along grain boundaries under an angle of  $45^\circ$  to the loading axis coinciding with the direction of maximum shear stress for structures well below 10 nm [48]. In less favorably oriented grain boundaries stacking faults bridged the gap between the strain concentrations located at the grain boundaries. It can be imagined, that at larger grain sizes in the UFG regime the formation of shear bands must be more related to dislocation based mechanisms, as the grain boundary fraction decreases significantly. However, as computational approaches are not accessible in this grain size regime closer insights into shear band initiation and propagation are missing at the UFG length scale.

*Nanolaminates*

Sevillano et al. have noted that not only severely work hardened materials, but also highly anisotropic materials are prone to strain localization [40]. As deformation and failure mechanisms are expected to be highly anisotropic in layered materials, strain localizations need to be considered as important issue. Indeed numerous experiments have shown that independent of the material type, thus whether the layered structures consist of metals, ceramics or bulk metallic glasses, a layered structure collapses, when a shear band developed [35] [49] [50] [52] as shown exemplarily in Fig. 2.4b. Furthermore, the response of the lamellar architecture to strain localization, e.g. the cementite within the pearlite, is strongly influenced by the lamellar orientation with respect to the loading direction [53].

In these lamellar structures not the grain boundaries but the interfaces become the most important defects controlling the nature of the strain localization. The interface properties, such as coherency, defect structure or interfacial shear strength can vary significantly depending on the processing route or material system, thereby controlling the shear band characteristics [50] [51]. Irrespective of these important parameters the geometrical realignment of the layers into the shearing direction and their consequent codeformation occurs independently of the processing route and the type of material [35] [49] [50] [51] [52]. Such a local realignment of the lamellae along the direction of large strain may induce a geometrical softening promoting further deformation within the inclined shear bands [49]. However, layer consistency is not always the case. The lamellar architecture can be destroyed by crossing of shear bands, as observed in a heavily cold drawn pearlitic steel [53].

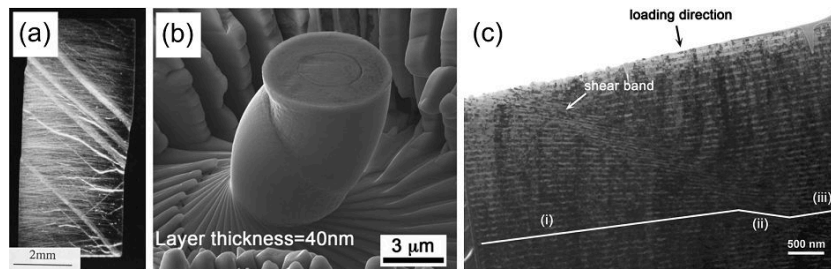


**Figure 2.4** Examples of shear bands during static loading a) in a Fe-Cu alloy [43] and b) Cu-Nb multilayer, c) where a geometrical realignment of the lamellae into the shear band direction occurs [50].

### Cyclic loading conditions

The concentration of cyclic strain in local bands is known to occur also upon cyclic loading in coarse grained materials [54]. Their structure consists of a ladder-like morphology, with almost dislocation free volumes separated by narrow regions of high dislocation density [55]. In this structure plastic strain is supposed to be accommodated by a movement of dislocations between the ladders. Thus, in softer regions less dislocation interaction processes will occur [56]. Due to their recurring occurrence at the sample surface after polishing, they are denoted as persistent slip bands [57] and are detectable by surface intrusions and extrusions [58]. Observations of extrusions in the sense of material squeezed out of the surface has also been depicted for UFG materials under LCF conditions [59], however, ladder-like dislocation structures were not observed as the typical size of the ladder structures observed in conventional coarse grained metals exceeds the size of ultrafine grains. The shear bands in UFG structures also had a persistent nature [60] [14] and mostly developed along the maximum shear stress direction under  $45^\circ$  to the loading axis [61] [59] [62] [63]. In some cases they have been found to be aligned with the shear direction of the last ECAP step [14]. Their appearance on the surface could be step-like [62] as shown in Fig. 2.5a or similar to extrusions [59] [60] [64] [14] as shown in Fig. 2.5b. The thickness of these shear bands usually exceeds the size of the ultrafine grains [61] [60] [65] but can also be narrow, consisting of a dense dislocation network, which is able to penetrate grain boundaries [62]. Furthermore, shear banding can be accompanied by grain growth inside or nearby the band, thus a combination of two instability mechanisms can occur [65] [66] [67]. For this type of shear band a strong dependence on the initial structure [67] and the type of the material was found [65]. In copper the coarsening occurred in narrow shear bands consisting of one grain in thickness, whereas in aluminum the shear band comprised of several coarsened grains, realigned into the shear direction [65].

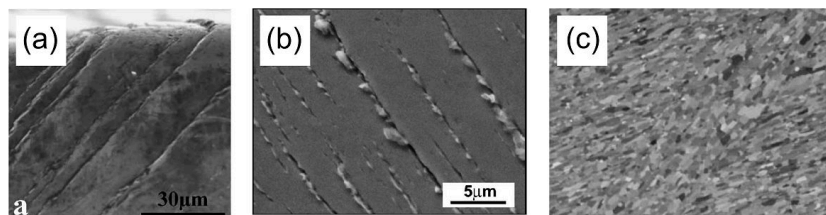


**Figure 2.5** Morphologies of cyclically induced shear bands occurring as a) step-like [64], b) extrusion-like features [14] or c) in combination with grain growth [65].

In summary, multiple observations of shear localization within bands have been described in the past for various loading conditions and different materials. However,

a thorough explanation on the questions of why and how these shear bands develop is still missing.

### 2.2.3 Grain growth

In coarse grained structures grain growth is commonly classified into static and dynamic grain growth. In the static case the grain growth occurs exclusively due to thermal energy, while during dynamic recrystallization thermal and mechanical driving forces simultaneously trigger grain nucleation and subsequent growth. Different processes are considered to realize the growth of a grain, which are atomic flux between adjacent crystallite surfaces through the grain boundary, movement of atomic groups or secondary grain boundary dislocations and atomic shuffling [68]. While grain growth and grain boundary migration during deformation in coarse grained metals is occurring only at elevated temperatures, for UFG or even NC materials grain growth can often occur during static or cyclic deformation processes even below a homologous temperature of 0.3. Especially, high purity NC and UFG metals are prone for deformation induced grain coarsening [69] [70] [71] [72] [73]. The segregation of impurities can pin the grain boundaries to some extent, making them more stable against grain growth [74] [75]. First observations of cyclically induced grain coarsening were depicted by Agnew et al. [59] during low cycle fatigue (LCF), revealing a heterogeneous coarsening at low strain amplitudes of  $\Delta\epsilon_{pl} \approx 10^{-3}$  akin to reports about the evolution of a bimodal grain size distribution [14]. At higher strain amplitudes the coarsening became more homogeneous. However, the opposite case was also reported [13], where the coarsening process became more pronounced at lower strain amplitudes. Controversial observations also exist for the role of the testing mode, e.g. strain or stress control, and most importantly for the underlying mechanisms and driving forces for grain growth. Generally, the three concepts describing grain growth under cyclic and static loading conditions are the following:

1. Grain rotation
2. Dynamic recrystallization
3. Shear-stress coupled grain boundary migration

In case 1) crystallographic orientations of adjacent grains converge due to rotation induced by the deformation process, coalesce and thereby cause grain coarsening, as schematically shown in Fig. 2.6. This certainly plays a role for NC structures [69] [24] and has also been evidenced experimentally for UFG metals [76]. Case 2) is based on the observation of grain growth becoming more pronounced at low strain rates and strain amplitudes due to the longer life time which extend the time for diffusion processes [13] [63]. This concept concludes that for UFG materials room temperature is sufficient to thermally activate grain growth processes. Quite on the contrary, case

## 2 Introduction

3) suggests that a mechanical activation of grain boundaries is sufficient to initiate its movement, as shown schematically in Fig. 2.6b. Several studies have proposed that the applied stress can solely migrate the boundary [77] [71] [74] [78] [29] [73]. Although a mechanical activation of the boundary has been reported frequently [59] [60] [70], clear evidence for shear-stress coupled boundary migration is rare. Moreover, other experimental data point out to the importance of the applied strain, as grain coarsening was increased in the necking area of tensile samples, thus at areas of strain concentration during static loading [79] and by increased strain amplitudes during LCF [75].

Despite the numerous observations of grain growth a clear conclusion about the impact of the strain amplitude, the crystallography of the initial structure, the underlying mechanisms and driving forces are missing. Especially, during cyclic loading the role of the accumulated strain on grain coarsening has not been discussed at all. A thorough investigation of grain growth processes by utilization of in-situ methods and statistical approaches are therefore of utmost importance to provide a detailed understanding.

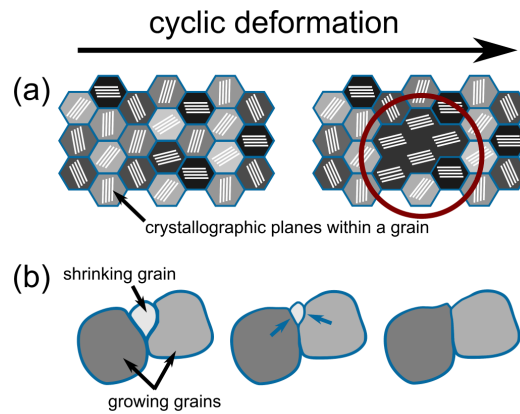


**Figure 2.6** Possible processes causing cyclically induced grain growth are a) grain rotation [2] and b) grain boundary migration.

## 2.3 Experimental methodology

In this study, the stability of materials deformed by high pressure torsion was investigated for single phase copper and nickel as well as for a nanolamellar pearlitic steel. The copper and nickel provided model systems for studying the structural stability in single phase metals, while the nanolamellar pearlitic steel belongs to the strongest known structural materials. Therefore, static loading experiments were

conducted on pearlitic micro pillars and cyclic loading experiments were performed for copper, nickel and the pearlitic steel. Appropriate experimental procedures were selected to address the particular questions of interest regarding UFG materials in general:

- i) Basic mechanisms of static and cyclically induced shear band formation and grain growth;
- ii) Driving forces for the migration of grain boundaries during grain growth;
- iii) Influence of material characteristics, such as the crystallographic orientation, the grain boundary type and a second phase;
- iv) Influence of testing conditions, such as temperature, strain amplitude and accumulative strain;
- v) Impact of grain growth and shear banding on the mechanical behavior;

And with respect to the lamellar architecture of the pearlitic high strength steel in especially:

- vi) Effect of lamellar loading direction on plastic stability during static and cyclic loading;
- vii) Tailoring mechanical properties by selective loading directions.

For points i) and vi-vii) in-situ testing techniques within a scanning electron microscope enable the unique possibility to watch and track structural changes induced by the deformation process and relate them to local stress-strain states induced by static or cyclic loading. Therefore, in-situ cyclic micro bending experiments partly supported by quasi in-situ EBSD measurements and in-situ micro compression experiments were conducted. This approach allows to identify the onset of structural instabilities, to correlate them to a specific critical stress or strain value and to further track the evolution of the specific instability mechanisms with increasing strain. In addition to the micro mechanical experiments, cyclic high pressure torsion (CHPT) experiments were conducted, an alternative technique for low cycle fatigue testing enabling solutions for points ii-v). This method inhibits sample failure up to large cyclic strains and therefore allows to measure the mechanical response due to grain growth and shear bands exclusively. Furthermore, a statistical analysis of material and testing parameters is possible by assessing multiple strain amplitudes with a single sample and imposing various testing temperatures. The applied techniques and their scientific purpose are summarized for static loading conditions in Table 2.1 and for cyclic loading conditions in Table 2.2:

## 2 Introduction

**Table 2.1** Overview of the experimental investigations on plastic instability mechanisms based on static loading.

<b>Experimental procedure</b>	<b>Material</b>	<b>Instability mechanism</b>	<b>Scientific purpose</b>
Micro compression	Pearlite	Shear and kink bands	Impact of lamellar orientation on the evolution of plastic instabilities and their effect on mechanical properties
Micro bending	Pearlite	Small slip steps	Preventing plastic instabilities by a load path change

**Table 2.2** Overview of the experimental investigations on plastic instability mechanisms based on cyclic loading.

<b>Experimental procedure</b>	<b>Material</b>	<b>Instability mechanism</b>	<b>Scientific purpose</b>
Cyclic micro bending	Copper (Sxx)	Slip on defined glide planes	Basic dislocation processes under bending of micro cantilevers
Cyclic micro bending	Copper	Grain growth	Revealing the basic mechanisms of cyclically induced grain coarsening
CHPT	Copper, Nickel	Grain growth and shear bands	Studying the evolution of grain growth and shear bands systematically for different microstructures and processing parameters to reveal driving forces
Cyclic micro bending	Pearlite	Cracks	Exceeding the limits of cyclic strength by suppressing cyclic instabilities

### 2.3.1 Microsample testing

The in-situ approach was utilized for three loading conditions: micro compression experiments on the nanolamellar pearlitic steel, unidirectional micro bending experiments on the nanolamellar pearlitic steel and cyclic micro bending experiments on ultrafine-grained copper and the nanolamellar pearlitic steel. The experimental setup of these tests will be outlined briefly in the following.

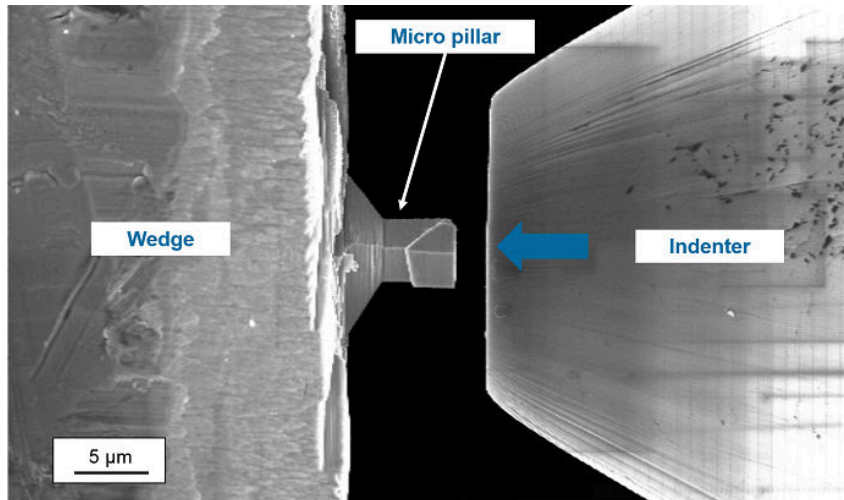


**Figure 2.7** Setup micro compression experiments within the scanning electron microscope.

### Micro compression testing

In order to evaluate the structural stability of the pearlitic nanocomposite during static loading micro compression experiments were performed. Due to the lamellar architecture of the pearlitic steel an anisotropic behavior can be expected. Therefore, three different types of compression pillars were fabricated with the cementite and ferrite lamellae aligned parallel, perpendicular and inclined by  $45^\circ$  with respect to the loading direction. This was not only done for the HPT processed nanolamellar case but also for the ultrafine-lamellar initial microstructure, exhibiting a ferrite-cementite lamellae spacing of 15 nm and 3 nm for nanolamellae and 200 nm and 20 nm for ultrafine-lamellae, respectively. Therefore, colonies of a suitable lamellae orientation had to be selected to fabricate micro pillars of the undeformed pearlite conditions as well. Micro pillars of  $3 \times 3 \mu\text{m}^2$  in cross section and  $6 \mu\text{m}$  in length, thus with an aspect ratio of 1:2 were focused ion beam milled. The samples were then tested with an ASMEC UNAT micro indenter within a Zeiss LEO 982 scanning electron microscope. An electrical conductive diamond flat punch was used to compress the pillars at a nominal strain rate of  $\dot{\epsilon} = 10^{-3} \text{ s}^{-1}$  to displacements of 1500 - 3000 nm in one or two loading steps. The setup within the SEM is shown in Fig. 2.7.

### Unidirectional micro bending testing

In order to evaluate the impact of the strain path on the deformation behavior, the nanolamellar pearlitic steel was also loaded in bending mode. Therefore, the setup

## 2 Introduction

of the ASMEC UNAT micro indenter had to be modified slightly by replacing the flat punch with a cube corner indenter to enable the load to be applied in a single point rather than on an extended area (Fig. 2.8). The micro cantilever was FIB milled on a macroscopic pearlitic steel needle, prepared with a  $20\ \mu\text{m}$  tip radius following methods for atom probe tomography needle preparation. The dimensions of the cantilever gauge section were  $10 \times 10 \times 20\ \mu\text{m}^3$  for the height, width, length and  $40\ \mu\text{m}$  for the bending length. The cantilever was subjected to multiple loading-unloading steps at a nominal strain rate of  $\dot{\epsilon} = 10^{-3}\text{s}^{-1}$ .

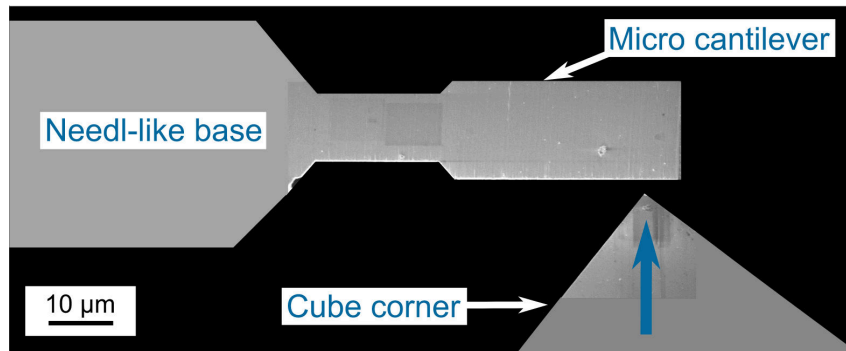


**Figure 2.8** Setup micro bending experiments within the scanning electron microscope.

### Cyclic micro bending testing

To evaluate cyclically induced microstructural changes, cyclic micro bending experiments have been conducted. These experiments allow to correlate microstructural changes with the local stress-strain state. This was done for UFG Cu, as a model material, with the focus on revealing the basic mechanism for grain growth or shear banding in a comparatively easier system. In addition, the role of interfaces was then investigated with a more complex system of the nanolamellar pearlitic steel. Due to the different strength of the materials, two different micro indenters had to be utilized. For the nanolamellar pearlitic steel the experiments were performed with the ASMEC UNAT micro indenter due to the larger displacement that can be realized and the Hysitron PI85 micro indentation system was used for the ultrafine-grained copper samples due to the significantly better force resolution. The pearlitic cantilevers were  $7 \times 7 \times 21\ \mu\text{m}^3$  in size with a bending length of  $42\ \mu\text{m}$ , whereas the copper cantilevers had a size of  $3 \times 3 \times 3\ \mu\text{m}^3$  and  $12\ \mu\text{m}$  bending length because of the limited displacement range in the back and forth movement of the Hysitron indenter. For both cases, a FIB milled tungsten double blade gripper was used to load the cantilevers, by moving the gripper up and down (see Fig. 2.9). Both materials were loaded under displacement control with a nominal strain rate of  $\dot{\epsilon} = 10^{-3}\text{s}^{-1}$ .

The ultrafine-grained copper cantilever was loaded at a plastic strain amplitude of  $3.2 \cdot 10^{-3}$  for 400 cycles. In addition to conventional SEM investigations, the micro cantilever was dismantled every 100 cycles to perform EBSD scans which allow to track changes in the grain structure with the full crystallographic information. The pearlitic nanocomposite was subjected to a block test, where the strain amplitude was sequentially increased until cyclic softening was observed. Here, the focus was put on identifying the critical plastic strain amplitude at which the structure becomes unstable causing a drop in the cyclic stress and how it evolves with cyclic strain

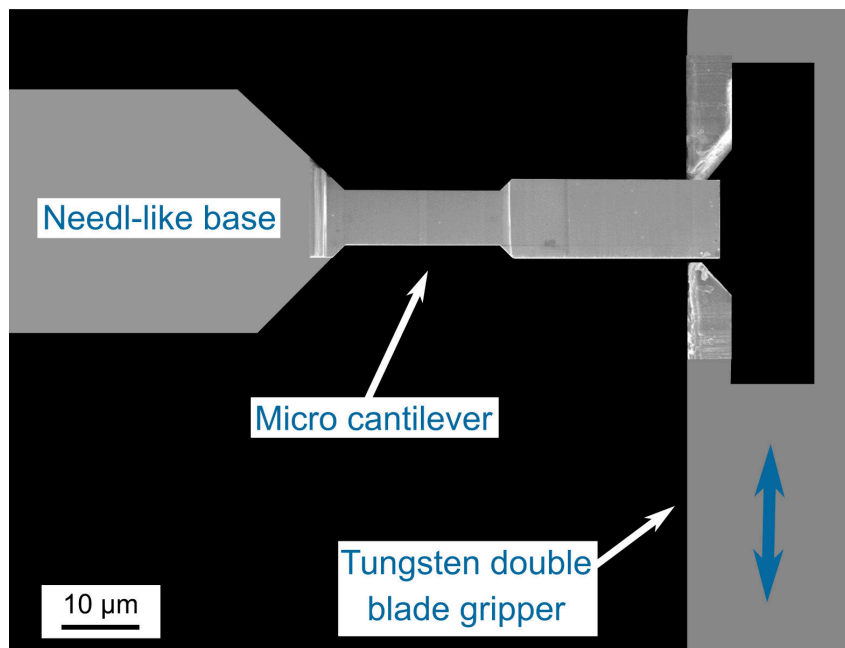


**Figure 2.9** Setup cyclic micro bending experiments within the scanning electron microscope.

#### Sample preparation

The micron sized compression and bending samples, as well as the tungsten double blade gripper were machined by focused ion beam (FIB) milling with a Zeiss LEO 1540 XB dual beam work station. The FIB method allows for a locally defined sample preparation with the aid of a focused  $\text{Ga}^+$  ion beam of 20 kV acceleration voltage, removing the redundant material by sputtering processes. Coarse cutting was done at a current of 10 nA to remove large volume parts in a reasonable time but for polishing 200 pA were used to guarantee a smooth sample surface and a reduced thickness of the ion induced damage layer [80]. During this final step the

## 2 Introduction

samples were tilted by  $1.2^\circ$  in order to remove the taper caused by redepositing. For details on FIB sample fabrication see [81] [82]. In order to reduce the FIB milling time, macroscopic samples were first prepared with thicknesses of around  $20\ \mu\text{m}$ . To do so, for the micro compression setup, thin wedge shaped slices were prepared from pearlitic HPT discs as well as from the undeformed pearlite with a cross section slicer. In this thinned area multiple compression samples could be FIB milled next to each other. For the bending experiments, needles were used instead of wedges because bending experiments require more free space around them for the application of the displacement than the compression samples. Therefore, from the HPT discs rods were cut and subsequently etched to a needle. Only one cantilever could be FIB milled on this needle-shaped macro samples.

### 2.3.2 Cyclic high pressure torsion

The HPT setup described in chapter 2.1 can simply be adapted for cyclic torsional deformation experiments. For this, the rotation direction of the lower anvil is continuously reversed after a certain twist angle,  $\pm\theta$ . The cyclic strain amplitude,  $\epsilon_a$ , can be calculated by adapting the equation for the v. Mises strain:

$$\epsilon_a = \frac{2\pi r\theta}{\sqrt{3}t360} \quad (2.3)$$

By varying the number of cycles,  $N$ , the accumulated strain,  $\epsilon_{acc}$ , can be adjusted:

$$\epsilon_{acc} = 4N\epsilon_a \quad (2.4)$$

The measurement of the twist angle,  $\theta$ , is realized by a 1 m long non-magnetic rod, attached to the lower HPT anvil and is, thus rotating simultaneously with the HPT sample. At its end a series of point magnets is fixed to the rod and causes a targeted activation of a Hall sensor, which is connected to a control unit, actuating the HPT motor to change the rotation direction. Thereby, two Hall sensors are used, spanning an adjustable distance which yields the desired twist angle. By cyclic high pressure torsion (CHPT) not only the strain amplitude and accumulated strain can be adapted, but also different testing temperatures can be applied. Although most experiments were run at room temperature for certain cases cryogenic conditions were required in order to subdue thermal activation of grain growth. This was possible by simply placing the HPT anvils with the sample in a bath of liquid nitrogen, thereby realizing constant temperatures of 77 K.

# 3

## Experimental observations and summary of publications

The purpose of this thesis was to deepen the understanding about structural instabilities, such as shear bands or grain coarsening initiated during static and cyclic plastic deformation. As mentioned earlier, two specific experimental procedures were used. First, in-situ micro mechanical approaches for static and cyclic loading conditions, because they directly enable a correlation between structural changes and the mechanical response by tracking changes of the same sample area throughout the deformation experiment. Second, CHPT was found to be indispensable for a systematic study on the effect of different loading conditions, such as strain amplitude, accumulated strain or temperature on grain coarsening because failure of the sample is inhibited up to large cyclic strains. The main conclusions of these experiments, which have already been published to a great extent (see also list of publications), will be summarized in the following chapters.

### 3.1 List of Publications

#### Publication A

*Importance of dislocations pile-ups on the mechanical properties and the Bauschinger effect in micro cantilevers.*

M.W. Kapp, C. Kirchlechner, R. Pippan and G. Dehm  
Journal of Materials Research 30 (2015) 791-797.

### 3 Experimental observations and summary of publications

#### **Publication B**

*Anisotropic deformation characteristics of an ultrafine- and nanolamellar pearlitic steel.*

M.W. Kapp, A. Hohenwarter, S. Wurster, B. Yang and R. Pippan  
Acta Materialia 106 (2016) 239-248.

#### **Publication C**

*Structural instabilities during cyclic loading of ultrafine-grained copper studied with micro bending experiments.*

M.W. Kapp, T. Kremmer, C. Motz, B. Yang, R. Pippan  
Acta Materialia 125 (2017) 351-358.

#### **Publication D**

*Ultra-strong and damage tolerant metallic bulk materials: A lesson from nanostructured pearlitic steel wires.*

A. Hohenwarter, B. Völker, M.W. Kapp, Y. Li, S. Goto, D. Raabe, R. Pippan  
Scientific Reports 6 (2016) 33228.

#### **Publication E**

*Cyclically induced grain growth within shear bands investigated in UFG Ni by cyclic high pressure torsion.*

M.W. Kapp, O. Renk, T. Leitner, P. Ghosh, B. Yang, R. Pippan  
Accepted for publication in Journal of Materials Research.

#### **Publication F**

*Strength and ductility of heavily deformed pearlitic microstructures.*

A. Hohenwarter, M.W. Kapp, B. Völker, O. Renk, R. Pippan  
Accepted for Publication in IOP Conference Series: Materials Science and Engineering.

#### **Publication G**

*Fatigue induced instabilities studied by inexhaustible ultrafine-grained samples.*

M.W. Kapp, O. Renk, P. Ghosh, T. Leitner, B. Yang, R. Pippan  
Manuscript in Preparation, will be submitted to SCI journal.

### 3.2 Microstructural instabilities during static loading conditions

The high pressure torsion deformed pearlitic steel, denoted as nanolamellar (NL) in the following due to the ferrite and cementite (actually carbon rich phase due to stoichiometric deviations from  $\text{Fe}_3\text{C}$ ) lamellae spacing of 15-20 nm and 3 nm, respectively, was compared with the ultrafine lamellar (UFL) initial state, consisting of lamellar spacings of 200 nm and 20 nm for the ferrite and cementite, respectively. To account for a possible anisotropic behavior inherent to the lamellar architecture, three different lamellar orientations, being parallel, normal and inclined with respect to the loading direction were tested.

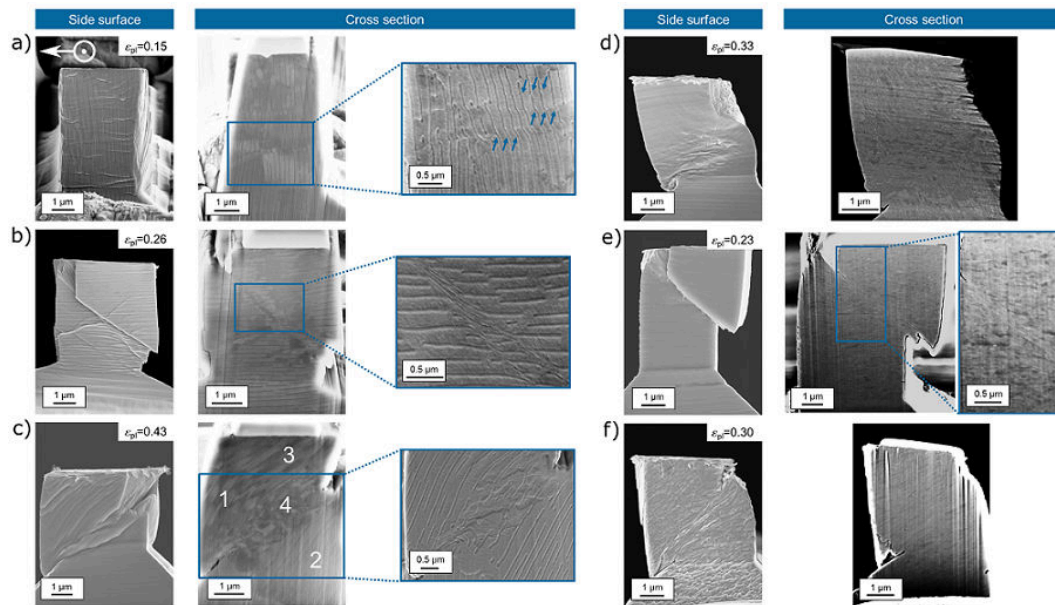


**Figure 3.1** SEM images of the side surfaces and cross sections of the a-c) UFL and d-f) NL compressed pearlitic pillars showing a,d) kink bands for the parallel orientation, b,e) shear bands for the normal orientation and c,f) inclined orientation aligned along the lamellae similar to [85].

SEM images, shown in Fig. 3.1, were taken after compression and revealed local deformation within bands irrespective of the lamellar orientation or spacing. Interestingly, in the NL pillars (Fig. 3.1d-f) the imposed strain was accommodated in only one dominant band, whereas multiple bands were initiated in the UFL pillars (Fig. 3.1a-c). The cross sections reveal, that the intrinsic localization mechanism varies for the three different lamellar orientations, but is similar irrespective of the lamellar

### 3 Experimental observations and summary of publications

spacing. When the harder cementite lamellae are aligned parallel with respect to the compression axis a cumulative buckling of adjacent lamellae over a confined height is observed for the UFL (Fig. 3.1a) and the NL (Fig. 3.1d) case and is therefore, denoted as kink band similar to earlier reports [53]. Loading the lamellae normal with respect to the compression axis, locally reorients adjacent ferrite and cementite lamellae into the shearing direction (Fig. 3.1b,e), commonly denoted as shear band. Although cementite is an intermetallic phase, it behaves in a ductile manner during deformation of pearlite, when its lamellar thickness is below  $\approx 10$  nm [83] [84]. Therefore, the lamellae stay intact when being realigned into the shear direction, which is consistent with co-deformation in other multilayer systems [35] [50] [49]. For the inclined orientation of the UFL (Fig. 3.1c) and NL (Fig. 3.1f) pillars shear bands form within the ferritic phase via confined layer slip [32] and parallel to the cementite lamellae. For the formation of the shear band the cementite lamellae neither have to be bent or buckled into the shearing direction, thus it can form at stress values below the elastic limit of the cementite. This is in contrast to the other two orientations where the plastic deformation of the cementite is obligatory to form a shear or kink band. The observations, that the type of plastic instability is governed by the lamellar orientation rather than the lamellar spacing applies to earlier suggestions [53].

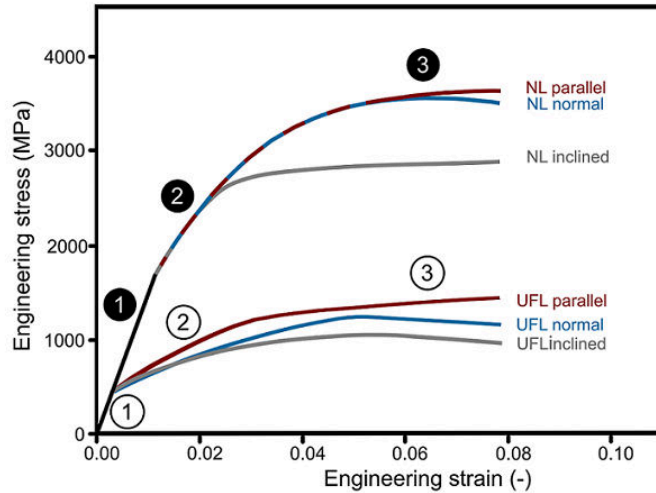


**Figure 3.2** Schematic of the engineering stress-strain curves of the pearlitic pillars, exhibiting three deformation regimes: 1) both phases deform elastically; 2) the softer ferrite becomes plastic, the harder cementite stays elastic; 3) both phases deform plastically similar to [85].

### 3.2 Microstructural instabilities during static loading conditions

In-situ capturing of the surface morphology enables correlation of the deformation characteristics with the evolution of the stress-strain curve. Figure 3.2 shows schematics of the measured stress-strain curves, which clearly reflect the composite behavior of the UFL and NL pearlitic steel. According to the different slopes three deformation regimes can be identified [86]. In the first deformation regime both phases behave elastically (labelled 1, black for NL and white for UFL in Fig. 3.2) until the softer ferritic phase starts to plastically deform at around 600 MPa for UFL and about 1900 MPa for the NL pillars (labelled 2 in Fig. 3.2). In this second deformation regime tremendous strain hardening is realized. At the transition to the third deformation regime (labelled 3 in Fig. 3.2) shear and kink bands become active as the harder cementite has exceeded its elastic limit and allows for the collapse of the lamellar architecture in the normal and parallel case. The onset of strain localization in shear bands occurs at distinctively lower stress levels for the inclined orientation. This is attributed to the not required plastic deformation of the cementite, thus allowing for early strain localization. It is also noteworthy, that an essential contribution to the strength increase of more than two times of the NL pearlite is caused by enhanced strain hardening in the second deformation regime that can be realized in nanolaminates [34]. Unfortunately, the evolution of plastic instabilities does not only lead to catastrophic failure of the pillars, but also shuts off strain hardening and thereby limits the strength potential of these nanolaminates.

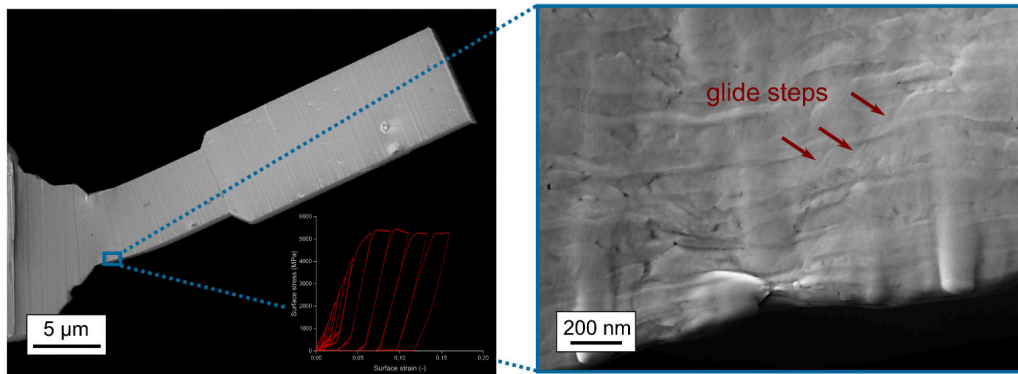


**Figure 3.3** SEM image of the bent pearlitic cantilever, where a magnified image shows tiny slip steps within the ferrite, which do not accumulate to a large scale, catastrophic shear band.

An attempt to overcome structural instabilities could be the use of a different load path. Therefore, micro bending beams were tested with the lamellae being aligned normal to the loading direction. This testing direction leads to immediate strain softening and failure due to shear band formation during compression. The pearlitic

cantilever was bent in multiple steps to a total outer fiber strain of 12 %. Large scale shear bands still have not developed (Fig. 3.3), although in this strain regime deformation was already confined in a dominant shear band during compression testing. At higher magnifications a damaged region becomes visible, where the layers are not perfectly straight anymore and a roughening occurred. However, pronounced shear bands are not detectable. Within the ferritic lamellae multiple slip steps are visible, which are confined by the adjacent cementite, as they are not able to overcome it. The gradient-like distribution of strains and stresses along the cantilever, with the maximum at its outer fiber and diminishing towards the neutral axis, seems to hinder the formation of large scale shear bands, therefore promotes homogeneous deformation and prevents early failure.

## 3.3 Microstructural instabilities during cyclic loading conditions

### 3.3.1 High purity model materials

As mentioned earlier, the appearance of shear bands or grain coarsening is typically observed during fatigue testing of NC and UFG structures [87] [63] [88] [89]. Cyclic micro bending experiments on UFG copper performed within the thesis revealed the basic mechanism of cyclically induced grain growth for the first time. Comparison of EBSD scans performed on the same area after 100, 200, 300 and 400 cycles at a plastic strain amplitude of  $\epsilon_{a,pl} = 3.2 * 10^{-3}$  (Fig. 3.4) showed that a continuous migration of HAGBs leads to the growth of certain grains (detail 1 in Fig. 3.4). Thereby, larger grains tend to grow, whereas smaller ones shrink, which is consistent to grain growth observations during static loading experiments [69] [72] [29] [90] [76]. The difference in strain energy density between the growing larger grains (low strain energy density) and the shrinking smaller grains (higher strain energy density) seems to govern the direction of boundary migration [90] [91]. LAGBs stay unaffected unless structural modifications in adjacent grains cause their disappearance (detail 2 in Fig. 3.4). Therefore they might be classified as geometrically necessary boundaries [92]. Rarely, completely new grains were appearing (detail 3 in Fig. 3.4) following the same grain growth procedure as outlined above. Most probably they have grown from a region just beneath the cantilever surface, rather than being nucleated there. With these observations it was possible to disprove the ideas about classical recrystallization being the underlying grain growth mechanism [87]. Present experimental evidences are essential to reasonably intensify the understanding about driving forces for mechanically induced grain coarsening.

### 3.3 Microstructural instabilities during cyclic loading conditions

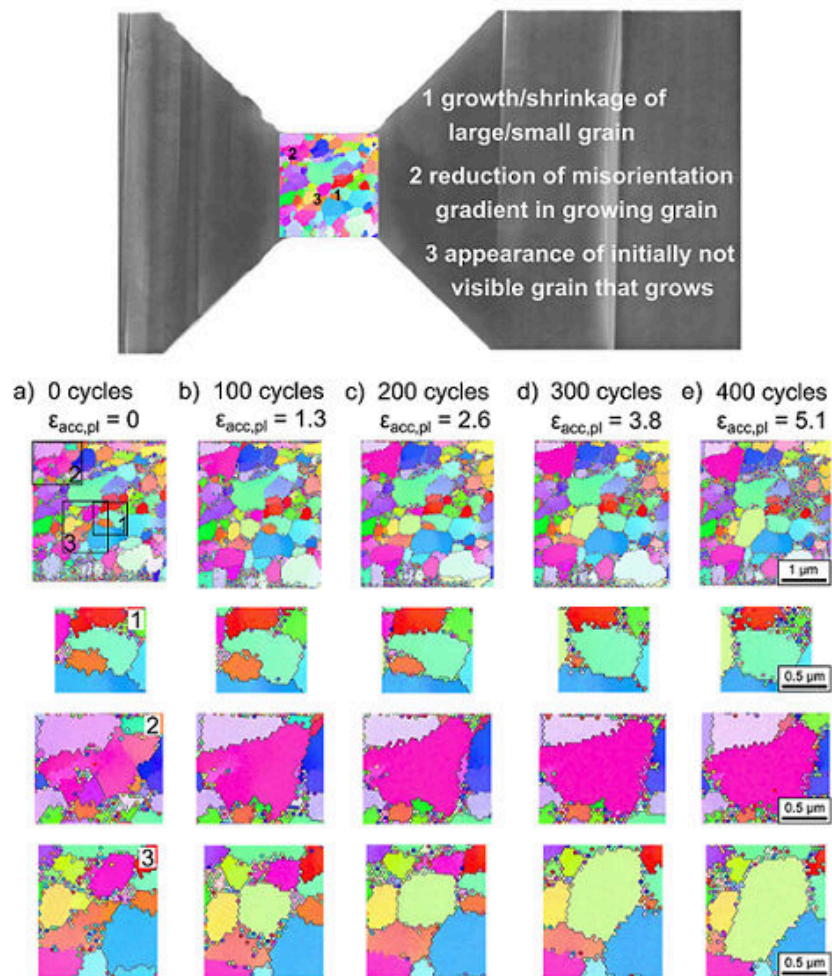


**Figure 3.4** EBSD scans following the evolution of the structure within a copper cantilever gauge section during cyclic loading of the a) initial structure and after b) 100, c) 200, d) 300 and e) 400 cycles taken from [93].

### 3 Experimental observations and summary of publications

The structure in the cyclically deformed cantilever gauge section gets continuously modified by growing and shrinking of grains, however, the formation of a shear band was not observed. This might be a consequence of the small tested volume, being  $3 \times 3 \times 3 \mu\text{m}^3$  in size, which is too small for developing shear bands of multiple grains in thickness [94] [67]. On the other hand, in macroscopic samples deformed by CHPT a pronounced shear band has already developed in the center of the HPT disc after 50 cycles (Fig. 3.5, see N50 in first row). Back scatter electron (BSE) images show the development of a wedge like shape of the shear band, being thinner near the center of the HPT disc (smaller nominal strain amplitude) and increasing in thickness towards the edge (higher nominal strain amplitude). Thus, the thickness of the shear band seems to level out with the nominal strain amplitude. Thus, the local strain amplitude within the shear band does not differ significantly along the HPT disc anymore (compare Table 3.1). With increasing number of cycles the thickness of the shear band grows, maintaining its wedge-like shape, as exemplarily shown for 100 cycles (Fig. 3.5, see N100 in fourth row). Grain size modifications were observed within the shear band (Fig. 3.5, see N50 in third row, TAN viewing direction), as compared to the still equiaxed structure outside the SB (Fig. 3.5, see N50 second row). The grains within the shear band have not only coarsened but are also elongated along the RAD direction.

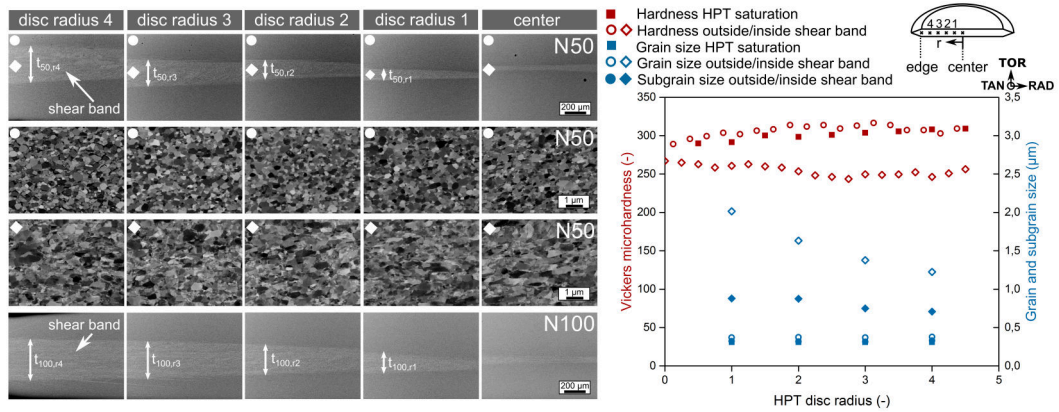


**Figure 3.5** Microhardness inside and outside of the shear band varies according to the subgrains rather than the grains in a sample cycled for 50 times. Doubling the number of cycles to 100 leads to a thickening of the wedge-shaped shear band similar to [95].

The coarsening of the structure is also reflected in the microhardness plots (Fig. 3.5, data points in red), where the hardness drops within the shear band (rhomboids) are attributed to the increase of the structural size, as the damage of the sample is

### 3.3 Microstructural instabilities during cyclic loading conditions

**Table 3.1** Nominal strain amplitudes,  $\epsilon_{a,nom}$ , nominal accumulated strains,  $\epsilon_{acc,nom}$ , shear band thicknesses,  $t_{SB}$ , and local strain amplitude normalized by the shear band thickness setting  $t = t_{SB}$  in Eq. 3,  $\epsilon_{a,loc}$ , are given for 50 and 100 cycle numbers at a twist angle of  $5^\circ$ .

HPT disk radius	$\epsilon_{a,nom}$		$\epsilon_{acc,nom}$		$t_{SB}$ [ $\mu\text{m}$ ]		$\epsilon_{a,loc}$	
	N50	N100	N50	N100	N50	N100	N50	N100
1	0.06		12	24	100	180	0.50	0.28
2	0.13		26	47	180	260	0.56	0.39
3	0.19		38	71	240	330	0.63	0.46
4	0.25		50	95	310	360	0.65	0.56

prohibited by the hydrostatic pressure during CHPT deformation. Similar to the hardness evolution within the shear band, the subgrain size (full blue rhomboids) is also nearly constant along the HPT disc radius, whereas the grain size (empty blue rhomboids) clearly decreases. This suggests that the subgrain boundaries rather than HAGB govern the hardness as observed in other studies [96]. Furthermore, hardness values of Ni samples with  $2 \mu\text{m}$  grain size would be significantly smaller. Although grain size calculations from EBSD scans yielded a slight growth outside of the shear band (blue full and empty circles), it is clearly accelerated within the region of strain localization. Intensified grain growth within the shear band indicates that the applied cyclic strain triggers grain growth and undermines the role of stress assisted grain boundary migration [71] [77] [73] [72]. The importance of cyclic strain on grain growth in UFG metals has not been emphasized so far, although numerous experimental observations point in this direction [65] [79] [66] [67].

To investigate the impact of the strain in more detail it is necessary to differentiate between two parameters that can be adapted during CHPT, which are the strain amplitude per cycle,  $\epsilon_{a,nom}$  (see Eq. 2.3 in experimental part), and the accumulated strain,  $\epsilon_{acc,nom}$  (see Eq. 2.4 in experimental part). Variations of the nominal strain amplitude along the HPT disc radius are inherent to the disc shaped sample, whereas the accumulated strain can be adjusted by the number of cycles applied. Exemplary values are given for 50 and 100 cycles in Table 3.1. As mentioned before, the wedge shape of the shear band along the HPT disc radius balances the nominal strain amplitude, this reduces the actual differences in the local strain amplitudes (see Table 3.1) and may account for the small differences in the subgrain size and microhardness along the HPT disc radius. However, coarsening proceeds further with increasing cycle numbers and so the accumulated strains (Fig. 3.6). The continuous increase of the grain size with cycle number leads to a continuous drop of the microhardness. Analyses of the inverse pole figure (IPF) maps calculated from EBSD data reveal a tendency for specific crystallographic orientations of the coarsened structure (Fig. 3.6). Despite an initial scatter between [101] and [112] in TAN direction, which corresponds to the shear direction in CHPT, a clear preference for [101] becomes visible for the heavily coarsened grains at huge accumulated strains of

### 3 Experimental observations and summary of publications

$\epsilon_{acc,nom} = 6583$  after 4900 cycles. In TOR direction, coarsened grains consist preferentially of (111) planes parallel to the HPT shear plane, allowing for easy plastic deformation. Following [98] the torsional texture components  $\{111\}\langle 101\rangle$  require only a single slip system, which may favor dislocation glide on this system and could account for the preferred coarsening of these grains. The importance of dislocation interaction with grain boundaries for boundary migration in UFG metals has been evidenced from in-situ TEM straining experiments [30] [97]. The interactions lead to the formation of disconnections and their movement cause subsequent displacement of the grain boundary. Thus, enhanced dislocation plasticity in favorably oriented grains could increase the dislocation interactions with grain boundaries and therefore also the generation of such grain boundary defects.

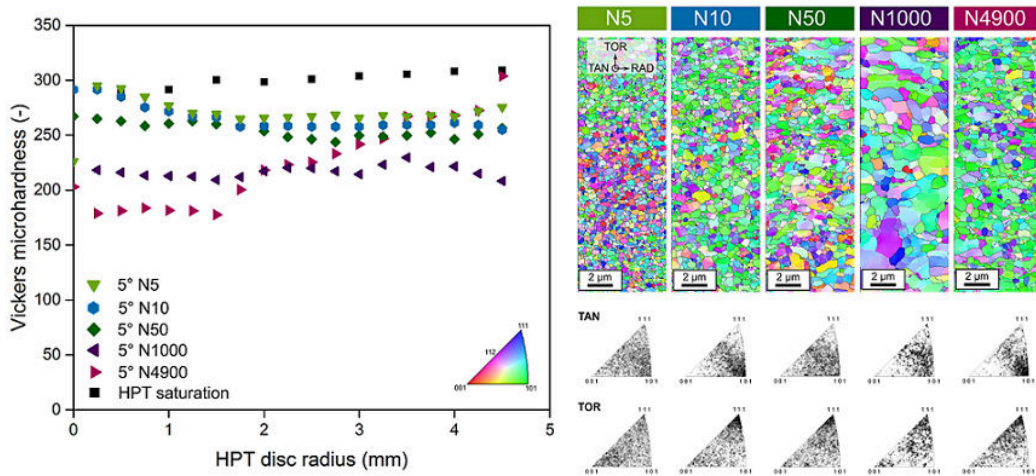


**Figure 3.6** Evolution of microhardness, EBSD scans (taken at an HPT disc radius of 4 mm) as well as crystallographic orientations plotted in IPF maps within the shear band for increasing cycle numbers, thus, increasing accumulated strain. Clearly, with increasing number of cycles the grain size increases and additionally preferred crystallographic orientations develop.

As the growth of grains proceeds with ongoing cyclic strain accumulation an 'ever-lasting' coarsening process could be assumed. This is, however, not the case, which can be shown for the most cycled sample ( $N = 4900$ ). EBSD analysis along the HPT disc radius of this sample (Fig. 3.7) reveal a distinct dependence of the grain and subgrain size and consequently also of the microhardness on the HPT disc radius. As the height of the EBSD scans in the background, spans the entire thickness of the HPT disc and except for the innermost radius fine scaled regions are not visible anymore, the shear band comprises the entire HPT disc volume. Consequently, the measured grain size and hardness values have to depend on the nominal strain amplitude, as variations of the local strain amplitude, e.g. within and outside of

### 3.3 Microstructural instabilities during cyclic loading conditions

the shear band, have vanished. This allows for the conclusion, that once the shear band occupies the entire HPT disc the coarsening process is governed by the nominal strain amplitude, determining the coarsened grain sizes which are smaller for high nominal strain amplitudes and larger for smaller strain amplitudes according to earlier CHPT experiments [99]. The grain size of the most cycled sample ( $N = 4900$ ) is  $1.6 \mu\text{m}$  at an HPT disc radius of 4 mm which is not significantly larger as compared to the grain size of  $1.2 \mu\text{m}$  of a sample cycled for only 50 times (compare Fig. 3.5). It is interesting to note that during the period of shear band growth grains have already grown up to  $7 \mu\text{m}$  after 1000 cycles. Thus, it appears that a refinement of the structure has taken place again once the thickness of the shear band equalled the HPT disc, e.g. between 1000 and 4900 cycles (compare EBSD scans in Fig. 3.6). This means that the coarsening process cannot proceed to 'infinity' as eventually the coarsened grain size is determined by the nominal strain amplitude.

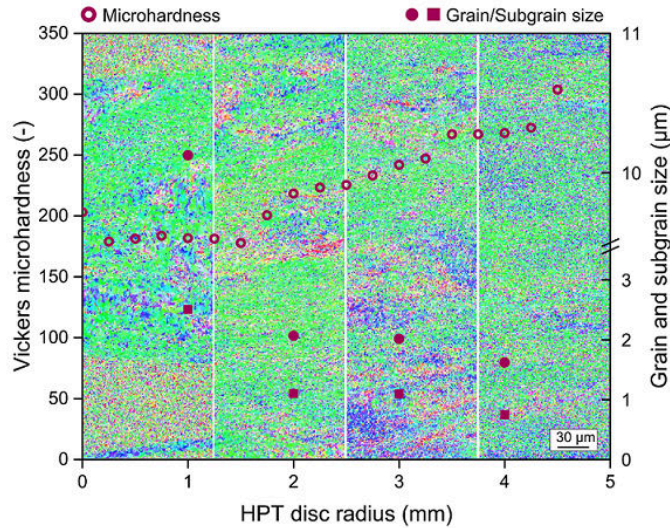


**Figure 3.7** Microhardness, grain and subgrain size as a function of the HPT disc radius, thus nominal strain amplitude for  $N=50$  at  $\Theta=5^\circ$ . EBSD scans in the background span the entire HPT disc height and show that except for the very center the shear bands comprises the entire sample.

The observations of grain coarsening being accelerated by a strain localization and further amplified by the accumulated strain during the shear band growth period, together with the evolution of torsional deformation texture components strongly points out to a mechanical activation of grain growth by the applied cyclic strain. The possibility to mechanically activate grain growth during cyclic loading without thermal contribution is still debated in literature [13] [87]. Although the occurrence of only deformation texture components already questions recrystallization arguments, additional CHPT experiments have been performed under cryogenic

### 3 Experimental observations and summary of publications

conditions (77 K) to clarify this possibility. Similarities in the coarsening procedure to CHPT performed at room temperature confirm that thermal activation of grain boundaries is not required for their migration (Fig. 3.8). Already after 50 cycles shear bands traversing the center of the HPT disc are visible in BSE images. EBSD scans taken within the shear band show a significant coarsening of the structure compared to the steady state grain size before cycling. Increasing the cycle number to 500 leads to the formation of multiple shear bands, consisting of a similar coarsened structure. Microhardness indents located in the shear band beyond an HPT disc radius of 3 mm demonstrate cyclic softening and further prove that thermal activation is not a prerequisite for cyclically induced grain growth.

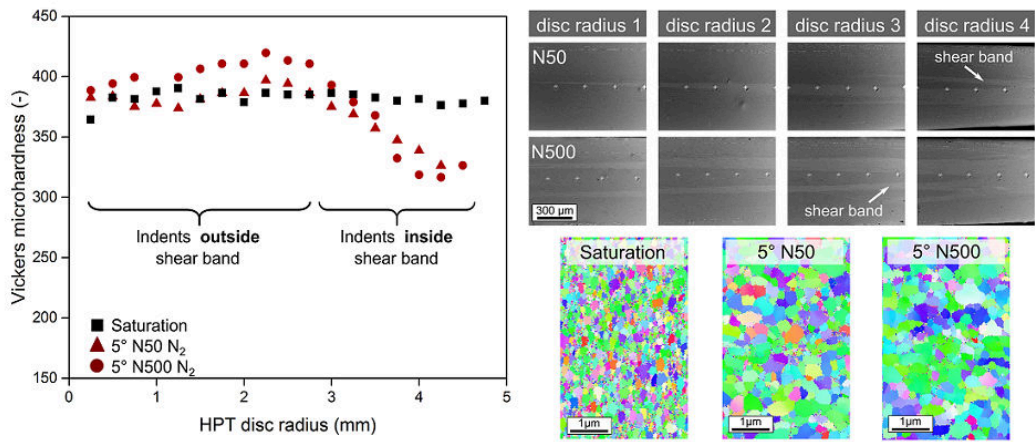


**Figure 3.8** Microhardness and shear band evolution after CHPT at 77K for 50 and 500 cycles. BSE images along the HPT disc radius show the formation of shear bands after 50 and 500 cycles and EBSD scans of the shear band demonstrate significant coarsening.

#### 3.3.2 Pearlitic steel

The micro compression experiments revealed a strong influence of the lamellar orientation on the type of strain localization and, thus, on the achievable strength. Modifying the load path from compression to bending, enabled suppression of catastrophic shear band development when the lamellae were aligned normal with respect to the loading direction. However, as shown for the copper cantilevers under cyclic loading conditions still grain growth can modify the HPT processed structure and deteriorate the mechanical performance. Therefore, similar experiments were conducted on the NL pearlitic steel to elucidate the effect of interfaces on a potential coarsening process. The cyclic loading of the pearlitic steel revealed pronounced softening at  $\epsilon_{a,pl} = 2.5 \times 10^{-3}$  (Fig. 3.9) although at a somewhat lower strain am-

### 3.3 Microstructural instabilities during cyclic loading conditions

plitude at which first observations of grain growth in the copper cantilevers were depicted ( $\epsilon_{a,pl} = 3.2 * 10^{-3}$ ). Within 200 cycles the surface stress dropped by 655 MPa, which would in principal suggest a collapse of the structure. SEM images taken from the cantilever surface neither show signs of grain coarsening nor catastrophic shear bands (Fig. 3.10) but damage in the highly strained region of the cantilever. Two pronounced cracks grow from the outer fiber towards the neutral axis and account for the pronounced stress drop as the effective cantilever cross section sustaining the imposed strain is reduced significantly. Similarly to unidirection bending experiments large scale shear bands are probably infeasible to develop due to the gradient distribution of the stress and strains, getting smaller towards the neutral axis. Thus, a cyclic stress range of 6 GPa (assuming predominantly elastic deformation) could be achieved by preventing shear banding and grain growth in layered structures.

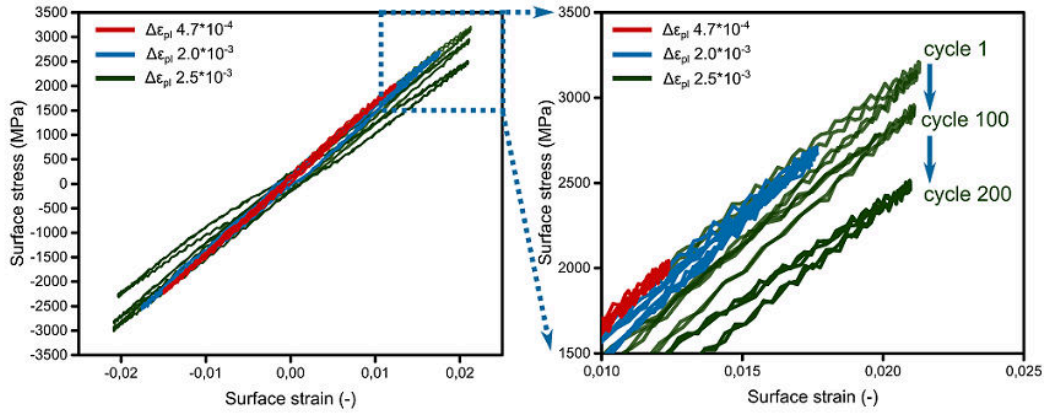


**Figure 3.9** Cyclic stress-strain curves of the pearlitic nanocomposite for different strain amplitudes. Only the last cycle per strain amplitude is shown for  $\epsilon_a = 4.7 * 10^{-4}$  and  $\epsilon_a = 2.0 * 10^{-3}$ , whereas for  $\epsilon_a = 2.5 * 10^{-3}$  the softening from the 1. over the 100. to the 200. cycle is visible.

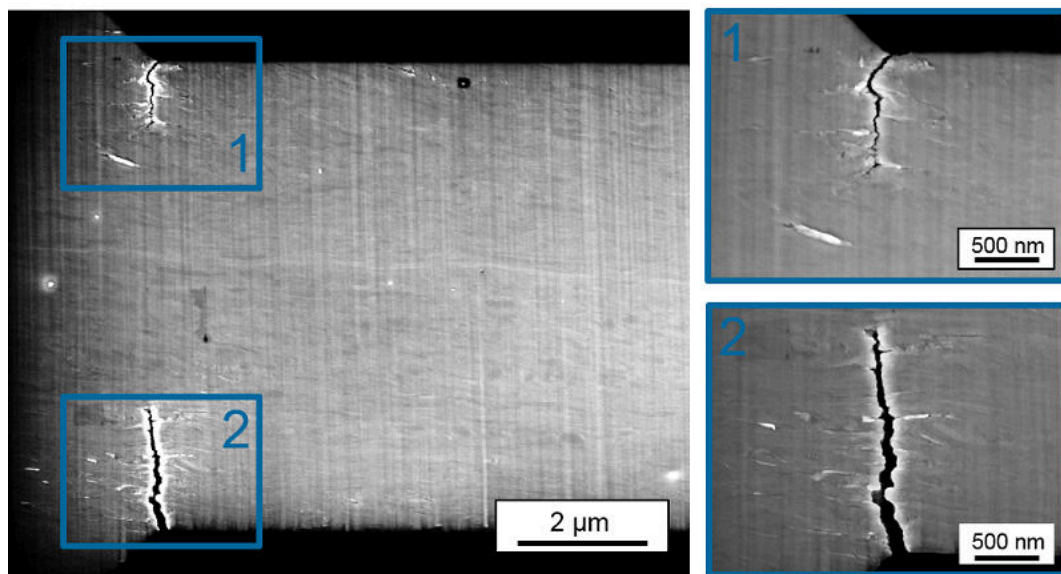


**Figure 3.10** SEM images of the cycliced pearlitic micro cantilever. Cracks have grown from the outer fiber towards the neutral axis, but significant grain coarsening and shear bands are not detectable.

# 4

## Conclusions

Static and cyclic mechanical experiments have been conducted on UFG copper and nickel, as well as on a nanolamellar pearlitic high strength steel. The manifold experimental efforts led to a deeper knowledge about the evolution of grain coarsening and shear banding. Cyclic loading of pure UFG metals leads to the coarsening of the grain structure and in the formation of shear bands in macro samples. The main findings are the following:

1. Shear bands develop only in sufficiently large samples accompanied by a coarsening of the structure. The resulting cyclic softening in that region further promotes cyclic slip and strain localization.
2. Grain growth occurs by the continuous migration of high angle grain boundaries, whereas small angle grain boundaries persist unless their neighborhood is significantly altered. The preferential growth of grains favorably aligned for cyclic torsional slip strengthens the idea that the interactions of lattice dislocations with grain boundaries trigger the growth process.
3. The occurrence of enlarged grains within shear bands even at cryogenic conditions confirms that a thermal activation of grain boundaries is not a prerequisite for their migration. This is further supported by the evolution of deformation texture components in the coarsened regions. Amplified grain growth observed within regions of strain localization and its acceleration by the accumulated strain emphasize the importance of the cyclic strain over the stress.
4. Although grain coarsening is accelerated by the accumulated strain during the period of shear band growth, once the thickness of the shear band comprises

#### 4 Conclusions

the entire HPT disc height the nominal strain amplitude determines the size of coarsened grains.

5. Grain coarsening significantly deteriorates the cyclic strength of these materials, which could be depicted by a steady drop of the microhardness with increasing size of the grains. Such correlation up to large numbers of cycles was only feasible because the hydrostatic pressure during CHPT offers the unique possibility to suppress the evolution of damage in the sample, e.g. the formation of cracks.

The pearlitic steel is prone to shear banding leading subsequently to softening and catastrophic failure in static compression experiments, but turned out to be stable when loaded in bending mode. The primary conclusions are as follows:

6. The stress-strain response for the parallel and normal loading of the lamellae is a fingerprint for a composite-like behavior, characterized by three deformation regimes: 1) ferrite and cementite deform elastically; 2) softer ferrite starts to yield, cementite stays elastic; 3) harder cementite contributes to plastic deformation.
7. Exceptional strain hardening within the ferrite phase in deformation mode 2, causing in part the strength of almost 4 GPa, is realized by the elastic response of the cementite (carbon rich phase). Plastic deformation of the cementite permits strain localization, shutting of strain hardening and cause catastrophic failure.
8. The type of instability mechanism is sensitive to the lamellar alignment with respect to the loading direction: shearing of the cementite for perpendicular loading induces a shear band, buckling of the cementite for parallel loading originates in a kink band, confined layer slip in the ferrite parallel to the cementite lamellae introduces shear band in the inclined pillars at stress levels well below the elastic limit of the cementite.
9. Changing the load path from compression to bending prevents catastrophic shear bands to form. The distribution of the imposed stresses and strain in form of a gradient impedes the expansion of small shear bands initiated at the outer fiber, as the decreasing stresses towards the neutral axis may not be sufficient to bend the cementite and destroy the lamellar structure.
10. In case of cyclic bending deterioration of the 6 GPa cyclic stress range is caused by crack initiation at the highly strained outer fiber and its subsequent growth towards the neutral axis. The lamellar architecture consisting of two phases turns out to be stable against cyclically induced grain growth.

# Bibliography

- [1] R.Z. Valiev, R.K. Islamgaliev, I.V. Alexandrov, Bulk nanostructured materials from severe plastic deformation, *Prog. Mater. Sci.* 45 (2000) 103-189.
- [2] M.A. Meyers, A. Mishra, D.J. Benson, Mechanical properties of nanocrystalline materials, *Prog. Mater. Sci.* 51 (2006) 427-556.
- [3] M. Dao, L. Lu, R. Asaro, J. Dehossan, E. Ma, Toward a quantitative understanding of mechanical behavior on nanocrystalline metals, *Acta Mater.* 55 (2007) 4041-4065.
- [4] O.E. Hall The Deformation and Ageing of Mild Steel: III Discussion of Results, *Proc. Phys. Soc.* 64 (1951) 747-753.
- [5] H. Gleiter, Nanocrystalline materials, *Prog. Mater.Sci.* 33 (1989) 223-315.
- [6] V.M. Segal, Equal channel angular extrusion: from macromechanics to structure formation, *Mater. Sci. Eng. A* 271 (1999) 322-333.
- [7] Y. Saito, H. Utsunomiya, N. Tsuji, T. Sakai, Novel ultra-high straining process for bulk materials - development of the accumulative roll bonding (ARB) process, *Acta Mater.* 47 (1999) 579-583.
- [8] R.Z. Valiev, Y. Estrin, Z. Horita, T.G. Langdon, M.J. Zehetbauer, Y.T. Zhu, Producing bulk ultrafine-grained materials by severe plastic deformation, *JOM* 58 (2006) 33-39.
- [9] R. Wadsack, R. Pippan, B. Schedler, Structural refinement of chromium by severe plastic deformation, *Fusion Eng. Des.* 66-68 (2003) 265-269.
- [10] M. Faleschini, H. Kreuzer, D. Kiener, R. Pippan, Fracture toughness investigations of tungsten alloys and SPD tungsten alloys, *J. Nucl. Mater* 367-370 (2007) 800-805.
- [11] Y. Li, D. Raabe, M. Herbig, P. Choi, S. Goto, A. Kostka, Segregation Stabilizes Nanocrystalline Bulk Steel with Near Theoretical Strength, *Phys. Rev. Lett.* 113 (2014) 106104.
- [12] A. Hohenwarter, B. Völker, M.W. Kapp, Y. Li, S. Goto, D. Raabe, R. Pippan, Ultra-strong and damage tolerant metallic bulk materials: A lesson from nanostructured pearlitic steel wires, *Sci. Rep.* 6 (2016) 33228.

## Bibliography

- [13] H.W. Höppel, Z.M. Zhu, H. Mughrabi, R.Z. Valiev, Microstructural study of the parameters governing coarsening and cyclic softening in fatigued ultrafine-grained copper, *Philos. Mag. A* 82 (2002) 1781-1794.
- [14] L.Kunz, P. Lukáš, M. Svoboda, *Mater. Sci. Eng. A* 424 (2006) 97-104.
- [15] P.W. Bridgeman, Effects of High Shearing Stress Combined with High Hydrostatic Pressure, *Phys. Rev.* 48 (1935) 825-847.
- [16] A. Vorhauer, R. Pippan, On the homogeneity of deformation by high pressure torsion, *Scripta Mater.* 51 (2004) 921-925.
- [17] R. Pippan, S. Scheriau, A. Taylor, M. Hafok, A. Hohenwarter, A. Bachmaier, *Annu. Rev. Mater. Res.* 40 (2010) 319-343.
- [18] Q. Liu, X. Huang, D.J. Lloyd, N. Hansen, Microstructure and strength of commercial purity aluminium (AA 1200) cold-rolled to large strains, *Acta Mater.* 50 (2002) 3789-3802.
- [19] Y. Li, C. Borchers, S. Goto, D. Raabe, R. Kirchheim, Atomic-scale mechanisms of deformation induced cementite decomposition in pearlite, *Acta Mater.* 59 (2011) 3965-3977.
- [20] F. Wetscher, R. Pippan, S. Sturm, F. Kauffmann, C. Scheu, G. Dehm, TEM investigations of the structural evolution in a pearlitic steel deformed by high-pressure torsion, *Metall. Mater. Trans. A* 37 (2006) 1963-1968.
- [21] X. Sauvage, Y. Ivanisenko, The role of carbon segregation on nanocrystallisation of pearlitic steels processed by severe plastic deformation, *J. Mater. Sci.* 42 (2007) 1615-1621.
- [22] A. Hohenwarter, A. Taylor, R. Stock, R. Pippan, Effect of Large Shear Deformation on the Fracture Behavior of a Fully Pearlitic Steel, *Metall. Mater. Trans. A* 42 (2011) 1609-1618.
- [23] Y. Ivanisenko, W. Lojkwski, R.Z.Valiev, H.-J. Fecht, The mechanism of formation of nanostructure and dissolution of cementite in a pearlitic steel during high pressure torsion, *Acta Mater.* 51 (2013) 5555-5570.
- [24] Z. Shan, E.A. Stach, J.M.K. Wiezorek, J.A. Knapp, D.M. Follstaedt, S.X. Mao, Grain boundary-mediated plasticity in nanocrystalline nickel, *Science* 305 (2004) 654-657.
- [25] D.A. Hughes, N. Hansen, Exploring the Limit of Dislocation Based Plasticity in Nanostructured Metals, *Phys. Rev. Lett.* 112 (2014) 13504.
- [26] H. van Swygenhoven, P.M. Derlet, A. Hasnaoui, Atomic mechanism for dislocation emission from nanosized grain boundaries, *Phys. Rev. B* 66 (2002) 024101.

- [27] N. Wang, Z. Wang, K.T. Aust, U. Erb, Room temperature creep behavior of nanocrystalline nickel produced by an electrodeposition technique, *Mater. Sci. Eng. A* 237 (1997) 150-158.
- [28] M. Ke, S.A. Hackney, W.W. Milligan, E.C. Aifantis, Observation and measurement of grain rotation and plastic strain in nanostructured metal thin films, *Nanostruct. Mater* 5 (1995) 689-697.
- [29] F. Momprou, M. Legros, A. Bo e, M. Coulobrier, J.-P. Raskin, T. Pardoen, Inter- and intragranular plasticity mechanisms in ultrafine-grained Al thin films: An in situ TEM study, *Acta Mater.* 61 (2013) 205-216.
- [30] A. Rajabzadeh, M Legros, N. Combe, F. Momprou, D.A. Molodov, Evidence of grain boundary dislocation step motion associated to shear-coupled grain boundary, *Philos. Mag.* 93 (2013) 1299-1316.
- [31] F. Momprou, D. Caillard, M. Legros, H. Mughrabi, In situ TEM of reverse dislocation motion upon unloading in tensile-deformed UFG aluminium, *Acta Mater.* 60 (2014) 3402-3414.
- [32] A. Misra, J.P. Hirth, R.G. Hoagland, J.D. Embury, H. Kung, Dislocation mechanisms and symmetric slip in rolled nano-scale metallic multilayers, *Acta Mater.* 52 (2004) 2387-2394.
- [33] A. Misra, J.P. Hirth, R.G. Hoagland, Length-scale-dependent deformation mechanisms in incoherent metallic multilayered composites, *Acta Mater.* 53 (2005) 4817-4824.
- [34] A. Misra, M. Verdier, Y.C. Lu, H. Kung, T.E. Mitchell, M. Nastasi, J.D. Embury, Structure and mechanical properties of Cu-X(X=Nb,Cr,Ni) nanolayered composites, *Scripta Mater.* 39 (1998) 555-560.
- [35] N.A. Mara, D. Bhattacharyya, J.P. Hirth, P. Dickerson, A. Misra, Mechanism for shear banding in nanolayered composites, *Appl. Phys. Lett.* 97 (2010) 021909.
- [36] M. Janecek, F. Louchet, B. Doisneau-Cottignies, Y. Br chet, N. Guelton, Specific dislocation multiplication mechanisms and mechanical properties in nanoscaled multilayers: The example of pearlite, *Philos. Mag.* 80 (2009) 1605-1619.
- [37] F. Louchet, B. Doisneau-Cottignies, O. Calonne, A. Fraczkiewicz, M. Janecek, N. Guelton, Is dislocation flow always controlled by dislocation mobility? An answer from in situ transmission electron microscopy straining tests, *J. Microsc.* 203 (2011) 84-89.
- [38] N. Abdolrahim, H.M Zbib, D.F. Bahr, Multiscale modeling and simulation of deformation in nanoscale metallic multilayer systems, *Int. J. Plasticity* 52 (2014) 33-50.

## Bibliography

- [39] F. Adcock, The internal mechanism of cold-work and recrystallization in Cupro-Nickel, *J. Inst. Met.* 27 (1922) 73-92.
- [40] J. Gil Sevillano, P. van Houtte, E. Aernoudt, The contribution of macroscopic shear bands to the rolling texture of FCC metals, *Scripta Metall. Mater.* 11 (1977) 581-585.
- [41] I.L. Dillamore, J.G. Roberts, A.C. Bush, Occurrence of shear bands in heavily rolled cubic metals, *Met. Sci.* 13 (1979) 73-77.
- [42] J.D. Embury, J.P. Hirth, On dislocation storage and the mechanical response of fine sclaе microstructure, *Acta Metall. Mater.* 42 (1994) 2015-2056.
- [43] J.E. Carsley, A. Fisher, W.W. Milligan, E.C. Aifantis, Mechanical behavior of a bulk nanostructured iron alloy, *Metall. Mater. Trans. A* 29 (1998) 2261-2271.
- [44] D. Jia, K.T. Ramesh, E. Ma, Effects of nanocrystalline and ultrafine grain sizes on constitutive behavior and shear bands in iron, *Acta Mater.* 51 (2003) 3495-3509.
- [45] Q. Wei, K.T. Ramesh, E. Ma, L.J. Kesckes, R.J. Dowding, V.U. Kazykhanov, R.Z. Valiev, Plastic flow localization in bulk tungsten with ultrafine microstructures, *Appl. Phys. Lett.* 86 (2005) 101907.
- [46] R. Zhu, J. Zhou, H. Jiang, X. Ling, Investigation of shear-banding mechanism in fully dense nanocrystalline Ni sheet, *Mater. Charact.* 61 (2010) 396-401.
- [47] B.J. Duggan, M. Hatherly, W.B. Hutchinson, P.T. Wakefield, Deformation structures and textures in cold-rolled 70:30 brass, *Met. Sci.* 12 (1978) 343-351.
- [48] T.J. Rupert, Strain localization in a nanocrystalline metal: Atomic mechanisms and the effect of testing conditions, *J. Appl. Phys.* 114 (2013) 033527.
- [49] I. Knorr, N.M. Cordero, E.T. Lilleodden, C.A. Volkert, Mechanical behavior of nanoscale Cu/PdSi Multilayers, *Acta Mater.* 61 (2013) 4984-4995.
- [50] S.J. Zheng, J. Wang, J.S. Carpenter, W.M. Mook, P.O. Dickerson, N.A. Mara, I.J. Beyerlein, Plastic instability mechanisms in bimetallic nanolayered composites, *Acta Mater.* 79 (2014) 282-291.
- [51] I. Beyerlein, N.A. Mara, J.S. Carpenter, T. Nizolek, W.M. Mook, T.A. Wynn, Interface-driven microstructure development and ultra high strength of bulk nanostructured Cu-Nb multilayers fabricated by severe plastic deformation, *J. Mater. Res.* 28 (2013) 1799-1812.
- [52] W. Guo, B. Gan, J.M. Molina-Aldareguia, J.D. Poplawsky, D. Raabe, Structure and dynamics of shear bands in amorphous-crystalline nanolaminates, *Scripta Mater.* 110 (2016) 28-32.

- [53] D.A. Porter, K.E. Easterling, G.D.W. Smith, Dynamic studies of the tensile deformation and fracture of pearlite, *Acta Metall. Mater.* 26 (1978) 1405-1422.
- [54] J.A. Ewing, J.C.W. Humfrey, The Fracture of Metals under Repeated Alternations of Stress, *Philos. Trans. R. Soc. Lond.* 200 (1903) 241-250.
- [55] E.E. Laufer, W.N. Roberts, Dislocations and persistent slip bands in fatigued copper, *Philos. Mag.* 14 (1966) 65-78.
- [56] H. Mughrabi, Fatigue, an everlasting materials problem - still en vogue, *Proc. Eng.* 2 (2010) 3-26.
- [57] N. Thomson, N. Wadsworth, N. Louat, The origin of fatigue fracture in copper , *Philos. Mag.* 1 (1956) 113-126.
- [58] A.H. Cottrell, D. Hull, Extrusion and Intrusion by Cyclic Slip in Copper, *Proc. R. Soc. A* 242 (1957) 211-213.
- [59] S.R. Agnew, J. Weertman, Cyclic softening of ultrafine grain copper, *Mat. Sci. Eng. A* 244 (1998) 145-153.
- [60] S.R. Agnew, A.Y. Vinogradov, S. Hashimoto, J.R. Weertman, Overview of fatigue performance of Cu processed by severe plastic deformation, *J. Electron. Mater.* 28 (1999) 1038-1044.
- [61] A. Vinogradov, Y. Kaneko, K. Kitagawa, S. Hashimoto, R.Z. Valiev, On the Cyclic Response of Ultrafine-Grained Copper, *Mater. Sci. Forum* 269-272 (1998) 987-992.
- [62] W. Wong, W. Kao, J. Lui, C. Chang, P. Kao, Cyclic deformation of ultrafine-grained aluminum, *Acta Mater.* 55 (2007) 715-725.
- [63] H. Mughrabi, H.W. Höppel, Cyclic deformation and fatigue properties of very fine-grained metals and alloys, *Int. J. Fatigue* 32 (2010) 1413-1427.
- [64] S.D. Wu, Z.G. Wang, C.B. Jiang, G.Y. Li, I.V. Alexandrov, R.Z. Valiev, Shear bands in cyclically deformed ultrafine grained copper processed by ECAP, *Mater. Sci. Eng. A* 387-389 (2004) 560-564.
- [65] H.W. Höppel, C. Xu, M. Kautz, N. Barta-Schreiber, T.G. Langdon, H. Mughrabi, Cyclic Deformation Behaviour and Possibilities for Enhancing the Fatigue Properties of Ultrafine-Grained Metals. In: M. Zehetbauer, R.Z. Valiev (Eds.) *Nanomaterials by Severe Plastic Deformation* (2004) 677-683.
- [66] C.F. Kwan, Z. Wang, A composite nature of cyclic strain accommodation mechanisms of accumulative roll bonding (ARB) processed Cu sheet materials, *Mater. Sci. Eng. A* (2011) 2042-2048.

## Bibliography

- [67] S. Malekjanie, P.D. Hodgson, N.E. Stanford, T.B. Hilditch, Shear bands evolution in ultrafine-grained aluminium under cyclic loading, *Scripta Mater.* 68 (2013) 821-824.
- [68] G. Gottstein, L.S. Shvindlerman, Grain boundary migration in metals: Thermodynamics, Kinetics, Applications, CRC press (2009).
- [69] M. Jin, A.M. Minor, E.A. Stach, J.W. Morris, Direct observation of deformation-induced grain growth during the nanoindentation of ultrafine-grained Al at room temperature, *Acta Mater.* 52 (2004) 5381-5387.
- [70] K. Zhang, J.R. Weertman, J.A. Eastman, Rapid stress-driven grain coarsening in nanocrystalline Cu at ambient and cryogenic temperatures, *Appl. Phys. Lett.* 87 (2005) 061921.
- [71] D.S. Gianola, D.H. Warner, J.F. Molinari, K.J. Hemker, Increased strain rate sensitivity due to stress-coupled grain growth in nanocrystalline Al, *Scripta Mater.* 55 (2006) 649-652.
- [72] M. Legros, D.S. Gianola, K.J. Hemker, In situ TEM observations of fast grain-boundary motion in stress nanocrystalline aluminum films, *Acta Mater.* 56 (2008) 3380-3393.
- [73] Y. Zhang, J.A. Sharon, G.L. Hu, K.T. Ramesh, K.J. Hemker, Stress-driven grain growth in ultrafine grained Mg thin film, *Scripta Mater.* 68 (2013) 424-427.
- [74] D.S. Gianola, B.G. Mendis, X.M. Cheng, K.J. Hemker, Grain-size stabilization by impurities and effect on stress-coupled grain growth in nanocrystalline Al thin films, *Mater. Sci. Eng. A* 483-484 (2008) 637-640.
- [75] D. Canadunca, T. Niendorf, H.J. Maier, A comprehensive evaluation of parameters governing the cyclic stability of ultrafine-grained FCC alloys, *Mater. Sci. Eng. A* 528 (2011) 6345-6355.
- [76] F. Momprou, M. Legros, Quantitative grain growth and rotation probed by in-situ TEM straining and orientation mapping in small grained Al thin films, *Scripta Mater.* 99 (2015) 5-8.
- [77] T.J. Rupert, D.S. Gianola, Y. Gan, K.J. Hemker, Experimental observations of stress-driven grain boundary migration, *Science* 326 (2009) 1686-1690.
- [78] F. Momprou, D. Caillard, M. Legros, Grain boundary shear-migration coupling - I. In situ TEM straining experiments in Al polycrystals, *Acta Mater.* 57 (2009) 2198-2209.
- [79] T.H. Fang, W.L. Li, N.R. Tao, K. Lu, Revealing extraordinary intrinsic tensile plasticity in nano-grained copper, *Science* 331 (2011) 1587-1590.

- [80] D. Kiener, C. Motz, M. Rester, M. Jenko, G. Dehm, FIB damage of Cu and possible consequences for miniaturized mechanical tests, *Mater. Sci. Eng. A* 459 (2007) 262-272.
- [81] L.A. Gianuzzi, ed. *Introduction to focused ion beams: instrumentation, theory, techniques and practice*, Springer Science & Business Media (2006).
- [82] S. Wurster, R. Treml, R. Fritz, M.W. Kapp, E. Langs, M. Alfreider, C. Ruhs, P.J. Imrich, G. Felber, D. Kiener, Novel Methods for the Site Specific Preparation of Micromechanical Structures, *PM* 52 (2015) 131-146
- [83] J.D. Embury, R.M. Fisher, The structure and properties of drawn pearlite, *Acta Metall. Mater.* 14 (1966) 147-159.
- [84] G. Langford, Deformation of pearlite, *Metall. Trans. A* 8 (1977) 861-875.
- [85] M.W. Kapp, A. Hohenwarter, S. Wurster, B. Yang, R. Pippan, Anisotropic deformation characteristics of an ultrafine- and nanolamellar pearlitic steel, *Acta Mater.* 106 (2016) 239-248.
- [86] L. Thilly, M. Véron, O. Ludwig, F. Lecouturier, J.P. Peyrade, S. Askénazy, High-strength materials: in-situ investigations of dislocation behaviour in Cu-Nb multifilamentary nanostructured composites, *Phil. Mag. A* 82 (2002) 925-942.
- [87] H. Mughrabi, H.W. Höppel, M. Kautz, Fatigue and microstructure of ultrafine-grained metals produced by severe plastic deformation, *Scripta Mater.* 51 (2004) 807-812.
- [88] T. Hanlon, Grain size effects on the fatigue response of nanocrystalline metals, *Scripta Mater.* 49 (2003) 675-680.
- [89] T. Hanlon, E. Tabachnikova, S. Suresh, Fatigue behavior of nanocrystalline metals and alloys, *Int. J. Fatigue* 27 (2005) 1147-1158.
- [90] O. Renk, A. Hohenwarter, S. Wurster, R. Pippan, Direct evidence of grain boundary motion as the dominant restoration mechanism in the steady-state regime of extremely cold-rolled copper, *Acta Mater.* 77 (2014) 401-410.
- [91] P. Ghosh, O. Renk, R. Pippan, Microtexture analysis of restoration mechanisms during high pressure torsion of pure nickel, *Mater. Sci. Eng. A* 684 (2017) 101-109.
- [92] A. Rollett, F.J. Humphreys, G.S. Rohrer, M. Hatherly, *Recrystallization and Related Annealing Phenomena*, Elsevier (2004).
- [93] M.W. Kapp, T. Kremmer, C. Motz, B. Yang, R. Pippan, Structural instabilities during cyclic loading of ultrafine-grained copper studied with micro bending experiments, *Acta Mater.* 125 (2017) 351-358.

## *Bibliography*

- [94] H.W. Höppel, Mechanical Properties of Ultrafine Grained Metals under Cyclic and Monotonic Loads: An Overview, *Mater. Sci. Forum* 503-504 (2006) 259-266.
- [95] M.W. Kapp, O. Renk, T. Leitner, P. Ghosh, B. Yang, R. Pippan, Cyclically induced grain growth within shear bands investigated in UFG nickel by cyclic high pressure torsion, Accepted for publication in *J. Mat. Res.*
- [96] E. Schafler, R. Pippan, Effect of thermal treatment on microstructure in high pressure torsion (HPT) deformed nickel, *Mater. Sci. Eng. A* 387-389 (2004) 799-804.
- [97] A. Rajabzadeh, F. Momprou, S. Lartigue-Korinek, N. Combe, M. Legros, D.A. Molodov, The role of disconnections in deformation-coupled grain boundary migration, *Acta Mater.* 77 (2014) 223-235.
- [98] L. Toth, P. Gilormini, J. Jonas, Effect of rate sensitivity on the stability of torsion textures, *Acta Metall. Mater.* 36 (1988) 3077-3091.
- [99] F. Wetscher, R. Pippan, Cyclic high-pressure torsion of nickel and Armco iron, *Philos. Mag.* 86 (2006) 5867-5883.

# 5

## List of appended papers

### Paper A

M.W. Kapp, C. Kirchlechner, R. Pipan and G. Dehm

*Importance of dislocation pile-ups on the mechanical properties and the Bauschinger effect in microcantilevers*

Journal of Materials Research, 2015; 30:791-797

### Paper B

M.W. Kapp, A. Hohenwarter, S. Wurster, B. Yang and R. Pippan

*Anisotropic deformation characteristics of an ultrafine- and nanolamellar pearlitic steel*

Acta Materialia 2016; 106:239-248

### Paper C

A. Hohenwarter, B. Völker, M.W. Kapp, Y. Li, S. Goto, D. Raabe and R. Pippan

*Ultra-strong and damage tolerant metallic bulk materials: A lesson from nanostructured pearlitic steel wires*

Scientific Reports 2016; 6:33228

### Paper D

M.W. Kapp, T. Kremmer, C. Motz, B. Yang and R. Pippan

*Structural instabilities during cyclic loading of ultrafine-grained copper studied with micro bending experiments*

Acta Materialia 2017; 125:351-358

5 *List of appended papers*

**Paper E**

M.W. Kapp, O. Renk, P. Ghosh, T. Leitner, B. Yang and R. Pippan

*Cyclically induced grain growth within shear bands investigated in UFG nickel by cyclic high pressure torsion*

Accepted for publication in Journal of Materials Research

**Paper F**

A. Hohenwarter, M.W. Kapp, B. Völker, O. Renk and R. Pippan

*Strength and ductility of heavily deformed pearlitic microstructures*

Accepted for publication in Proceedings of the 38th Risø Symposium on Materials Science

**Paper G**

M.W. Kapp, O. Renk, P. Ghosh, T. Leitner, B. Yang and R. Pippan

*Fatigue induced instabilities studied by inexhaustible ultrafine-grained samples*

Manuscript in preparation, will be submitted to SCI journal.

## Remark

In the appended papers, myself, Marlene Kapp, performed all experiments, the data analyses and the composition of the publications with the following exceptions:

- **In paper B**  
Dr. Anton Hohenwarter performed the macroscopic compression test.
- **In paper C**  
Dr. Anton Hohenwarter performed the macroscopic fracture experiments and Dr. Bernhard Volker prepared the micro cantilevers by FIB milling, but myself, Marlene Kapp, was responsible for the entire micro mechanical testing procedure.
- **In paper D**  
Dr. Thomas Kremmer performed one of the fatigue experiments and prepared the sample by FIB milling.
- **In paper E**  
Dr. Thomas Leitner developed the control unit for the cyclic high pressure torsion setup.
- **In paper F**  
Dr. Anton Hohenwarter performed the macroscopic fracture experiments, but myself, Marlene Kapp, was responsible for the entire micro mechanical fracture and compression experiments.
- **In paper G**  
Dr. Thomas Leitner developed the control unit for the cyclic high pressure torsion setup.
- My supervisors Prof. Dr. Reinhard Pippan and Dr. Bo Yang participated in all the papers by giving the basic ideas for the publications and with helpful discussions during their preparation.





# Importance of dislocation pile-ups on the mechanical properties and the Bauschinger effect in microcantilevers

M.W. Kapp<sup>a,b</sup>, C. Kirchlechner<sup>b,c</sup>, R. Pippan<sup>a</sup>, G. Dehm<sup>a,b,c</sup>

<sup>a</sup>Erich Schmid Institute of Materials Science, Austrian Academy of Sciences, 8700 Leoben, Austria

<sup>b</sup>Department of Materials Physics, Montanuiversität Leoben, Jahnstrasse 12, 8700 Leoben, Austria

<sup>c</sup>Max-Planck-Institut für Eisenforschung, Düsseldorf 40237, Germany

## Abstract

Copper microcantilevers were produced by focused ion beam milling and tested in situ using a scanning electron microscope. To provide different interfaces for piling up dislocations, cantilevers were fabricated to be single crystalline, bicrystalline, or single crystalline with a slit in the region of the neutral axis. The aim of the experiment was to study the influence of dislocation pile-ups on (i) strength and (ii) Bauschinger effects in micrometer-sized, focused ion beam milled bending cantilevers. The samples were loaded monotonically for several times under displacement control. Even though the cantilevers exhibited the same nominal strain gradient the strength varied by 34% within the three cantilever geometries. The Bauschinger effect can be promoted and prohibited by the insertion of different interfaces.

## A.1 Introduction

Mechanical properties of micrometer-sized, single crystalline copper bending beams are strongly influenced by the arrangement of geometrically necessary dislocations (GNDs) leading to two main phenomena inherent to the bending geometry: (i) size effects of the flow stress [1,2] and (ii) a pronounced Bauschinger effect or nonlinear elastic unloading behavior [35].

Size effects and the importance of internal material length scales are well known and have been widely discussed [6,7] and investigated over several decades. Studies have also been performed for geometries with inherent strain gradients [8]. For instance, Stölken and Evans [9] performed the first foil bending of 12.5-50  $\mu\text{m}$  thick Ni foils to study the influence of length scales on the mechanical behavior, which had been found to be in the range of 3-5  $\mu\text{m}$  in pure Ni foils. The flow stress increase with reduced foil thickness was well explained by strain gradient plasticity [8]. Recently, the possibility to produce micrometer- and submicrometer-sized samples by focused ion beam (FIB) milling and to test them either *ex situ* or *in situ* allows for sample size effects in a broad context down to the submicrometer range to be studied. These types of experiments have been commonly performed over the last decade in micro torsion [8,10], micro compression [11,12], micro tensile [13,14] and micro bending [1,2] geometries. Motz et al. [1] were the first who applied micro bending onto single crystalline, FIB milled bending cantilevers and observed that the increase of flow stress cannot solely be explained by strain gradient plasticity and assumed that this could be due to sparsely distributed dislocation sources and the formation of dislocation pile-ups. Later, three-dimensional discrete dislocation dynamics (3D-DDD) simulations [15] support this view and provide evidence that the dislocation arrangement in micrometer-sized copper cantilevers is characterized by a pile-up of GNDs on distinct glide planes close to the neutral axis. The strong localization of GNDs in the pile-up thereby stems from the activation of single dislocation sources in the small sample volume. The long range stress field of the pile-up and its back stress on the dislocation source is responsible for the pronounced flow stress increase.

Another consequence of the pile-up stress in microcantilevers is a pronounced nonlinear unloading curve due to the Bauschinger effect (or springback during monotone unloading), which was macroscopically observed in the 18th century [16]. Until today, Bauschinger effects had widely been studied in pure and dispersion hardened copper [17], in nanocrystalline gold films [18] as well as in passivated and unpassivated copper thin films [19]. Demir and Raabe recently [3] described this phenomenon in single crystalline FIB milled micro cantilevers as a drop in the flow stress and a smooth elastic-plastic transition when the load sign is reversed. They also recognized an incomplete reversibility of the GND structure close to the sample surface by electron backscatter diffraction (EBSD). More recent  $\mu\text{Laue}$  experiments in single slip oriented copper samples [5] showed that the reversible backflow of GNDs already takes place during unloading. Other data published in the literature [1,5,20,21] show pronounced deviations from the elastic unloading behavior in

micrometer-sized bending beams, which can be associated to a dislocation pile-up in most cases. In this study, we aim for a better understanding of the effect of different dislocation arrangements on the mechanical behavior of microcantilevers. Based on the FIB milled microcantilevers with different sample geometries we either foster or prohibit the plastic back-flow by confining the dislocation pile-up.

## A.2 Experimental details

In situ micro bending tests with multiple monotone loading-unloading sequences on single crystalline and bicrystalline copper microcantilevers in three different geometrical designs [Figs. 1(a)-1(c)] have been performed. In single crystalline bending beams [Type 1; Fig. 1(a)] the neutral axis acts as a “strain“-interface for dislocation motion due to the change in sign of the resolved shear stress across the neutral axis. Hence, the majority of dislocations will be trapped, but a few dislocations might be able to penetrate the neutral axis, spreading in regions with reversed load sign, clearly shown by 3D-DDD simulations [15]. However, dislocations emitted from the same source will pile up leading to a back stress on the dislocation source. This long range stress field of the pile-up is responsible for hardening at low strains as described by Motz and co-workers [1] and a dissolution of the pile-up upon unloading [5] which results in a pronounced Bauschinger effect furthermore. In the case of bicrystalline bending beams (Type 2 samples) with a grain boundary at the position of the neutral plane, the confinement of the pile-up should be much more pronounced: dislocations are not able to penetrate the general grain boundary leading to a shorter pile-up length, to a higher back stress on the dislocation source, and to a more pronounced Bauschinger effect [Fig. 1(b)]. In contrast, removing the material close to the neutral axis (i.e., milling a slit in the bending sample, Type 3) should lead to an escape of dislocations at the slit [Fig. 1(c)] and thus, no, or depending on the sample geometry a weak, pile-up will be formed and no Bauschinger effect should occur.

The three different cantilever types were FIB milled using a macroscopic sized copper bicrystal, which was prepared following the approach of Moser et al. [22]. The single crystalline cantilever as well as the slit sample was milled with the  $[3\bar{6}1]$  crystallographic axis parallel to the cantilever axis and the  $[\bar{8}41]$  crystallographic direction parallel to the loading axis. The second grain in the bicrystalline cantilever is rotated by  $24^\circ$  around the  $[314]$  crystallographic direction of the single crystalline cantilever. The microcantilevers were manufactured using a ZEISS 1540 XB FIB workstation (Oberkochen, Germany) with 30 keV  $\text{Ga}^+$  ions and a coarse milling current of 10 nA, followed by a final polishing current of 500 pA. The dimensions of all cantilevers are summarized in Table I.

A Hysitron PicoIndenter PI 85 (Hysitron, Minneapolis, MN) with a nominal force resolution of  $0.1 \mu\text{N}$  equipped with a doped diamond Berkovich indenter tip was used for the bending experiments. To facilitate the accurate alignment between the micrometer-sized samples and the indenter tip, the experiments were conducted

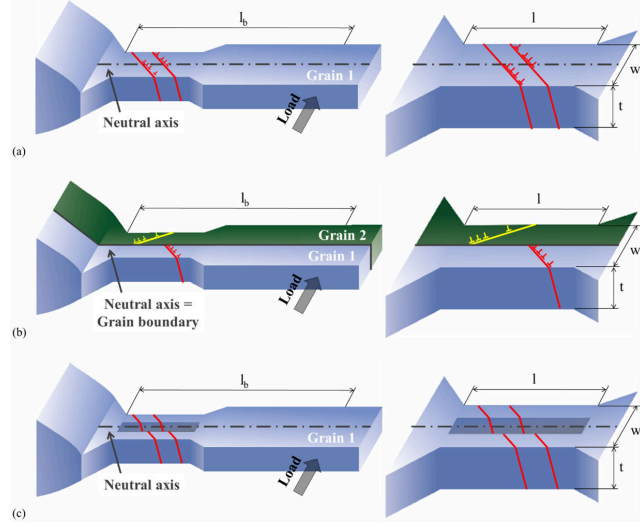


**Figure A.1** (a) Schematic drawing of the dislocation structure in single crystalline cantilever Type 1 with a pile-up formed at the neutral axis; (b) bicrystalline cantilever with a grain boundary aligned along the neutral axis (geometrically restricted pile-up, Type 2); (c) single crystalline cantilever with a slit along the neutral axis (no pile-up, Type 3).

inside a scanning electron microscope (SEM). Prior to the experiment, indents have been performed on a FIB milled surface on the same macroscopic sample close to the bending cantilever. These indents were made to correct for the stiffness of the wedge-shaped macroscopic sample. Several loading and unloading steps were performed in displacement controlled mode with step sizes of 50, 150, and 500 nm, using a strain rate of  $10^{-4} - 10^{-5} \text{ s}^{-1}$ . Bending lengths,  $l_b$ , [Figs. 1(a)-1(c)] of roughly  $60 \mu\text{m}$  were realized to avoid unwanted shear forces. The calculation of the stress versus strain curves is based on linear elastic bending beam theory. Therefore, the maximum stress at the outer fiber,  $\sigma$ , was calculated using Eq. (1), with  $F$  being the measured force and  $W$  or  $W_{slit}$  being the section modulus for cantilever Types 1 and 2 or Type 3, respectively, according to Eqs. (2) and (3), whereas cantilever thickness,  $t$ , and cantilever width,  $w$ , are listed in Table I.

$$\sigma = \frac{Fl_b}{W} \quad (\text{A.1})$$

$$W = \frac{tw^2}{6} \quad (\text{A.2})$$

$$\sigma = \frac{t \left( w^2 - \frac{w_{slit}^3}{w} \right)}{W} \quad (\text{A.3})$$

SEM images of the bent cantilevers taken after the experiments should document changes in the surface morphology with the main focus lying on resolving the slip step

formation. Due to the limited sensitivity concerning surface topography, provided by the SEM, slip steps became only visible at strains above 0.03-0.07.

### A.3 Results

The first 21 loading steps of cantilever Type 1 are shown in the stress versus strain diagram in Fig. 2(a). The loading curve (black) of the single crystal agrees well with the results obtained by Motz and co-workers [1]. At very low surface strains, the flow stress is increasing tremendously, indicating the aforementioned formation of the pile-up structure. The curve is subsequently followed by a steady state region exhibiting moderate hardening.

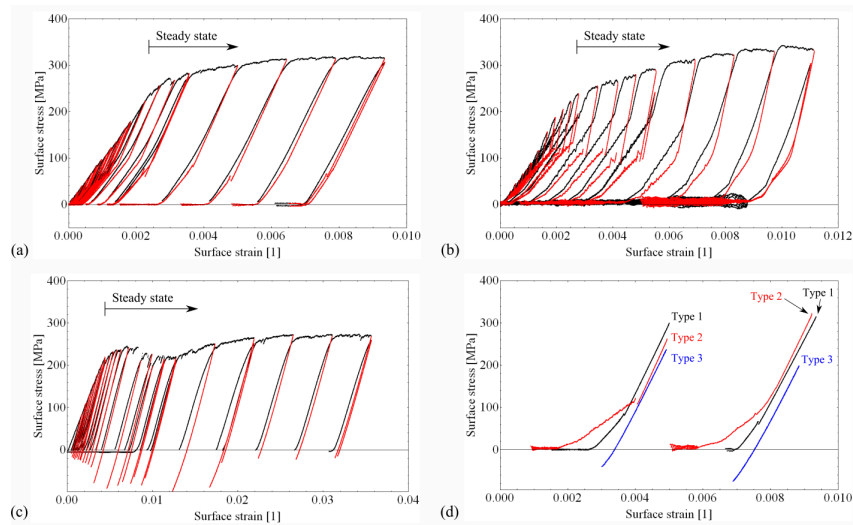


**Figure A.2** (a) Stress versus strain curves of cantilever Type 1 exhibit nonideal elastic unloading behavior, with the amount of reverse strain getting weaker with ongoing deformation steps. (b) Cantilever Type 2 shows amplified reverse strain and serrated flow during unloading, whereas (c) ideal elastic unloading is achieved for cantilever Type 3. (a-c) Loading curves are plotted in black, unloading curves in red. (d) Comparison of the unloading behavior of the three cantilever types at low and high strain values-set of curves left and right, respectively. The compliance of wedge and sample holder was corrected for each curve.

A discontinuous unloading behavior is observed: each unloading step starts with a linear elastic unloading and is followed by a less steep slope (Bauschinger effect). During reloading, the curve predominantly follows the unloading curve, however, slightly shifted to higher stress values meaning at low applied stresses there is no purely elastic loading. With increasing total strain, the Bauschinger effect during unloading is significantly decreasing.

The bicrystalline cantilever [Type 2, Fig. 2(b)] exhibits the same initial hardening and comparable stress during the transition to the steady state region with respect to Type 1. However, large differences can be found by a close examination of the

unloading curve, where the elastic unloading portion is much smaller and the reverse strain is increased with respect to the single crystal. Also, the back-flow during unloading is serrated at low total strains [Fig. 2(b)]. With higher surface strain, the back-flow becomes smoother and its magnitude is clearly reduced.

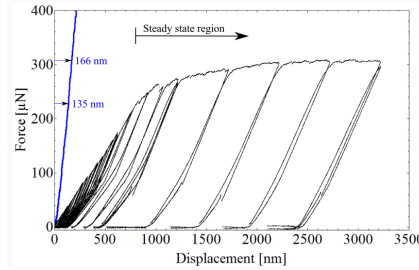


**Figure A.3** Contribution of the indentation depth caused by the Berkovich indenter (blue curve on the left, from an additional indent made in the close vicinity of the single crystalline cantilever) to the measured force-displacement data (black curves on the right) during loading of the single crystalline cantilever. Indentation depths are exemplarily given at the transition to the steady state regime (135 nm) and at the maximum displacement (166 nm), which results in 31 nm additional displacement during the steady state deformation.

In the case of the slit sample [Type 3, Fig. 2(c)], the transition from the initial region exhibiting very high hardening to the steady state is at slightly higher strains but at comparable stresses. The unloading curve is linear elastic and does not show any kink. The shape of the different unloading slopes is presented in Fig. 2(d) for comparison.

Besides the shape of the loading curves, the maximum stresses also differ. Comparing the stresses at 0.01 surface strain an intermediate strength for the single crystal of 315 MPa, an increased strength of 343 MPa for the bicrystal, and a reduced strength of 226 MPa for the sample with the slit are observed.

Due to the experimental setup the stress versus strain and hence, force versus displacement curve (Fig. 3, black) accommodates the force-displacement data from the cantilever bending as well as from the indent caused by the Berkovich indenter during loading. The loading curve of an additional indent (Fig. 3, blue) made in the close vicinity of the cantilever (Type 1 as an example) exemplifies its contribution to strain immediately from the onset of loading. Therefore, a sincere determination of the transition from elastic loading to the regime exhibiting pronounced hardening is impeded and would require a different experimental setup preventing the plastic strain input from the indenter (for instance, by using a flat punch indenter and larger bending lengths). Anyway, the contribution of the indentation depth to the total displacement is most prominent for early loading steps and becomes less important for loading steps at higher strains, where the indentation depth gets small with respect to the total displacement. In the steady state region, the indentation depth does not increase significantly anymore and so the contribution from the indenter to the total displacement diminishes: an additional indentation depth of 31 nm out of 2400 nm total displacement during the whole steady state regime compared to a 135

nm indentation depth contributing to a total displacement of 800 nm from the onset of loading until steady state. Consequently, no efforts were made to distinguish the particular plastic strain portions for Type 13 cantilevers since they are negligible for large displacements.

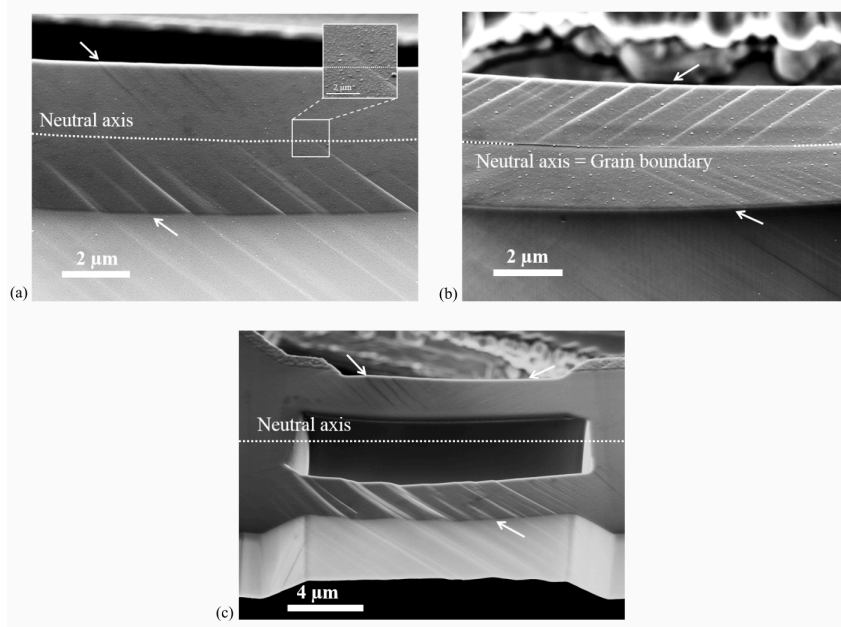


**Figure A.4** SEM images at 0.03-0.07 surface strain of all the three cantilevers: (a) single crystalline Type 1; (b) bicrystalline Type 2; (c) slit sample Type 3. White arrows mark the position and orientation of occurring glide steps.

In the case of single crystalline Type 1 samples, only one glide system was activated and slip steps are visible on the surface [Fig. 4(a)]. A slight rotation between the slip plane orientation on the tension (in the front) and compression side (in the back) can be attributed to a bent after an applied surface strain of 0.03, at which the SEM image was recorded. Careful analysis of the slip step orientation at different distances from the sample base confirms even a very small rotation within the same side of the cantilever. The slip step height decreases from its maximum at the highly strained outer fiber toward the neutral axis and diminishes somewhere around the neutral axis in a less abrupt manner than observed for the bicrystalline Type 2 cantilever [Fig. 4(b)]. There the slip steps are forced to instantly stop at the neutral axis, because the grain boundary situated there acts as an impenetrable barrier as slip planes do not continue into another grain. In contrast, in the single crystalline Type 1 sample at least one weak slip step extends about 600 nm into the cantilever side exhibiting the reversed sign in shear stress. In Type 3 cantilevers, glide steps penetrate the whole cross section of the beam on the tension side [Fig. 4(c), in the front] without any noticeable reduction in glide step height. Note that the SEM images shown in Figs. 4(a)-4(c) were taken at much higher strains (0.03-0.07) than

the presented stress versus strain curves in Figs. 2(a)-2(c), since at very low strains the slip steps are too faint to be resolved by SEM.

## A.4 Discussion

The observation of only a few slip steps in the SEM image of the single crystalline Type 1 cantilever [Fig. 4(a)] confirms localized deformation by one favorable oriented slip system. Due to the strongly bent cantilever the orientation of the slip steps varies slightly, however they still proceed on the same slip system. This is similar to findings from Motz et al. [1] who further argued that the operation of single dislocation sources on a limited number of slip planes results in a pile-up formation of GNDs at the neutral axis and hence, in pile-up stresses of opposite sign as the applied load. This pile-up approach provides a reasonable explanation for the experimentally observed nonlinear unloading curves [Fig. 2(a)], since the reduction in plastic strain in single crystalline cantilevers was attributed to the reverse motion of GNDs observed by  $\mu$ Laue experiments reported by Kirchlechner et al. [5].

The amplified back-flow observed in the stress versus strain curve of the bicrystalline Type 2 cantilever indicates higher pile-up stresses. This is consistent with the confinement of the dislocation pile-up by the impenetrable boundary [Fig. 4(b)]. Furthermore, this restriction requires a higher number of activated slip systems as can be estimated from the SEM images (0.37; 0.55; 0.13 in slip steps/ $\mu\text{m}$  normalized for 0.01 strain for Type 1; Type 2; Type 3, respectively). The serrated curve reveals the plastic character of the back-flow and agrees to the observations of discrete dislocation events [23] being a fingerprint of the avalanche-like back-flow of dislocations in the pile-ups. The serrated dissolution of pile-ups requires a temporary blocking of the dislocations in the pile-up, for instance, by a limited number of nonprimary dislocations. At high total strains, the plastic unloading curve becomes smooth, indicating that nonprimary dislocations entangle the pile-up dislocations and the avalanche-like back-flow of dislocations is suppressed. Also the amount of reverse strain is significantly reduced, which is in good agreement with the proposed entanglement of GNDs and SSDs which hinders a complete dissolution of the pile-ups.

The weaker reversibility of GNDs in Type 1 compared to Type 2 samples [Fig. 2(d), black and red unloading curves] is attributed to smaller pile-up stresses as a consequence of a weaker confinement of the GND pile-up at the neutral axis compared to an impenetrable grain boundary. Thus, it seems that the neutral axis acts as a weaker barrier for dislocations than the grain boundary and at least some GNDs must be able to propagate beyond the neutral axis. Although several slip steps were revealed in the vicinity of the neutral axis shown in Fig. 4(a), distinct signs for slip activity across the neutral axis are rare. The magnification in Fig. 4(a) shows such a rare case of a slip step extending across the neutral axis. The restricted visibility of slip beyond the neutral axis is most probably an unfavorable interplay of small slip step heights, carbon contamination of the sample surface, and the limited resolution of the SEM, which is insufficient to resolve slip steps derived from only a

few dislocations. Higher applied strains in the bicrystalline cantilever (0.043 total strain) caused higher slip step heights and thereby improved the visibility in the SEM compared to the single crystalline cantilever (0.03 total strain), especially in the region around the neutral axis. It is strongly assumed that more pronounced slip steps penetrating the neutral axis would have been detected in the single crystalline cantilever at higher applied strains.

The lack of the Bauschinger effect in Type 3 cantilever and the slip steps penetrating from the outer surface to the inner surface confirm the role of the neutral axis as a “strain“-interface in the single crystalline cantilever. The free inner surface of the slit sample allows for an escape of dislocations and thus, either no or a very little amount of pile-up dislocations form. Pile-up stresses are significantly reduced compared to the single crystalline Type 1 samples or are even lacking, and no back-flow is observed.

Besides understanding the reversibility of dislocation motion at the micrometer scale, these experiments allow for a deeper understanding of hardening in micrometer-sized samples, in particular to unravel different hardening mechanisms present at the micrometer scale. Since the glide steps are strongly localized and only a limited number of initial dislocations exist, work hardening does not take place at low strains. However, at higher strains the smoothing and disappearance of the reverse part of the unloading curve suggests an increase in total dislocation density, and thus, work hardening can play a role. However, work hardening is not responsible for the major strength increase with respect to macroscopically sized copper bending beams.

Strain gradients and their effect on hardening are inherent to the bending geometry in micrometer-sized cantilevers. However, Motz et al. [1] showed that the strain gradients cannot solely be responsible for the increased flow stress in micrometer-sized FIB milled cantilevers. Here, we can support the ideas of Motz and co-workers [1] in copper or later by Gong and Wilkinson [2] in  $\alpha$ -titanium single crystals by a simple comparison: the strain gradients in the three types of equally sized bending beams do not nominally differ. Still, the strength of the cantilevers is significantly different (compare 315, 343, and 226 MPa at 0.01 surface strain) and strain gradients cannot solely be responsible for the observed flow stress increase with respect to macroscopic flow stresses.

From bending experiments conducted in the SEM one may expect to see the location of dislocation sources and to calculate the activation stress. Indeed, one can conclude that most of the dislocation sources will be activated in the highly stressed region near the outer fiber, where the slip step height gains its maximum for Type 1 and 2 cantilevers [Figs. 3(a) and 3(b)]. However, identifying the exact location of the site where dislocation sources had been activated is not possible, which hinders the determination of source activation stresses in micrometer-sized bending beams. Thus, no conclusions can be drawn at the elastic limit where the source requiring the lowest activation stress is expected to be activated. The exact determination of surface stresses at the elastic limit is further complicated by the smooth transition from elastic loading to pronounced hardening at very low strains.

In the plateau region of the stress versus strain curve, the strength of the material

is not only determined by the source activation stress, but even more by the long range stress field of the pile-up acting as back stress on the dislocation source. The cantilever without pronounced pile-up (Type 3) exhibits the lowest surface stress at 0.01 surface strain (226 MPa); the sample with intermediate pile-up sizes (the single crystalline sample) has the second highest surface stress at 0.01 surface strain (315 MPa). Finally, the sample with the confined pile-up exhibits the highest plateau stress at comparable surface strains (343 MPa). This fits well with the observed unloading behavior where the Bauschinger effect also scales with pile-up stresses. Nevertheless, a quantitative investigation of the dislocation structure and the GND as well as SSD density is compulsory for quantitative conclusions on the hardening behavior of micrometer-sized bending cantilevers in the future, however is complicated by the dissolution of the pile-up during unloading.

## A.5 Conclusion

In situ loading-unloading micro bending experiments were performed on three different cantilever geometries. The size of the pile-up predominantly controls the mechanical properties of the bending beam, as confining the pile-up in a bicrystalline cantilever led to the amplification of the Bauschinger effect, as well as a more pronounced hardening behavior. In contrast, the reduction of the pile-up causes the absence of the Bauschinger effect and a strongly reduced hardening behavior, even though all the samples exhibit a comparable strain gradient.

## Acknowledgements

The authors thank Prof. Z. F. Zhang from the Shenyang National Laboratory (China) for providing one macroscopic bicrystal, Prof. C. Motz from Universitt des Saarlandes, Saarbrcken (Germany) for valuable discussion, and Dr. S. Brinckmann from the MPIE for additional FEM analysis justifying the assumed stress distribution in the cantilever. Financial support by the FWF Austrian Science Fund through project number P24429-N20 is gratefully acknowledged.

## References

- [1] C. Motz, T. Schberl, and R. Pippan, Mechanical properties of micro-sized copper bending beams machined by the focused ion beam technique, *Acta Mater.* 53(15) (2005) 4269-4279.
- [2] J. Gong and A.J. Wilkinson, A microcantilever investigation of size effect, solid-solution strengthening and second-phase strengthening for  $\langle a \rangle$  prism slip in alpha-Ti, *Acta Mater* 59(15) (2011) 5970-5981.
- [3] E. Demir, D. Raabe, and F. Roters, The mechanical size effect as a mean-field breakdown phenomenon: Example of microscale single crystal beam bending, *Acta*

- Mater. 58(5) (2010) 1876-1886.
- [4] D. Kiener, C. Motz, W. Grosinger, D. Weygand, and R. Pippan, Cyclic response of copper single crystal micro-beams, *Scr. Mater.* 63(5) (2010) 500-503.
- [5] C. Kirchlechner, W. Grosinger, M.W. Kapp, P.J. Imrich, J.S. Micha, O. Ulrich, J. Keckes, G. Dehm, and C. Motz: Investigation of reversible plasticity in a micron-sized, single crystalline copper bending beam by x-ray  $\mu$ Laue diffraction, *Philos. Mag.* 92(25-27) (2012) 3231-3242.
- [6] O. Kraft, P.A. Gruber, R. Mnig, and D. Weygand, Plasticity in confined dimensions, *Annu. Rev. Mater. Res.* 40 (2010) 293-317.
- [7] J.R. Greer and J.T.M. De Hosson, Plasticity in small-sized metallic systems, Intrinsic versus extrinsic size effect, *Prog. Mater. Sci.* 56(6)(2011) 654-724.
- [8] N.A. Fleck, G.M. Muller, M.F. Ashby, and J.W. Hutchinson, Strain gradient plasticity: Theory and experiment, *Acta Metall. Mater.* 42(2) (1994) 475-487.
- [9] J.S. Stölken and A.G. Evans, A microbend test method for measuring the plasticity length scale, *Acta Mater.* 46(14) (1998) 5109-5115.
- [10] A.J. Bushby and D.J. Dunstan, Size effects in yield and plasticity under uniaxial and non-uniform loading: Experiment and theory, *Philos. Mag.* 91(7-9) (2010) 1037-1049.
- [11] M.D. Uchic, D.M. Dimiduk, J.N. Florando, and W.D. Nix, Sample dimensions influence strength and crystal plasticity, *Science* 305(5686) (2004) 986-989.
- [12] C.A. Volkert and E.T. Lilleodden, Size effects in the deformation of sub-micron Au columns. *Philos. Mag.* 86(33-35) (2006) 5567-5579.
- [13] D. Kiener, W. Grosinger, G. Dehm, and R. Pippan, A further step towards an understanding of size-dependent crystal plasticity: In situ tension experiments of miniaturized single-crystal copper samples, *Acta Mater.* 56(3) (2008) 580-592.
- [14] J.Y. Kim, D.C. Jong, and J.R. Greer, Tensile and compressive behavior of tungsten, molybdenum, tantalum and niobium at the nanoscale, *Acta Mater.* 58(7) (2010) 2355-2363.
- [15] C. Motz, D. Weygand, J. Senger, and P. Gumbsch, Initial dislocation structures in 3-D discrete dislocation dynamics and their influence on microscale plasticity, *Acta Mater.* 56(6) (2008) 1942-1955.
- [16] S. Suresh, *Fatigue of Materials*, Cambridge University Press, Cambridge (1998).
- [17] O.B. Pedersen, L.M. Brown, and W.M. Stobbs, The Bauschinger effect in copper, *Acta Metall.* 29(11) (1981) 1843-1850.
- [18] J. Rajagopalan, C. Rentenberger, H. Peter Karnthaler, G. Dehm, and M.T.A. Saif, In situ TEM study of microplasticity and Bauschinger effect in nanocrystalline metals, *Acta Mater.* 58(14) (2010) 4772-4782.
- [19] Y. Xiang and J.J. Vlassak, Bauschinger and size effects in thin-film plasticity, *Acta Mater.* 54(20) (2006) 5449-5460.
- [20] J. Gong and A.J. Wilkinson, Anisotropy in the plastic flow properties of single-crystal  $\alpha$  titanium determined from microcantilever beams, *Acta Mater.* 57(19) (2009) 5693-5705.
- [21] R. Maaß, S. Van Petegem, D. Ma, J. Zimmermann, D. Grolimund, F. Roters, H. Van Swygenhoven, D. Raabe, Smaller is stronger: The effect of strain hardening,

## *A Publications*

Acta Mater. 57(20) (2009) 5996-6005.

[22] G. Moser, H. Felber, B. Rashkova, P.J. Imrich, C. Kirchlechner, W. Grosinger, C. Motz, G. Dehm, and D. Kiener, Sample preparation by metallography and focused ion beam for nanomechanical testing, *Prakt. Metallogr.* 49(6) (2012) 343-355.

[23] F.F. Csikor, C. Motz, D. Weygand, M. Zaiser, and S. Zapperi, Dislocation avalanches, strain bursts, and the problem of plastic forming at the micrometer scale, *Science* 318(5848) (2007) 251-254.

# B

## Anisotropic deformation characteristics of an ultrafine- and nanolamellar pearlitic steel

M.W. Kapp<sup>a</sup>, A. Hohenwarter<sup>b</sup>, S. Wurster<sup>b</sup>, B. Yang<sup>a</sup> and R. Pippan<sup>a</sup>

<sup>a</sup>Erich Schmid Institute of Materials Science, Austrian Academy of Sciences, 8700 Leoben, Austria

<sup>b</sup>Department of Materials Physics, Montanuniversität Leoben, Jahnstrasse 12, 8700 Leoben, Austria

### Abstract

Micromechanical experiments with  $3 \times 3 \times 6 \mu\text{m}^3$  sized micro pillars were used to examine orientation dependencies of the mechanical properties in a severely plastically deformed high strength steel and compared with the undeformed state. For the synthesis, an initially ultrafine-lamellar (UFL) fully pearlitic steel was subjected to high pressure torsion (HPT) transforming the steel into a nanolamellar (NL) composite. Both microstructural states were then tested in-situ inside a scanning electron microscope. Within the individual micro pillars, fabricated by focused ion beam milling, the ferrite and cementite lamellae were aligned parallel, normal or inclined to the loading direction. The main findings are: First, the strength and strain hardening capacity is more than doubled comparing the UFL with the NL composite. Second, an anisotropic mechanical response exists in terms of i) strain hardening capacity and ii) stress level at the onset of plateau formation. Third, deformation and localization mechanisms at large compressive strains vary with the lamellae orientation, however they are independent of the lamellae thickness.

## **B.1 Introduction**

Nanocrystalline (NC) and ultrafine-grained (UFG) materials have gained a lot of attraction due to their remarkable strength. Different procedures of severe plastic deformation (SPD) have been developed to refine microstructures, such as, equal channel angular pressing (ECAP), accumulative roll bonding (ARB) or high pressure torsion (HPT) [1-4]. Thereby, large amounts of strain can be imposed to the material, which causes a tremendous reduction of the structural sizes. For single phase materials, the grain refinement saturates at several hundred nanometers, whereas, for multiphase materials, even the nanometer regime can be attained, such as for pearlitic steels [5].

Pearlitic steels possess a widespread field of applications, as for instance for rails, cables for suspension bridges or steel cord wires. The great potential to control their strength by tailoring the interlamellar spacing has been extensively discussed [6-8]. Similar to single phase metallic materials, an inverse proportionality between strength and interlamellar spacing was found, also known as modified Hall-Petch effect. Hence, by strongly confining the dislocation movement in severely deformed pearlitic steels, ultrahigh strength materials can be produced [9]. To date, a cold drawn cord wire holds the highest tensile strength of all structural metallic materials with  $\sim 7$  GPa and thereby approaches approximately one third of the theoretical strength limit [10].

A prominent method capable of producing nanostructured materials and so also SPD bulk pearlitic steels is HPT, where a disk-shaped sample is deformed up to large amounts of shear strain [5,11-16]. The microstructural evolution during HPT deformation is characterized by (i) the rearrangement of the colony structure into a well aligned nanolamellar (NL) composite throughout the specimen, (ii) a reduction of the ferrite and cementite lamellae spacing to approximately 25 nm and 2 nm ( $\epsilon_{eq} = 8$ ) [12] and (iii) a disruption of initially unfavorably aligned cementite lamellae. On the atomic scale, a modification of the chemical composition of the cementite phase takes place. Such observations have been initially reported for pearlitic steels after wire drawing [17] and later on also for HPT deformed materials [15,16], suggesting a partial or even full dissolution of the cementite. EELS measurements on the same material as used in this study, support this view by revealing a change in the electron energy-loss near-edge-fine structure of the carbon-rich areas after an equivalent strain of 8 [12].

As widely known from composite materials, the aligned pearlitic structure is prone to possess orientation dependent mechanical properties. Up to now, the lamellae alignment has been described as an essential deformation characteristic during SPD [8,18,19], however, only few publications deal with the impact of the lamellae alignment and orientation on the mechanical properties, as for instance scrutinized for the fracture toughness [13]. The major challenge in probing the anisotropic mechanical properties of NL pearlitic steels obtained by HPT is to perform technically reliable experiments considering the small sample dimensions delivered by this technique. To our best knowledge, other SPD-processes such as ECAP or ARB cannot provide

comparable high strength materials due to technical processing limitations. Another problem arises regarding the comparison with the ultrafine-lamellar (UFL) pearlitic steel of initial interlamellar spacing having a random distribution of the pearlite colonies. A careful selection and mechanical measurement of a distinctive lamellae orientation is experimentally challenging. A micromechanical testing setup, initially developed to investigate sample size effects [20], was found to satisfy both demands and further allows an in-situ investigation of the deformation behavior within a scanning electron microscope (SEM).

In this study, in-situ micro compression experiments were conducted on a NL pearlitic steel produced by HPT and compared with the undeformed state, which consists of UFL pearlitic colonies. Micro pillars were focused ion beam (FIB) milled with different lamellae orientations with respect to the subsequent loading direction including a normal, parallel and inclined one. The mechanical response, such as strength and strain hardening capacity, as well as the qualitative deformation and failure characteristics were found to be strongly dependent on the lamellae orientation in the NL as well as in the UFL state.

## B.2 Experimental

A fully pearlitic rail steel R260 with 0.76 wt% C, 0.35 wt% Si, 1 wt% Mn, 0.017 wt% P and 0.014 wt% S was used, consisting of ferrite and cementite lamellae with an average lamellae spacing of 200 nm and a cementite thickness of 25 nm. HPT was used to refine the microstructure and further details concerning the applied HPT deformation procedure can be found in Ref. [21]. The disk-shaped sample had a thickness,  $t$ , of 5.9 mm and a diameter of 26 mm, the number of rotations,  $n$ , was two and the nominal applied hydrostatic pressure was 5 GPa. The material used for the subsequent micro compression experiments was extracted at a radius  $r$  of 12 mm, which results in an equivalent v. Mises strain  $\epsilon_{eq}$  of 15 according to Eq. (1)

$$\epsilon = \frac{2\pi rn}{t\sqrt{3}}. \quad (\text{B.1})$$

The ferrite lamellae thickness at  $\epsilon_{eq} = 14.8$  is between 15 nm and 20 nm and the cementite thickness is approximately 2 nm according to earlier TEM work [12,13]. As mentioned earlier, for the described experimental conditions, the chemical composition of the cementite becomes off-stoichiometric during HPT. Nevertheless, for simplicity the term cementite will be maintained for the severely deformed, off-stoichiometric carbon rich phase in the NL pearlitic steel.

Fig. 1 shows the fabrication sequence for the NL micro pillars. For that, a one millimeter thick slice was cut from the HPT disk (Fig. 1a).  $3 \times 1.5 \text{ mm}^2$  sized rectangular platelets were cut from this slice in such a way, that the ferrite and cementite lamellae were aligned parallel, normal and inclined ( $50^\circ$ ) to the later loading direction (Fig. 1b). Subsequently, these platelets were locally thinned with a Hitachi E-3500 cross section polisher to a wedge of 20  $\mu\text{m}$  thickness [22,23], which facilitates

quicker focused ion beam milling (Fig. 1c). Final fabrication of the micro pillars was carried out with a Zeiss LEO 1540 XB dual beam focused ion beam workstation enabling a precise control of the microstructural orientation of the cementite and ferrite lamellae with respect to the pillar axis (Fig. 1d). Therefore, coarse milling currents of 2 nA were used, followed by a final polishing of the pillar surface with 200 pA, in order to reduce the impact of ion damage [24] to the very surface area and to ensure a smooth specimen surface. The taper-free micro pillars are  $3 \times 3 \times 6 \mu\text{m}^3$  in size, resulting in an aspect ratio of two, which should prevent plastic buckling [25]. Using the same fabrication process, micro pillars were also cut into single pearlitic colonies of the undeformed UFL material, which were between 10 and  $20 \mu\text{m}$  large, for comparison. Since in this case no macroscopically aligned structure was present (no HPT process was applied), it was required to use a platelet including multiple pearlite colonies with arbitrary orientations and selecting appropriate lamella orientations with the FIB being aligned parallel, normal and inclined ( $22^\circ$  and  $45^\circ$ ) to the later loading direction.

Micro compression experiments were performed in-situ inside a SEM (Zeiss LEO982) in compression mode. An ASMEC UNAT micro indenter with a diamond flat punch indenter tip of  $20 \mu\text{m}$  in diameter was used to load the micro pillars. Misalignment between the micro pillar and the flat punch top surface was minimized by overtilting the pillar top surface by  $1.3^\circ$  during FIB milling.

The micro pillars were loaded under displacement control to total displacements of 1500-3000 nm in either one or two loading steps with a constant initial strain rate of  $10^{-3} \text{ s}^{-1}$ . Videos were recorded in terms of SEM-image sequences, which were taken every few seconds and allow to link the mechanical data with the material's deformation behavior. Furthermore, post-mortem SEM investigations of each micro pillar side surface were carried out to examine changes in the surface morphology. Cross-sections of the tested micro pillars were obtained by FIB milling and subsequently studied with a SEM in order to gain further insights into the underlying deformation mechanisms of the bulk material.

The non-specimen related elastic contributions of the measured displacement stemming from the wedge, SEM-stage, specimen holder, as well as from the pillar sink-in Ref. [26] were accounted for by correcting the compliance with a method implemented by Wurster et al. [27]. Finally, engineering stress-strain curves were calculated from the corrected displacement data and the measured force values.

To elucidate the mechanical behavior of the UFL polycrystalline pearlitic steel, compression experiments were performed on comparably large samples with  $3 \times 3 \times 6 \mu\text{m}^3$ . The samples were tested on a conventional testing rig from Zwick with an initial strain rate of  $2 \cdot 10^{-4} \text{ s}^{-1}$ .

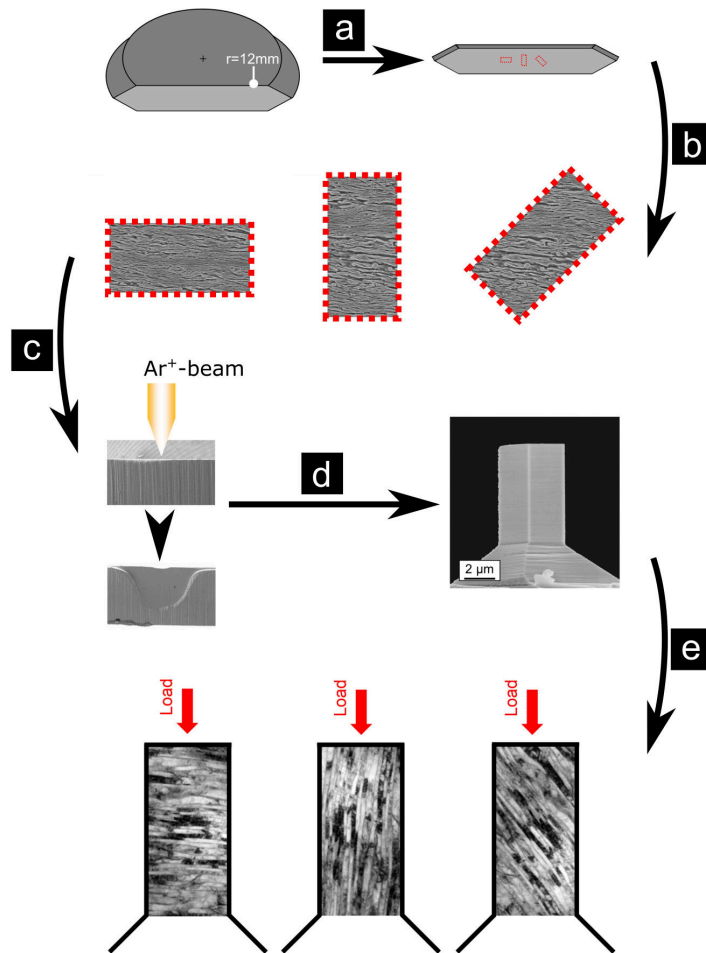


**Figure B.1** Fabrication sequence from the HPT disk to the final micro pillars: (a) a 1 mm thick slice is cut from the HPT disk at a radius of 12 mm ( $\epsilon_{eq} \sim 15$ ). (b) The thin foil is cut into platelets being aligned parallel, normal and inclined with respect to the ferrite and cementite lamellae orientation. (c) These platelets get locally thinned with a cross section polisher. (d) Final shaping of the pillars via FIB milling. (e) In the schematic the final alignment of the pearlitic structure within the micro pillars is depicted (interlamellar spacing is not to scale).

## B.3 Results

### B.3.1 Microhardness measurements

The microhardness distribution within the HPT-processed steel sample increases from the disk center with 270 HV1 by a factor of three to about 740 HV1 at a radius of 12 mm, similarly to [13]. This hardness gradient along the disk radius reflects the gradual decrease of the interlamellar spacing with increasing strain [5]. Under this experimental conditions a hardness plateau, as reported for many pure metals, is not observed, because of an insufficiently high applied deformation strain. Larger number of rotations would lead to a failure of the HPT-anvils or a slipping of the sample within the tool, which would not increase the strain or microstructural fragmentation any further. From the edge area, having a hardness of about 740 HV1, the platelets were extracted.

### B.3.2 Micro pillar testing

The engineering stress-strain curves (first loading step) from the NL and UFL micro pillars, as well as from an UFL macroscopic polycrystalline sample are presented in Fig. 2. Due to experimental artefacts affecting the mechanical data at large strains (i.e. contact between the sheared upper micro pillar half with the sample base increasing the measured force) the main focus lies on the early strain range up to 0.08. This range of interest is presented in Fig. 2 for all tested samples.

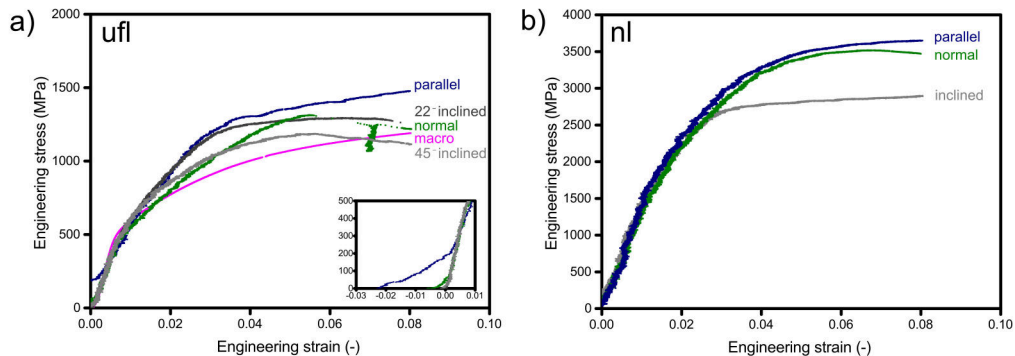


**Figure B.2** Engineering stress-strain curves of the a) UFL and b) NL micro pillars with the lamellae orientation parallel, normal, 22°-inclined, 45°-inclined (UFL) and 50°-inclined (NL).

Stress-strain curves of the UFL micro pillars with the ferrite and cementite lamellae being aligned parallel, normal, inclined under 45° and inclined under 22° to the loading direction are shown in Fig. 2a up to a strain of 0.08. The accuracy in the determination of the yield point in micro compression experiments is smaller compared to conventional macro-sized experiments, since it is easily altered by misalignment effects of the loading slope. The yield stress values at a plastic strain

of 0.2% are listed in Table 1. For the UFL pillars they are 544 MPa (normal), followed by 604 MPa (45°-inclined), 654 MPa (22°-inclined) and 819 MPa (parallel). The yield stress of the macroscopic polycrystalline sample (549 MPa) is in the same range. The highest yield-stress for the parallel orientation should be treated cautiously since a contact problem between the micro pillar and the indenter at the onset of loading (see low slope in insert of Fig. 2a) causes a lower slope in the subsequent elastic regime. However, when macro yielding commences, the impact of this misalignment on the mechanical data diminishes. For comparison the flow stress at 1% and 5% plastic strain as well as the flow stress increase  $\Delta\sigma$  from 0.2% to 5% plastic strain and the total applied elongation,  $\epsilon$ , are listed in Table 1.  $\Delta\sigma$  is used as a measure for the strain hardening capacity, considering that pronounced strain localization is not observed before 5% plastic strain. Strain hardening ranges from 551 MPa (45°-inclined), over 635 MPa (22°-inclined) and 661 MPa (parallel) to 710 MPa (normal). In the plateau region, the different orientations require different flow stress levels. The parallel micro pillar deforms at the highest flow stress, showing slight hardening, followed by the 22°-inclined, the normal and the 45°-inclined one, showing slight softening. In short, for the UFL pearlitic steel the lamellae orientation has a substantial influence on the stress-strain response in terms of the strain hardening behavior and the flow stress in the plateau regime.

**Table B.1** The flow stress values  $\sigma_{0.2}$ ,  $\sigma_1$  and  $\sigma_5$  at a plastic strain of 0.2%, 1% and 5% as well as the total elongation values  $\epsilon$  are listed for the UFL and NL samples. The difference  $\Delta\sigma$  of the flow stress values  $\sigma_{0.2}$  and  $\sigma_5$  was calculated as a measure for the strain hardening capacity.

	UFL normal	UFL parallel	UFL 22°-inclined	UFL 45°-inclined	UFL macro-sample	NL normal	NL parallel	NL 50°-inclined
$\sigma_{0.2}$ [MPa]	544	819	654	604	549	1918	1943	1605
$\sigma_1$ [MPa]	859	1290	1035	892	734	2890	2848	2375
$\sigma_5$ [MPa]	1254	1480	1289	1155	1123	3488	3633	2850
$\Delta\sigma$	710	661	635	551	574	1570	1690	1245
$\epsilon$ [%]	26.6	17.0	20.2	31.3	21.0	27.6	38.5	32.7

An anisotropy of the strain hardening capacity and the plateau stress is observed for the NL pearlitic steel in Fig. 2b as well. Contrary to the UFL case, the parallel and normal lamellae orientation show a similar hardening capacity and also the onset of yielding is about the same. For the inclined NL micro pillar the yield stress is about 300 MPa lower and also the strain hardening capacity  $\Delta\sigma$  is 325 MPa - 445 MPa smaller compared to the normal and parallel ones, respectively. The only difference between the parallel and normal orientation becomes visible in the evolution of the flow stress in the plateau regime, where slight softening is observed for the normal orientation, but the parallel one shows slight hardening.

Comparing the UFL and NL pearlitic steel of the corresponding lamellae orientation a doubling (inclined, parallel) or even triplication (normal) of the yield stress at 0.2% plastic strain is observed in the NL pearlitic steel. Also the strain hardening capacity in terms of  $\Delta\sigma$  is increased for the NL pearlitic steel, which is for the NL parallel

orientation even 2.5 times higher than for its UFL counterpart.

### B.3.3 SEM characterization of the deformed microstructure after testing

In Fig. 3, the surface morphologies of the UFL and NL micro pillars at different plastic strains  $\epsilon_{pl}$  are presented. Irrespective of the interlamellar spacing and lamellae orientation the strain is not homogeneously distributed along the micro pillar height at total nominal strains larger than 0.15 but rather concentrated in more or less narrow bands. For the UFL pearlitic steel this strain localization occurs as multiple small kink bands (parallel, see Fig. 3a) or shear bands (normal and inclined, see Fig. 3b and c). A similar behavior is observed for the NL pearlitic steel. For the parallel orientation (see Fig. 3d) plastic strain localizes in a single, but more extended kink band and for the normal and inclined orientation in narrow shear bands, Fig. 3e and f.

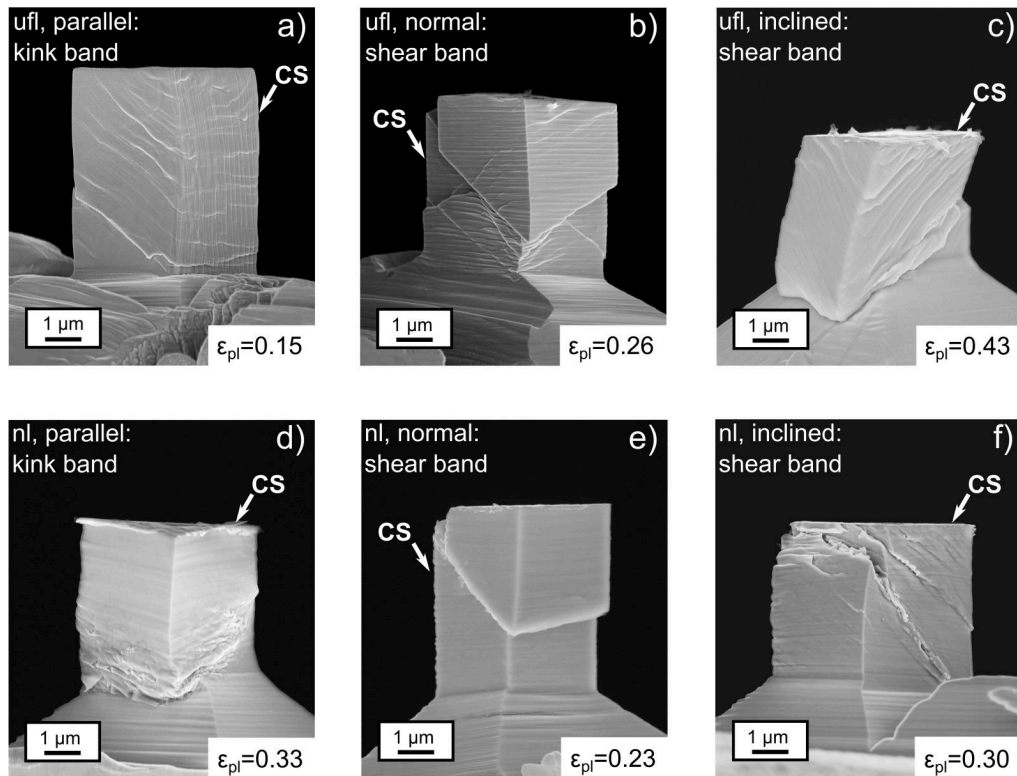


**Figure B.3** SEM images of the UFL a-c) and NL d-f) micro pillars after the final deformation step with the lamellae being aligned a,d) parallel, b,e) normal, c) 45°-inclined and f) 50°-inclined with respect to the loading axis. Note that the SEM images of the individual micro pillars were taken at different plastic strains (see inserts). Side surfaces further investigated by FIB milled cross sections presented in Figs. 4 and 5 are marked with CS.

The different nomenclature for kink and shear band becomes plausible by incorporating the SEM images taken from the pillar cross sections for the UFL (Fig. 4a-c) and NL pearlitic steel (Fig. 5a-c) into the discussion. Although the surface morphologies for the UFL parallel and normal orientation appear to be similar, their bulk appearance and thus the underlying deformation characteristics are different. In the case of the parallel orientation, localized bands appear inclined to the pillar axis (see left side surface in Fig. 3a) and exit as straight lines on the neighboring side surface (see right side surface in Fig. 3a). From the cross section in Fig. 4a, it can be inferred that the shear to the left requires local buckling events of the harder cementite phase (marked by arrows), which takes place in the area of the localized bands. Since the cementite lamellae buckle or kink in a cumulative manner (see schematic in Fig. 4a) along the whole pillar width these bands are denoted kink bands. Although SEM images of the surface (Fig. 3a-c) suggest similar localization also for the normal and inclined orientations, the SEM images of the cross sections reveal different deformation mechanisms of the cementite (Fig. 4b and c). The magnified view in Fig. 4b shows the major shear band for the normal orientation, where bending and massive elongation of the cementite lamellae in the shearing direction is visible, making it plausible to denote this structure as shear band. The interlamellar spacing within the shear band of the UFL pillar has been significantly reduced compared to the sample volume above and below the shear band. Due to the larger imposed strain to the inclined orientation, the deformation characteristics visible in the cross section in Fig. 4c demand careful interpretation: i) lamellae in region 1 are parallel to the initial lamellae orientation and are still preserved as in the pillar base region 2, ii) lamellae in region 3 start to heavily bend at large strains above 20%, supposedly supported by friction between pillar top and flat punch, iii) in region 4 fragmentation of the cementite lamellae occurs within the major shear band, iv) cementite lamellae remain consistent at the pillar top (region 1, 3), where smaller shear bands realize a smaller amount of strain compared to the major one. A description of the cross section SEM images of the NL pillars, see Fig. 5, are complicated due to their small interlamellar spacing and the limited resolution provided by the SEM. Despite these difficulties, a description of the deformation characteristics from the SEM images is attempted, as they provide a valuable input in understanding deformation instabilities for NL pearlitic structures. The deformation of the parallel oriented micro pillar is characterized by a kinking of the nanoscaled lamellae in Fig. 5a similar to its UFL counterpart, although here multiple small kink bands are displaced by a single large one, see also schematic in Fig. 5a. This large kink band also controls the shape of the micro pillar presented in the corresponding surface SEM image (Fig. 3d). Whereas the lamellae at the pillar top are almost parallel, they are perpendicularly aligned in the middle part, before they continue their parallel progression towards the pillar base. The strain imposed to the normal oriented pillar is sustained by shearing the upper against the lower pillar half in a very localized shear band (see Fig. 5b). The magnified cross section SEM image of the shear band reveals a bending of the ferrite lamellae in the shearing direction within a thickness of roughly 100 nm, whereas the upper and lower pillar half seem

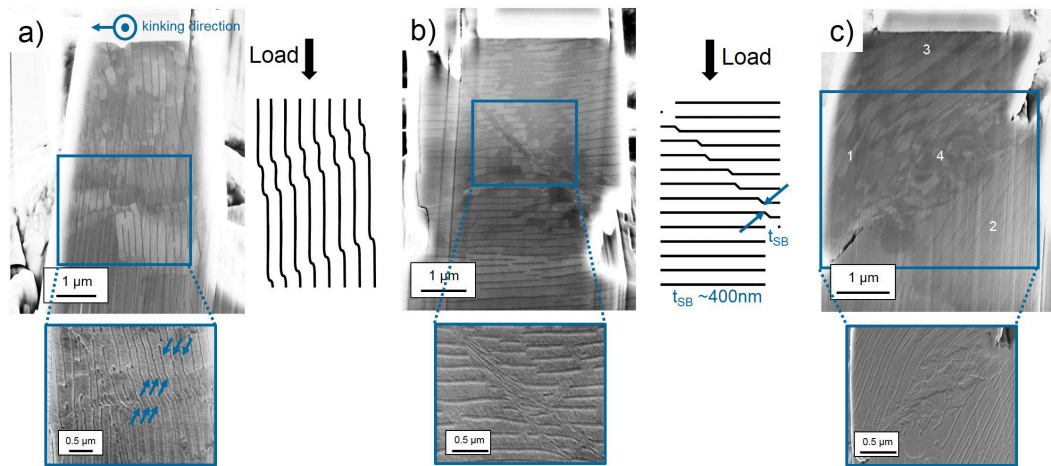


**Figure B.4** Cross-sectional investigations were performed parallel to the side surfaces of the a) parallel, b) normal and c) 50°-inclined oriented UFL micro pillars (same as in Fig. 3a-c). Subsequent SEM investigations on these cross sections reveal different deformation characteristics for the individual lamellae orientations. A schematic picture is depicted for two of the different deformation processes.

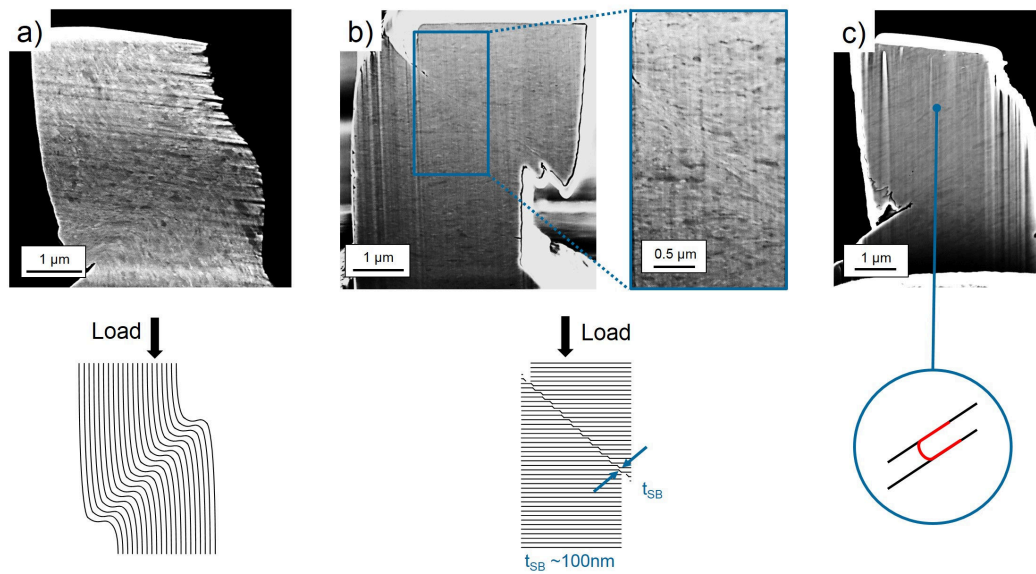


**Figure B.5** Cross-sectional investigations were performed parallel to the side surfaces of the a) parallel, b) normal and c) 45°-inclined oriented NL micro pillars (same as in Fig. 3d-f). Subsequent SEM investigations on these cross sections reveal different deformation characteristics for the individual lamellae orientations. A schematic picture is depicted for the three different deformation processes: a) kink formation, b) shear banding, c) dislocation segment moving parallel to the lamellae (confined layer slip).

to be unaffected by this localization process. It cannot be determined whether the cementite is bent or broken. Within the shear bands of the inclined pillar orientation in Fig. 5c the lamellae do not show signs of bending, nor kinking, but rather retain their orientation. It is important to point out that localized deformation processes for the UFL and NL micro pillars, obvious in the presented SEM images, did not occur before 5% total strain, which could be inferred from the video sequences.

## B.4 Discussion

The mechanical response presented in the stress-strain curves varies according to the interlamellar spacing (UFL and NL) and the lamellae orientation with respect to the loading direction (parallel, normal, inclined). The main differences can be found in i) the increased yield stress of the NL compared to the UFL micro pillars, ii) the large differences in the hardening capacity of the different lamellae orientations, as well as their iii) different flow stress levels for the onset of localized deformation, iv) the flow stress evolution in the plateau regime, and v) the orientation dependent deformation mechanism during localization. These peculiarities will be in the center of the following discussion:

### B.4.1 Onset of yielding

Surprisingly, within one microstructural state the yield stress,  $\sigma_{0.2}$ , is not significantly affected by the lamellae orientation and ranges between 550 and 650 MPa for the UFL state and 1600 - 1900 MPa for the NL state. However, there are large differences between the UFL and NL microstructures, where an increase of 1374 MPa (normal), 1124 MPa (as a lower bound for parallel) and 1001 MPa (50°-/45°-inclined) occurs depending on the corresponding lamellae orientations. In literature, the origin of the pronounced strength increase of nanolaminates caused by severe plastic deformation is controversially discussed [10,28,29]. The main mechanisms considered for SPD pearlitic steels are dislocation confinement following a Hall-Petch relation or Orowan bowing of single dislocations, solid solution hardening and Taylor hardening. These mechanisms are discussed regarding the main structural changes during high pressure torsion or wire drawing, which are the decrease of the ferrite and cementite lamellae spacing [12], a potential increase of the dislocation density similar to pearlitic wires [29] and the dissolution of the cementite [12]. The dominating mechanisms controlling the increase in strength will be discussed in more detail in the following. The explanations usually used for the strengthening effect of a refined grain size or lamellar structure are the Halle-Petch and Orowan concepts. A simple estimation of their applicability can be done by setting the ferrite lamellae spacing (exemplarily for normal orientation) in the UFL,  $d_f^{ufl}$ , and NL state,  $d_f^{nl}$  with the corresponding yield stresses  $\sigma_y^{ufl}$  and  $\sigma_y^{nl}$  into relation. Both values for  $\sigma_{0.2}$  ( $\sigma_y^{nl,ufl} = \sigma_{0.2}^{nl,ufl} - \sigma_{friction}$ ) need to be reduced by the friction stress  $\sigma_{friction}$ , which is around 120 MPa for pure iron [30]. The ratio NL to UFL yields to:

$$\frac{\sigma_y^{nl}}{\sigma_y^{ufl}} \sim \frac{1798}{424} \sim 4.2 \quad (\text{B.2})$$

In the UFL state,  $d_f^{ufl}$  is approximately 200 nm and in the NL state,  $d_f^{nl}$  is in the range between 15 and 20 nm. For classical dislocation pile-up behavior (Hall-Petch) one can write:

$$\frac{\sigma_y^{nl}}{\sigma_y^{ufl}} \sim \frac{\sqrt{d_f^{ufl}}}{\sqrt{d_f^{nl}}} \sim \frac{\sqrt{200}}{\sqrt{15}} \div \frac{\sqrt{200}}{\sqrt{20}} \sim 3.7 \div 3.2 \quad (\text{B.3})$$

For confined layer slip (Orowan):

$$\frac{\sigma_y^{nl}}{\sigma_y^{ufl}} \sim \frac{d_f^{ufl}}{d_f^{nl}} \sim \frac{200}{15} \div \frac{200}{20} \sim 13.3 \div 10.0 \quad (\text{B.4})$$

From the simple estimation it seems that the Hall-Petch concept approaches better to the observed behavior. However, we believe that the classical Hall-Petch explanation cannot be used to explain the yield strength of the NL structure, because the lamellar spacing is too small to allow for a pile-up formation. This is supported by results from the multilayer community [31], where it is well known that at a critical lamellae spacing, a transition from the classical pile-up formation following Hall-Petch law to confined layer slip following the Orowan mechanism occurs.

A similar estimate can be done in order to assess the impact of the dislocation density. Taking a dislocation density  $\rho_f^{nl}$  of  $8.8 \cdot 10^{15} \text{ m}^{-2}$  for the NL and  $\rho_f^{ufl}$  of  $7.5 \cdot 10^{13} \text{ m}^{-2}$  as a higher bound for the UFL state from Zhang et al. [29] we obtain:

$$\frac{\sigma_y^{nl}}{\sigma_y^{ufl}} \sim \frac{\sqrt{\rho_f^{nl}}}{\sqrt{\rho_f^{ufl}}} \sim \frac{\sqrt{8.8 \cdot 10^{15}}}{\sqrt{7.5 \cdot 10^{13}}} \sim 10 \quad (\text{B.5})$$

The pre-factor,  $\alpha$ , and the shear modulus,  $G$ , in the Taylor relation  $\Delta\sigma = \alpha G b \sqrt{\rho}$  might be different for the undeformed and the HPT deformed state, but the required large difference would be difficult to explain on a solid physical basis. Similar to the Orowan estimate, the Taylor hardening approach clearly overestimates the observed yield strength increase from the UFL to the NL state and justifies that it cannot be the solely strength controlling factor.

A further hardening mechanism could be related to the dissolution of the cementite, reflected by a small increase of the carbon concentration within the ferritic phase [10,16], which was inferred from EELS measurements in the present pearlitic steel [12]. Recently, Li et al. [10] showed that the main effect of the carbon segregation on strength is the stabilization of the ferritic subgrain structure. Hence, the nanosized subgrain structure is stabilized up to large strains and thereby confine dislocation glide paths, which further results in a tensile strength of up to 7 GPa. However, these findings become only relevant at smaller structural sizes as in the current case

and should not play the dominant role in this work, where the lamellar structure with a larger interlamellar spacing between 15 and 20 nm is still present.

The foregoing estimates and comparison of the results indicate that a single strength and hardening controlling mechanism cannot fully explain the difference between the NL and UFL pearlitic steel. Nevertheless, it is evident that in the NL state the ferrite lamellae spacing is the main microstructural feature governing the yield strength.

### B.4.2 Strain hardening

NL and UFL pearlitic steels exhibit a strong hardening [32] up to a certain plastic strain between 1.7% and 3.4%, depending on the lamellar orientation and lamellae spacing. However, there are significant differences in the orientation dependence and the amount of hardening in the NL and UFL structure.

#### UFL pearlitic steel

The stress-strain curves in Fig. 2a and idealized in Fig. 6a consist of three different regimes. Therefore, we assume the occurrence of three deformation modes (see Fig. 6a, numbered dots) similarly as reported by Thilly et al. for Cu-Nb wires [33]: 1) Elastic behavior below the ferrite yield point (F, see Fig. 6a); 2) Plastic and elastic behavior of the ferrite and cementite, respectively, above the ferrite yield point (F); 3) Plastic behavior of both phases beyond the cementite yield point (C, see Fig. 6a). The major amount of hardening is realized for all lamellae orientations in deformation mode 2.

Loading parallel to the lamellae exhibits a significant stronger hardening rate compared to the normal and inclined orientation. In both cases the hardening is nearly linear between the yield points of the ferrite (F) and cementite (C). This indicates that a very simple composite model with plastic ferrite lamellae and linear elastic cementite lamellae can be used to explain the hardening and orientation dependence. Thus, for the parallel loading, the flow stress  $\sigma_f(\epsilon)$  can be calculated according to

$$\sigma_f(\epsilon) = \sigma_f^f(\epsilon) * f^f + E^c * \epsilon * f^c \quad (\text{B.6})$$

where  $\sigma_f^f(\epsilon)$  is the strain dependent flow stress of the ferrite,  $f^f$  the ferrite fraction,  $E^c$  the Young's modulus of the cementite,  $\epsilon$  the applied strain and  $f^c$  the fraction of the cementite. The limit of this strong hardening is determined by the plastic deformation or the plastic buckling of the cementite lamellae, as shown in Fig. 4a, when the applied strain equals the yield strain of the cementite ( $\epsilon = \epsilon_y^c$ ), which is  $\epsilon_y^c \sim 1.5\%$  at  $\sigma_y^c \sim 3$  GPa [34]. In other words, the high yield stress of the cementite  $\sigma_y^c$  stabilizes dislocation multiplication within the ferritic phase as schematically shown in Fig. 7a, which requires the co-deformation of both phases. Once a kink band forms at the end of deformation mode 2, pronounced strain hardening terminates. For the loading perpendicular to the lamellae, the plastic deformation of the ferrite in deformation mode 2 (see Fig. 7b) is constrained by the lateral flow which is confined

by the elastic lateral deformation of the cementite. Assuming the Youngs' moduli of the ferrite and cementite are about the same  $E^f \sim E^c$ , furthermore, the yield stress of the ferrite  $\sigma_y^f$  is very small compared to the cementite  $\sigma_y^c$  and the volume fraction of the cementite  $f^c$  is small compared to the ferrite  $f^f$ , a very simple relation can be used to estimate the early hardening until yielding of the cementite starts at the onset of the stress plateau:

$$\sigma_f(\epsilon) = \sigma_f^f(\epsilon) * f^f + \frac{1}{2} E^c * \epsilon * f^c \quad (\text{B.7})$$

The second term describes the increase of flow stress due to the constrain in lateral flow of the ferrite (the hydrostatic stress component). The plastic strain in lateral direction,  $\epsilon_{lateral}$ , is half of the one in the loading direction,  $\epsilon$ , since in the fully plastic range the lateral contraction of the ferrite can be set to 0.5 ( $\epsilon_{lateral}/\epsilon = 0.5$ ). The limit of this strong hardening is reached when the cementite starts to deform plastically at  $\epsilon = 2\epsilon_y^c$ .

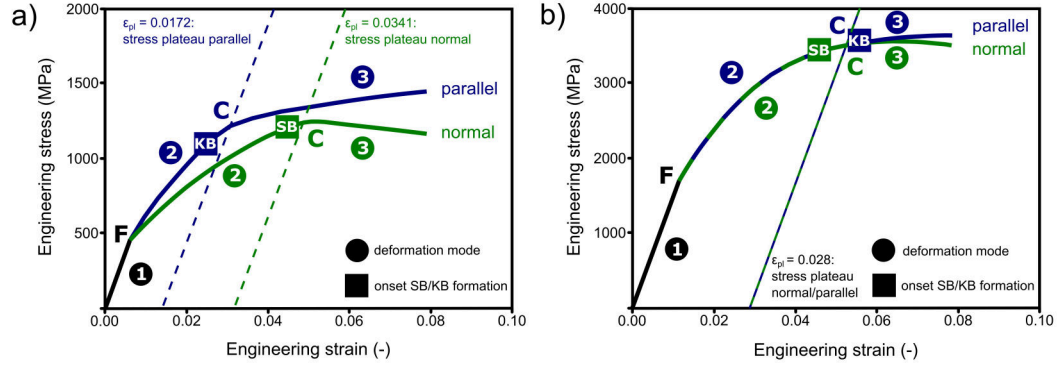


**Figure B.6** Schematic of stress-strain curves of the parallel and normal oriented a) UFL and b) NL micro pillars, where squares mark the formation of the dominant shear band (SB) or kink band (KB). The dotted lines mark the plastic strain where plateau formation for the parallel and normal orientation is observed.

### NL pearlitic steel

Similar to the UFL state the major amount of strain hardening is realized in the regime, where the ferrite lamellae deform plastically and the cementite stays elastic (see Fig. 2b and idealized Fig. 6b). However, the early hardening in the NL pearlitic steel is significantly larger than in the UFL microstructure. This indicates that the reduced lamellae thickness does not allow for a simple dislocation pile-up model anymore, but favors plasticity carried by single dislocations, moving from one boundary to another [35,36]. This is also supported by reconsidering Section 4.1 which showed that the strength in the NL state does not fully correspond to the

dislocation pile-up approach. To realize a plastic strain of 2.8% (see Fig. 6b) in the 15 nm or 20 nm thick ferrite lamellae, one or two dislocations need to be pushed through the lamellae until the leading segment is stored in the opposite interface as schematically shown in Fig 7c. Multiple activation of dislocations along the ferrite lamellae could account for the in the experiment observed homogenous deformation up to a flow stress of more than 3 GPa tremendous hardening.

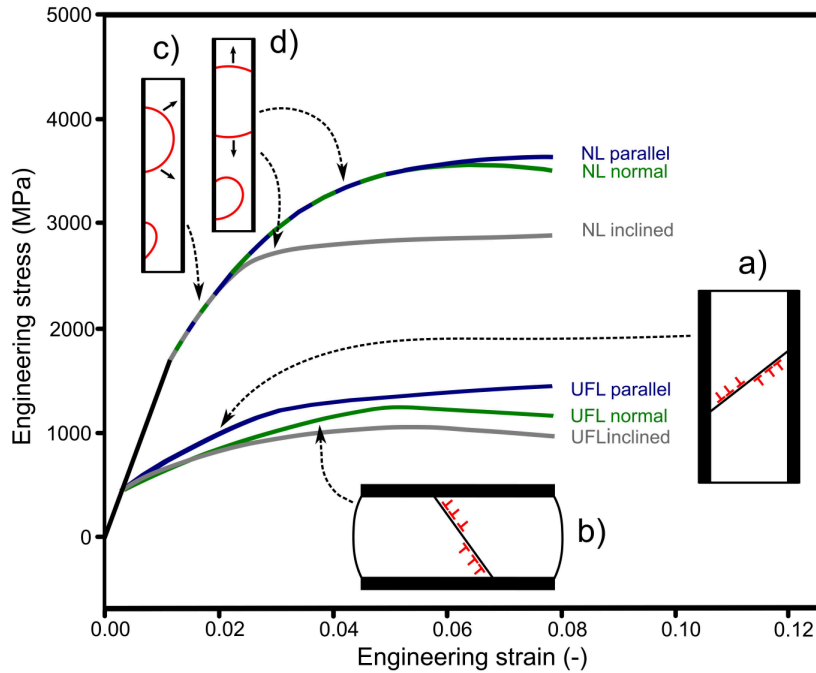


**Figure B.7** Schematic of the assumed dominant plastic deformation processes within the ferrite in the major strain hardening regime, which is pile-up formation for the UFL a) parallel and b) normal orientation and c) dislocation generation from interfaces and consequent bulging through the lamellae for all NL pillars. d) Dislocation segments can move by bowing out parallel to the interface (confined layer slip) at larger stresses in the NL pillars.

For the discussion of this hardening one has to take into account that the NL pearlitic steel is a heavily deformed ferrite and cementite where the cementite is chemically and, therefore, mechanically not identical with the cementite of the UFL microstructure. This could explain the similar hardening rates and also the same strain values at the limit of strain hardening for the parallel and normal orientation in the NL structure, which is not observed for the UFL structure. A lower strain hardening capacity was found for the inclined lamellae orientation, where plastic deformation or fracture of the cementite is not required for localization processes. Shear bands form parallel to the cementite lamellae and thereby terminate pronounced strain hardening in the end of deformation mode 2. It is rather the case, that dislocation segments being stored within the ferritic channel at low strains, bow out and

thereby, move within the ferrite lamellae when the Orowan stress  $\sigma_{or}$  is exceeded, according to

$$\sigma_{or} \sim 3\tau_{or} = \frac{Gb}{\pi(1-\nu)d} \ln\left(\frac{\lambda}{2\pi b}\right) \quad (\text{B.8})$$

with the ferrite shear modulus  $G$  (80 GPa [37]), burgers vector  $b$  (0.248 nm), Poisson's ratio  $\nu$  in the elastic case (0.29), lamellae thickness  $d$  and dislocation spacing  $\lambda = \rho^{-1}$  with the dislocation density within the ferrite  $\rho$  ( $8.8 \cdot 10^{15} \text{ m}^{-2}$  [29]). This rough approximation yields 3477 MPa and 2608 MPa for a 15 nm and 20 nm ferrite lamellae thickness, respectively, which is perfectly in the range of the hardening limit at 2650 MPa for the inclined loading condition. Thus, it seems that for the inclined loading situation not the yield or fracture stress of the cementite, but the bowing of dislocation segments in the confined situation of the narrow ferrite lamellae is the critical step for the formation of shear bands and subsequently shuts off the strain hardening. Such dislocation mechanisms, better known as confined layer slip (CLS), are frequently reported to operate in multilayers below a layer thickness of 50 nm [31]. It is very likely, that CLS also operates within the ferritic phase of the parallel and normal orientations at larger strains as schematically shown in Fig. 7d, but there it will certainly not trigger the onset of localized deformation.

One may assume that the crystal orientation in the UFL and the texture in the NL pillars should affect the flow stress and the hardening behavior. However, the yield stress and the hardening rate in the NL normal and parallel case are very similar. Also for the UFL the onset of yielding is in a similar range, as well as the hardening rate for the normal and inclined lamellae orientation. Therefore, we assume that the impact of the crystal orientation is minor compared to the lamellar architecture.

### B.4.3 The stress-strain behavior at larger strains

For both pearlitic structures a stress plateau forms, when the cementite starts to plastically deform or confined layer slip in the ferrite sets in. Within this region local stress drops  $\Delta\sigma_{drop}$  appear for the NL normal, UFL normal and  $22^\circ$ -inclined micro pillars, when the shear bands have fully transversed the pillar width. These stress drops are quantified in Table 2. Localized deformation terminates the pronounced hardening and only weak hardening or even softening occurs, mainly depending on the specific deformation mechanisms during strain localization of the lamellae orientation. Whereas localized deformation via kink bands sustains moderate hardening, localization in shear bands causes strain softening. Consequently, the strength at 5% plastic strain is for the parallel lamellae orientation somewhat larger as for the normal loaded lamellae irrespective of the lamellae thickness. Although the inclined oriented pillars deform both via shear bands, strain softening occurs for the UFL and strain hardening for the NL state. This could be the consequence of a very pronounced localization in one single shear band in the UFL state (geometrical softening), whereas in the NL state it is more homogeneously distributed in multiple shear bands.

**Table B.2** Initial stress drops occurring in the UFL normal, UFL 22°-inclined and NL normal micro pillars, when a local shear band fully transverses the pillar width.

	<b>UFL normal</b>	<b>UFL 22°- inclined</b>	<b>NL normal</b>
$\Delta\sigma_{drop}$ [MPa]	173	281	1124
$\epsilon_{drop}$ [%]	7.4	9.1	19.0

#### B.4.4 The deformation behavior at larger strains

For the parallel oriented micro pillars pronounced kink band formation is observed in the UFL (Figs. 3a and 4a) and NL state (Figs. 3d and 5a), which seems to be the inherent deformation mechanism whenever the cementite lamellae are axially loaded under compression. Similar observation were made by Porter et al. [8] and Toribio et al. [18] in pearlitic wires, where cementite lamellae laterally loaded under compression deformed via kinking and buckling. At total strains above about 5% the collective kinking of lamellae leads to a localization of plastic deformation in terms of one pronounced kink band extended in a broader range of the pillar height (NL state, Fig. 5a) or in many little kink bands distributed along the pillar height (UFL state, Fig. 4a).

For the NL and UFL normally oriented micro pillars the deformation characteristics visible in SEM images of the side surface are almost identical (Fig. 3b and e). Both localize via shear band formation at total strains larger than 5%. Unlike earlier work from Porter et al. [8] a breaking of the harder cementite phase probably caused by interphase crossing of dislocations within the shear bands of the UFL pearlitic steel is not observed. The cross section images from the UFL pillar (Fig. 4b) confirm a bending and elongation of the cementite in the shear direction, which coincides with earlier observations of a ductile behavior of cementite [7]. Consistent layers within shear bands have also been reported for different types of nanoscaled multilayers, such as CuNb [38,39] or Cu-PdSi [40] and lead combined with the present SEM-investigations to the assumption, that also for the NL pearlitic steel the cementite stays intact. Although interface crossing by dislocations [28] cannot be excluded, the realignment of the ferrite lamellae in the shear direction visible in the cross section (Fig. 5b) accounts for a ductile deformation and consistency of the cementite [35]. It could be demonstrated that not the interlamellar spacing but rather the lamellae orientation is determining the present deformation, localization and failure mechanism, which is in good agreement with earlier works from Porter et al. about tensile tests on coarse and fine lamellar pearlitic steels [8]. A similar strong lamella orientation influence has been also found for the fracture behavior [13,14]. The initial step for localization in the parallel and normal oriented pillars is the deformation of the harder cementite phase. This is not the case for the inclined lamellae orientation, since shear bands can easily propagate via confined layer slip of dislocations parallel to the harder cementite phase [8,41]. This is further confirmed by the absence of kinking or bending of the cementite suggesting Orowan bowing of dislocation loops

within the ferritic lamellae.

#### **B.4.5 Remarks to the macro behavior of a pearlitic steel**

The UFL micro pillars are fabricated within one colony and therefore represent a composite array of single crystals. A polycrystalline pearlitic steel contains abundant colonies with various lamellae orientations. Hence, one could assume that the mechanical response of the macroscopic sample lies between the extreme cases of the parallel micro pillar with the highest strength and the 45°-inclined one with the lowest strength. From the stress-strain curve in Fig. 2a it becomes clear, that the macroscopic response approaches more to the 45°-inclined micro pillar at low strains and to the 22°-inclined one at larger strains. We conclude, that the macroscopic stress-strain behavior is dominated by the softer colonies with similar inclined orientations as present in the single colony specimens.

In addition to an intrinsic size effect due to the reduced lamellae spacing, also an extrinsic sample size effect has recently been reported for Cu/Zr multilayers [42] similar as observed earlier for copper single crystals [43]. However, the yield stress at 0.2% plastic strain of the macroscopically sized UFL compression samples (3 x 3 x 6 mm<sup>3</sup>) with 549 MPa is well within the range of the UFL micro pillars (3 x 3 x 6 μm<sup>3</sup>). Hence, for a UFL pearlitic steel down to a sample size of 3 μm an extrinsic sample size effect is not apparent. Since the number of layers per sample volume is even higher in the NL pillars, it is evident that the presented data of the micron-sized pillars represent a bulk-like behavior.

### **B.5 Conclusion**

We have presented micro compression experiments of a nanolamellar, NL, and ultrafine-lamellar, UFL, pearlitic steel, where special focus was put onto the influence of the ferrite and cementite lamellae orientation on the mechanical response. Micro pillars were FIB milled with the lamellae being aligned parallel, normal and inclined to the loading direction. The results indicate that both, the interlamellar spacing and the lamellae orientation, have a strong influence on the mechanical response and deformation characteristics. In particular it could be shown that:

- i) The yield stress measured at 0.2% plastic strain is largely affected by the interlamellar spacing. Hence, HPT deformation ( $\epsilon_{eq} \sim 15$ ) causes a yield strength increase up to three times as a consequence of the stronger confinement of the dislocation within the ferrite lamellae. Surprisingly, the effect of lamellar orientation on  $\sigma_{0.2}$  is not very pronounced.
- ii) Both, the NL and UFL pearlitic steel show a strong initial hardening followed by a stress plateau regime.
- iii) The interlamellar spacing and the orientation with respect to the loading direction has a significant effect on the hardening capacity.

- iv) The strong orientation effect on the initial hardening in the UFL microstructure can be explained by a composite model, where plastic deformation is governed by the ferrite, while the cementite deforms elastically.
- v) The hardening in the NL structure is even stronger, however, the onset of the plateau regime is sensitive to the lamellar orientation. The exceptional strain hardening capacity seems to be a consequence of the movement of single dislocation loops in such fine scaled structures instead of pile-up formation.
- vi) The deformation and failure mechanisms at large strains are controlled also by the orientation of the lamellae with respect to the loading direction. Whereas deformation of the cementite in the UFL and NL state is not incorporated in the shear band formation of the inclined orientation, ductile bending in the shear direction is required for the normal and kinking for the parallel orientation (UFL).

### Acknowledgements

The authors would like to thank Prof. Daniel Kiener for valuable discussion. Financial support by the FWF Austrian Science Fund within project number P24429-N20 is gratefully acknowledged.

### References

- [1] R.Z. Valiev, R.K. Islamgaliev, I.V. Alexandrov, Bulk nanostructured materials from severe plastic deformation, *Prog. Mater. Sci.* 45 (2000) 103-189.
- [2] M.A. Meyers, A. Mishra, D.J. Benson, Mechanical properties of nanocrystalline materials, *Prog. Mater. Sci.* 51 (2006) 427-556.
- [3] R.Z. Valiev, Y. Estrin, Z. Horita, T.G. Langdon, M.J. Zehetbauer, Y.T. Zhu, Producing bulk ultrafine-grained materials by severe plastic deformation, *JOM* 58 (2006) 33-39.
- [4] A. Zhilyaev, T.G. Langdon, Using high-pressure torsion for metal processing: fundamentals and applications, *Prog. Mater. Sci.* 53 (2008) 893-979.
- [5] F. Wetscher, A. Vorhauer, R. Stock, R. Pippan, Structural refinement of low alloyed steels during severe plastic deformation, *Mater. Sci. Eng. A* 387-389 (2004) 809-816.
- [6] J. Embury, R. Fisher, The structure and properties of drawn pearlite, *Acta Metall. Mater.* 14 (1966) 147-159.
- [7] G. Langford, Deformation of pearlite, *Metall. Trans. A* 8 (1977) 861-875.
- [8] D.A. Porter, K.E. Easterling, G.D.W. Smith, Dynamic studies of the tensile deformation and fracture of pearlite, *Acta Metall. Mater.* 26 (1978) 1405-1422.
- [9] D. Raabe, P. Choi, Y. Li, et al., Metallic composites processed via extreme deformation: toward the limits of strength in bulk materials, *MRS Bull.* 35 (2010)

982-991.

- [10] Y. Li, D. Raabe, M. Herbig, P. Choi, S. Goto, A. Kostka, H. Yarita, C. Borchers, R. Kirchheim, Segregation stabilizes nanocrystalline bulk steel with near theoretical strength, *Phys. Rev. Lett.* 113 (2014) 106104.
- [11] F. Wetscher, B.H. Tian, R. Stock, R. Pippan, High pressure torsion of rail steels, *Mater. Sci. Forum* 503-504 (2006) 455-460.
- [12] F. Wetscher, R. Pippan, S. Sturm, F. Kauffmann, C. Scheu, G. Dehm, TEM investigations of the structural evolution in a pearlitic steel deformed by high pressure torsion, *Metall. Mater. Trans. A* 37 (2006) 1963-1968.
- [13] A. Hohenwarter, A. Taylor, R. Stock, R. Pippan, Effect of large shear deformations on the fracture behavior of a fully pearlitic steel, *Metall. Mater. Trans. A* 42 (2011) 1609-1618.
- [14] C. Kammerhofer, A. Hohenwarter, S. Scheriau, H.P. Brantner, R. Pippan, Influence of morphology and structural size on the fracture behavior of a nanostructured pearlitic steel, *Mater. Sci. Eng. A* 585 (2013) 190-196.
- [15] Y. Ivanisenko, W. Lojkowski, R.Z. Valiev, H. Fecht, The mechanism of formation of nanostructure and dissolution of cementite in a pearlitic steel during high pressure torsion, *Acta Mater.* 51 (2003) 5555-5570.
- [16] X. Sauvage, Y. Ivanisenko, The role of carbon segregation on nanocrystallisation of pearlitic steels processed by severe plastic deformation, *J. Mater. Sci.* 42 (2007) 1615-1621.
- [17] Y.J. Li, P. Choi, C. Borchers, S. Westerkamp, S. Goto, D. Raabe, R. Kirchheim, Atomic-scale mechanisms of deformation-induced cementite decomposition in pearlite, *Acta Mater.* 59 (2011) 3965-3977.
- [18] J. Toribio, E. Ovejero, Effect of cumulative cold drawing on the pearlite interlamellar spacing in eutectoid steel, *Scr. Mater.* 39 (1998) 323-328.
- [19] J. Toribio, Relationship between microstructure and strength in eutectoid steels, *Mater. Sci. Eng. A* 387-389 (2004) 227-230.
- [20] M.D. Uchic, D.M. Dimiduk, J.N. Florando, W.D. Nix, Sample dimensions influence strength and crystal plasticity, *Science* 305 (2004) 986-989.
- [21] A. Hohenwarter, A. Bachmaier, B. Gludovatz, S. Scheriau, R. Pippan, Technical parameters affecting grain refinement by high pressure torsion, *Int. J. Mater. Res.* 100 (2009) 1653-1661.
- [22] S. Wurster, C. Motz, M. Jenko, R. Pippan, Micrometer-sized specimen preparation based on ion slicing technique, *Adv. Eng. Mater.* 12 (2010) 61-64.
- [23] S. Wurster, R. Treml, R. Fritz, M.W. Kapp, et al., Novel methods for the site specific preparation of micromechanical structures, *Prakt. Metallogr. Pr. M.* 52 (2015) 131-146.
- [24] D. Kiener, C. Motz, M. Rester, M. Jenko, G. Dehm, FIB damage of Cu and possible consequences for miniaturized mechanical tests, *Mater. Sci. Eng. A* 459 (2007) 262-272.
- [25] H. Zhang, B.E. Schuster, Q. Wei, K.T. Ramesh, The design of accurate micro-compression experiments, *Scr. Mater.* 54 (2006) 181-186.
- [26] H. Wörgötter, D. Kiener, J.M. Purswani, D. Gall, G. Dehm, Testing thin films

- by microcompression: benefits and limits, *BHM* 153 (2008) 257-262.
- [27] S. Wurster, C. Motz, R. Pippan, Characterization of the fracture toughness of micro-sized tungsten single crystal notched specimens, *Philos. Mag.* 92 (2012) 1803-1825.
- [28] A. Misra, J.P. Hirth, R.G. Hoagland, Length-scale-dependent deformation mechanisms in incoherent metallic multilayered composites, *Acta Mater.* 53 (2005) 4817-4824.
- [29] X. Zhang, A. Godfrey, X. Huang, N. Hansen, Q. Liu, Microstructure and strengthening mechanisms in cold-drawn pearlitic steel wire, *Acta Mater.* 59 (2011) 3422-3430.
- [30] M. Srinivas, G. Malakondaiah, R.W. Armstrong, P. Rama Rao, Ductile fracture toughness of polycrystalline armco iron of varying grain size, *Acta Metall. Mater.* 39 (1991) 807-816.
- [31] A. Misra, M. Verdier, Y.C. Lu, H. Kung, T.E. Mitchell, M. Nastasi, J.D. Embury, Structure and mechanical properties of Cu-X (XNb,Cr,Ni) nanolayered composites, *Scr. Mater.* 39 (1998) 555-560.
- [32] J. Gil Sevillano, P. van Houtte, E. Aernoudt, Large strain work hardening and textures, *Prog. Mater. Sci.* 25 (1980) 69-134.
- [33] L. Thilly, M. Véron, O. Ludwig, F. Lecouturier, J.P. Peyrade, S. Askénazy, High strength materials: in-situ investigations of dislocation behaviour in Cu-Nb multifilamentary nanostructured composites, *Philos. Mag. A* 82 (2002) 925-942.
- [34] B. Karlsson, G. Lindén, Plastic deformation of eutectoid steel with different cementite morphologies, *Mater. Sci. Eng.* 17 (1975) 153-164.
- [35] J.D. Embury, J.P. Hirth, On dislocation storage and the mechanical response of fine scale microstructures, *Acta Metall. Mater.* 42 (1994) 2051-2056.
- [36] M. Janecek, F. Louchet, B. Doisneau-Cottignies, Y. Bréchet, N. Guelton, Specific dislocation multiplication mechanisms and mechanical properties in nanoscaled multilayers: the example of pearlite, *Philos. Mag. A* 80 (2009) 1605-1619.
- [37] G.R. Speich, A.J. Schwoeble, W.C. Leslie, Elastic constants of binary iron-base alloys, *Metall. Trans.* 3 (1972) 2031-2037.
- [38] N.A. Mara, D. Bhattacharyya, J.P. Hirth, P. Dickerson, A. Misra, Mechanism for shear banding in nanolayered composites, *Appl. Phys. Lett.* 97 (2010) 021909.
- [39] S.J. Zheng, J. Wang, J.S. Carpenter, W.M. Mook, P.O. Dickerson, N.A. Mara, I.J. Beyerlein, Plastic instability mechanisms in bimetallic nanolayered composites, *Acta Mater.* 79 (2014) 282-291.
- [40] I. Knorr, N.M. Cordero, E.T. Lilleodden, C.A. Volkert, *Acta Mater.* 61 (2013) 4984-4995.
- [41] A. Misra, J.P. Hirth, R.G. Hoagland, J.D. Embury, H. Kung, Dislocation mechanisms and symmetric slip in rolled nano-scale metallic multilayers, *Acta Mater.* 52 (2004) 2387-2394.
- [42] J.Y. Zhang, S. Lei, Y. Liu, J.J. Niu, Y. Chen, G. Liu, X. Zhang, J. Sun, Length scale dependent deformation behavior of nanolayered Cu/Zr micropillars, *Acta Mater.* 60 (2012) 1610-1622.
- [43] D. Kiener, W. Grosinger, G. Dehm, R. Pippan, A further step towards an

*B Publications*

understanding of size-dependent crystal plasticity: in situ tension experiments of miniaturized single-crystal copper samples, *Acta Mater.* 56 (2008) 580-592.



# Ultra-strong and damage tolerant metallic bulk materials: A lesson from nanostructured pearlitic steel wires

A. Hohenwarter<sup>a</sup>, B. Völker<sup>a</sup>, M.W. Kapp<sup>b</sup>, Y. Li<sup>c</sup>, S. Goto<sup>c,d</sup>, D. Raabe<sup>c</sup> and R. Pippan<sup>b</sup>

<sup>a</sup>Department of Materials Physics, Montanuniversität Leoben, Jahnstrasse 12, 8700 Leoben, Austria

<sup>b</sup>Erich Schmid Institute of Materials Science, Austrian Academy of Sciences, 8700 Leoben, Austria

<sup>c</sup>Max-Planck Institut für Eisenforschung, Max-Planck-Strasse 1, 40237 Dsseldorf, Germany.

<sup>d</sup>Akita University, Tegata Gakuencho, Akita 010-8502, Japan.

## Abstract

Structural materials used for safety critical applications require high strength and simultaneously high resistance against crack growth, referred to as damage tolerance. However, the two properties typically exclude each other and research efforts towards ever stronger materials are hampered by drastic loss of fracture resistance. Therefore, future development of novel ultra-strong bulk materials requires a fundamental understanding of the toughness determining mechanisms. As model material we use today's strongest metallic bulk material, namely, a nanostructured pearlitic steel wire, and measured the fracture toughness on micron-sized specimens in different crack growth directions and found an unexpected strong anisotropy in the fracture resistance. Along the wire axis the material reveals ultrahigh strength combined with so far unprecedented damage tolerance. We attribute this excellent property

combination to the anisotropy in the fracture toughness inducing a high propensity for microcrack formation parallel to the wire axis. This effect causes a local crack tip stress relaxation and enables the high fracture toughness without being detrimental to the material's strength.

## **C.1 Introduction**

The quest for ever stronger engineering materials has a natural upper limit, the so-called theoretical strength, which is around 10 - 20% of the Young's modulus [13]. Nevertheless, today's ultimate tensile strength of most engineering materials including iron, nickel, aluminium or titanium-alloys seem to have a much lower, seemingly unsurpassable strength limit around 10% of their theoretical limit [4,5], or 12% of the Young's modulus. The maximum attainable strength and hence the ultimate failure of a material is determined by its resistance against cracks. The damage tolerance of a material, i.e. its capability to sustaining defects without fatal damage, is characterized by its fracture toughness and describes under which loading conditions defects or cracks propagate. To bridge the gap between today's materials real strength limits and the theoretical strength, better understanding of the fracture toughness is therefore of crucial importance.

However, reviewing material databases a basic conflict between strength and fracture toughness can be observed [6,7]. For metallic materials increasing the strength typically leads to the deterioration of the fracture toughness because the materials become more sensitive to defects, which are generally present in metallic engineering materials. This leads to a dilemma where on the one hand, a huge gap remains between the current high strength levels of metallic materials and their actual ultimate strength potential determined by their respective theoretical limits. On the other hand, efforts in increasing the strength by various strengthening mechanisms is associated with a loss in fracture toughness. Consequently, in the material design a compromise between strength and fracture toughness must be widely entered. Today's strongest metallic bulk material, characterized by its 7 GPa tensile strength, is found in a plain steel first described about 130 years ago [8]. It is a so called pearlitic steel in which two phases, iron and cementite ( $\text{Fe}_3\text{C}$ ), form a lamellar arrangement. Decreasing the inter-lamellae spacing by deformation turns the alloy into a nanolaminate, leading to a drastic increase in strength [9-11]. In the material studied here, which has recently been microstructurally investigated by Li et al. [12], the lamellae spacing is reduced to only a few nanometers and the alloy reaches up to 30% of its theoretical strength. From a microstructural viewpoint the origin of this extraordinarily high strength level can be related to the confinement of dislocation motion [12,13], which is a fundamental strengthening mechanism in nanocrystalline materials [14,15]. However, its high damage tolerance is most surprising, since at these high strength levels one would rather expect very low fracture toughness [4,5,7]. In contrast, without sufficient damage tolerance failure during the synthesis of the material would become very likely. Equally severely, reaching strength levels up to

30% of the theoretical strength could be impeded by crack growth and failure below the microstructural strength limit in the elastic regime.

The main question of this study is how sufficient damage tolerance in terms of fracture toughness can be realized at strength levels far beyond those typical of current engineering materials. To address this question the nanostructured pearlitic steel introduced above was examined by advanced fracture mechanical testing. A clarification could pave the way for the future design of new ultra-strong and damage tolerant engineering materials.

## C.2 Material and Experimental Approach

Classical pearlitic steels form laminate structures consisting of alternating ferrite and cementite layers. The layers differ in their chemical composition and crystal structure. The ferrite is body-centered cubic iron, whereas the cementite layers consist of  $\text{Fe}_3\text{C}$  carbides with orthogonal structure in the undeformed state. The wire investigated here was produced by severe cold drawing. The chemical composition is outlined in the Methods section. For comparison two different wires, cold-drawn to true strains of 3.1 and 6.52 with ultimate strengths of nearly 4 and 7 GPa, respectively, were studied. Wire diameters were 120  $\mu\text{m}$  ( $\epsilon_{\log} = 3.1$ ) and 24  $\mu\text{m}$  ( $\epsilon_{\log} = 6.52$ ), respectively, and we refer to these as the “low“ and “high“ deformed state in the following. Even though the wire diameters are quite small the samples can be well regarded as a bulk material in comparison with other material types such as powders or coatings owing to its comparably tiny characteristic internal length scales which amount to only a few nm. According to atom probe tomography investigations [12,16] the two wires exhibit differences in the microstructure. In the lower deformed state, with a strength of almost 4 GPa, a nanolamellar structure was found, similar to the one observed in classical pearlitic steels. In the higher deformed states the carbide phase gradually dissolves. The lamellar structure transforms into a nanoscaled carbon-enriched columnar subgrain structure [12,17]. TEM-investigations of the wires reveal in both deformation states a strong alignment of the microstructural constituents parallel to the drawing direction, which is exemplarily shown for the 7 GPa wire in Fig. 1a. In the viewing direction parallel to the drawing axis a curled structure can be found, see Fig. 1b. In-depth analyses of the present microstructures can be found elsewhere [12,16].

To examine the damage tolerance of these wires, orientation sensitive fracture experiments in two different principal testing directions with the crack growth directions parallel and perpendicular to the drawing axis of the wires were defined. For the parallel orientation micrometer-sized cantilevers were fabricated with a focused ion beam (FIB) cutting technique, see Fig. 2a. To produce the micrometer-sized cantilevers large parts of the wire around the actual specimen had to be removed. Therefore, it can be assumed that also first order residual stresses, if any were present in the wire, are eliminated. For the perpendicular orientation single-edge notched tension (SENT) specimens, utilizing in this way the full wire dimensions, Fig. 2b,

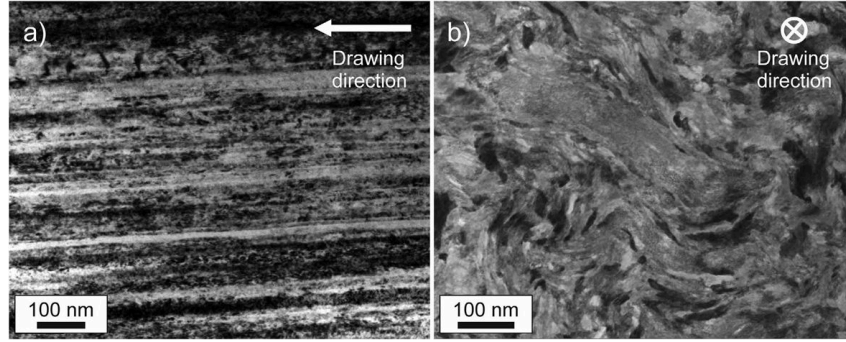


**Figure C.1** Microstructure of the high deformed state of the wire. (a) In the viewing direction perpendicular to the drawing direction the pronounced alignment of the phases and interfaces parallel to the drawing direction is revealed by bright-field TEM. (b) View parallel to the drawing direction using STEM exhibiting the characteristic curled microstructure.

were used. In both types of specimens the FIB was also utilized to introduce a pre-crack like notch. Since the SENT-specimens did not exhibit bending after the introduction of the pre-crack the extent of residual stresses seem to be rather low.

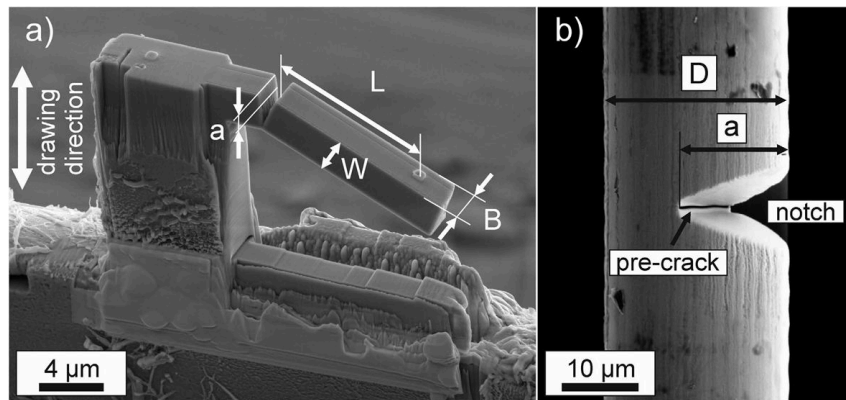


**Figure C.2** The two different specimen types. (a) Micrometer-sized cantilever used for the parallel orientation with indicated sample dimensions, designating the width,  $W$ , the thickness,  $B$ , of the beam, crack length,  $a$ , and the bending length,  $L$ . (b) Single-edge-notched specimen used for the perpendicular orientation with crack length,  $a$ , and diameter  $D$ . In both specimen types a fine pre-crack was introduced by focused ion beam milling. The geometry examples originate from measurements on the high deformed state ( $\epsilon_{log} = 6.52$ ), where (a) stems from the sample after and (b) before the experiment was performed.

Due to the small wire dimensions, the experiments with the micrometer-sized cantilevers, probing the fracture resistance parallel to the wire axis, had to be performed inside a scanning electron microscope (SEM). The SEM enables accurate positioning of the specimens with respect to the loading direction and monitoring of crack growth during the experiment. The SENT-specimens could be tested conventionally outside the SEM with a small scale tensile testing machine. For each direction and

material state two experiments were performed. From a statistics viewpoint this number is rather small, however, sufficient to confirm the general trends presented in this report. Details on the testing procedures and the consecutive data analysis are outlined in the Methods section. The dimensions of the samples can be found in Supplementary Tables S1 and S2. As will be shown, the fracture properties can be generally described by means of linear elastic fracture mechanics (LEFM), which implies that the presented results are also applicable to larger dimensions of the material that may be synthesized in the future.

## C.3 Results and Discussion

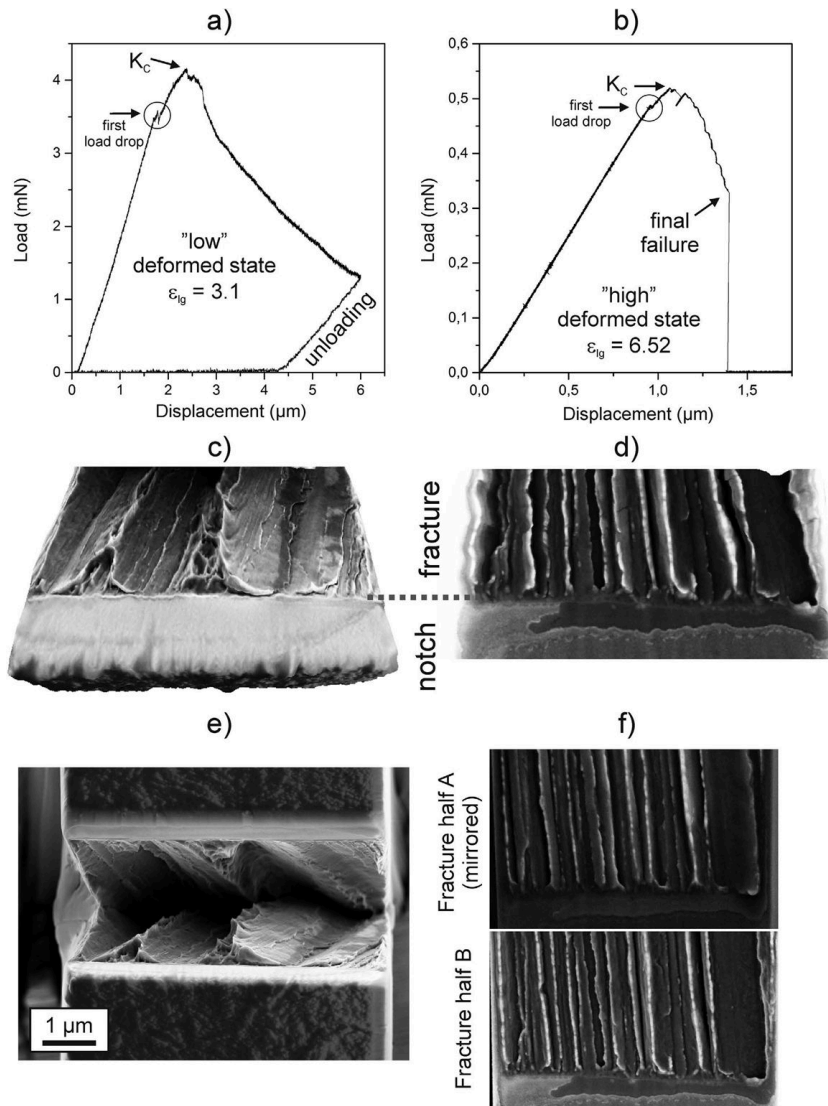
### C.3.1 Parallel testing orientation

Figure 3 shows typical load-displacement curves obtained for the crack growth direction parallel to the drawing axis for both strength levels. At the beginning both types of specimens show pure linear elastic loading, accompanied by a small load-drop, which can be associated with the onset of subcritical crack growth (see videos provided in the Supplementary Material). After reaching the maximum load the force decreases with stable crack growth within the specimens. In the lower deformed state the decrease in load ceases by reaching a maximum pre-defined displacement followed by an unloading sequence, Fig. 3a, whereas the higher deformed state fails catastrophically with a load-drop to zero, Fig. 3b.

**Table C.1** Overview of the collected fracture toughness results for both testing directions. Between both specimen orientations the fracture toughness varies between a factor of 5-8. It should be noted that for the high-deformed material with perpendicular specimen orientation the crack strongly deviates from its designated Mode-I crack propagation direction and, hence, cannot be regarded as a pure Mode-I fracture toughness. The calculated values can only be seen as lower bound values for the Mode-I fracture toughness and are therefore put into parentheses.

Specimen	$K_{IC,parallel}$ (MPam <sup>1/2</sup> )	$K_{IC,perpendicular}$ (MPam <sup>1/2</sup> )
low deformed-1	5.1	40.1
low deformed-2	4.9	42.5
high deformed-1	3.7	(19.7)
high deformed-2	3.8	(21.1)

To evaluate the fracture toughness for the parallel orientation, the critical fracture toughness,  $K_{IC}$ , derived from the maximum load is calculated and summarized in Table 1. The results of a second set of experiments in Table 1 prove the consistency of the results. For this testing direction the fracture toughness is in the range of 5 MPam<sup>1/2</sup> for the low deformed state and decreases to approximately 4 MPam<sup>1/2</sup> for the higher deformed material. Calculation of the initiation toughness at the first visible load drop would lead to even somewhat smaller values. On account of the low values of fracture toughness and the high strength levels of the wires the plastic zone



**Figure C.3** Mechanical test records and typical fractographs presenting significant fracture features in the parallel orientation. (a) Load-displacement curve for the low deformed state ( $\epsilon_{log} = 3.1$ ). (b) Load-displacement curve for the high deformed state ( $\epsilon_{log} = 6.52$ ). Three-dimensional reconstruction of the fracture surface for the low (c) and high deformed (d) state. (e) Direct comparison of both fracture halves by looking into the broken specimen for the low deformed state. (f) Contrasting juxtaposition of both fracture surfaces for the high deformed state. One fracture surface was mirrored horizontally in order to show the complete accordance of both fracture halves. The width of the fracture surfaces, which is equivalent to the full thickness of the specimens is in (c,e)  $\sim 6.2 \mu\text{m}$  and  $\sim 1.5 \mu\text{m}$  in (d,f).

size is very small compared to the other dimensions of the cantilevers (see for that also Supplementary) proving that LEFM theory as used here is applicable. Putting the present values in perspective with other materials classes reveals that they are comparable to materials with low fracture toughness such as refractory metals, like pure tungsten [18], many engineering ceramics [5] or conventional glasses [5], which are known as being very sensitive to flaws which renders them unsuited for structural applications. More details to the surprisingly low fracture resistance can be given by fractographic investigations.

Three dimensional reconstructions of the fracture surfaces reveal in both cases, Fig. 3c,d, a distinctive zig-zag fracture surface compared to the flat notch surface. At first sight, this feature could originate from intense local plasticity such as typically observed in ductile materials. However, comparing both corresponding fractured sample portions, Fig. 3e,f, shows that these features mutually match, which excludes strong plastic deformation during crack growth. The fracture morphology therefore represents a rather brittle material behavior which corresponds to the unusually low measured fracture toughness values. The zig-zag structure can be correlated to a curling structure, typically evolving for bcc-iron deformed by wire drawing [19,20]. For the low deformed state, Fig. 3c, the local smooth surface features combined with the zig-zag structure suggest that the crack follows the lamellar alignment present in the drawn wire. For the higher deformed structure, Fig. 3d, the lamellar structure is principally dissolved according to ATP-measurements [12]. Nevertheless, the fractographs are fairly akin to the low deformed state keeping in mind that the wire diameter between the low and high deformed state is reduced by a factor of 5, which means that the periodicity of the zig-zag structure will decrease in a similar fashion. Even though this testing direction exhibits a very low fracture toughness, ideal brittle fracture would correspond to an even lower fracture resistance. Considering the free surface energy,  $\gamma_0$ , with  $\sim 2.4 \text{ Jm}^{-2}$  referring to experimental data [21], and the Young's modulus of 210 GPa for iron, the Griffith toughness [22] that characterizes the ideal brittle fracture case can be calculated by  $K = (2\gamma_0 E)^{1/2}$  yielding a value of about  $1 \text{ MPam}^{1/2}$ . Compared to this estimate, the fracture toughness in the present materials is about a factor of 4-5 larger. This discrepancy implies, that at the nanoscale a distinct amount of plasticity during crack growth has occurred even though the fractographs exhibit fairly smooth and well matching features on both sides, Fig. 3e,f. In undeformed pearlitic steels a random orientation of the locally aligned structure (pearlitic colonies) is typically found leading to a tortuous crack path also called cleavage fracture, which has been comprehensively investigated in the last decades [23-25]. This yields for low and moderately deformed materials fracture toughness values higher than those measured here, however, at the expense of distinctively lower achievable strengths [26,27].

### C.3.2 Perpendicular testing orientation

Typical features of the perpendicular testing direction, which is equivalent to the principal loading direction of wires, are compared in Figs 4 and 5. For the low deformed state, before failure a certain non-linearity occurs in the test record, Fig. 4a, which is in contrast to the high deformed state, Fig. 5a, where the response is purely linear elastic. Calculating the fracture toughness from the test records, a value of  $\sim 40 \text{ MPam}^{1/2}$  is measured for the low deformed state and approximately  $20 \text{ MPam}^{1/2}$  for the high deformed state. A second set of measurements with comparable results is given in Table 1. To verify and confirm these exceptionally high values the crack tip opening displacement for crack initiation ( $CTOD_i$ ) was measured on the fractured samples of the perpendicular testing orientation. With this SEM-method that is based on three-dimensional reconstructions of the fracture surface, the critical deformation of the crack tip before crack extension takes place can be evaluated and related to the fracture toughness measured from the stress-based K-analysis [28,29]. A detailed example of such a measurement and the re-calculation of the corresponding critical fracture toughness in terms of  $K_{IC}$  for both wire types are presented in the Supplementary Material section. The measurements yield values between 38.1 and 43.8  $\text{MPam}^{1/2}$  for the low deformed state and results between 17.5 and 20.5  $\text{MPam}^{1/2}$  for the high deformed state in the perpendicular testing direction (see Supplementary Table S3). This is in good agreement with the results obtained from the global measurements (Table 1). This result demonstrates the applicability of the linear elastic approach and the agreement with the stress-based analyses suggests that residual stresses do not influence the fracture toughness strongly. In summary, the results show an unusually high difference in the fracture toughness in both materials between the parallel and perpendicular testing orientation, indicating a very strong anisotropy in fracture behavior. To explore the mechanistic origins of the large differences typical fracture surfaces are presented in Figs 4 and 5 for both wire types.

### C.3.3 Fractography

Inspecting the failed sample of the low deformed state, a certain amount of necking can be recognized, Fig. 4b, and secondary cracks have developed, Fig. 4c. These propagate along the wire drawing direction and are referred to as delaminations. Between the large delaminations, smaller ones can be observed at higher magnifications, Fig. 4d. Between the delaminations ductile fracture with dimple rupture is visible, Fig. 4e, which is an indication for good fracture toughness. In the high deformed state, see Fig. 5b, the crack strongly deviates from the anticipated crack path and propagates for a certain length along the drawing direction, i.e. along the direction of the aforementioned low fracture toughness before a smoother final fracture surface is formed. The fracture surface is still micro-ductile, Fig. 5c, and displays again various delaminations, Fig. 5d, surrounded by nano-scaled ductile voids.

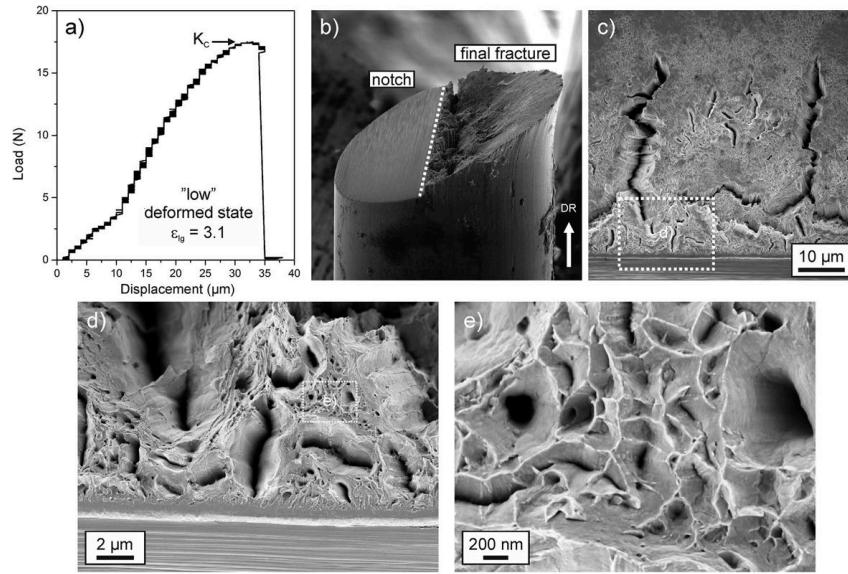


**Figure C.4** Mechanical test records and typical fractographs presenting significant fracture features in the perpendicular orientation of the low deformed state ( $\epsilon_{log} = 3.1$ ). (a) Load-displacement curve showing pronounced plasticity before failure. The change in the slope in the elastic regime after about  $10 \mu\text{m}$  is due to an adjustment of the unloaded specimen into the tensile direction. (b) Side-view onto a broken sample depicting the pre-notch and the final fracture surface. Sample diameter is  $120 \mu\text{m}$ . (c) Typical fractograph looking parallel to the drawing direction. Several large delamination can be observed, which seem to have no specific alignment. (d) Enlarged view of inset in (c) demonstrating a large variety of smaller delaminations adjacent to the precrack. (e) Magnified view of detail shown in (d). Between the delaminations typical features of ductile fracture with dimples in the range of several hundred of nanometers can be seen.

As shown in both deformation states the delaminations are a crucial feature and are required for achieving superior fracture toughness: In general, crack fronts carry pronounced tensile stress triaxiality, which controls the deformation of the crack tip and the onset of crack propagation. Calculations show that the maximum stress in this region is about 3 times the yield strength [30,31], see also the Supplementary Materials section. Keeping in mind that the present material in the highly deformed state has a strength of approximately 30% of the theoretical strength, the stresses near the crack tip indeed approach the theoretical limit. However, the theoretical strength is associated with a de-cohesion of the atomic bonds and would lead to brittle cleavage-type fracture with low fracture toughness. Despite this, a relatively high fracture toughness could be measured and can be explained with the occurrence of the delamination zones. Through the occurrence of delaminations the stress component perpendicular to them, and thus the stress triaxiality is reduced leading to higher crack resistance. To be effective for the fracture toughness enhancement delaminations need to form very close to the pre-existing crack, as observed in Figs

4d and 5e. This mechanism leads to globally higher fracture toughness and has also been observed in samples after rolling [7,32] or severe plastic deformation [33]. A significant aspect for the understanding of these exceptional fracture toughness values is the origin of the delaminations. Figures 4c,d and 5c-e reveal that their crack opening direction is the same as for cracks propagating along the wire axis, which has been found to have an extremely low fracture toughness probed with the parallel orientation measurements. From that it can be rationalized that the weak crack path along the lamella structure with its low fracture resistance is an important requirement for the formation of the delaminations. During loading they are initiated at the weak interfaces and allow a distinctively higher fracture toughness in the principal loading direction as expected from the theoretical viewpoint, suggesting brittle fracture for such ultra-strong materials due to the high stresses at the crack tip close to the theoretical strength.

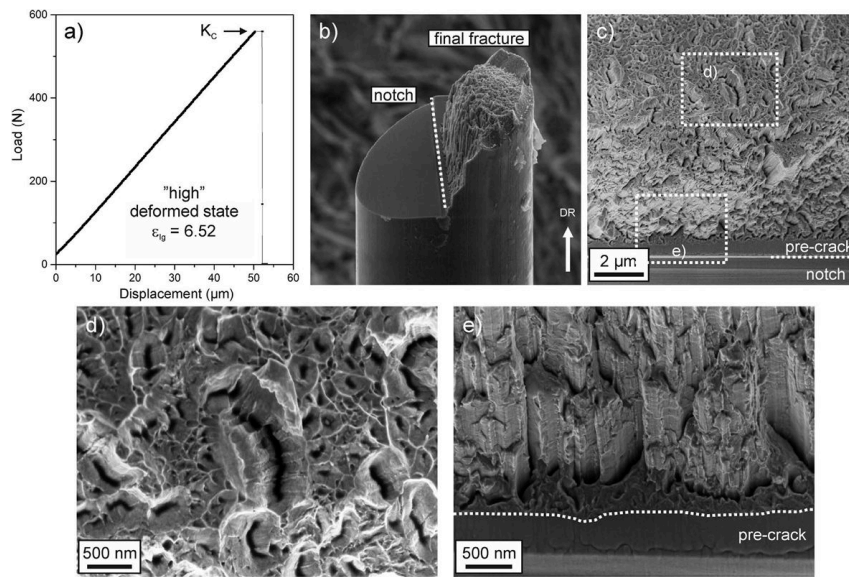


**Figure C.5** Mechanical test records and typical fractographs presenting significant fracture features in the perpendicular orientation of the high deformed state ( $\epsilon_{log} = 6.52$ ). (a) Load-displacement curve with pure linear-elastic behavior before failure. (b) Side-view onto a broken sample with indicated pre-notch and final fracture surface. Sample diameter is  $24 \mu\text{m}$ . (c) Typical fractograph recorded looking parallel to the drawing direction at low magnifications. (d) Magnification of detail indicated in (c) with ductile fracture features. (e) Inclined view onto the transition from pre-crack to final fracture that shows various delaminations before the crack deflects and propagates into the drawing direction. The view is about  $30^\circ$  inclined to the drawing direction to give a better view onto the transition zone with its delaminations and the final crack deflection.

In addition to the occurring delaminations present in both deformation states, a pronounced crack deflection occurs in the high deformed state, see Fig. 5b. It is a consequence of the aligned microstructure, which exhibits a much stronger crack growth resistance perpendicular to the lamellar structure than parallel to it. This

leads to the deflection into the weaker crack growth direction during loading. The real Mode-I fracture toughness would be even higher than the measured K-value as otherwise the crack would not deflect and run into the weak direction. This consideration implies that the results obtained here (around  $20 \text{ MPam}^{1/2}$ ) should only be regarded as a lower bound value for the real Mode-I fracture toughness. An upper bound value for this testing direction can be given with the value of the low deformed structure ( $\epsilon_{log} = 3.1$ ), exhibiting a fracture toughness of approximately  $40 \text{ MPam}^{1/2}$  for this testing direction, see Table 1. This is because with increasing strain the fracture toughness will decrease or stay nearly constant but very unlikely increase. Therefore, the fracture toughness measurements of the low deformed state represent the upper bound value for the real Mode-I fracture toughness in the high deformed state. An inspection of the crack path for the low deformed state, Fig. 4b, demonstrates a slight deflection of the crack as well. Compared to the high deformed state, the deflection only occurs after some global Mode-I crack growth, which determines the fracture toughness. In contrast to the high deformed state, this deflection seems to be an effect of the Mixed-Mode loading conditions introduced by the additional bending torque when the crack becomes very long. To conclude, there is a very fine line between brittle and ductile behavior in such microstructurally nano-scaled highly oriented materials. The accomplishment of high damage tolerance in the main loading direction requires the exploitation of the microstructural anisotropy.

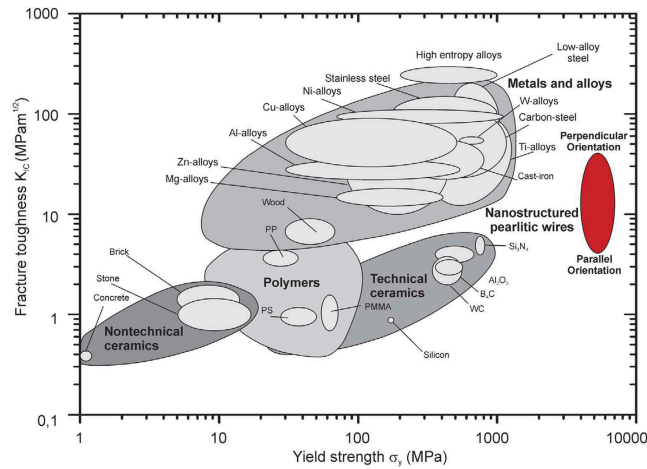


**Figure C.6** Ashby map presenting the fracture toughness plotted against the yield strength of several important engineering material classes. The investigated steel variants set themselves apart from all other material classes [4,5,38] with strength values between 4-7 GPa and fracture toughness values between 4 and  $40 \text{ MPam}^{1/2}$  depending on the testing direction. Even though they do not exceed the fracture toughness of several alloy groups, their damage tolerance in the main loading direction along the wire axis is exceptional and makes them one of the most damage tolerant and strongest materials in the world.

## **C.4 Conclusions**

The significance of the results is clearly demonstrated in an Ashby-map, where fracture toughness is plotted against the yield strength, see Fig. 6. The comparison reveals that these nanostructured pearlitic steels exceed in their joint tensile strength plus fracture toughness than any other conventional material class. Even though the fracture toughness of other alloy classes can exceed that of pearlite, the combination of strength and fracture toughness along the loading direction of these pearlitic steel wires is unique. Similar concepts of toughening as presented here are also often discussed in the context of biological and bio-inspired materials [34,35] and often considered as a new design philosophy. With that in mind, it is fascinating to learn that the steel discussed in this study, often regarded as an allegedly “old-fashioned“ material, shows such a remarkable damage tolerance and the best known combination of high tensile strength and toughness. The underlying toughening mechanism based on the presence of weak interfaces represents an interesting design concept stimulating further innovative ultra-strong and simultaneous tough metallic alloys.

## C.5 Methods

### Material synthesis

The steel has a hypereutectoid composition with 0.98 C, 0.31 Mn, 0.20 Si, 0.20 Cr, 0.01 Cu, 0.006 P, 0.007 S and Fe in balance (wt.%). The steel was austenitized at 1223 K for 80 s followed by the pearlitic transformation, which took place at 853 K for 20 s. This pre-material with an initial diameter of 0.54 mm was then subjected to a cold drawing process. Depending on the diameter reduction, the true (logarithmic) strain amounts to:

$$\epsilon_{log} = \ln \frac{d_0^2}{d_i^2} \quad (\text{C.1})$$

where  $d_0$  is the initial diameter and  $d_i$  is the reduced diameter of the wire. Two specific states were studied, namely, wires deformed to 3.1 and 6.52 with a thickness of 120  $\mu\text{m}$  ( $\epsilon_{log} = 3.1$ ) and  $\sim 24 \mu\text{m}$  ( $\epsilon_{log} = 6.52$ ), respectively.

### Microstructural investigations

The microstructure was investigated using a JEOL JEM-2200FS TEM (transmission electron microscope) operated at 200 KV in both TEM and scanning TEM (STEM) modes. Samples were prepared using a dual-beam Focused Ion Beam/SEM instrument (FEI Helios NanoLab 600TM) with 30 kV Ga ions and a final low voltage milling at 5 kV Ga ions.

### Sample preparation

Micrometer-sized notched cantilevers, suitable for fracture toughness measurements along the drawing axis, were fabricated using a Zeiss LEO 1540 XB dual beam focused ion beam workstation. From the different wire diameters small sections were lift out for further fabrication steps and adequately positioned onto a FIB lift-out grid, which could be conveniently transferred to the testing stage for the consecutive mechanical experiment. Coarse milling currents of 2 nA to 500 pA were used to fabricate the rough shape, followed by a final polishing of the surfaces with 500-100 pA, in order to reduce the impact of ion damage. Finally, the notch was introduced with a milling current of 50 pA with the ion beam cutting direction parallel to the later loading direction allowing a constant crack depth and notch radius across the thickness of the specimen. From both wire diameters two specimens were fabricated and the characteristic dimensions of the test specimens, including the width,  $W$ , the thickness,  $B$ , the crack length,  $a$ , and the bending length,  $L$ , are listed in Supplementary Table S1. Due to the large difference in wire diameter the dimension between the two testing conditions along the wire axis are different.

Using the same fabrication process cracks were introduced into the macroscopic specimens used for testing the fracture behavior perpendicular to the drawing axis. For

the coarse notch milling currents of 25 nA and for the final crack a milling current of 100 pA was in use. The characteristic dimensions, represented by the diameter,  $D$ , the crack length,  $a$ , of the crack front are outlined in Supplementary Table S2.

### Sample testing

Due to the different specimen sizes and maximum testing loads various testing machines inside and outside the SEM differing in their maximum load and displacement capacity were utilized to record the mechanical response of the test samples. The fracture experiments accounting for the parallel orientation were performed in-situ inside a SEM (Zeiss LEO982). Two different micro indenter system were used. The ASMEC UNAT micro indenter equipped with a diamond indenter tip was the main testing machine for the micro-cantilever experiments. In addition, one experiment was performed with a Hysitron Pico-Indenter (PI-85). The cantilevers were loaded under displacement control to total displacements of 2-6  $\mu\text{m}$  with a constant displacement rate of 1  $\mu\text{m}/\text{minute}$ . Videos in terms of SEM-image sequences were recorded, which enables linking the mechanical test record to the crack tip deformation during loading. In total, for each drawing strain and loading condition two experiments were performed, providing consistent results.

The SENT-specimens (single-edge notched tension) of the low-deformed wire sample ( $\epsilon_{log} = 3.1$ ) were tested on a miniaturized testing gear provided from Kammrath and Weiss with a maximum load capacity of 200 N. The SENT-specimens of the high deformed wire ( $\epsilon_{log} = 6.52$ ) were tested on a fibre testing module from the same company with a maximum attainable load of approximately 1 N. The test length of the wires was 1 mm. Similar to the cantilever experiments, described above, for each drawing strain two experiments were performed with consistent results.

### Fracture toughness evaluation

From the load-displacement curves the critical stress intensity,  $K_{IC}$ , was evaluated. The stress intensity of the cantilever specimens used for the evaluation of the fracture toughness parallel to the drawing direction can be calculated according to [36]:

$$K = \frac{FL}{BW^{3/2}} f\left(\frac{a}{W}\right) \quad (\text{C.2})$$

where  $F$  is the force, taken from test record,  $L$  the bending length,  $B$  the thickness of the beam,  $W$  the width of the specimen and  $a$  the crack length. From the test record the maximum load,  $F_{max}$ , was taken to determine the fracture toughness,  $K_{IC}$ . The geometry factor  $f(a/W)$  can be written as:

$$f\left(\frac{a}{W}\right) = 4 \frac{3\left(\frac{a}{W}\right)^{0.5} \left(1.23 - \frac{a}{W} \left(1 - \frac{a}{W}\right) \left(-6.09 + 13.96\frac{a}{W} - 14.05\left(\frac{a}{W}\right)^2\right)\right)}{2\left(1 + 2\frac{a}{W}\right) \left(1 - \frac{a}{W}\right)^{1.5}} \quad (\text{C.3})$$

and was derived by using two-dimensional Abaqus finite element simulations [36]. The stress intensity of the single-edge notched (SENT) specimens subjected to tensile loading conditions used to measure the fracture toughness perpendicular to the drawing axis was evaluated according to:

$$K = \sigma\sqrt{\pi a}f\left(\frac{a}{D}\right) \quad (\text{C.4})$$

where  $\sigma$  is the applied stress of the round bar with  $\sigma = 4F/(\pi D^2)$ ,  $F$  is the force,  $D$ , the diameter of the wire and  $a$  the length of the transverse semi-elliptical surface crack. In each case the maximum load was used to calculate  $K_{IC}$ . The geometry factor,  $f(\frac{a}{D})$ , was numerically obtained with the finite element method [37]:

$$f\left(\frac{a}{D}\right) = 1.4408 - 3.6364\left(\frac{a}{D}\right) + 19.3500\left(\frac{a}{D}\right)^2 - 34.7849\left(\frac{a}{D}\right)^3 + 36.8446\left(\frac{a}{D}\right)^4. \quad (\text{C.5})$$

For details concerning the fractographic investigations and video-sequences of the testing process please refer to the Supplementary information.

## References

- [1] E. Orowan, Fracture and strength of solids, Reports Prog. Phys. 12 (1949) 185-232.
- [2] N.H. MacMillan, The theoretical strength of solids, J. Mater. Sci. 7 (1972) 239-254.
- [3] J. Pokluda, M. Èerný, P. Šandera, M. Šob, Calculations of theoretical strength: State of the art and history, J. Comput. Mater. Des. 11 (2004) 1-28.
- [4] M.F. Ashby, On the engineering properties of materials, Acta Metall. 37 (1989) 1273-1293.
- [5] M.F. Ashby, Materials selection in mechanical design, Butterworth-Heinemann/Elsevier (2010).
- [6] R.O. Ritchie, The conflicts between strength and toughness, Nat. Mater. 10 (2011) 817-822.
- [7] R.W. Hertzberg, Deformation and fracture mechanics of engineering materials, Wiley (1996).
- [8] H.C. Sorby, On the application of very high powers to the study of the microscopical structure of steel, JISI 1 (1886) 140-147.
- [9] J.D. Embury, R.M. Fisher, The structure and properties of drawn pearlite, Acta Metall. 14 (1966) 147-159.
- [10] G. Langford, Deformation of pearlite, Metall. Trans. A 8 (1977) 861-875.
- [11] D. Raabe, P. Choi, Y. Li, et al., Metallic composites processed via extreme deformation: toward the limits of strength in bulk materials, MRS Bull. 35 (2010) 982-991.
- [12] Y. Li, D. Raabe, M. Herbig, P. Choi, S. Goto, A. Kostka, H. Yarita, C. Borchers,

- R. Kirchheim, Segregation stabilizes nanocrystalline bulk steel with near theoretical strength, *Phys. Rev. Lett.* 113 (2014) 106104.
- [13] Y. Li, A. Kostka, P. Choi, S. Goto, D. Ponge, R. Kirchheim, D. Raabe, Mechanisms of subgrain coarsening and its effect on the mechanical properties of carbon-supersaturated nanocrystalline hypereutectoid steel, *Acta Mater.* 84 (2015) 110-123.
- [14] H. Gleiter, Nanocrystalline materials, *Prog. Mater. Sci.* 33 (1989) 223-315.
- [15] M.A. Meyers, A. Mishra, D.J. Benson, Mechanical properties of nanocrystalline materials, *Prog. Mater. Sci.* 51 (2006) 427-556. [16] M. Herbig, D. Raabe, Y. Li, P. Choi, S. Zaeferrer, S. Goto, Atomic-scale quantification of grain boundary segregation in nanocrystalline material, *Phys. Rev. Lett.* 112 (2014) 126103.
- [17] S. Djaziri, Y. Li, G. Nematollahi, B. Grabowski, S. Goto, C. Kirchlechner, A. Kostka, S. Doyle, J. Neugebauer, D. Raabe, G. Dehm Deformation-Induced Martensite: A New Paradigm for Exceptional Steels, *Adv. Mater.* 28 (2016) 7753-7757.
- [18] B. Gludovatz, S. Wurster, A. Hoffmann, R. Pippan, Fracture toughness of polycrystalline tungsten alloys, *Int. J. Refract. Met. Hard Mater.* 28 (2010) 674-678.
- [19] W.F. Hosford, Microstructural changes during deformation of [011] fiber-textured metals, *Trans. Metall. Soc. AIME* 230 (1964) 12-15.
- [20] G. Langford, A study of the deformation of patented steel wire, *Metall. Mater. Trans. B* 1 (1970) 465-477.
- [21] W.R. Tyson, W.A. Miller, Surface free energies of solid metals: Estimation from liquid surface tension measurements, *Surf. Sci.* 62 (1977) 267-276.
- [22] A.A. Griffith, The Phenomena of Rupture and Flow in Solids, *Philos. Trans. R. Soc. London A Math. Phys. Eng. Sci.* 221 (1921) 163-198.
- [23] L.E. Miller, G.C. Smith, Tensile Fractures in carbon steels, *J Iron Steel Inst* 208 (1970) 998-1005.
- [24] Y.J. Park, I.M. Bernstein, The process of crack initiation and effective grain size for cleavage fracture in pearlitic eutectoid steel, *Metall. Trans. A* 10 (1979) 1653-1664.
- [25] J.J. Lewandowski, A.W. Thompson, Microstructural effects on the cleavage fracture stress of fully pearlitic eutectoid steel, *Metall. Mater. Trans. A* 17 (1986) 1769-1786.
- [26] J.M. Hyzak, I.M. Bernstein, The role of microstructure on the strength and toughness of fully pearlitic steels, *Metall. Trans. A* 7 (1976) 1217-1224.
- [27] J. Toribio, J. Ayaso, Micromechanics of fracture in notched samples of heavily drawn steel. *Int. J. Fract.* 115 (2002) 29-34.
- [28] J. Stampfl, S. Scherer, M. Berchthaler, M. Gruber, O. Kolednik, Determination of the fracture toughness by automatic image processing, *Int. J. Fract.* 78 (1996) 35-44.
- [29] T.L. Anderson, *Fracture mechanics*, CRC Press (1991).
- [30] K.-H. Schwalbe, *Bruchmechanik metallischer Werkstoffe*, Hanser Munchen (1980).
- [31] J.R. Rice, M.A. Johnson, The role of large crack tip geometry changes in plane strain fracture, Division of Engineering, Brown University (1969).
- [32] K.T. Venkateswara Rao, W. Yu, R.O. Ritchie, Cryogenic toughness of commercial aluminum-lithium alloys: Role of delamination toughening, *Metall. Trans. A*

20 (1989) 485-497.

[33] A. Hohenwarter, A. Taylor, R. Stock, R. Pippan, Effect of large shear deformations on the fracture behavior of a fully pearlitic steel, *Metall. Mater. Trans. A* 42 (2011) 1609-1618.

[34] O. Kolednik, J. Predan, F.D. Fischer, P. Fratzl, Bioinspired design criteria for damage-resistant materials with periodically varying microstructure, *Adv. Funct. Mater.* 21 (2011) 3634-3641.

[35] U.G.K. Wegst, H. Bai, E. Saiz, A.P. Tomsia, R.O. Ritchie, Bioinspired structural materials. *Nat. Mater.* 14 (2015) 23-36.

[36] S. Wurster, C. Motz, R. Pippan, Characterization of the fracture toughness of micro-sized tungsten single crystal notched specimens, *Philos. Mag.* 92 (2012) 1803-1825.

[37] J. Toribio, N. Álvarez, B. González, J.C. Matos, A critical review of stress intensity factor solutions for surface cracks in round bars subjected to tension loading, *Eng. Fail. Anal.* 16 (2009) 794-809.

[38] B. Gludovatz, A. Hohenwarter, D. Catoor, E. Chang, E. George, R. Ritchie, A fracture-resistant high-entropy alloy for cryogenic applications, *Science* 345 (2014) 1153-1158.

### Acknowledgements

Funding of this work has been provided by the European Research Council under ERC Grant Agreement No. 340185 USMS and by the Austrian Science Fund in the framework of research project P26729-N19. The authors thank Dr. H. Yarita, Suzuki Metal Industry Co. Ltd. Japan for producing the cold drawn specimens. We also thank Mr. Andreas Sturm for TEM sample preparation and Dr. Aleksander Kostka for his help with TEM measurements.





# Structural instabilities during cyclic loading of ultrafine-grained copper studied with micro bending experiments

M.W. Kapp<sup>a</sup>, T. Kremmer<sup>a,b</sup>, C. Motz<sup>a,c</sup>, B. Yang<sup>a</sup> and R. Pippan<sup>a</sup>

<sup>a</sup>Erich Schmid Institute of Materials Science, Austrian Academy of Sciences, 8700 Leoben, Austria

<sup>b</sup>Chair of Nonferrous Metallurgy, University of Leoben, Franz-Josef-Str. 18, 8700, Leoben, Austria

<sup>c</sup>Department Materials Science and Engineering, Saarland University, Gebäude D2.2, 66041, Saarbrücken, Germany

## Abstract

The cyclic mechanical properties and microstructural stability of severe plastically deformed copper were investigated by means of micro bending experiments. The ultrafine-grained structure of OFHC copper was synthesized utilizing the high pressure torsion (HPT) technique. Micron sized cantilevers were focused-ion-beam milled and subsequently tested within a scanning electron microscope in the low cycle fatigue regime at strain amplitudes in the range of  $1.1 - 3.2 \cdot 10^{-3}$ . It was found that HPT processed ultra-fine grained copper is prone to cyclic softening, which is a consequence of grain coarsening in the absence of shear banding in the micro samples. Novel insights into the grain coarsening mechanism were revealed by quasi in-situ EBSD scans, showing i) continuous migration of high angle grain boundaries, ii) preferential growth of larger grains at the expense of adjacent smaller ones, iii) a reduction of misorientation gradients within larger grains if the grain structure in the

neighborhood is altered and iv) no evidence that a favorable crystallographic orientation drives grain growth during homogeneous coarsening at moderate accumulated strains, tested here.

## **D.1 Introduction**

Grain size reduction by severe plastic deformation (SPD) is well established to synthesize bulk ultrafine-grained (UFG) or nanocrystalline (NC) samples. Similar to the static strength, the performance in the high cycle fatigue (HCF) regime has been proven to be enhanced significantly compared to the coarse grained (CG) counterparts for UFG [1-4] and NC materials [5-8]. The reason for enhanced fatigue limits or HCF performance can be explained by a shift of the onset of microplasticity, necessary to induce fatigue damage, to higher stress levels than in the CG condition. Unfortunately, the performance of such materials in the low cycle fatigue (LCF) regime, where higher plastic strain amplitudes are present, is deteriorated and cyclic softening is promoted. For UFG materials, which will be in the focus of the current work, cyclic softening has been found to occur not only under strain controlled conditions (decreasing stress amplitude) for purity levels above 99.9% [9-12], but also in stress controlled experiments above a certain stress amplitude, where the softening is reflected in a continuously increasing strain amplitude [11,12]. However, these studies have conflicting viewpoints about the impact of the strain amplitude. Although it is frequently reported that cyclic softening is more pronounced at higher strain amplitudes [1,13,14], other experiments show that low strain amplitudes and the concomitant enhanced lifetime enable time dependent thermally activated processes to occur and promote cyclic softening [11]. Also, material parameters can be decisive for the occurrence or magnitude of cyclic softening, for instance, a high purity level [14] or the grain shape [1]. Although it is well known that different SPD procedures generate materials of different grain boundary structures, the grain boundary misorientation has been disregarded in the context of the cyclic mechanical response for a long time. Although cyclic softening was revealed for structures consisting of major fractions of low angle grain boundaries (LAGB) [1] or high angle grain boundaries (HAGB) [11], their direct influence has not been investigated systematically.

For UFG materials, three mechanisms have been found to contribute to the observed cyclic softening, which are i) shear band formation, ii) coarsening of the fine scaled grain structure [15,16] as well as iii) a reduction of the defect density, in especially dislocation density [3,9], or a combination of them. These mechanisms can lead to early strain localization, fatigue damage and failure of the samples. The small grain size and the resulting large grain boundary fraction was suspected to be responsible for these microstructural instabilities as it offers large driving forces for grain growth.

Despite the extensive work carried out on this topic, detailed knowledge about the initiation and evolution of these structural instabilities is still at its infancy. As

an example, the nature of the grain growth process in these fine-scaled structures is currently not completely understood. A thorough description, whether grain growth proceeds in discrete events or in a rather continuous manner, if a certain incubation time is needed, or which grains will start to grow, is still unclear. Further issues include whether a certain crystallographic orientation is favored to grow or shrink, as well as the importance of the grain boundary type (LAGB, HAGB).

The ambiguities about the processes inducing structural instabilities prevent an understanding of how cyclically stable materials need to be designed. A sound identification of the driving forces for the underlying processes and how they evolve are of utmost importance to control the microstructural stability in a successful way.

To gain a thorough understanding about the mechanisms occurring during cyclic loading of UFG structures, a suitable experimental setup was looked for. Cyclic micro bending experiments, conducted inside a scanning electron microscope (SEM), allow for a unique correlation between changes in the microstructure and the local stress-strain state. Further, tracing the same sample area throughout the entire experiment enables the detection of crucial changes in the surface morphology, for instance shear bands or fatigue cracks which in turn may affect the softening process. Special emphasis was placed on the identification of possible correlations between boundary misorientation and crystallographic orientations with structural instabilities.

## D.2 Experimental

Quasi constrained high pressure torsion (HPT) [17] was used to synthesis an oxygen free high conductivity (OFHC) copper (99.95%) with ultrafine grains. The HPT disk diameter  $d$  and its thickness  $t$  were 15 mm and 7.5 mm, respectively. Deformation was conducted at a pressure of 3.5 GPa for 15 revolutions  $n$ , which resulted in an equivalent v. Mises strain  $\epsilon_{eq}$  of 87 at an HPT radius  $r$  of 12 mm, from which the sample was extracted, according to Eq. (1)

$$\epsilon_{eq} = \frac{2\pi rn}{t\sqrt{3}}. \quad (\text{D.1})$$

Such strains are sufficient to obtain constant mechanical and structural properties throughout the entire HPT disk, except the very center ( $r < 1$  mm). In this steady state region the grain size was measured by electron back scatter diffraction (EBSD) to be 530 nm (area weighted).

For the cyclic micro bending experiments, a platelet was extracted from regions of saturated microstructure, which was subsequently cut into rods of  $1 \times 1$  mm<sup>2</sup> in cross-section. The top of the rods were electrochemically etched to form tips, where the final bending beam was focused-ion-beam (FIB) milled with a Zeiss LEO 1540 XB dual beam FIB workstation. For the bending beams, thickness to length ratios between 1:1 and 1:2 were used. A schematic drawing of a bending beam is shown in Fig. 1. The actual size of all samples tested can be found in Table 1.

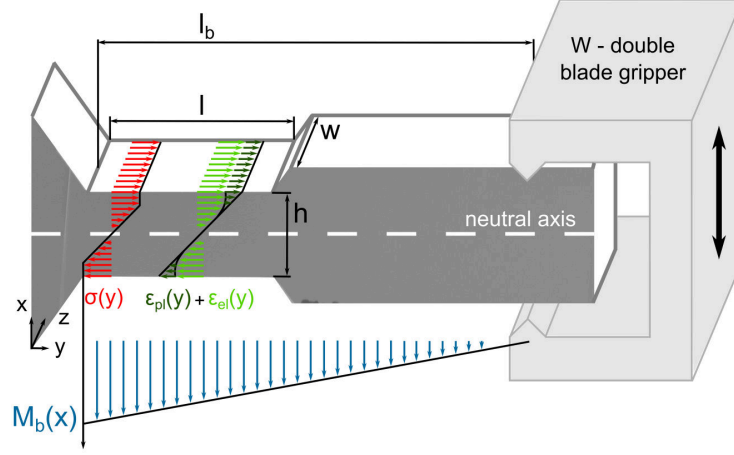


**Figure D.1** Schematic drawing of a miniaturized bending beam with dimension labels of the width  $w$ , height  $h$ , length  $l$  and bending length  $l_b$ , as well as the distribution of the normalized bending moment  $M_b(x)$  along the  $x$ -axis. Strain  $\epsilon(y)$  and stress  $\sigma(y)$  values along the  $y$ -axis are indicated.

To illustrate the mechanical and the structural changes, two samples have been selected for this study, denoted sample A and B. The cyclic micro bending experiments were conducted inside a SEM (Zeiss LEO982) using an ASMEC UNAT (sample A) and a Hysitron PI85 (sample B) microindentation system to impose the strain amplitude. A FIB milled tungsten double blade gripper was used to impose the cyclic load onto the samples. The bending beams were loaded under displacement control, resulting in plastic strain amplitudes  $\epsilon_{a,pl}$  of  $1.1 - 3.2 \cdot 10^{-3}$  at the outer fiber, with a stress ratio  $R = -1$  at a strain rate  $\dot{\epsilon}$  in the range of  $2.6 - 3.8 \cdot 10^{-3} \text{ s}^{-1}$  (for details see Table 1). For sample B EBSD scans were conducted after 100, 200, 300 and 400 cycles to track the coarsening process.

The elastic contributions of the measured displacement stemming from the needle, SEM-stage and the specimen holder were taken into account by correcting the measured compliance using a method according to Wurster et al. [18]. The outer fiber stress  $\sigma_s$  was calculated from the force-displacement data, based on elastic bending beam theory according to Eq. (2):

$$\sigma_s = \frac{6Fl_b}{wh^2}. \quad (\text{D.2})$$

Although this is a good approximation for small strain amplitudes, it overestimates the stress at larger strain amplitudes. The outer fiber strain  $\epsilon_s$  according to Eq. (3):

$$\epsilon_s = \frac{uh}{2ll_b}. \quad (\text{D.3})$$

is simply derived from the applied displacement and assumed to be constant in the

gauge length. The measured force is  $F$ , the bending length  $l_b$ , gauge section width  $w$ , gauge section height  $h$ , the beam deflection  $u$  and the gauge section length  $l$ .

**Table D.1** Dimensions in  $\mu\text{m}$  of the tested bending beams with width  $w$ , height  $h$ , length  $l$  and bending length  $l_b$  and the testing parameters strain rate  $\dot{\epsilon}$  in  $\text{s}^{-1}$ , plastic strain amplitude  $\epsilon_{a,pl}$ , the number of cycles  $N$  and the total applied accumulated plastic strain  $\epsilon_{acc,pl}$ .

	<b>h</b>	<b>w</b>	<b>l</b>	<b><math>l_b</math></b>	<b><math>\dot{\epsilon}</math></b>	<b><math>\epsilon_{a,pl}</math></b>	<b>N</b>	<b><math>\epsilon_{acc,pl}</math></b>
$\sigma_{0.2}$ [MPa]	5.0	7.5	10.0	42.0	$2.6 \cdot 10^{-3}$	$1.1 \cdot 10^{-3}$	5800	25.5
$\sigma_1$ [MPa]	5.0	7.5	10.0	42.0	$3.8 \cdot 10^{-3}$	$1.9 \cdot 10^{-3}$	1200	34.6
$\sigma_1$ [MPa]	3.4	3.3	2.7	12.6	$3.1 \cdot 10^{-3}$	$3.2 \cdot 10^{-3}$	400	5.1

## D.3 Results

### D.3.1 Cyclic hysteresis loops

The cyclic hysteresis loops of sample A are shown in Fig. 2 for two different plastic strain amplitudes,  $\epsilon_{a,pl} = 1.1 \cdot 10^{-3}$  (a) and  $1.9 \cdot 10^{-3}$  (b-d), respectively. For both strain amplitudes only certain cycle numbers (90, 990, 2990, 4990, 5790 for  $\epsilon_{a,pl} = 1.1 \cdot 10^{-3}$  and 90, 790, 990, 1190 after the increase to  $\epsilon_{a,pl} = 1.9 \cdot 10^{-3}$ ) are plotted to ensure a better visibility. The maximum tensile and compressive surface stresses at the lower strain amplitude  $\epsilon_{a,pl} = 1.1 \cdot 10^{-3}$  in Fig. 2a stay nearly constant up to 5790 cycles, corresponding to an accumulated plastic strain  $\epsilon_{acc,pl}$  of 25.5 according to Eq. (4):

$$\epsilon_{acc,pl} = 4 * \epsilon_{a,pl} * N. \quad (\text{D.4})$$

However, an increase of the applied plastic strain amplitude of sample A to  $1.9 \cdot 10^{-3}$  (Fig. 2b-d) causes a continuous drop in the maximum surface stresses during 1190 cycles, corresponding to an accumulated plastic strain of 34.6. The estimated maximum surface stress drops by 5% and 7% of the maximum stress, from 541 and -595 MPa to 515 MPa and -552 MPa, at the maximum of the positive and negative displacement deflection after 1190 cycles, respectively.

### D.3.2 Changes in the surface morphology

In addition to the cyclic stress-strain response of the samples, SEM images were taken to capture possible changes of the surface morphology. SEM images taken from the outer fiber side surface of sample A in Fig. 3a show that cyclic bending for 5800 cycles at  $\epsilon_{a,pl} = 1.1 \cdot 10^{-3}$  ( $\epsilon_{acc} = 25.5$ ) and for additional 1200 cycles at  $\epsilon_{a,pl} = 1.9 \cdot 10^{-3}$  ( $\epsilon_{acc} = 34.6$ ) already caused a significant degradation of the sample surface. A very local roughening becomes visible at the transition from sample head to the gauge section, where the maximum bending moment and thus, stresses and strains, are applied to the cantilever. Sample B (Fig. 3b) shows similar features of surface damage at the highly strained region of the cantilever consisting of severe depressions and protrusions. However, although surface roughening serves as a precursor for

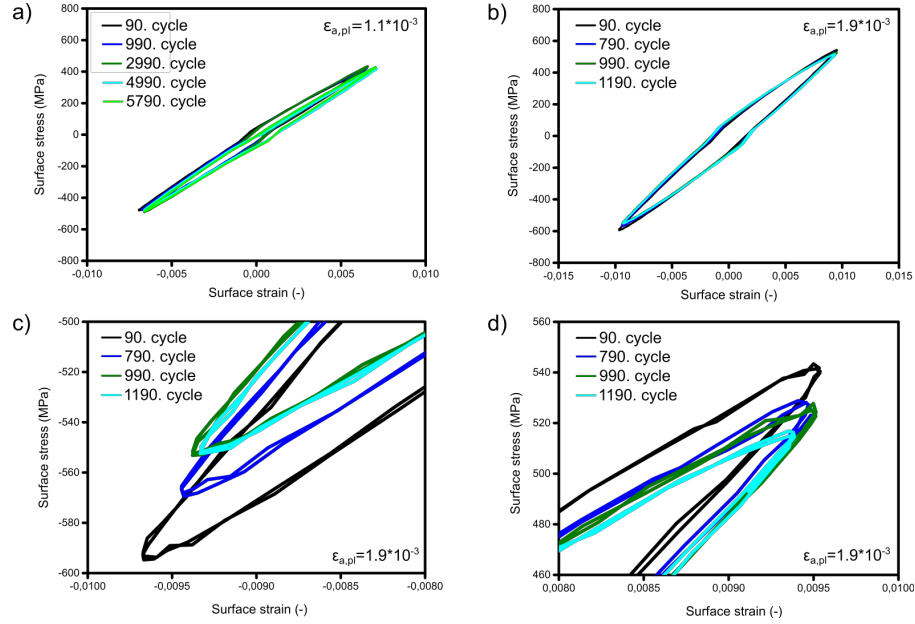


**Figure D.2** Cyclic hysteresis loops for strain amplitudes of a)  $\epsilon_{a,pl} = 1.1 * 10^{-3}$  and b-d)  $\epsilon_{a,pl} = 1.9 * 10^{-3}$ . a) No changes in the maximum surface stress were observed for the smaller strain amplitude, b) whereas cyclic softening occurred for the larger strain amplitude at the maximum of the c) negative and d) positive displacement deflection.

fatigue crack initiation, those have not been observed at the surface. Furthermore, shear or cyclic slip bands emerging at the sample surface are frequently reported for ECAP processed samples [3], but are not visible on the micro cantilever surfaces.

### D.3.3 Changes in microstructure

As mentioned earlier, the observed cyclic softening could be a consequence of grain coarsening. To capture structural changes during cyclic loading, BSE images of the cantilever were recorded. BSE images shown in Fig. 4 were taken from the side surface and from the top surface of FIB prepared cross-sections (labelled 1, 2, 3) of sample A in a certain distance from the neutral axis as marked in the schematically drawn cantilever. Considering that a plastic strain amplitude of  $1.9 * 10^{-3}$  is applied to a cantilever of  $7.5 \mu\text{m}$  width, the maximum plastic strains occur at the outer fiber region, whereas near the neutral axis, the cantilever will still deform approximately elastically (see stress-strain distribution schematically drawn in Fig. 1). Inherent to the bending geometry, the magnitudes of the elastic strains and stresses are applied in terms of a gradient along the side surface in Fig. 4, decreasing towards the neutral axis, where they finally disappear. As a consequence, during cyclic bending the grain size evolves heterogeneously along the cantilever width. Near the neutral axis, a region with low stress-strain values, the grain size has not changed significantly (Fig. 4, side surface), compared to the initial state. This is also visible in the BSE

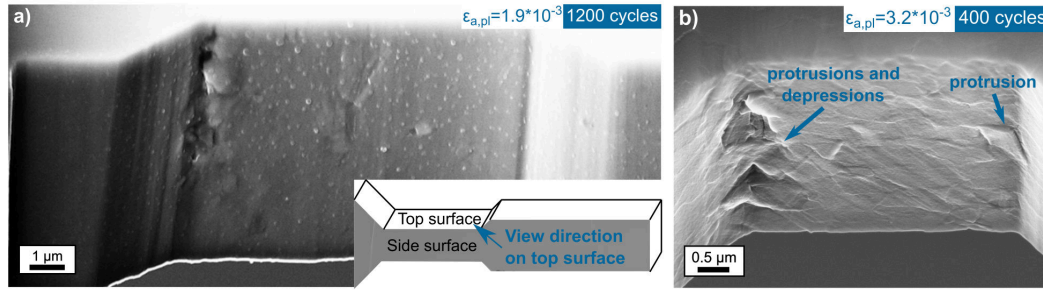


**Figure D.3** Localized damage initiation at the highly strained region (outer fiber, clamping) of a) sample A tested at  $\epsilon_{a,pl} = 1.9 \cdot 10^{-3}$  and b) of sample B tested at  $\epsilon_{a,pl} = 3.2 \cdot 10^{-3}$  taken after 400 cycles with protrusions and depressions.

images of the top surface (see image labelled 1), reflecting the microstructure in the thickness direction of the cantilever. In regions closer to the outer fiber, where larger strains are active, single grains have already coarsened, approaching more than 1 mm in size (see image labelled 2). This coarsening is even enhanced at the outer fiber, where the maximum stress and strain is present, resulting in single grains, which have grown up to almost 2 mm in size (see image labelled 3), still embedded in an UFG matrix, where limited grain growth occurred.

To analyze the mechanisms of grain coarsening in more detail (e.g. crystallographic orientation of growing grains), sequential EBSD scans of the gauge section were performed throughout the experiment on sample B. These results are depicted in Fig. 5. At first glance, a comparison of the IPF maps (top row) between the as-HPT processed material (0 cycles, Fig. 5a), the state after 100 cycles (Fig. 5b), 200 cycles (Fig. 5c), 300 cycles (Fig. 5d) and 400 cycles (Fig. 5e) does not yield major differences. However, a closer look manifests three different processes that occur manifoldly at various positions of the cantilever. The identified processes are: growth of larger grains, appearance of new grains and reduction of misorientation gradients. Examples at positions where these processes occurred are shown in the magnified details (labelled 1, 2, 3) in Fig. 5a-e). Firstly, a growth of larger grains at the expense of adjacent smaller grains was captured frequently (second row). For example, it can be seen that the grain boundary of the larger grain (turquoise) migrates towards the bottom left in the direction of the smaller adjacent grain (orange), which continuously shrinks until it finally disappears after 400 cycles (see Fig. 5e). Secondly, a new grain appeared and grows during cycling (see light green grain in third row). Although it cannot be proven, this process might be explained by the fact that a growing grain from just below the surface consumed grains partially covering the observed surface. Thirdly, a reduction of misorientation gradients, seen as LAGB with small misorientation angles, appeared in certain grains (fourth row). This is illustrated for a pink grain, exhibiting a misorientation of  $4.2^\circ$  in the undeformed state (Fig. 6a), which is removed after 100 cycles (Fig. 6c). However, misorientation gradients are not necessarily removed, as shown for a purple grain with an

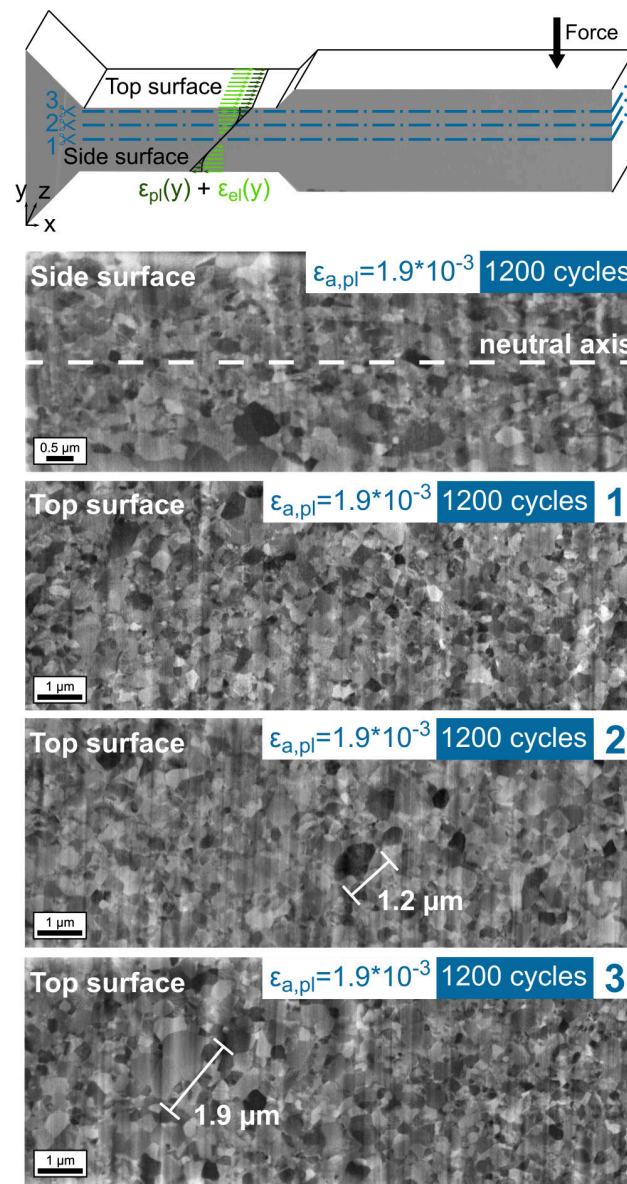


**Figure D.4** BSE images of the side surface of sample A after 1200 cycles at  $\epsilon_{a,pl} = 1.9 \cdot 10^{-3}$  show a gradient in the grain size evolution, which increases from the neutral axis towards the outer fiber. BSE images from the top surfaces confirm a smaller grain size in the region near the neutral axis (position 1), which increases with increasing strain amplitude (position 2) and shows grains with a size of a few micrometers near the outer fiber (position 3).

initial misorientation gradient of  $5.1^\circ$  (Fig. 6b) retaining a misorientation gradient of  $4.9^\circ$  after 100 cycles (Fig. 6d). It should be mentioned that these processes do not occur in an isolated way. Quite on the contrary, many structural changes of the grain structure occur as a consequence of a combination of the mentioned processes. For instance, in detail 2) a new grain appears (light green) and undergoes a growth procedure similar as remarked for detail 1) with the addition that growth occurs in every grain direction, so that it has eventually more than doubled its size. Similarly, also the reduction of misorientation gradients in detail 3) is accompanied by the migration of the grain boundary and a distinct expansion of the grain size.

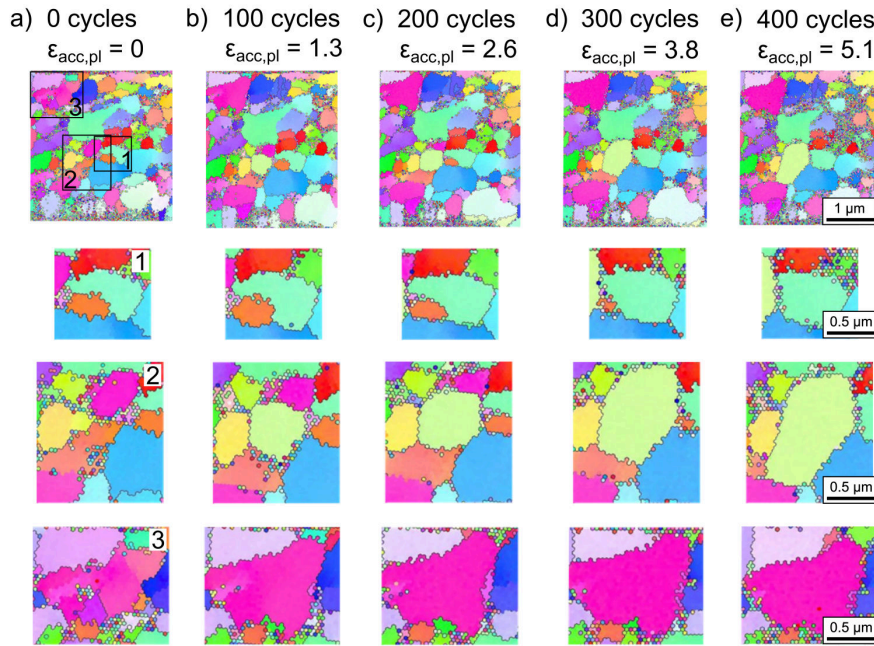


**Figure D.5** EBSD images of a) the initial structure and after b) 100, c) 200, d) 300 and e) 400 cycles show that in most cases large grains grow at the expense of smaller grains (example shown for position 1), a suddenly appearing grain continuously grows (example shown for position 2) and misorientation gradients disappear in large grains (example shown for position 3).

## D.4 Discussion

Cyclic softening in strain controlled fatigue experiments under LCF conditions has been frequently observed in the past for high purity copper or aluminum [1,3,9,11,12,19]. In these experiments, the principal structural changes responsible for early strain localization and thus a deteriorated mechanical performance have been identified. These changes include shear band formation, grain coarsening [11,19] and a reduction of the initial dislocation density [3]. Despite the vast number of studies, the

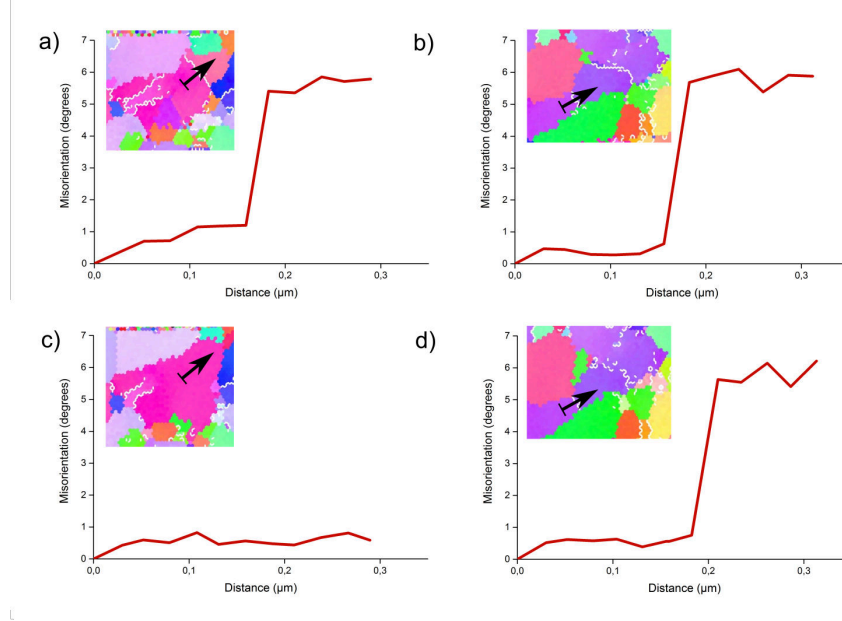


**Figure D.6** a-b) Misorientation profiles within two initial grains depicted from EBSD measurements; c) misorientation gradient disappears in certain grains after 100 cycles, d) while it remains in others after 100 cycles. Lines from where misorientation profile stems are marked in the small inserts, low angle grain boundaries are drawn in white.

basic mechanisms leading to structural instabilities, or how they can be avoided, could not be identified.

Most of the studies mentioned above have been conducted on UFG metals synthesized by ECAP. The reported mechanical and microstructural instabilities therein refer to microstructures of different grain shape (equiaxed, elongated) and grain boundary structures (different fraction of HAGB and LAGB), depending on the chosen ECAP route and number of passes [20]. ECAP structures synthesized by a large number of passes are especially characterized by a majority of HAGB, which is similar to HPT structures. Due to the large strains applied during HPT, the structure of the current work consists of about 80% HAGB and 20% LAGB [21]. The cyclic hysteresis loops in Fig. 2 confirm that also the HPT structure is prone to cyclic softening, akin to ECAP structures, where the cyclic stress decreases after just 20 cycles at a comparable plastic strain amplitude of  $\epsilon_{a,pl} = 1 \cdot 10^{-3}$  [11]. There, the pronounced macroscopic softening stems from a severe localization of the applied cyclic strain in shear bands, where the coarsening process seems to be enhanced. In the present study, SEM images of the tested cantilevers indicate that a homogeneous grain size increase after cyclic loading (Fig. 4) is responsible for the degradation of the stress response. Although the occurrence of grain coarsening correlates to observations for ECAP structures [11], no shear bands developed during the number of cycles tested (Figs. 3 and 4). It should be mentioned that the homogeneous and moderate grain coarsening could be a consequence of the micro

mechanical setup, which does not allow for large scale shear bands to form due to the confined sample dimensions. Furthermore, it is assumed that the homogeneous grain coarsening does not weaken the cyclic strength as much as in the case when severe grain growth is localized in large scale shear bands. Beside grain growth, a reduction of the dislocation density has been found to contribute to cyclic softening as the grain boundary becomes more defined during the fatigue experiment [3]. This results are consistent with the seminal work of Feltner and Laird, where cold worked structures, consisting mainly of cells of LAGB type, were tested in the LCF regime [22,23]. Similarly as in the ECAP structures, the cell walls appeared sharper after the fatigue experiment and in addition also defects in the cell interior were less frequently found [23]. Although defect densities have not been measured directly in the present work, such changes in the dislocation content have been found to occur most prominent during the very first cycles, while for larger cycle numbers changes in the hysteresis loops become negligible [23,24]. These results seem plausible even for UFG structures tested here, as excess dislocations may annihilate easily at the numerous grain boundaries until a certain density, sufficient to realize a given plastic strain amplitude is reached. However, the results of this micro bending experiment show continuous softening up to accumulated strains of 34.6. For this reason, although contributions to the softening from a reduction in the dislocation density cannot be excluded for the very first cycles, in the authors' opinion the main reason for the cyclic softening observed here, is a consequence of grain coarsening.

An often and controversially discussed parameter influencing the amount of cyclic softening is the applied strain amplitude. Whereas many studies report enhanced cyclic softening for larger strain amplitudes [1,14,25], other works show more pronounced softening for low strain amplitudes, where the extension of the lifetime should promote thermally activated grain growth. In that context, the accumulated plastic strain  $\epsilon_{acc,pl} = 4N\epsilon_{a,pl}$ , which additionally takes into account the number of cycles tested, is an often overlooked parameter. For instance in the work of Höppel and Mughrabi [11] the increased cycles to failure observed at a lower strain amplitude ( $N_f = 160014$  and  $\epsilon_{a,pl} = 2 \cdot 10^{-4}$ ) lead to a larger accumulated plastic strain as compared to a higher plastic strain amplitude ( $\epsilon_{a,pl} = 1 \cdot 10^{-3}$  and  $N_f = 6552$ ). Consequently, the enhanced cyclic softening ratio  $CSR = 1 - \frac{\frac{\Delta\sigma}{2}_{N_f/2}}{\frac{\Delta\sigma}{2}_{N=1}}$ , taking into account the stress drop at half of the sample lifetime  $\frac{\Delta\sigma}{2}_{N_f/2}$ , revealed for the lower plastic strain amplitude accords to a higher accumulated plastic strain. Solely considering the plastic strain amplitude in the current results would suggest that a minimum plastic strain amplitude is required for the onset of cyclic softening, which was absent until the plastic strain amplitude was increased to  $1.9 \cdot 10^{-3}$ . It is important to note, that cyclic softening did not only go along with an increased plastic strain amplitude, but also with an increased accumulated plastic strain due to an increased cycle number. Although the simultaneous linear increase of strain amplitude and accumulated strain of the experimental procedure does not allow to unambiguously differentiate, which parameter is responsible for the onset of cyclic

softening, the accordance with the work of Höppel and Mughrabi [11] suggests that the accumulated strain is decisive for the onset of softening mechanisms and the subsequent degradation of the cyclic stress.

For the comparison of the micro bending experiment with macro experiments it is important to take into account that i) micro bending samples have a strong strain gradient and hence, a gradient in strain amplitude and accumulated strain, ii) in macro samples the coarsening is related to the macroscopic strain amplitude and the accumulated macroscopic strain, however, coarsening occurs often in shear bands, iii) no shear bands are formed in micro samples, therefore homogeneous coarsening takes place, which is more pronounced at the outer fiber due to the mentioned gradient. Although the stress amplitude also obeys a gradient, the stresses applied to the outer fiber region are nearly constant as soon as the yield stress is reached. Assuming for simplicity a linear cyclic stress increase from the neutral axis to the outer fiber, one can calculate at which cantilever height the applied stress equals the yield stress, which has been found to be around 443 MPa UFG copper of 99.97% purity [26]. For the lower applied plastic strain amplitude of  $1.1 \cdot 10^{-3}$  the macroscopic yield stress barely catches the outer fiber region, whereas at the larger plastic strain amplitude of  $1.9 \cdot 10^{-3}$  the yield stress is reached at a distance of 500 nm from the outer fiber. Interestingly, grain growth occurs even in a larger distance of  $1.5 \mu\text{m}$  away from the outer fiber (Fig. 4, side surface view), where the cyclic stress is with 340 MPa, distinctly lower than the macro yield stress. However, micro yielding will take place.

As mentioned earlier, shear banding does not contribute to the observed softening, at least at these low accumulated plastic strains. Thus, the significant contribution to the observed softening must necessarily arise from grain coarsening. The main questions of the coarsening process are still unresolved, for instance: i) Is the nature of the grain growth process of continuous or discontinuous manner and does it occur immediately or is a certain incubation time needed? ii) Is the type of grain boundary relevant for grain coarsening? iii) Do crystallographic orientations exist, which preferentially grow? iv) Is the driving force for grain coarsening of thermal or mechanical nature? v) What is the direct impact on the mechanical response? The clarification of these ambiguities is of utmost importance and will be stressed with regard to the present results in the following paragraphs.

- i) It was argued in the past that grain coarsening in cyclically loaded OFHC UFG copper is similar to dynamic recrystallization [2,11]. However, in these experiments only the final structure could be analyzed, without any knowledge of what happened during the cyclic loading in the structure. From the quasi in-situ experiments it could be deduced that grain coarsening is most likely caused by a continuous migration of grain boundaries (Fig. 5). Although the structure was not continuously traced during cyclic bending, but only after 100 cycles for the first time, it is very unlikely that a certain critical strain has to be applied to initiate the boundary migration process, as observed

in classical dynamic recrystallization studies [27]. The structures tested here were already deformed to severe strains, where continuous boundary migration was found to occur, restoring an equilibrium structure which consists only of deformation texture components at low homologous temperatures [28,29]. Large grains were frequently observed to grow at the expense of smaller ones. This growth process seems to occur in a continuous manner, where the grain boundary migrates towards the smaller grain and continuously sweeps over it. Grain growth processes studied by in-situ TEM on UFG Al thin films under continuous loading conditions during nanoindentation [30] or tensile straining [31] similarly show a rapid movement of a general grain boundary whereby larger grains usually grew at the expense of adjacent smaller grains. The accordance in these two essential points with the present experiments suggests that the principal mechanisms for grain coarsening have to be the same for monotonic and cyclic loading conditions.

- ii) Approximately 80% of the boundaries generated during HPT are HAGB and 20% LAGB, which are mainly observed within larger grains. The current experiments show that they react differently to the applied cyclic strain. This is in contrast to early studies on ECAP structures exhibiting a large fraction of low angle grain boundaries, where the main coarsening procedure was characterized by a distinct growth of the cells having small misorientation angles [9]. The current experiments clearly show, while the HAGB were the ones that cause grain growth (see HAGB as black lines for detail 1 in Fig. 5), the LAGB within the grain interior remain pretty stable, with only minor misorientation changes (see LAGB as white lines in Fig. 6b,d). Only in cases where surrounding grains in the neighborhood disappear or a migration of the boundary is observed the misorientation of the LAGB is distinctively reduced (see for instance Fig. 6a,c where blue and orange grains at the top shrink and disappear), which allows for accommodation of plastic strains. Because considerable changes of the LAGB seem only to occur if a particular grain's surroundings are changing significantly, they are likely to be classified as geometrically necessary boundaries [27]. This means that they realize a certain misorientation gradient along the grain, necessary to accommodate plastic strain with respect to the neighborhood. If the surroundings change due to growth or shrinkage, the character of this boundary is also prone to change.
- iii) As not all of the grain boundaries within the sample cross-section migrate, it is of interest, whether grains of a certain crystallographic orientation are more susceptible to grow or shrink. In an earlier study focusing on grain boundary migration during severe monotonic cold rolling of HPT processed Cu, no preferred crystallographic orientation was found to grow [28]. Quite contrary, stress differences between neighboring grains arising from differences in the Taylor factor or the grain size led to differences in the strain energy density, which seemed to trigger the direction of the migration process [28].

## *D Publications*

However, under cyclic loading conditions, a preferential growth of a certain crystallographic orientations could not be identified in this study, at least within these low accumulated plastic strains of 5.1, as applied here.

- iv) We have shown that grain coarsening is the consequence of migrating grain boundaries. However, the decisive and most challenging question is: what drives the boundary to move? It has been argued that fatigue induced grain coarsening is thermally driven, since lower strain rates showed an enhanced effect [2]. Although certain thermal activation can never be neglected, the observation of large growing and small shrinking grains in monotonic loading tests at elevated temperatures led to the conclusion that the curvature of the grain boundary triggers the migration direction of the grain boundary [32]. Therefore, smaller grains exhibit a stronger concavity and tendency to shrink and disappear. However, this grain size effect can also be explained in lieu of the elastic strain energy. Thereby the variance in strain energy density, which is smaller in larger grains due to a lower yield stress, but larger in smaller grains due to an increased yield stress, may act as a driving force. However, since the portions are small, it is likely that at low homologous temperatures a thermal or further mechanical activation of the grain boundary is required, for instance given by the interaction between dislocations and grain boundaries [31]. Still such processes cannot explain the eventual movement direction of the grain boundary, which determines which grain has to disappear. In our opinion, at low homologous temperatures, the difference in yield stress as a consequence of different sizes of the adjacent grains determines the shrinking grain and so triggers the migration direction of the boundary [28].
- v) Although common agreement exists concerning the contribution of grain coarsening to cyclic softening [1,2,11], it could not be identified yet to what extent this is the case. The difficulty is to differentiate the portions contributing to cyclic softening that stem from grain coarsening, compared to those from shear banding, dislocation annihilation or already formed fatigue cracks. Although the current experiments reveal a major contribution to cyclic softening from the coarsening of the ultrafine-grained structure, the impact of dislocation annihilation cannot be excluded completely. Furthermore, fatigue cracks are not visible on the side surface, however, an initiation of nanocracks from the roughened cantilever top surface cannot be excluded by experimental evidence. Therefore, the softening portion solely stemming from the cyclically induced enlargement of the grain size will not be quantified and requires a different experimental approach.

## **D.5 Conclusion**

Cyclic micro bending experiments were performed on UFG OFHC copper micro cantilevers in the low cycle fatigue regime. Cyclic softening was observed, which

could be explained by a coarsening of the UFG structure. Contributions to softening by shear bands could not be revealed up to an accumulated plastic cyclic strain of 34.6 in these micron sized samples. The grain growth process was studied in more detail via quasi in-situ EBSD measurements revealing new aspects and confirming prior observations about cyclically induced grain growth mechanisms. Hence, the main conclusions that can be drawn about cyclically induced grain growth are as follows:

- i) Grain growth increases with the accumulated plastic strain.
- ii) No preferred crystallographic orientation was observed to grow or shrink, while there seems to be a tendency for larger grains to grow at the expense of smaller grains.
- iii) Grain growth and shrinkage is realized by a continuous migration of large angle grain boundaries.
- iv) Small angle grain boundaries within larger grains seem to be geometrically necessary, as they disappear only if their neighborhood is altered.
- v) As grain growth is occurring at low homologous temperatures in regions of high plastic strain, boundary migration seems to require a mechanical activation and not, as often assumed, only large applied stresses.
- vi) As small grains tended to disappear more frequently, the migration direction seems to be triggered by differences in the elastic strain energy.

## Acknowledgements

The authors would like to thank Dr. Oliver Renk for valuable discussions. Financial support by the FWF Austrian Science Fund within project number P24429-N20 is gratefully acknowledged.

## References

- [1] S.R. Agnew, A.Y. Vinogradov, S. Hashimoto, J.R. Weertman, Overview of fatigue performance of Cu processed by severe plastic deformation, *J. Electron. Mater.* 28 (1999) 1038-1044.
- [2] H. Mughrabi, H.W. Höppel, M. Kautz, Fatigue and microstructure of ultra-finegrained metals produced by severe plastic deformation, *Scr. Mater.* 51 (2004) 807-812.
- [3] L. Kunz, P. Lukáš, M. Svoboda, Fatigue strength, microstructural stability and strain localization in ultrafine-grained copper, *Mater. Sci. Eng. A* 424 (2006) 97-104.

- [4] P. Lukáš, L. Kunz, M. Svoboda, Effect of low temperature on fatigue life and cyclic stress-strain response of ultrafine-grained copper, *Metall. Mater. Trans. A* 38 (2007) 1910-1915.
- [5] T. Hanlon, Grain size effects on the fatigue response of nanocrystalline metals, *Scr. Mater.* 49 (2003) 675-680.
- [6] T. Hanlon, E. Tabachnicova, S. Suresh, Fatigue behavior of nanocrystalline metals and alloys, *Int. J. Fatigue* 27 (2005) 1147-1158. [7] B.L. Boyce, H.A. Padilla, Anomalous fatigue behavior and fatigue-induced grain growth in nanocrystalline nickel alloys, *Metall. Mater. Trans. A* 42 (2011) 1793-1804.
- [8] O. Renk, A. Hohenwarter, R. Pippan, Cyclic deformation behavior of a 316L austenitic stainless steel processed by high pressure torsion, *Adv. Eng. Mater.* 14 (2012) 948-954.
- [9] S. Agnew, J. Weertman, Cyclic softening of ultrafine grain copper, *Mater. Sci. Eng. A* 244 (1998) 145-153.
- [10] S. Hashimoto, Y. Kaneko, K. Kitagawa, A. Vinogradov, R.Z. Valiev, On the cyclic behavior of ultra-fine grained copper produced by equi-channel angular pressing, *JMNM* 2e6 (1999) 593-598.
- [11] H.W. Höppel, Z.M. Zhou, H. Mughrabi, R.Z. Valiev, Microstructural study of the parameters governing coarsening and cyclic softening in fatigued ultrafinegrained copper, *Philos. Mag. A* 82 (2002) 1781-1794.
- [12] L. Kunz, P. Lukáš, L. Pantelejev, O. Man, Stability of ultrafine-grained structure of copper under fatigue loading, *Procedia Eng.* 10 (2011) 201-206.
- [13] M. Wong, W. Kao, J. Lui, C. Chang, P. Kao, Cyclic deformation of ultrafine-grained aluminum, *Acta Mater* 55 (2007) 715-725.
- [14] D. Canadinca, T. Niendorf, H.J. Maier, A comprehensive evaluation of parameters governing the cyclic stability of ultrafine-grained FCC alloys, *Mater. Sci. Eng. A* 528 (2011) 6345-6355.
- [15] H.W. Höppel, Mechanical properties of ultrafine grained metals under cyclic and monotonic loads: an Overview, *Mater. Sci. Forum* 503-504 (2006) 259-266.
- [16] H. Mughrabi, H.W. Hoppel, Cyclic deformation and fatigue properties of very fine-grained metals and alloys, *Int. J. Fatigue* 32 (2010) 1413-1427.
- [17] T. Hebesberger, H.P. Stwe, A. Vorhauer, F. Wetscher, R. Pippan, Structure of Cu deformed by high pressure torsion, *Acta Mater* 53 (2005) 393-402.
- [18] S. Wurster, C. Motz, R. Pippan, Characterization of the fracture toughness of micro-sized tungsten single crystal notched specimens, *Philos. Mag.* 92 (2012) 1803-1825.
- [19] S.D. Wu, Z.G. Wang, C.B. Jiang, G.Y. Li, Scanning electron microscopy-electron channeling contrast investigation of recrystallization during cyclic deformation of ultrafine grained copper processed by equal channel angular pressing, *Philos. Mag. Lett.* 82 (2002) 559-565.
- [20] A. Mishra, B. Kad, F. Gregori, M. Meyers, Microstructural evolution in copper subjected to severe plastic deformation: experiments and analysis, *Acta Mater.* 55 (2007) 13-28.
- [21] A. Vorhauer, S. Scheriau, R. Pippan, In-situ annealing of severe plasticdeformed

- OFHC copper, *Metall. Mater. Trans. A* 39 (2008) 908-918.
- [22] C.E. Feltner, C. Laird, Cyclic stress-strain response of F.C.C. metals and alloys - I phenomenological experiments, *Acta Metal. Mater.* 15 (1967) 1621-1632.
- [23] C.E. Feltner, C. Laird, Cyclic stress-strain response of F.C.C. metals and alloys - II dislocation structures and mechanisms, *Acta Metal. Mater.* 15 (1967) 1633-1653.
- [24] J. Schrank, W. Prantl, H.P. Stwe, The influence of crystal orientation on the fatigue softening behavior of severely predeformed copper, *Mater. Sci. Eng. A* 110 (1989) 61-68.
- [25] E. Thiele, R. Klemm, L. Hollang, C. Holste, N. Schell, H. Natter, R. Hempelmann, An approach to cyclic plasticity and deformation-induced structure changes of electrodeposited nickel, *Mater. Sci. Eng. A* 390 (2005) 42-51.
- [26] A. Hohenwarter, R. Pippan, A comprehensive study on the damage tolerance of ultrafine-grained copper, *Mater. Sci. Eng. A* 540 (2012) 89-96.
- [27] F.J. Humphreys, M. Hatherly, *Recrystallization and Related Annealing Phenomena*, second ed., Elsevier, Amsterdam, Boston, 2004.
- [28] O. Renk, A. Hohenwarter, S. Wurster, R. Pippan, Direct evidence for grain boundary motion as the dominant restoration mechanism in the steady-state regime of extremely cold-rolled copper, *Acta Mater.* 77 (2014) 401-410.
- [29] P. Ghosh, O. Renk, R. Pippan, submitted manuscript.
- [30] M. Jin, A.M. Minor, E.A. Stach, J.W. Morris, Direct observation of deformation-induced grain growth during the nanoindentation of ultrafine-grained Al at room temperature, *Acta Mater.* 52 (2004) 5381-5387.
- [31] F. Momprou, M. Legros, A. Bo e, M. Coulombier, J. Raskin, T. Pardoen, Inter- and intragranular plasticity mechanisms in ultrafine-grained Al thin films: an in situ TEM study, *Acta Mater.* 61 (2013) 205-216.
- [32] F. Momprou, D. Caillard, M. Legros, Grain boundary shear-migration coupling I. In situ TEM straining experiments in Al polycrystals, *Acta Mater.* 57 (2009) 2198-2209.





# Cyclically induced grain growth within shear bands investigated in UFG nickel by cyclic high pressure torsion

M.W. Kapp<sup>a</sup>, O. Renk<sup>a</sup>, T. Leitner<sup>b</sup>, P. Ghosh<sup>a</sup>, B. Yang<sup>a</sup> and R. Pippan<sup>a</sup>

<sup>a</sup>Erich Schmid Institute of Materials Science, Austrian Academy of Sciences, 8700 Leoben, Austria

<sup>b</sup>Department of Materials Physics, Montanuniversität Leoben, Jahnstrasse 12, 8700 Leoben, Austria

## Abstract

Structural instabilities of nanocrystalline and ultrafine-grained materials have been recognized as a major challenge during cyclic loading, especially in the low cycle fatigue regime. Although a severe deterioration of the mechanical properties has been reported during cyclic deformation, quantification of the softening portion solely due to grain coarsening was not possible. It will be demonstrated that cyclic high pressure torsion is a versatile method to enable direct measurement of the impact of grain coarsening on cyclic softening, as failure of the sample is prevented. Here, cyclic high pressure torsion experiments have been performed on 99.99% ultrafine-grained nickel. Grain coarsening similar to conventional uniaxial fatigue experiments was observed and could be studied up to large cyclic accumulated macro strains of 50. The correlation of electron back scatter diffraction images with microhardness measurements facilitated quantification of the cyclic softening as a consequence of grain growth for the very first time. Further, structural investigations revealed distinctly

enhanced grain coarsening within shear bands. Thus, the cyclic strain seems to be the most important parameter controlling mechanically driven boundary migration during cyclic loading at low homologous temperatures.

## **E.1 Introduction**

Extensive grain refinement of metallic structures by severe plastic deformation (SPD) yields an enormous enhancement of the strength of materials. This improvement of the mechanical properties is also reflected in the high cycle fatigue (HCF) performance, making this material class ideal for frequent load reversal applications. Unfortunately, this holds true only for cases where the plastic strain amplitude is low. Under low cycle fatigue (LCF) conditions i.e. large plastic strain amplitudes, nanocrystalline (NC) or ultrafine-grained (UFG) structures become unstable due to their large amount of grain boundary area [1].

Various types of structural instabilities have been reported for static, dynamic and cyclic loading situations, when higher strains were applied. For instance, during the SPD process itself two recovery processes take place, namely grain boundary migration [2] and triple junction motion [3]. These processes continuously modify the microstructure in a way that a further refinement is impeded, even when the strain during SPD is increased. It seems that these processes not only determine the saturation grain size of a particular SPD process, but also the grain shape [4]. The design of structural components is dictated by the mechanical properties of a material, such as the yield, fracture or fatigue strength. Changes of the microstructure, such as grain growth, would seriously alter these properties during application and therefore their service life.

Significant changes of the microstructure have been reported for static loading conditions. For instance in the case of NC Al thin films grain coarsening was observed during tensile loading [57]. Further in-situ TEM work revealed that the coarsening process was due to shear-stress coupled migration of the boundary and in certain cases was linked to the coalescence of adjacent grains [8]. Both mechanisms increase the grain size and thereby affect the mechanical properties. Although the coalescence of grains contributes to coarsening in NC structures, for UFG materials motion of grain boundaries have been reported [9]. For UFG Al the migration of grain boundaries seems therefore to be closely related to interactions between dislocations and grain boundaries, as for instance it has been reported that grain boundary dislocation movement is assisting this process [10]. That these observations cannot only be an effect of thin-foil was demonstrated for NC Cu, where severe coarsening of the structure from 20 nm up to 700 nm for single grains was observed beneath a microhardness indent [11]. Similar observations have been made during high pressure torsion (HPT) of electrodeposited NC Ni [12]. With increasing shear strain the initially 22 nm sized structure significantly coarsened to a steady state size of about 200 nm. Interestingly, this value is similar to coarse grained HPT deformed Ni and shows that the resulting grain size after SPD is independent of the

starting grain size [13].

As indicated before, avoiding structural instability of NC and UFG materials during fatigue experiments remains challenging. Early observations have shown that cyclic softening of an UFG Cu structure during LCF is induced by grain growth, reduction of the dislocation density and change of the boundary misorientation [14]. In many cases cyclically induced coarsening does not affect the entire sample volume uniformly, but rather occurs locally. A shift from heterogeneously to homogeneously coarsened structures was often attributed to the increase of the applied strain amplitude. In cases of increased strain amplitudes generally amplified grain coarsening was observed [15, 16] supporting the idea of deformation-driven grain coarsening. Other studies reported the opposite trend, namely more pronounced cyclic softening and grain growth with decreasing strain amplitude [17]. The increase in sample lifetime for lower strain amplitudes increases simultaneously the diffusion time for the coarsening process which supports the concept of thermally assisted grain growth [1]. Although the driving forces behind cyclically induced grain coarsening are still debated, recent quasi in-situ experiments have confirmed that under LCF conditions a continuous migration of high angle grain boundaries is the basic mechanism of the coarsening process. These findings are in line with observations during static loading conditions [18].

Shear band formation may also occur during plastic deformation of NC and UFG alloys. This not only limits ductility under static loading conditions, but also decreases grain stability under cyclic conditions [19]. The refinement of the structure into the NC and UFG regime and the resultant higher strength levels are likely to favor inhomogeneous plastic deformation. This has frequently been shown for high strength nanolaminates [20-22] or nanocrystalline structures [23], where the formation of a shear band caused strain softening and catastrophic failure of the sample. Strain localization in shear bands has also been found after low cycle fatigue experiments [14, 15, 24-29]. Shear bands formed in UFG Al during cyclic loading can be smaller as the grain size and consist of a dense dislocation network, which is able to penetrate through grain boundaries and thereby form a path through plenty of grains [29]. Conversely, shear band thicknesses being several times larger than the grain size were reported for UFG Al [19]. Within the shear band the grains become aligned along the shear band direction and a homogeneous coarsening of the structure is observed. Thus, both structural instability mechanisms are combined.

The extensive experimental work of the last decades focused primarily on the impact of cyclic loading on mechanical properties and their relation to structural changes of the material. Still, a thorough understanding of the driving forces, the nature of the instability processes and their evolution with cyclic strain are not clear. A statistical approach to gain a deeper understanding about the impact of the crystallographic orientation, the grain boundary type or the strain amplitude on the coarsening process is often inhibited by early sample failure in conventional uniaxial fatigue experiments. Further, the coincidence of grain coarsening and sample damage does not allow for a quantification of their respective impact on cyclic softening separately.

In the present study a very simple cyclic deformation setup is introduced, which allows a study of cyclically induced grain coarsening up to large strains. It will be shown that cyclic high pressure torsion (CHPT) performed on high purity UFG nickel introduces structural instabilities, such as grain coarsening and shear bands, similar to conventional fatigue experiments. The sample constraint caused by this specific experimental setup prevents sample failure and therefore, enables to track structural changes up to extremely high cyclic strains. Thus, it was possible for the first time to exclusively quantify the impact of grain coarsening to cyclic softening.

## E.2 Experimental

A high purity nickel (99.99%) was processed by HPT. The HPT disc, being 10 mm in diameter and 0.8 mm in thickness,  $t$ , was monotonically deformed for 15 rotations,  $n$ , under a hydrostatic pressure of 5 GPa. At the outermost disc radius,  $r$ , of 5 mm this results in an equivalent strain of 340 according to Eq. 1:

$$\epsilon_{eq} = \frac{2\pi rn}{\sqrt{3}t}. \quad (\text{E.1})$$

At such large strains constant properties are achieved over the sample diameter, except for the very center of the HPT disc ( $r < 0.5$  mm). The steady state grain and subgrain size was calculated from electron back scatter diffraction (EBSD) data (area weighted, tangential view) to be 310 nm and 260 nm, respectively. By EBSD the grain boundary structure was also analyzed and was found to consist of 80% high angle grain boundaries (HAGB) and 20% low angle grain boundaries (LAGB). Cyclic loading was performed by CHPT, directly after the formation of the UFG structure via monotonic HPT. During CHPT the rotation of the lower anvil is simply changed from continuous to alternating twist mode allowing the sample to be rotated for certain degrees clockwise (first half cycle) and then the rotation direction is changed to anti-clockwise for the same amount of degrees (second half cycle).

**Table E.1** Nominal strain amplitudes,  $\epsilon_{a,nom}$ , accumulated strain,  $\epsilon_{acc}$ , thickness of the shear band,  $t_{SB}$ , as marked in Fig. 1 and local strain amplitude,  $\epsilon_{a,loc}$ , for samples cycled to  $5^\circ$  for 50 times are listed for HPT disc radii 1, 2, 3 and 4 mm. The local strain amplitude is estimated with Eq. 1 by setting  $t = t_{SB}$ .

HPT disc radius	$\epsilon_{a,nom}$	$\epsilon_{acc}$	$t_{SB}$	$\epsilon_{a,loc}$
[mm]	[—]	[—]	[ $\mu m$ ]	[—]
1	0.06	12	100	0.50
2	0.13	26	180	0.56
3	0.19	38	240	0.63
4	0.25	50	310	0.65

The nominal cyclic strain amplitude can be simply calculated from the applied twist angle shown in Table I. Due to experimental reasons the separation of the elastic

and plastic part is not possible. Eq. 2 shows the dependence of the cyclic strain amplitude on the HPT twist angle,  $\Theta$ , the thickness of the HPT disc and also on the HPT disc radius:

$$\epsilon_a = \frac{2\pi r}{\sqrt{3}t} \frac{\Theta}{360^\circ} \quad (\text{E.2})$$

The accumulated strain can be modified by changing the number of cycles,  $N$ , according to Eq. 3:

$$\epsilon_{acc} = 4\epsilon_a N \quad (\text{E.3})$$

and is shown in Tab. I for samples cycled to  $\Theta = 5^\circ$  for  $N = 50$ , which will be presented in this study. In conventional fatigue experiments hysteresis loops are recorded to allow for an investigation of the cyclic stability. In the case of CHPT a continuous measurement of the torque is in principle possible, although the measured torque does not correspond solely to the flow stress [30]. A much more reliable technique to quantify cyclic softening is to measure the microhardness along the HPT disc radius.

In addition to microhardness the microstructural stability was evaluated by back scatter electron (BSE) images recorded along the HPT disc radius in TAN direction (see insert Fig. 1). Furthermore EBSD was used to investigate the crystallographic orientation as well as the grain boundary misorientation of the cycled samples. These structural investigations were carried out at exactly the same positions where the microhardness was measured, which allows directly to correlate cyclic softening to structural parameters.

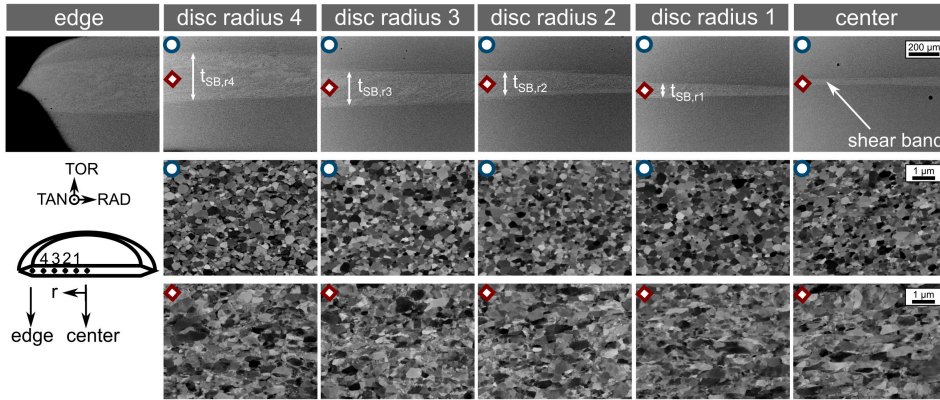


**Figure E.1** Formation of shear bands in the middle of the HPT disc height, with its thickness,  $t_{SB}$ , increasing from the center towards the edge for  $5^\circ$  and 50 cycles (first row). The grain size outside the shear band has not changed significantly (second row), whereas inside the shear band grains are coarser and elongated along the radial direction (third row).

## E.3 Results

### E.3.1 Shear band formation

Investigating the cross section of a HPT disc cycled 50 times for  $5^\circ$  by BSE images revealed two different regions with different contrast (Fig. 1, first row). A bright region in the middle of the disc height is surrounded by a darker region at the top and bottom of the disc. BSE images taken at higher magnification revealed a grain size and an equiaxed grain shape similar to the as-deformed material in the outer darker regions (Fig. 1, second row), whereas in the bright region a shear band has formed. Inside the shear band the grains are larger and appear elongated in the radial direction (Fig. 1, third row). No significant change of the grain size and the grain shape is observed along the HPT disc radius, although the nominal strain amplitude increases. However, the width of the shear band,  $t_{SB}$ , increases with increasing nominal strain amplitude along the HPT disc radius, forming a wedge shaped region throughout the disc (Fig. 1).

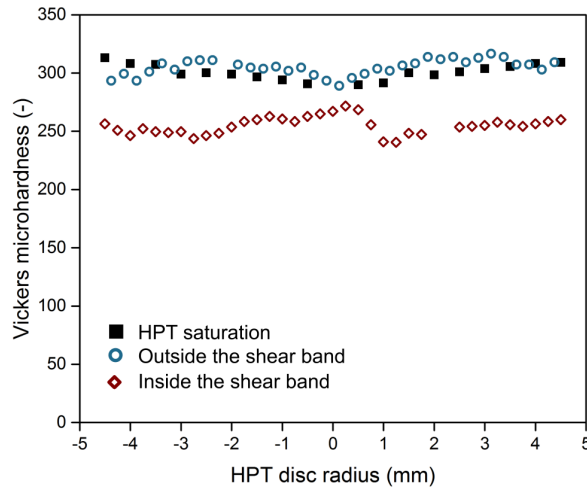


**Figure E.2** The Vickers microhardness inside the shear band drops by about 20% after cyclic loading at  $5^\circ$  for 50 cycles, whereas outside it remains nearly the same compared to the as-HPT deformed state.

### E.3.2 Microhardness

Microhardness measurements shown in Fig. 2 were conducted along the HPT disc radius in tangential direction (see TAN in insert of Fig. 1). Thus, modification of mechanical properties due to CHPT as a function of the changing nominal strain amplitude could be tracked. Microhardness was determined inside and outside of the shear band to clarify the effect of the different grain sizes. For a sample cycled

for 50 times at a twist angle of  $5^\circ$ , the microhardness inside and outside the shear band differs significantly (Fig. 2). Outside the shear band the microhardness along the HPT disc radius (blue empty dots) remained at about 305 HV almost constant compared to the microhardness of the as-HPT deformed discs (black full squares). Within the shear band the microhardness (red empty rhomboids) drops by 20% down to about 255 HV. No distinct correlation between the nominal strain amplitude and the hardness is visible and hardness within the shear bands remains nearly constant along the HPT disc radius. Although slight scatter can be observed along the disc radius, it is distinctively smaller than the differences between the areas outside the shear band and the as-deformed condition.

### E.3.3 Microstructural evolution

As evident from the BSE images (Fig. 1), the grain size differs significantly inside and outside of the shear band. The same trend is visible in EBSD scans taken along the radius of the disc (Fig. 3a), where a sharp transition from a coarsened to a still ultrafine-grained region is visible. The fraction of the coarsened region increases with increasing HPT disc radius, thus nominal strain amplitude, similar to the BSE images in Fig. 1. For detailed insights into the grain structure EBSD scans were performed at higher magnification in the ultrafine-grained region outside the shear band (Fig. 3b) and in the already heavily coarsened region within the shear band (Fig. 3c) along the HPT disc radius in tangential direction. Mostly HAGB (misorientation  $\geq 15^\circ$ , see black lines) accumulate in the structure, although in the larger grains additional cell boundaries of low angle type with misorientation between  $2\text{-}15^\circ$  also appear.

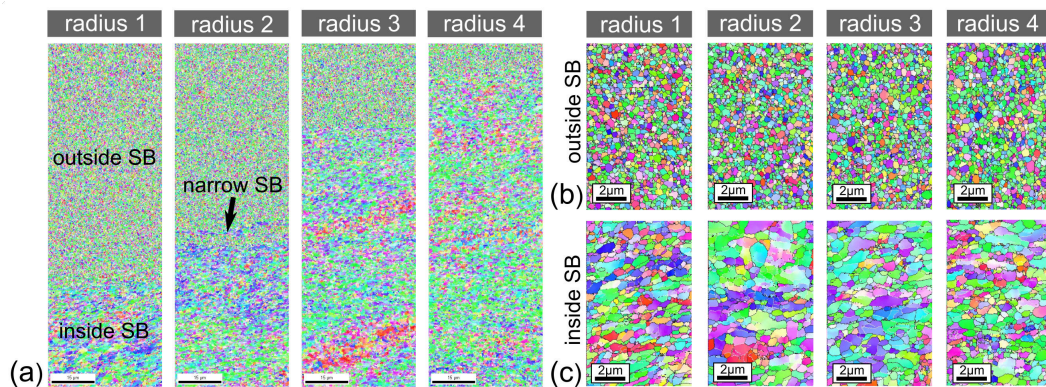


**Figure E.3** (a) EBSD scans were taken in tangential direction along the border between the major shear band and the matrix for a sample cycled 50 times at an HPT twist angle of  $5^\circ$ . The thickness of the shear band clearly increases with increasing nominal strain amplitude. At an HPT disc radius of 2 mm an additional narrow shear band is visible nearby the major one. EBSD scans of higher magnification taken (b) outside and (c) inside the shear band prove a severe coarsening of the grain structure within the shear band.

In Fig. 4 the structural sizes were analyzed for boundary misorientation angles of  $2\text{-}15^\circ$  (LAGB, empty symbols) and  $\geq 15^\circ$  (HAGB, full symbols) for both outside (circular symbols) and inside (rhomboid symbols) of the shear band. Although the structure outside the shear band does not seem to have coarsened significantly, grain size analysis revealed already a growth in size of about 20%. While the HPT steady state grain size was 310 nm taking into account HAGB after cyclic deformation it has grown up to 373 nm on average outside the shear band. However, this is clearly less pronounced compared to the grain growth within the shear band. Contrary to the observations from BSE images a strain amplitude dependency becomes visible, which is stronger if HAGB are considered. Both structural sizes increase with decreasing nominal strain amplitude (Fig. 4). For the smallest nominal strain amplitude at a radius of 1 mm the average grain size (HAGB,  $\geq 15^\circ$  boundary misorientation) became more than 6 times larger compared to the initial steady state structure. It should be noted that the measured structural sizes delineated by HAGB can only be considered as a lower bound, as the edge grains of the scan have exceeded the EBSD scan size and were therefore cut off. The scanning area chosen reflected a compromise between retaining sufficient resolution to detect small grains and minimizing scanning time to avoid sample drift.

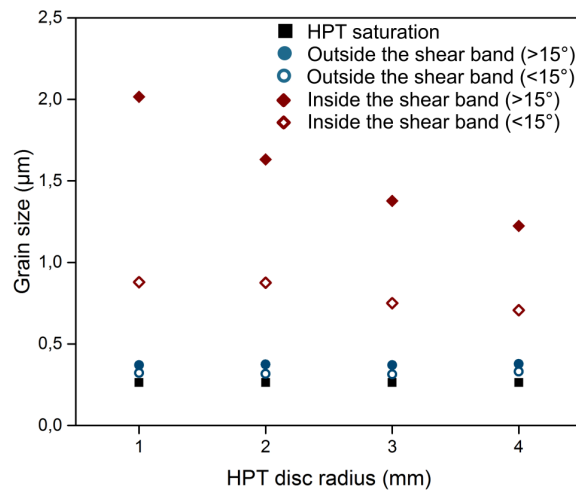


**Figure E.4** During cyclic loading the structural size calculated for boundary misorientation  $\geq 15^\circ$  (HAGB, filled symbols) and subgrains ( $2\text{-}15^\circ$  boundary misorientation, open symbols) significantly increases inside the shear band (red rhomboids). Even outside the shear bands (blue circles) slight coarsening can be noticed. Grain sizes for the as-HPT deformed starting material are given for comparison (black squares).

### E.3.4 Crystallographic orientation

The full crystallographic information of the EBSD scans taken from areas outside and inside of the shear band (Fig. 3b-c) allows for an analysis of orientation changes induced by CHPT. For an easier interpretation the data are plotted in inverse pole figures (IPF) in two directions (tangential, torsional, compare TAN and TOR in inset of Fig. 1) instead of ODF sections. Figures 5 and 6 show IPF maps for the as-HPT deformed structure (TAN in Fig. 5a, TOR in Fig. 6a) and for the same structure subjected to CHPT inside (TAN in Fig. 5b, TOR in Fig. 6b) and outside of the shear band (TAN in Fig. 5c, TOR in Fig. 6c) at different disc radii, respectively.

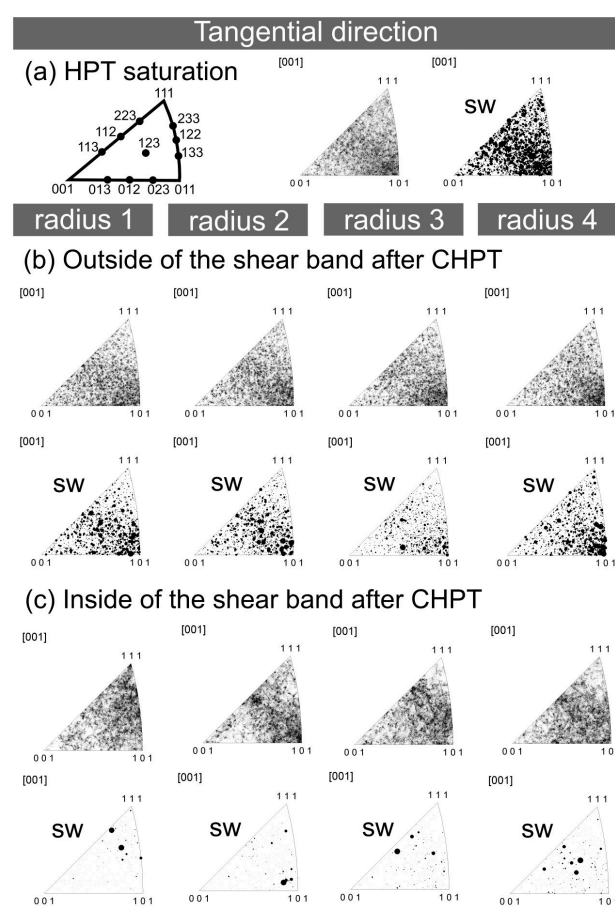


**Figure E.5** Inverse pole figure (IPF) maps from (a) the as-HPT deformed structure (first image) were compared to the cycled structure (b) outside and (c) inside of the shear band (first row each) with respect to the tangential (TAN) direction of the HPT disc. Further the IPF maps were weighted by the size (marked by *sw*) of the analyzed grain (second image in (a) and second row each in (b-c)). The dot size scales with the size of the analyzed grain.

Each data point in the conventional IPF maps (not marked by *sw* in Fig. 5 and Fig. 6) corresponds to the crystallographic orientation of one analyzed grain. Addition-

ally, each of these data points can be weighted by the size ( $sw$ ) of the corresponding grain, with larger dot sizes corresponding to grains of larger size (marked by  $sw$  for size-weighted in Fig. 5 and Fig. 6).

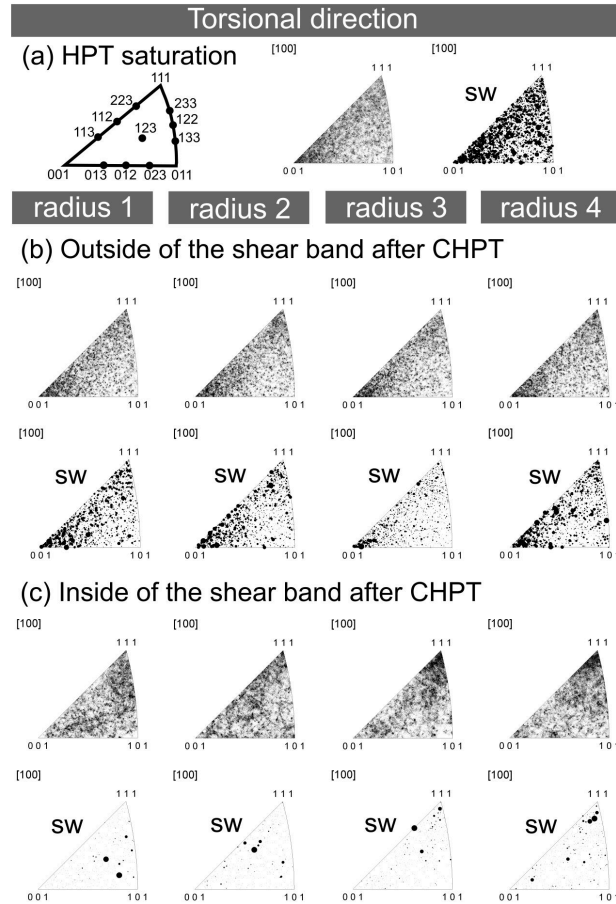


**Figure E.6** Inverse pole figure (IPF) maps from (a) the as-HPT deformed structure (first image) were compared to the cycled structure (b) outside and (c) inside of the shear band (first row each) with respect to the torsional (TOR) direction of the HPT disc. Further the IPF maps were weighted by the size (marked by  $sw$ ) of the analyzed grain (second image in (a) and second row each in (b-c)). The dot size scales with the size of the analyzed grain.

The monotonically deformed steady state structure exhibits a typical shear texture observed for medium or high stacking fault energy fcc metals [31, 32] (TAN in Fig. 5a and TOR in Fig. 6a). The shear texture is not very pronounced although  $\langle 110 \rangle$  directions align parallel to the shear direction (TAN direction) and  $\{100\}$  planes (TOR direction) are preferred, corresponding to the ideal texture components of shear [33]. Similar trends can be observed in the size-weighted IPFs, from which it is clear that large grains have a higher tendency for these orientations. After CHPT the crystallographic orientation outside the shear band (TAN in Fig. 5b and TOR

in Fig. 6b) progressively changes to some extent with increasing HPT disc radius. For larger radii, thus higher nominal strain amplitudes,  $[101]$  orientations become more intense in tangential direction and  $\{001\}$  and  $\{111\}$  in torsional direction especially for larger grains (see *sw* IPF in Fig. 5b and Fig. 6b). In tangential direction inside the shear band (Fig. 5c) a preference for  $[110]$  and  $[112]$  directions parallel to the shear direction is visible in the IPFs. The major difference from the as-HPT deformed structure is the reduced number of analyzed points in the size-weighted IPFs due to grain coarsening and therefore a reduction in the number of analyzed grains. However, compared to the region outside the shear band and the monotonically deformed sample a clear preference of  $\{111\}$  planes parallel to the shear plane can be noticed (Fig. 6c).

## E.4 Discussion

Two types of structural instabilities developed during CHPT of high purity UFG Ni: i) coarsening of the initially UFG grained structure and ii) formation a shear bands. The first case has been reported frequently for NC and UFG metals not only under fatigue [1, 14, 16-18, 34-37] but also under static loading conditions for a variety of materials [5-12, 38-40]. The formation of shear bands has also been observed macroscopically at the surface [14, 15, 19, 24-27, 34] and in the sample interior of cyclically deformed materials [29]. However, the combination of both instability mechanisms namely the observation of grain coarsening within shear bands has been shown for the very first time by Höppel et al. [19] and could be confirmed in this study. Although possible a persistent instability type of these fine scaled structures for specific loading situation or materials was not reported. Thus, it remains unclear why and how these instabilities form and develop. The use of CHPT allows the tracking of the evolution of such instabilities, as the experiment is not restricted by the rupture of the fatigue sample. The main questions to be answered are the driving forces for grain growth, why do shear bands form and how the loading conditions affect the occurrence and development of these instability mechanisms. Only a thorough understanding of these fundamental points will allow to develop nanostructured materials being resistant against the formation of such instabilities. As mentioned, shear band formation can be frequently observed in nanostructured materials, but also during deformation of coarse grained materials, see for example [41, 42]. In any case a shear band reflects a strain localization, which can be further promoted in case of limited work hardening, such as for severely deformed materials. Although generally there can be various reasons for shear band formation [43], for cyclic deformation of UFG structures it appears that grain coarsening causes local softening. The microhardness measurements of CHPT samples show that grains and subgrains can grow up to about 2000 nm and 880 nm, respectively, leading to a drop in the microhardness of 20%. Two explanations for the shear band initiation could be imagined: i) grains coarsen as a response to cyclic deformation causing local softening and thereby promote strain localization in these softer regions or ii)

due to the stress- and strain concentration at the edge of the HPT disc a shear localization develops through the middle of the disc, thereby amplifying grain growth within this region. Similar explanations for case i) already exist to describe instabilities in cyclically deformed coarse grained materials, where persistent slip bands develop above a certain strain amplitude [44]. These structures consist of channels of low dislocation density, thus softer regions, where dislocations can realize the cyclic strain more easily by moving forth and back. A similar explanation for the simultaneous occurrence of shear bands and grain coarsening in cyclically loaded UFG Al was utilized earlier by Höppel et al. [19]. The evolution of shear bands was attributed to the local softening induced by growth and rotation of adjacent grains. On the other hand, case ii) cannot be neglected as from Fig. 1 it is evident that the shear band formation will start at the disc edge, a location of maximum strain concentration, and develop almost completely through the middle of the disc after 50 cycles of deformation. Additionally, grain coarsening does also occur outside of the shear band, though less pronounced, but does not result in the formation of a large scale shear band. Thus, a conclusion about the exact mechanism generating a shear band cannot be drawn so far.

However, it is evident that grain coarsening is distinctively amplified in the shear band region. It is shown in Fig. 4 that grain growth occurs inside and outside of the shear band, but the grain size (HAGB,  $\geq 15^\circ$  boundary misorientation) within the shear band is more than 5 times larger than outside of it. As the starting grain size, the flow stress, texture and boundary characters of the monotonically deformed UFG Ni will be similar before CHPT, but the strain is localized in the shear band, it is evident that grain growth is enhanced significantly by the cyclic strain. The importance of the cyclic strain found in this study is deviating from earlier studies about shearstress coupled boundary migration [7]. In-situ TEM tension experiments at elevated temperatures on UFG Al revealed a migration of a HAGB immediately after a stress increment. However, this argument does not hold for grain growth during CHPT as the same stress is initially applied over the disc height, yet grain growth is concentrated in the middle of the disc (Fig. 1, 3, 4). Even though at higher cycle numbers the local stresses will become higher in the outer regions due to the somewhat smaller grains, the coarsening process is still accelerated in the middle of the disc. The importance of the strain for grain coarsening has also been shown in static tensile experiments on nanogradient structures [39] and in cyclic micro bending experiments [18]. There it was reported that in UFG structures grain growth proceeds by a continuous migration of HAGBs, which can be also assumed to occur for torsional cyclic deformation. Because the IPFs in Fig. 5 and Fig. 6 show the presence of ideal shear texture components outside and inside of the shear band after CHPT [32, 33], dislocation based plasticity will prevail and their interactions with grain boundaries may induce the migration of the boundary. Therefore, grain coarsening in UFG structures induced by cyclic loading cannot be explained by recrystallization as suggested in earlier works [1], as different texture components would have to appear.

Coarsening within the shear band occurred preferentially in grains having their (111)

plane oriented parallel to the shear plane (torsional direction) and the [110] direction parallel to the shear direction (tangential direction, see Fig. 5c and Fig. 6c). Compared with earlier studies on torsional deformation of Toth et al. [33] this crystallographic orientation requires the activation of only one single slip system to realize the torsional strain. Grains with this orientation can probably accommodate the intense cyclic strain within the shear band in a more efficient manner. Thus, enhanced plasticity might occur in these grains. The repeated interaction of dislocations with grain boundaries might induce the continuing formation of disconnections [45] whose motion will cause migration of corresponding grain boundaries leading to grain coarsening. Similar reasons may explain also frequent occurrence of coarsened grains with their [112] direction parallel to the shear direction. Although this texture component requires the activation of a second slip system, these slip systems are coplanar and possibly induce less dislocation interaction than for the other orientations, making this orientation also preferable for cyclic slip. In regions outside the shear band (Fig. 5b and Fig. 6b) only microplasticity is assumed to take place, which could explain the retention of the monotonic torsional texture components. Coarsened grains in the region outside the shear band at radius 4 mm have a tendency for (100) planes parallel to the shear plane and the [110] direction parallel to the shear direction. This ideal orientation known as “C” component requires the activation of two non-coplanar slip systems. This may induce more dislocation interactions, thus, reducing interaction of dislocations with grain boundaries.

As the strain seems to accentuate the coarsening process, it is necessary to discuss the effect of the strain amplitude as well. A comparison of the grain coarsening inside and outside the shear band suggests that larger strain amplitudes cause enhanced grain growth. However, within the shear band grains at smaller radii, i.e. reduced nominal strain amplitude, grow larger in size than at the edge of the disc (Fig. 4), contrary to what would be expected. It is important to note that the effective strain amplitude within the shear band will differ remarkably from the nominal one due to the varying thickness of the shear band. To estimate the effective strain amplitude within the shear band we assume the plastic strain to be entirely concentrated in the shear band and the matrix outside the shear band to deform microplastically. As grain growth outside the shear band is not pronounced (Fig. 4), this estimation should yield reasonable values. The local strain amplitude can then be calculated by normalizing the nominal strain amplitude by the shear band thickness, see Eq. 1 in that case with  $t = t_{SB}$ . This yields for 50 loading cycles to local strain amplitudes inside the shear bands of 0.50, 0.56, 0.63 and 0.65 at HPT disc radii of 1, 2, 3 and 4 mm, respectively. Although under this considerations the local strain amplitude differences are less pronounced compared to the nominal ones (see Tab. I), they still increase with increasing radii. Nevertheless, observing larger grain sizes at smaller strain amplitudes upon CHPT is not contradictory with the observations that the coarsening process is primarily strain driven at low temperatures. Earlier results of CHPT deformed nickel and iron [30] have already shown that for large strain amplitudes ( $\epsilon_{a,pl} \sim 1$ ), the structural size will be smaller at higher applied strain amplitudes. This trend has been explained with the understanding that at such

large strain amplitudes present also within the shear bands structural refinement will occur as in monotonic HPT, thus subduing the coarsening process. Of course, this effect will diminish for small strain amplitudes as usually applied in LCF experiments ( $\epsilon_{a,pl} \sim 0.001 - 0.01$ ) and the frequently observed trend of an amplifying effect of the strain amplitude on the coarsening process [15, 16] will prevail.

As mentioned earlier, distinct cyclically induced softening of about 20% occurs in the region of the shear band. This is attributed to the pronounced growth of grains and subgrains in the presence of strain localization. A reduction of the dislocation density within grains may take place, but will not contribute to a significant decrease in microhardness [31]. The evolution of the hardness does not show a correlation with the nominal strain amplitude in contrast to the grain size (HAGB,  $\geq 15^\circ$  boundary misorientation in Fig. 4). Their exceptional growth of more than 6 times at a radius of 1 mm does not correlate to the drop of 50 HV in microhardness. The moderate size dependence of subgrains on the nominal strain amplitude and their less pronounced coarsening suggests that the subgrain boundaries are the crucial barriers for dislocations and therefore govern the materials strength.

## **E.5 Conclusion and outlook**

Cyclic high pressure torsion experiments were performed on UFG Ni samples and led to the observation of cyclic instability mechanisms, namely shear banding and grain coarsening. The goal of the present investigation was to show the details of the evolved grain size, texture, boundary structure within a shear band and outside of it for a defined number of loading cycles ( $N = 50$ ) and consequences with respect to cyclic grain coarsening. The experimental setup prevents fatigue crack initiation and rupture due to a sample constraint in principle up to infinite accumulated strain. Therefore, the cyclic softening portion stemming solely from grain coarsening could be quantified and was measured by a drop of 20% in the microhardness due to a grain size and subgrain size increase of more than 6 and 3 times, respectively. Furthermore, it was found that grain coarsening is distinctively amplified in regions of shear localization, strengthening the concept of deformation driven boundary migration. This was supported by IPF maps revealing the evolution of shear texture components with increasing cyclic strain.

Details to the evolution of the shear band width as a function of loading cycles and the maximum applied shear strain, i.e. applied angle amplitude, the effect of temperature and initial structure are the subject of ongoing investigations.

## **Acknowledgements**

Financial support by the FWF Austrian Science Fund within project number P24429-N20 and by the European Research Council und ERC Gran Agreement No. 340185 USMS is gratefully acknowledged.

## References

- [1] H. Mughrabi, H.W. Höppel, M. Kautz, Fatigue and microstructure of ultrafine-grained metals produced by severe plastic deformation, *Scripta Mater.* 51(8) (2004) 807-812.
- [2] O. Renk, A. Hohenwarter, S. Wurster, R. Pippan, Direct evidence for grain boundary motion as the dominant restoration mechanism in the steady-state regime of extremely cold-rolled copper, *Acta Mater.* 77(100) (2014) 401-410.
- [3] T. Yu, N. Hansen, X. Huang, A. Godfrey, Observation of a New Mechanism Balancing Hardening and Softening in Metals, *Mat. Res. Lett.* 2(3) (2014) 160165.
- [4] O. Renk, P. Ghosh, R. Pippan, Generation of extreme grain aspect ratios in severely deformed tantalum at elevated temperatures, *Scripta Mater.* 137 (2017) 60-63.
- [5] D.S. Gianola, S. van Petegem, M. Legros, S. Brandstetter, H. van Swygenhoven, K.J. Hemker, Stress-assisted discontinuous grain growth and its effect on the deformation behavior of nanocrystalline aluminum thin films, *Acta Mater.* 54(8) (2006) 2253-2263.
- [6] D.S. Gianola, B.G. Mendis, X.M. Cheng, K.J. Hemker, Grain-size stabilization by impurities and effect on stress-coupled grain growth in nanocrystalline Al thin films, *Mater. Sci. Eng., A* 483-484 (2008) 637-640.
- [7] T.J. Rupert, D.S. Gianola, Y. Gan, K.J. Hemker, Experimental observations of stress-driven grain boundary migration, *Science* 326(5960) (2009) 1686-1690.
- [8] M. Legros, D.S. Gianola, K.J. Hemker, In situ TEM observations of fast grain-boundary motion in stressed nanocrystalline aluminum films, *Acta Mater.* 56(14) (2008) 3380-3393.
- [9] M. Jin, A.M. Minor, E.A. Stach, J.W. Morris, Direct observation of deformation-induced grain growth during the nanoindentation of ultrafine-grained Al at room temperature, *Acta Mater.* 52(18) (2004) 5381-5387.
- [10] F. Momprou, M. Legros, A. Boé, M. Coulombier, J.-P. Raskin, T. Pardoen, Inter- and intragranular plasticity mechanisms in ultrafine-grained Al thin films: An in situ TEM study, *Acta Mater.* 61(1) (2013) 205-216.
- [11] K. Zhang, J.R. Weertman, J.A. Eastman, Rapid stress-driven grain coarsening in nanocrystalline Cu at ambient and cryogenic temperatures, *Appl. Phys. Lett.* 87(6) (2005) 061921.
- [12] B. Yang, H. Vehoff, A. Hohenwarter, M. Hafok, R. Pippan, Strain effects on the coarsening and softening of electrodeposited nanocrystalline Ni subjected to high pressure torsion, *Scripta Mater.* 58(9) (2008) 790-793.
- [13] R. Pippan, S. Scheriau, A. Taylor, M. Hafok, A. Hohenwarter, A. Bachmaier, Saturation of Fragmentation During Severe Plastic Deformation, *Annu. Rev. Mater. Res.* 40(1) (2010) 319-343.
- [14] S. Agnew, J. Weertman, Cyclic softening of ultrafine grain copper, *Mater. Sci. Eng. A* 244(2) (1998) 145-153.
- [15] L. Kunz, P. Lukáš, M. Svoboda, Fatigue strength, microstructural stability and

strain localization in ultrafine-grained copper, *Mater. Sci. Eng. A* 424(1-2) (2006) 97-104.

[16] D. Canadinca, T. Niendorf, H.J. Maier, A comprehensive evaluation of parameters governing the cyclic stability of ultrafine-grained FCC alloys, *Mater. Sci. Eng. A* 528 (2011) 6345-6355.

[17] H.W. Höppel, Z.M. Zhou, H. Mughrabi, R.Z. Valiev, Microstructural study of the parameters governing coarsening and cyclic softening in fatigued ultrafine-grained copper, *Philos. Mag. A* 82 (2002) 1781-1794.

[18] M.W. Kapp, T. Kremmer, C. Motz, B. Yang, R. Pippan, Structural instabilities during cyclic loading of ultrafine-grained copper studied with micro bending experiments. *Acta Mater.* 125 (2017) 351-358.

[19] H.W. Höppel, C. Xu, M. Kautz, N. Barta-Schreiber, T.G. Langdon, H. Mughrabi, Cyclic Deformation Behaviour and Possibilities for Enhancing the Fatigue Properties of Ultrafine-Grained Metals, In: Zehetbauer, M., Valiev, R.Z. (eds.) *Nanomaterials by Severe Plastic Deformation* (2004) 677-683.

[20] N. A. Mara, D. Bhattacharyya, J.P. Hirth, P. Dickerson, A. Misra, Mechanism for shear banding in nanolayered composites, *Appl. Phys. Lett.* 97(2) (2010) 021909.

[21] S.J. Zheng, J. Wang, J.S. Carpenter, W.M. Mook, P.O. Dickerson, N.A. Mara, I.J. Beyerlein, Plastic instability mechanisms in bimetallic nanolayered composites, *Acta Mater.* 79 (2014) 282-291.

[22] M.W. Kapp, A. Hohenwarter, S. Wurster, B. Yang, R. Pippan, Anisotropic deformation characteristics of an ultrafine- and nanolamellar pearlitic steel, *Acta Mater.* 106 (2016) 239-248.

[23] D. Jia, K.T. Ramesh, E. Ma, Effects of nanocrystalline and ultrafine grain sizes on constitutive behavior and shear bands in iron, *Acta Mater.* 51(12) (2003) 3495-3509.

[24] S.R. Agnew, A.Y. Vinogradov, S. Hashimoto, J.R. Weertman, Overview of fatigue performance of Cu processed by severe plastic deformation, *J. Electron. Mater.* 28(9) (1999) 1038-1044.

[25] A. Vinogradov, Y. Kaneko, K. Kitagawa, S. Hashimoto, R.Z. Valiev, On the Cyclic Response of Ultrafine-Grained Copper, *MSF* 269-272 (1998) 987-992.

[26] S.D. Wu, Z.G. Wang, C.B. Jiang, G.Y. Li, Scanning electron microscopy-electron channelling contrast investigation of recrystallization during cyclic deformation of ultrafine grained copper processed by equal channel angular pressing, *Philos. Mag. Lett.* 82(10) (2002) 559-565.

[27] S.D. Wu, Z.G. Wang, C.B. Jiang, G.Y. Li, I.V. Alexandrov, R.Z. Valiev, Shear bands in cyclically deformed ultrafine grained copper processed by ECAP, *Mater. Sci. Eng. A* 387-389 (2004) 560-564.

[28] H. Mughrabi, H.W. Höppel, Cyclic deformation and fatigue properties of very fine-grained metals and alloys, *Int. J. Fatigue* 32(9)(2010) 1413-1427.

[29] M. Wong, W. Kao, J. Lui, C. Chang, P. Kao, Cyclic deformation of ultrafine-grained aluminum, *Acta Mater.* 55(2) (2007) 715-725.

[30] F. Wetscher, R. Pippan, Cyclic high-pressure torsion of nickel and Armco iron,

- Philos. Mag. 86(36) (2006) 5867-5883.
- [31] E. Schafler, R. Pippan, Effect of thermal treatment on microstructure in high pressure torsion (HPT) deformed nickel, Mater. Sci. Eng. A 387-389 (2004) 799-804.
- [32] P. Ghosh, O. Renk, R. Pippan, Microtexture analysis of restoration mechanisms during high pressure torsion of pure nickel, Mater. Sci. Eng. A 684 (2017) 101-109.
- [33] L. Toth, P. Gilormini, J. Jonas, Effect of rate sensitivity on the stability of torsion textures, Acta Metall. Mater. 36(12) (1988) 3077-3091.
- [34] L. Kunz, P. Lukáš, L. Pantelejev, O. Man, Stability of ultrafine-grained structure of copper under fatigue loading, Procedia Eng. 10 (2011) 201-206.
- [35] B.L. Boyce, H.A. Padilla, Anomalous Fatigue Behavior and Fatigue-Induced Grain Growth in Nanocrystalline Nickel Alloys, Metall. Mater. Trans. A 42(7) (2011) 1793-1804.
- [36] R.A. Meirum, D.H. Alsem, A.L. Romasco, T. Clark, R.G. Polcawich, J.S. Pulskamp, M. Dubey, R.O. Ritchie, C.L. Muhlstein, Fatigue-induced grain coarsening in nanocrystalline platinum films, Acta Mater. 59(3) (2011) 1141-1149.
- [37] O. Glushko, M.J. Cordill, The driving force governing room temperature grain coarsening in thin gold films, Scripta Mater. 130 (2017) 42-45.
- [38] S. Brandstetter, K. Zhang, A. Escudro, J.R. Weertman, H. van Swygenhoven, Grain coarsening during compression of bulk nanocrystalline nickel and copper, Scripta Mater. 58(1) (2008) 61-64.
- [39] T.H. Fang, W.L. Li, N.R. Tao, K. Lu, Revealing extraordinary intrinsic tensile plasticity in gradient nano-grained copper, Science 331(6024) (2011) 1587-1590.
- [40] F. Momprou, M. Legros, Quantitative grain growth and rotation probed by in-situ TEM straining and orientation mapping in small grained Al thin films, Scripta Mater. 99 (2015) 5-8.
- [41] J.E. Carsley, A. Fisher, W.W. Milligan, E.C. Aifantis, Mechanical behavior of a bulk nanostructured iron alloy, Metall. Mater. Trans. A 29(9) (1998) 2261-2271.
- [42] B.J. Duggan, M. Hatherly, W.B. Hutchinson, P.T. Wakefield, Deformation structures and textures in cold-rolled 70:30 brass, Met. Sci. 12(8) (2013) 343-351.
- [43] F.J. Humphreys, M. Hatherly, Recrystallization and related annealing phenomena, 2nd edn. Elsevier (2004).
- [44] J.M. Finney, C. Laird, Strain localization in cyclic deformation of copper single crystals, Philos. Mag. 31(2) (1975) 339-366.
- [45] A. Rajabzadeh, M. Legros, N. Combe, F. Momprou, D.A. Molodov, Evidence of grain boundary dislocation step motion associated to shear-coupled grain boundary migration, Philos. Mag. 93(10-12) (2013) 1299-1316.





# Strength and ductility of heavily deformed pearlitic microstructures

A. Hohenwarter<sup>a</sup>, M.W. Kapp<sup>b</sup>, B. Völker<sup>b</sup>, O. Renk<sup>b</sup> and R. Pippan<sup>b</sup>

<sup>a</sup>Department of Materials Physics, Montanuniversität Leoben, Jahnstrasse 12, 8700 Leoben, Austria

<sup>b</sup>Erich Schmid Institute of Materials Science, Austrian Academy of Sciences, 8700 Leoben, Austria

## Abstract

The fracture toughness and deformation behavior of heavily deformed pearlitic steels are investigated. A strong anisotropy of the fracture toughness and the plastic deformation behavior with respect to the lamellar orientation has been observed. The consequences of this anisotropy for processing and application as well as for the limits in strengthening are discussed.

## F.1 Introduction

Eutectoid and hypereutectoid pearlitic steels are commonly used in industry. For example, nearly all of the rail steels have a fully pearlitic microstructure. Heavily cold drawn pearlitic wires are the standard materials for cable wires from suspension bridges, steel cord wires for tires or the steel strings for musical instruments. In the last decades a significant increase in strength of such cold drawn pearlitic wires has been obtained [19]. Exceeding 6 GPa strength in tension, such wires have further enhanced the interest in this classical structural material. In these wires the tensile strength has now reached about 1/3 of the theoretical limit and is significantly

higher than of all other currently used structural materials. Additionally, it is a model material for material scientists to clarify how the theoretical limit of strength of other metallic materials can be obtained.

Our interest in the last few years was devoted to the analysis of the evolution of fracture toughness as a function of cold deformation and the study of the anisotropy in the deformation behavior and ductility of the nanolamellar arrangements of ferrite and cementite. The goal of the present paper is to summarize these new findings and to discuss the impact of these results with respect to the limits for processing and strengthening.

## F.2 Fracture toughness as a function of cold working

For the processing, as well as for the in-service use of pearlitic steels, the evolution of ductility and fracture toughness as a function of strain are essential parameters. The special importance of fracture toughness and its anisotropy for ultra-strong materials has been discussed recently in [10-12]. In this section the evolution of the fracture toughness as a function of strain of High Pressure Torsion (HPT) deformed pearlitic steels and of cold drawn wires are summarized. For more details, see [10,12].

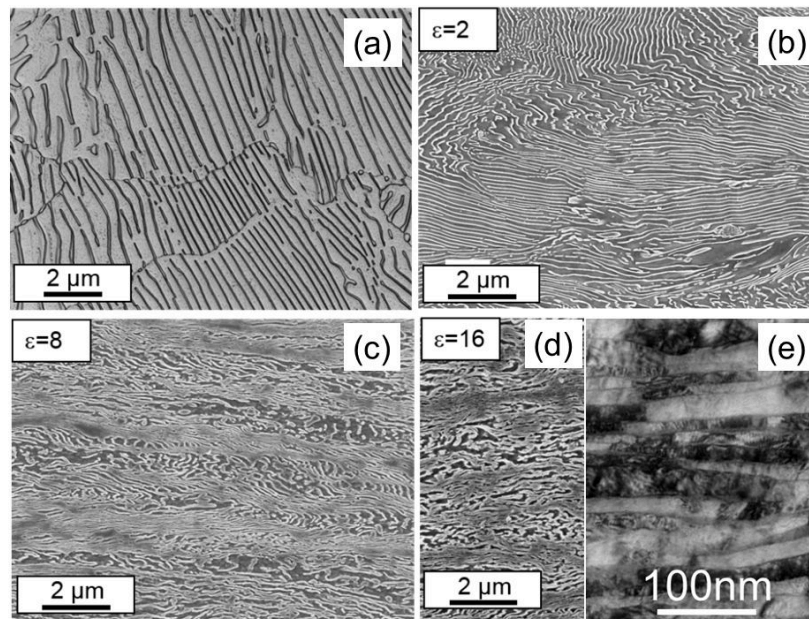


**Figure F.1** Scanning electron microscope images of (a) the undeformed state, (b) at an equivalent strain of  $\epsilon = 2$ , (c)  $\epsilon = 8$ , (d)  $\epsilon = 16$  and (e) transmission electron microscope image at  $\epsilon = 16$ .

The HPT processed pearlitic steel was an R 260 with a chemical composition of 0.76 wt% C, 0.35 wt% Si, 1 wt% Mn, 0.017 wt% P and 0.014 wt% S. Figure 1 contains the scanning electron microscope (SEM) and Transmission Electron Microscope (TEM)

## F.2 Fracture toughness as a function of cold working

images of the undeformed and the HPT deformed microstructure for different equivalent strains looking into the radial direction of the HPT sample. The size of the pearlite colonies in the undeformed material is in the range of 10-20  $\mu\text{m}$  and the colonies are randomly oriented (figure 1a). Within the colonies the cementite lamellae spacing is in the undeformed state about 200 nm. With increasing strain the lamellae align parallel to the shear plane and the lamellar spacing decreases. The with the imposed strain path unfavorably aligned lamellae become heavily bent and broken into smaller pieces, which align with further shearing (figure 1b). At equivalent strains larger than 8 the lamellae are almost fully aligned (figure 1c).

At an equivalent strain of 16 the lamellar spacing is reduced to 15-20 nm as observed in the SEM (figure 1d) and TEM micrograph in figure 1e. In figure 2 the corresponding increase of hardness as a function of strain is plotted. The refinement of the microstructure is reflected in the change of the hardness. It increases strongly from 270 HV in the undeformed state to 770 HV at an equivalent strain of  $\sim 16$ . Along with the microstructural changes several studies have proven a distinctive change in the chemistry of the cementite phase leading to a non-stoichiometric composition and a supersaturation of the ferrite phase. Therefore, the classical description of heavily deformed pearlite as “ferrite-cementite“ composite is not fully straightforward [13-15].

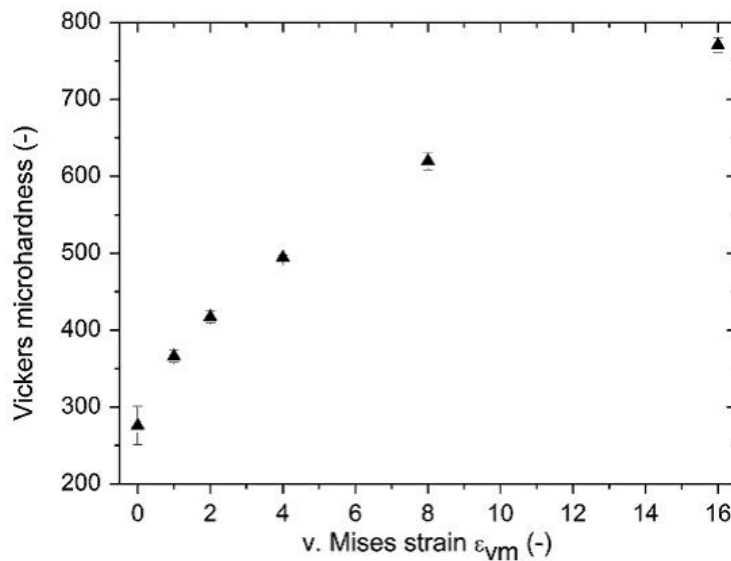


**Figure F.2** Evolution of Vickers microhardness with increasing equivalent strain from [10].

Compact tension (CT) specimens for fracture toughness measurements are machined from the HPT samples deformed to different numbers of rotations. Depending on the number of rotations and the sample extraction radius the fracture toughness can be measured as a function of equivalent strains. The miniaturized CT specimens had a width of 5.2 mm and a thickness of 2 mm. The fracture toughness for the

three different crack plane orientations labelled as A, B and C were investigated, [10] figure 3. In the samples with orientation A, the crack plane is parallel to the shear plane and the propagation direction is in tangential direction of the HPT sample or parallel to the shear direction. For orientation B, not presented here, the crack plane is perpendicular to the shear plane and the desired crack growth direction is in the axial direction of the HPT sample, or perpendicular to the shear plane. For orientation C the crack plane is perpendicular to the shear plane as in orientation B, but the crack propagation direction is in the radial direction of the HPT sample. The fracture toughness results for orientations A and C are summarized in figure 3. With increasing equivalent strain a significant anisotropy of the fracture toughness develops. For orientation A the fracture toughness decreases at smaller shear strains very quickly and reaches a nearly constant low value at higher strain levels, which is only slightly larger than the fracture toughness of a ceramic. For crack orientation C the fracture toughness increases for lower strains, but decreases at higher strains to values similar to the undeformed material (about 40 MPa m<sup>1/2</sup>). Fracture toughness values of orientation B, not shown in figure 3, lie between those of orientation A and C. However, the crack immediately deflects into the shear plane (perpendicular to the actual crack plane), and follows the direction of lowest toughness. Therefore, these values do not characterize the Mode-I fracture toughness and correspond only to a lower limit for this loading case.

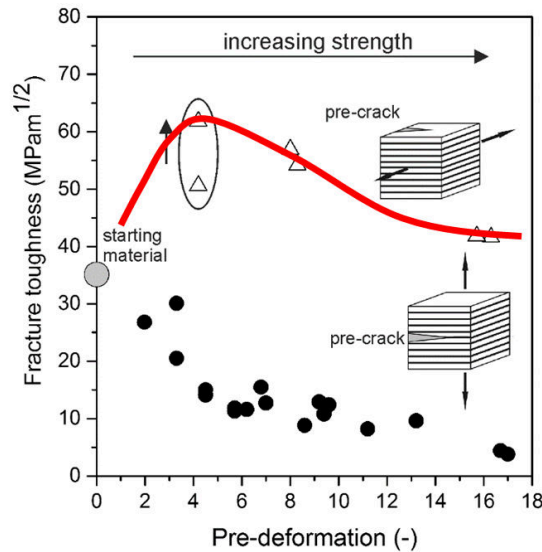


**Figure F.3** Fracture toughness evolution with increasing pre-deformation, thus, equivalent strain, for two different loading directions: pre-crack parallel (orientation A, black dots) and perpendicular (orientation C, open triangles) to the lamellar alignment from [10].

Similar fracture toughness experiments have been performed on heavily cold drawn

## F.2 Fracture toughness as a function of cold working

pearlitic wires [12]. The chemical composition of this hypereutectoid steel was Fe, 0.98 wt.% C, 0.31 wt.% Mn, 0.2 wt.% Cr, 0.006 wt.% P and 0.007 wt.% S. Two wires cold drawn to a true strain of 3.1 and 6.52 with an ultimate tensile strength of about 4 and 6.5 GPa, respectively, were investigated. The diameter of the wires was 120  $\mu\text{m}$  and 24  $\mu\text{m}$ , respectively. Again the anisotropy of these wires has been investigated. The microstructure in the view perpendicular to the drawing direction is very similar to the HPT microstructure perpendicular to shear plane. The thicker wire ( $\epsilon = 3.1$ ) has a lamellar spacing similar to the HPT sample with  $\epsilon = 16$  (figure 1d-e). In the thinner wire ( $\epsilon = 6.52$ ) the microstructure is significantly finer. The microstructure in the view of the drawing direction is very different to the HPT deformed microstructure, showing a characteristically curled microstructure. For more details regarding the microstructure and tensile properties of these wires see [9].

**Table F.1** Fracture toughness values for a pearlitic wire drawn to  $\epsilon = 3.1$  (low deformed) and  $\epsilon = 6.52$  (high deformed). Pre-cracks were introduced parallel and perpendicular to the lamellae orientation [12].

Specimen	$\mathbf{K}_{IC,parallel}$ (MPam <sup>1/2</sup> )	$\mathbf{K}_{IC,perpendicular}$ (MPam <sup>1/2</sup> )
low deformed-1	5.1	40.1
low deformed-2	4.9	42.5
high deformed-1	3.7	(19.7)
high deformed-2	3.8	(21.1)

In order to measure the fracture toughness micrometer-sized cantilevers with the crack propagation direction parallel to the drawing direction and single-edge-notched tension samples for crack propagation perpendicular to the drawing direction were tested. The measured anisotropy of the fracture toughness values of the thicker wire ( $\epsilon = 3.1$ ) are comparable to the HPT samples deformed to high strains (compare Table 1 and figure 3). The low fracture toughness in the drawing direction (parallel to the lamellae) is comparable or somewhat larger than the lowest values measured parallel to the shear plane of the HPT sample (orientation A). In both cases this is the brittle loading direction. The measured fracture toughness for orientation C of the HPT-processed material is similar to the crack plane perpendicular to the drawing direction in the wire and is in both cases distinctively higher. For both processing techniques this is the ductile loading direction. For the thinner wire ( $\epsilon = 6.52$ ), the material with the highest tensile strength, the fracture toughness decreases somewhat for the crack propagation direction in the drawing direction, but more significantly in the crack propagation direction perpendicular to the drawing direction. Thus, a pronounced anisotropy of the fracture toughness remains. The reason for the pronounced anisotropy in the HPT-processed material and the drawn wires are clearly visible from the fractographs in figures 4 and 5, for the brittle and the ductile loading direction, respectively. In all cases the transition from the pre-

crack to the overload fracture is depicted. For the crack propagation parallel to the shear plane and the drawing direction, which is in both cases the brittle direction, a debonding of the aligned lamellar structure is evident (figure 4). In addition, the difference in the lamellar arrangement between HPT and wire drawing namely the planar or curled microstructural arrangement is reflected by the topography of the fractographs.

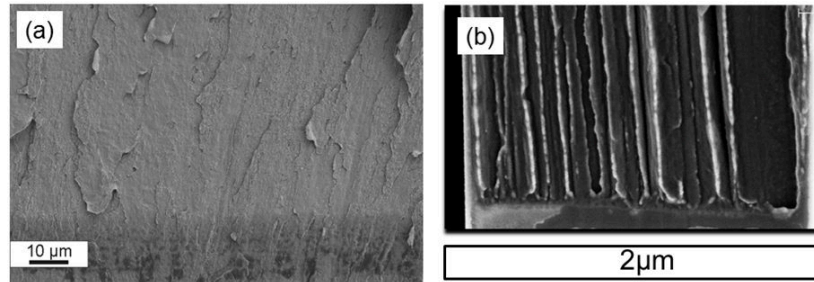


**Figure F.4** SEM images of the fracture surfaces with the pre-crack parallel to the lamellae, thus parallel to (a) the HPT shear plane (orientation A) [10] and (b) the wire axis [12].

Contrary for orientation C in the HPT sample and the crack orientation perpendicular to the drawing direction of the wire (figure 5) the formation of delaminations results in a reduction of the triaxiality in front of the crack and permits a ductile failure. For further details see [10,12].

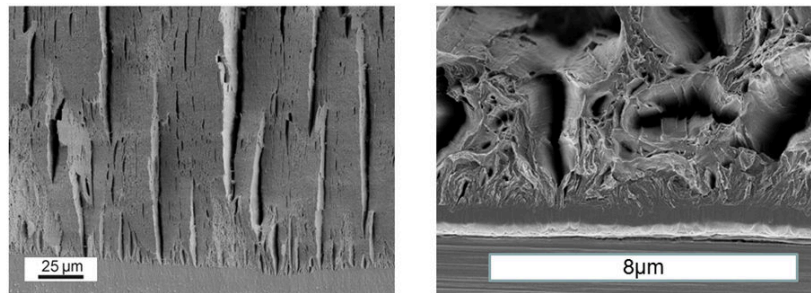


**Figure F.5** SEM images of the fracture surfaces with the pre-crack perpendicular to the lamellae, thus (a) along the radial direction of the HPT disc (orientation C) [10] and (b) perpendicular to the wire axis [12].

### F.3 Effect of the lamellar arrangement during compression loading

In order to compare the mechanical behavior of an undeformed and heavily cold worked lamellar “ferrite-cementite“ arrangement micromechanical experiments with about  $3 \times 3 \times 6 \mu\text{m}^3$  sized micro pillars have been performed. The details of this study

### F.3 Effect of the lamellar arrangement during compression loading

are described in [16]. A fully pearlitic rail steel R260 with a chemical composition as described in section 1 was used. As already mentioned the lamellar spacing in the undeformed pearlite is about 200 nm (see figure 1) and a colony size of 10-20  $\mu\text{m}$ . To study the orientation dependency of such lamellar composites on the plastic deformation, the sample size for the undeformed pearlite has to be significantly smaller than the colony size. The heavily deformed samples were taken from a HPT sample in a region with an applied strain of 14.8, the lamellar spacing was in this case about 15 nm. For better comparison, both the undeformed and the heavily deformed samples had about the same dimensions. All samples have been machined by focused ion beam (FIB) milling. For each material, three loading conditions, schematically depicted in figure 6 have been investigated to study potential plastic anisotropy.

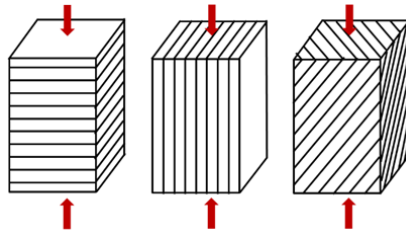


**Figure F.6** Schematic diagrams of the principal compression directions (normal, parallel, inclined) with respect to the ferrite and cementite lamellae alignment.

The loading directions are denoted as parallel (parallel to the aligned lamellae), normal (perpendicular to the ferrite and cementite lamellae) and an inclined loading direction between these two extrema (inclination angle of about  $45^\circ$ ). Measured load-displacement curves, i.e. technical stress-strain curves, are presented in [16]. In figure 7 the characteristic features are replotted in a schematic diagram to point out more clearly the differences in the deformation behavior, as a function of the loading direction for the undeformed and heavily deformed pearlite.

Clearly evident is the enormous effect of HPT deformation, or in other words, the reduction of lamellar spacing from about 200 nm to 15 nm on the mechanical behavior. Despite the significant differences in the flow stress of the two materials, there are several similarities, but also some differences with respect to the orientation dependence. The inclined direction is for both microstructures always the softest. A further pronounced similarity is the formation of only one (HPT pre-deformed to  $\epsilon = 14.8$ ) or two (non pre-deformed) distinct and narrow shear bands for both lamellar spacings in the normal loading direction, which are clearly visible in the SEM images of the deformed samples in figure 8. The formation of these shear bands is associated with a load drop. It seems that the realignment of the lamellar arrangement into the shear direction, compare [16], causes initially some softening and when the lamellar spacing is again sufficiently reduced, or the formed substructure is sufficiently refined (hardened), again a stable deformation takes place, by assumed a growing of the size of the shear band. Common for all three orientations is the start of plastic

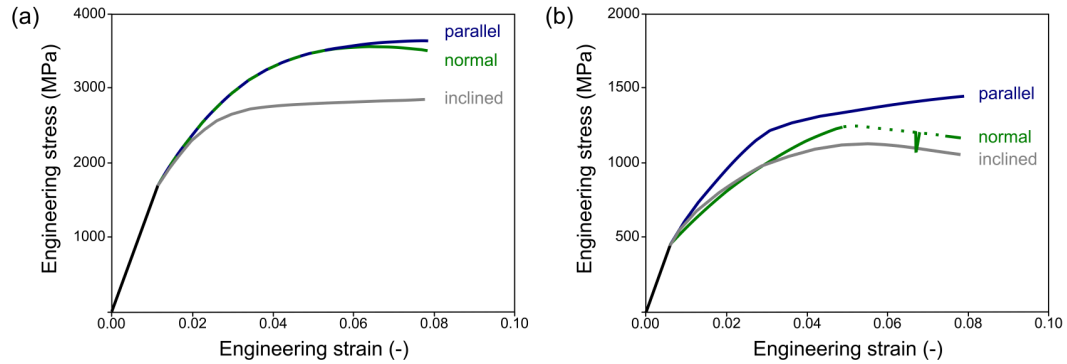


**Figure F.7** Schematic stress-strain curves from [16] (a) for the HPT processed state after an equivalent strain of  $\epsilon = 16$  and (b) for the non HPT processed state, for the lamellae being aligned parallel, normal and inclined with respect to the loading direction.

yielding, which is for the undeformed state at somewhat below 500 MPa and the nanolamellar ( $\epsilon = 14.8$ ) at about 2 GPa. However, it should be noted that the exact determination of the onset of plastic yielding cannot be determined very precisely in such micro-compression experiments.

For the parallel and the normal lamellae arrangements with respect to the loading direction, in the undeformed material the early pronounced hardening can be explained easily by a composite model. The cementite behaves elastic and the ferrite already nearly ideal plastic during this first few percent of plastic deformation. When the plastic deformation of the cementite starts, pronounced hardening diminishes or is even displaced by softening for the normal loading direction due to the formation of a shear band.

In the heavily deformed material the parallel and normal orientations behave very similar during hardening, which indicates that the composite model cannot be applied anymore. After the initial pronounced hardening regime at a flow stress of about 3.5 GPa the parallel orientation exhibits a nearly ideal plastic behavior, whereas the normal orientation shows softening due to the pronounced shear band. The shape of the pillars after the compression experiment is compared in figure 8 by one representative pillar for each loading direction and lamellar spacing. All samples deform at higher strains on this scale in the form of shear or kink bands, but only the normally oriented one deforms primarily in a single band.

#### F.4 Concluding remarks with respect to processing and applications

The presented results have important consequences for the processing and applications, but also for the limits of obtainable strength and ductility of cold worked pearlitic steels. There are a large number of papers dealing with the strength of cold worked fully pearlitic steels, see for example [19]. In most cases it is assumed

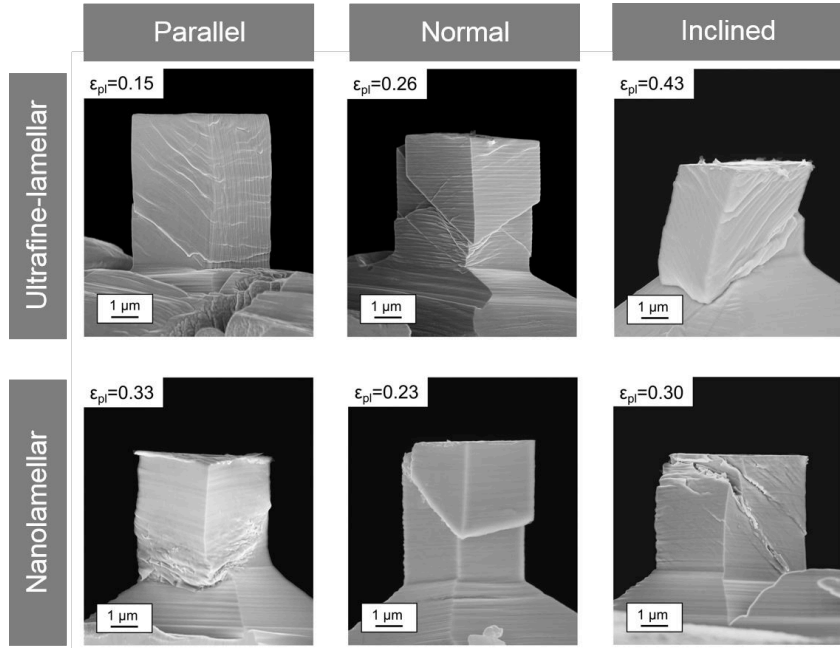


**Figure F.8** SEM images of the undeformed (ultrafine-lamellar) and HPT pre-deformed (nanolamellar) compressed micro pillars, with the lamellae aligned parallel, normal and inclined with respect to the loading direction.

that the strength is a sum of different contributions, where the most important assumed mechanisms are Hall-Petch or Orowan mechanism, dislocation hardening and solution hardening by carbon dissolution [8]. To the authors' opinion, at the limit of strength of this type of materials not all of these mechanisms are of similar importance. Although the micro-compression experiments provide some hints to the hardening phenomena, in the present paper only the consequences for the cold working and application are shortly discussed.

The anisotropy of fracture toughness is a common feature of many highly stressed biomaterials like wood or bone. The exceptional properties in certain loading directions cannot be explained without this anisotropy. This is also the case for cold drawn pearlitic wires, where the anisotropy in fracture toughness is a pre-request for its exceptional combination of properties.

In the typical loading direction of the wires and sheets for technical applications or the directions where the highest tensile deformation during the processing occurs, the fracture resistance is high. It is exceptionally high if one takes into account the strength of these materials [12]. In the directions where the stresses during application are low or during processing compressive stresses are present, the fracture toughness is very low. Cracks on the microscale are unavoidable during processing and in service. In the case of tensile loading of sheets or wires such cracks always experience a high fracture resistance due to crack deflection or crack delamination. The decrease in fracture toughness and the decrease in the anisotropy for cold drawn

hypereutectoid steel wires with strengths above 6.5 GPa might be one of the main reasons why it becomes more and more difficult to further deform such wires. An important feature of the micro compression experiment was the pronounced formation of a single “macro” shear band for the loading of the lamellar microstructure in normal direction, i.e. compression loading perpendicular to the lamellar plane. A consequence of this anisotropy in the shear localization seems to be responsible that during rolling the occurrence of macro shear bands at higher strains is much more pronounced than during wire drawing.

From simple geometric considerations in rolling the lamellae become nearly perfectly aligned to the rolling plane at strains of about 1.5. Such an arrangement is very sensitive to form localized macro shear bands, see figure 9, whereas during wire drawing a curled arrangement of the lamellae develops being less sensitive to macro shear bands. Hence, it seems to be easier to reduce the lamellar spacing in wire drawing than in sheet rolling without failure.



**Figure F.9** Optical micrograph of a pearlitic steel (R260) cold rolled at 298 K to a logarithmic thickness reduction of  $\varphi = 1.5$ . Macroscopic shear bands are clearly visible in the transverse section.

The shear deformation in HPT or on the surface of rails is realized by a relatively homogeneous shearing. This shear deformation corresponds to deformation of the inclined micro pillar, which has the lowest flow stress. Thus, in HPT or at the surface of a rail the macro shear direction matches well with shear direction with the lowest flow stress, shearing in any other direction would require higher shear stresses. Hence, this anisotropy stabilizes the homogenous shear deformation during HPT or the shear deformation near the surface of a rail.

### **Acknowledgements**

Financial support by the FWF Austrian Science Fund within project number P24429-N20 and by the European Research Council und ERC Gran Agreement No. 340185 USMS is gratefully acknowledged.

## References

- [1] G. Langford, Deformation of pearlite, *Metall. Trans. A* 8 (1977) 861-875.
- [2] D.A. Porter, K.E. Easterling, G.D.W. Smith, Dynamic studies of the tensile deformation and fracture of pearlite, *Acta Metall. Mater.* 26 (1978) 1405-1422.
- [3] J. Gil Sevillano, Substructure and strengthening of heavily deformed single and two-phase metallic materials, *J. Phys. III* 1 (1991) 967-988.
- [4] J. Toribio, Relationship between microstructure and strength in eutectoid steels, *Mater. Sci. Eng. A* 387-389 (2004) 227-230.
- [5] F. Wetscher, A. Vorhauer, R. Stock, R. Pippan, Structural refinement of low alloyed steels during severe plastic deformation, *Mater. Sci. Eng. A* 387-389 (2004) 809-816.
- [6] F. Wetscher, B.H. Tian, R. Stock, R. Pippan, High pressure torsion of rail steels, *Mater. Sci. Forum* 503-504 (2006) 455-460.
- [7] F. Wetscher, R. Stock, R. Pippan, Changes in the mechanical properties of a pearlitic steel due to large shear deformation, *Mater. Sci. Eng. A* 445-446 (2007) 237-243. [8] X. Zhang, A. Godfrey, X. Huang, N. Hansen, Q. Liu, Microstructure and strengthening mechanisms in cold-drawn pearlitic steel wire, *Acta Mater.* 59 (2011) 3422-3430.
- [9] Y. Li, D. Raabe, M. Herbig, P. Choi, S. Goto, A. Kostka, H. Yarita, C. Borchers, R. Kirchheim, Segregation stabilizes nanocrystalline bulk steel with near theoretical strength, *Phys. Rev. Lett.* 113 (2014) 106104.
- [10] A. Hohenwarter, A. Taylor, R. Stock, R. Pippan, Effect of large shear deformations on the fracture behavior of a fully pearlitic steel, *Metall. Mater. Trans. A* 42 (2011) 1609-1618.
- [11] C. Kammerhofer, A. Hohenwarter, S. Scheriau, H.P. Brantner, R. Pippan, Influence of morphology and structural size on the fracture behavior of a nanostructured pearlitic steel, *Mater. Sci. Eng. A* 585 (2013) 190-196.
- [12] A. Hohenwarter, B. Völker, M.W. Kapp, Y. Li, S. Goto, D. Raabe, R. Pippan, Ultra-strong and damage tolerant metallic bulk materials: A lesson from nanostructured pearlitic steel wires, *Sci. Rep.* 6 (2016) 33228.
- [13] F. Wetscher, R. Pippan, S. Sturm, F. Kauffmann, C. Scheu, G. Dehm, TEM investigations of the structural evolution in a pearlitic steel deformed by high pressure torsion, *Metall. Mater. Trans. A* 37 (2006) 1963-1968.
- [14] X. Sauvage, Y. Ivanisenko, The role of carbon segregation on nanocrystallisation of pearlitic steels processed by severe plastic deformation, *J. Mater. Sci.* 42 (2007) 1615-1621.
- [15] Y.J. Li, P. Choi, C. Borchers, S. Westerkamp, S. Goto, D. Raabe, R. Kirchheim, Atomic-scale mechanisms of deformation-induced cementite decomposition in pearlite, *Acta Mater.* 59 (2011) 3965-3977.
- [16] M.W. Kapp, A. Hohenwarter, S. Wurster, B. Yang, R. Pippan, Anisotropic deformation characteristics of an ultrafine- and nanolamellar pearlitic steel, *Acta Mater.* 106 (2016) 239-248.





# Fatigue induced instabilities studied by inexhaustible ultrafine-grained samples

M.W. Kapp<sup>a</sup>, O. Renk<sup>a</sup>, T. Leitner<sup>b</sup>, P. Ghosh<sup>a</sup>, B. Yang<sup>a</sup> and R. Pippan<sup>a</sup>

<sup>a</sup>Erich Schmid Institute of Materials Science, Austrian Academy of Sciences, 8700 Leoben, Austria

<sup>b</sup>Department of Materials Physics, Montanuniversität Leoben, Jahnstrasse 12, 8700 Leoben, Austria

## Abstract

Structural instabilities in UFG nickel introduced by cyclic deformation were studied systematically by cyclic high pressure torsion (CHPT), an alternative setup for performing low cycle fatigue (LCF) experiments. Thereby, the grain structure was altered similarly to conventional LCF testing by grain coarsening and shear band formation. Different to conventional LCF testing, the large hydrostatic pressure prevents fatigue induced damage of the samples, e.g. the formation of cracks. This allows to study the development of these cyclically induced instabilities up to huge amounts of accumulated cyclic strain. Additionally, it allows to measure the fraction of cyclic softening solely originating from the coarsening of the structure, not accessible in conventional experiments. It is shown that grain coarsening in shear bands progresses with increasing accumulated strain, although the resulting grain size is further determined by the strain amplitude. Cyclic loading under cryogenic conditions proved that thermal activation is not a prerequisite for grain boundary migration and hence grain coarsening. Finally, a comparison of CHPT performed on coarse grained and nanocrystalline materials revealed that the strain hardening

capability of the coarse grained materials and its absence in the nanocrystalline material governs the tendency for strain localization within shear bands significantly.

## **G.1 Introduction**

The refinement of metallic structures into the ultrafine-grained (UFG) and nanocrystalline (NC) regime is capable of increasing the monotonic but also the cyclic strength tremendously [13]. Extensive research showed, that these materials are perfect aspirants for the high cycle fatigue (HCF) regime, where only moderate plastic strain amplitudes are applied due to their significant enhanced flow stresses. However, when larger cyclic plastic strains have to be accommodated in such fine scaled structures, they can be significantly altered by the formation of shear bands or a coarsening of the structure [4]. Thus, in the low cycle fatigue (LCF) regime a deterioration of the cyclic mechanical response is generally observed [4] affecting the sustainability and therefore the reliability of these materials.

The appearance of cyclically induced shear bands is manifold, ranging from surface features [511] to observations in the sample interior [12] over to a narrow appearance, that can be more step-like [9] but also extrusion-like [5,6,9,10] or even flat, when consisting of coarsened grains [13]. The observations of coarsened grains within shear bands turned out to vary strongly with the materials structure generated by the processing method [14]. Whereas for UFG copper processed by equal channel angular pressing (ECAP) the shear band width was limited to a few coarsened grains, the shear band width in aluminum was distinctly larger. In some cases, the grains within the shear bands were found to become aligned along the shear direction [13]. In a foregoing study on UFG Ni applied to cyclic torsional straining, grain coarsening was reported to take place also outside the shear band [15]. Though, the coarsening process was clearly accelerated within the shear band. There, grains tend to align along crystallographic orientations preferred for cyclic slip.

Although the observation of amplified coarsening within shear bands emphasizes the importance of cyclic strain in triggering the migration of grain boundaries [13-15] most studies argue that a coupling of grain boundaries to shear stresses [16-20] account for grain growth, similar to observations in bicrystals [21,22]. Elsewhere, grain coarsening upon LCF experiments has been found to correlate with a thermal activation, as it was more pronounced when the time for diffusion controlled processes was increased [23]. Thus, different opinions about the driving forces exist, as a full understanding of the coarsening process and its underlying mechanisms has still not been achieved.

Deeper insights into the underlying mechanisms of grain coarsening were provided by in-situ approaches conducted inside scanning electron microscopes (SEM) or transmission electron microscopes (TEM). Both enable to track deformation induced structural changes as throughout the entire experiment the same sample area is under investigation. In doing so in-situ SEM cyclic bending experiments revealed that structural coarsening is caused by the continuous migration of high angle grain

boundaries (HAGB) [24]. Thereby, larger grains tend to grow at the expense of smaller grains, suggesting that the migration direction is governed by differences in the strain energy density [25,26]. On an even smaller scale in-situ TEM straining experiments evidenced the crucial role of disconnections for boundary migration [27]. Such boundary defects consist of a step associated with a grain boundary dislocation and will be continuously produced by the interaction of lattice dislocations with grain boundaries [28].

Although, these type of experiments reveal unique insights into the basic grain growth mechanisms they also have limitations, in especially concerning investigations on the shear banding mechanism. TEM experiments are restricted to a very small investigated sample volume and as the initiation sites for shear bands cannot be predicted they can be easily overlooked with this method. Further, it seems that the formation of shear bands is not possible in small sample volumes such as micron sized cantilevers [24]. They require sample volumes on the macroscopic scale which excludes in-situ approaches utilizing micron and submicron sized samples.

In order to study the development of shear bands and their evolution with strain a different experimental approach is necessary. In a previous work [15] cyclic high pressure torsion (CHPT) on UFG Ni has been found to reproducibly initiate shear bands coupled to cyclically induced grain growth. The main advantage of this methodology is the prevention of cyclic damage, i.e. fatigue crack initiation by the applied hydrostatic pressure. Contrary to conventional fatigue experiments the infinite sample life time therefore allows to track the evolution of the shear bands and grain coarsening up to huge accumulated cyclic strains, being in the focus of this study. Only such detailed studies are able to decouple the various parameters that may influence cyclically induced instabilities, impossible with conventional testing routes. The different materials and testing parameters used in studies so far may explain the different results and ideas of the vast number of studies outlined before. A systematic study on the influence of experimental parameters such as the strain amplitude, accumulated strain and temperature will be presented. Furthermore, also material parameters like crystallography, grain boundary type and starting grain size will be evaluated with respect to structural instabilities. This systematic study and the variation of influencing parameters will allow for the first time to gain insights into structural instabilities and their underlying driving forces in such UFG and NC materials.

## G.2 Experimental

To study cyclically induced structural changes high purity nickel (99.99%) was used as a model material as the relatively high melting point allows to study the cyclic deformation behavior at low homologous temperatures (about 0.16 at room temperature). The UFG structure was synthesized by applying monotonic high pressure torsion (HPT). Discs with 10 mm in diameter and 0.8 mm in thickness,  $t$ , were used. The coarse grained nickel was deformed for 15 revolutions,  $n$ , resulting in an equivalent v. Mises strain,  $\epsilon_{eq}$ , of 340 at an HPT disc radius,  $r$ , of 5 mm according

to Eq. 1:

$$\epsilon_{eq} = \frac{2\pi rn}{\sqrt{3}t}. \quad (\text{G.1})$$

This strain is sufficient to obtain a constant grain size along the HPT disc radius, except for the very center of the sample ( $r < 0.5$  mm). The steady state structure exhibits an equiaxed structure in tangential (TAN) viewing direction of the HPT disc (Fig. 1a). The grain and subgrain size was calculated from electron back scatter diffraction (EBSD) data to be 317 nm and 269 nm (area weighted), respectively, yielding a microhardness of about 300 HV. For more details on the HPT setup used, see [29,30].

To compare the effect of different starting grain sizes on the evolution of structural instabilities upon cyclic loading in addition to the UFG structures coarse grained (CG) high purity nickel (99.99%) and nanocrystalline (NC) nickel were used (Fig. 1b-c). For the CG structure the as-received materials was annealed for 1 hour at 973 K. It should be noted that the CG and UFG material were produced from the same rod and are of same purity (99.99%). The NC nickel of commercial purity was processed by electrodeposition resulting in a mean grain size of 22 nm [31].

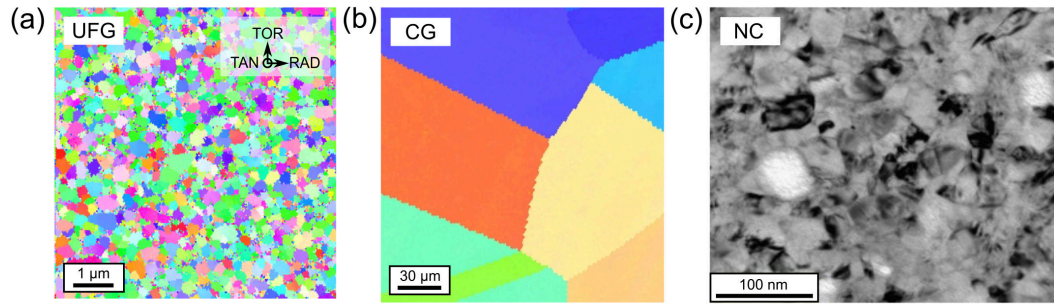


**Figure G.1** Initial microstructure of the cyclically torsioned samples a) UFG Ni, b) CG Ni and c) NC Ni [31].

Cyclic high pressure torsion (CHPT) was used as an alternative assessment for displacement controlled fatigue. As mentioned before, this setup suppresses damage evolution, e.g. roughening and cracking, during the deformation experiment due to the applied hydrostatic pressure. The sample initially processed by monotonic HPT is left inside the sample anvils for the UFG condition, as the fatigue experiments can be performed immediately afterwards. The setup is similar to conventional HPT except for the requirement of an additional control unit, allowing for a change of the rotation direction of the lower HPT anvil after a desired twist angle,  $\Theta$ . A long rod with permanent magnets on its end is mounted to the lower anvil, which rotates between two Hall sensors, activating them once the chosen twist angle is reached and forcing the motor of the HPT tool to change its rotation direction. Further, the number of cycles, which should be imposed to the sample can be set. The rotation speed was 0.2 rotations per minute.

By adjusting the twist angle,  $\Theta$ , during CHPT the nominal strain amplitude can be calculated following Eq. 2

$$\epsilon_a = \frac{2\pi r}{\sqrt{3}t} \frac{\Theta}{360^\circ} \quad (\text{G.2})$$

According to Eq. 2, the strain amplitude varies along the HPT disc radius, but also for samples of different thicknesses. The three different used parameters are summarized in Table 1.

**Table G.1** The nominal strain amplitude,  $\epsilon_{a,nom}$ , increases along the HPT disc radius depending on the HPT twist angle and the HPT disc thickness according to Eq.2.

HPT twist angle	HPT disc thickness	$\epsilon_{a,nom}$ at HPT disc radius			
		1 mm	2 mm	3 mm	4 mm
5°	0.80 mm	0.06	0.13	0.19	0.25
5°	0.65 mm	0.08	0.16	0.23	0.31
1.25°	0.80 mm	0.03	0.06	0.09	0.12

The accumulated strain can be adapted by changing the number of cycles,  $N$ , according to Eq. 3

$$\epsilon_{acc} = 4N\epsilon_a \quad (\text{G.3})$$

For this study various parameters that could influence shear band formation and grain growth were systematically studied, e.g. strain amplitude, accumulated strain, temperature. All analyzed conditions are summarized in Table 2.

**Table G.2** Overview of the different experimental conditions used during cyclic deformation of three different initial structures.

HPT twist angle	HPT disc thickness	Number of cycles	Starting material	Temperature
5°	0.80 mm	50, 250, 1000	UFG	273 K
5°	0.65 mm	5, 4900	UFG	273 K
1.25°	0.80 mm	25, 250, 1000, 4000	UFG	273 K
5°	0.80 mm	50, 500	UFG	-77 K
5°	0.80 mm	100, 250, 1000, 5000	CG	273 K
5°	0.80 mm	50, 250	NC	273 K

### G.3 Results

#### G.3.1 Shear band evolution in UFG structures with increasing strain

A previous study [15] revealed the development of a shear band in UFG nickel during CHPT with  $5^\circ$  twist angle for 50 cycles. Back scatter electron (BSE) images show the entire sample height (Fig. 1 in first row, reprinted from [15]) and reveal a shear band traversing the entire HPT disc, which is visible by the brighter contrast in the middle. It was shown that compared to the initial UFG structure within the shear band has coarsened significantly and the grains are elongated along the shear band direction, whereas outside of the shear band an equiaxed structure, which only slightly coarsened, prevails [15]. The thickness of the shear band,  $t_{SB}$ , (Tab. 3 and Fig. 2) does not only increase along the HPT disc radius, thus, with increasing nominal strain amplitude, but also by an increase of the cycle number, thus, with increasing accumulated strain. The presence of a shear band and the softening due to grain coarsening will localize the cyclic deformation within this region. The strain localization in just a certain thickness of the HPT disc results in higher local strain amplitudes within the shear band, but due to its wedge-like shape also in smaller differences of the local strain amplitude over the HPT disc radius. The local strain amplitude can be estimated by normalizing the nominal strain amplitude by the shear band thickness setting  $t = t_{SB}$  in Eq. 2, given exemplarily for the 50 and 100 times cycled sample in Table 3.

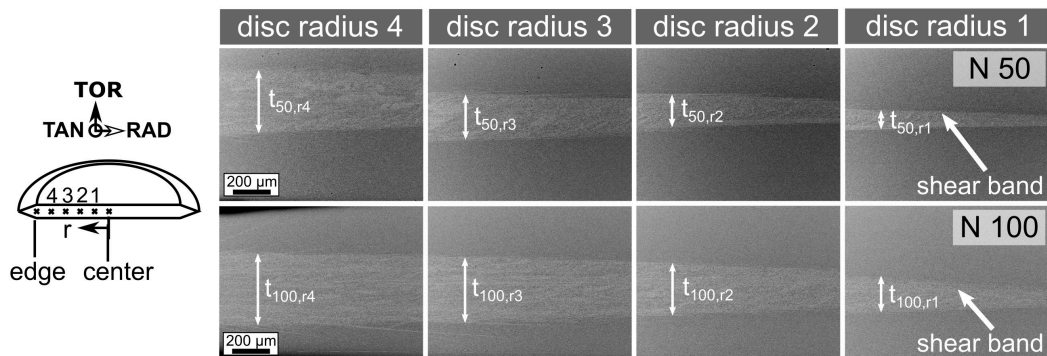


**Figure G.2** BSE images of initially UFG Ni a) cycled for 50 times at  $5^\circ$  twist angle reveal a wedge-shaped shear band located in the center of the HPT disc, which is brighter in contrast [15] and b) which grows in thickness when the cycle number is doubled to 100 times.

#### G.3.2 Microhardness and structural evolution with accumulated strain for different strain amplitudes

To study the evolution of grain growth and cyclic softening with increasing accumulated strain samples cycled for 5, 50, 250 and 1000 times at a twist angle of  $5^\circ$  were investigated by microhardness measurements and EBSD scans. Focusing first on the

**Table G.3** Nominal strain amplitudes,  $\epsilon_{a,nom}$ , thickness of the shear band,  $t_{SB}$ , as marked in Fig. 2 and estimated local strain amplitudes inside the shear band,  $\epsilon_{a,loc}$ , are calculated for different HPT disc radii for samples cycled for 50 and 100 times at  $5^\circ$  twist angle. The local strain amplitude is calculated with Eq. 2 by setting  $t = t_{SB}$  and is enhanced due to the strain localization, but does not differ significantly over the HPT disc radius.

HPT disc radius (mm)	$\epsilon_{a,nom}$ (-)		$t_{SB}$ ( $\mu\text{m}$ )		$\epsilon_{a,loc}$ (-)	
	N50	N100	N50	N100	N50	N100
1	0.06		100	180	0.05	0.28
2	0.13		180	260	0.56	0.39
3	0.19		240	330	0.63	0.46
4	0.25		310	360	0.65	0.56

shear band region a nearly constant distribution of the hardness along the HPT disc radius can be observed for all cycle numbers (Fig. 3a). The microhardness drops from 301 HV for the UFG starting material to average values of 272 HV, 254 HV, 252 HV and 217 HV after 5, 50, 250 and 1000 cycles, respectively. The continuous cyclic softening is a consequence of the ongoing structural coarsening with increasing cycle number confirmed by the EBSD scans taken at an HPT disc radius of 4 mm (Fig. 3b).

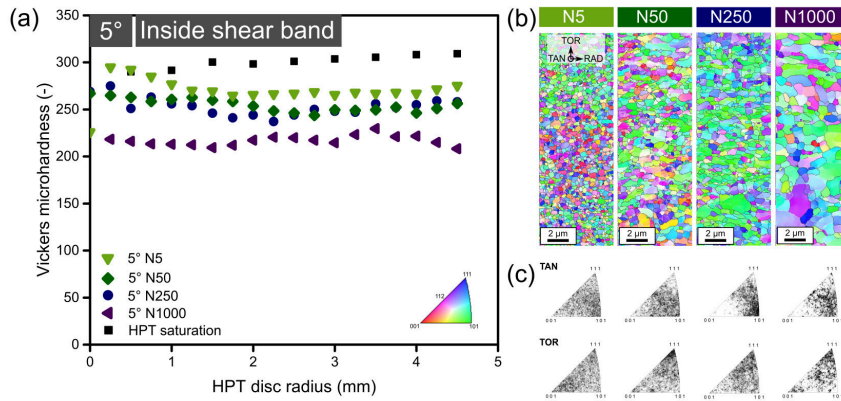


**Figure G.3** Evolution of (a) the microhardness along the HPT disc radius, (b) the grain structure in representative EBSD scans taken at  $r = 4$  mm and (c) the corresponding crystallographic orientations in IPFs calculated for the tangential and torsional direction for UFG samples subjected to CHPT at  $5^\circ$  twist angle for 5, 50 [15], 250 and 1000 times.

Grain ( $>15^\circ$  boundary misorientation) and subgrain sizes ( $2-15^\circ$  boundary misorientation) were calculated from EBSD data inside and outside of the shear band (Fig. 4). As their evolution along the HPT disc radius was nearly constant (compare exemplarily Fig. 8 for  $5^\circ$  twist angle and 5 cycles, first row) only the average values are plotted as a function the cycle number. For both, grains and subgrains, a coarsening

is observed, which is weak outside the shear band (Fig. 4b, compare EBSD data in Fig. 5a taken at  $r = 4$  mm) and pronounced inside the shear band (Fig. 4a, compare EBSD data in Fig. 3b). Both sizes increase steadily with the cycle number, thus accumulated strain. Note that calculations of the grain size for the samples cycled 1000 times can be considered only as a lower bound as the grains already exceed the size of the EBSD scan size. However, larger scan sizes were not accessible in order to ensure a sufficient resolution for still small grain sizes in a reasonable scanning time, necessary to avoid drift issues. In addition inverse pole figure (IPF) maps were calculated from the EBSD data taken at  $r = 4$  mm inside (Fig. 3c) and outside (Fig. 4b) of the shear band to track any changes with respect to crystallographic orientations. Inside the shear band a preference for  $\{111\}$  planes parallel to the shear plane was observed with increasing accumulated strain. In shear direction orientations from  $[101]$  to  $[112]$  are getting preferred with increasing accumulated strain. Outside the shear band the crystallographic orientations remain relatively similar to monotonic HPT conditions [26], although slightly intensified towards  $[101]$   $(001)$  with increasing accumulated strain.

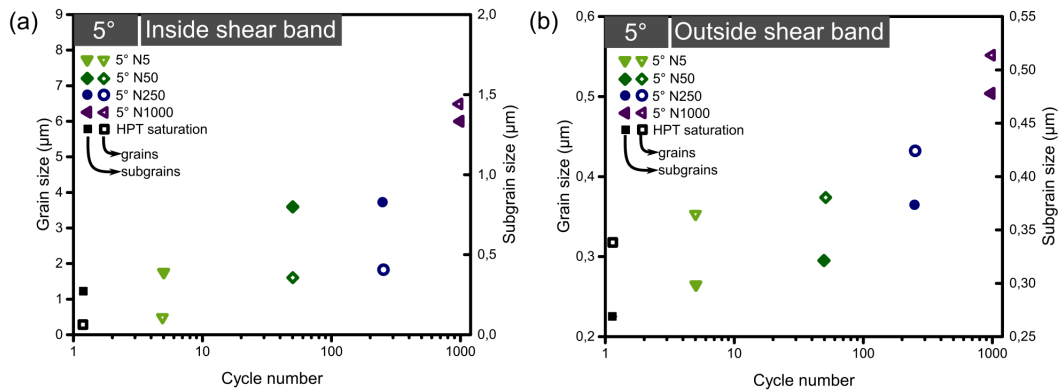


**Figure G.4** Calculations of grain and subgrain sizes (a) inside and (b) outside of the shear band for UFG samples cycled at  $5^\circ$  twist angle for 5, 50 [15], 250 and 1000 cycles. Please not different scale for grain (left) and subgrain sizes (right).

As mentioned earlier, due to the wedge-shaped evolution of the shear band differences of the nominal strain amplitude along the HPT disc radius were partly levelled out. This makes it difficult to study the influence of the strain amplitude on structural evolution in more detail with a single HPT disc. Therefore, a different twist angle of  $1.25^\circ$  was applied during CHPT, resulting in smaller nominal strain amplitudes as compared to the  $5^\circ$  twist angle. To compare samples deformed at different nominal strain amplitudes but the same accumulated strains the number of cycles were adjusted to 25, 250, 1000 and 4000 for  $1.25^\circ$  twist angle. Fig. 6 shows that for the smaller strain amplitude the mechanical and structural evolution is qualitatively similar, as the microhardness drops (Fig. 6a) and continuously grains grow within a shear band (Fig. 6b).

However, comparing the microhardness levels of both samples at the same accumu-

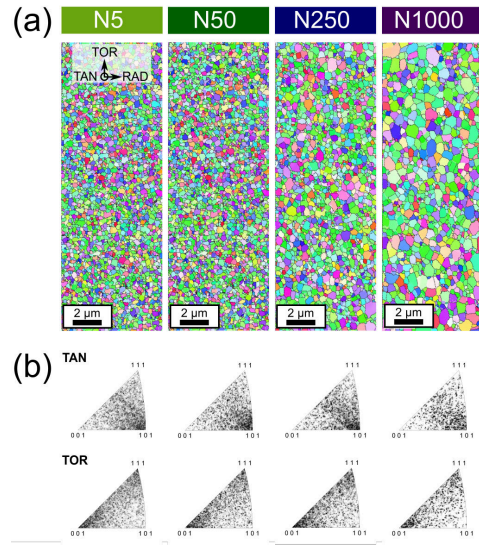


**Figure G.5** (a) EBSD scans taken outside the shear band at  $r = 4$  mm and (b) IPF maps calculated for the tangential and torsional HPT disc viewing direction for UFG samples cycled by  $5^\circ$  for 5, 50 [15], 250 and 1000 times.

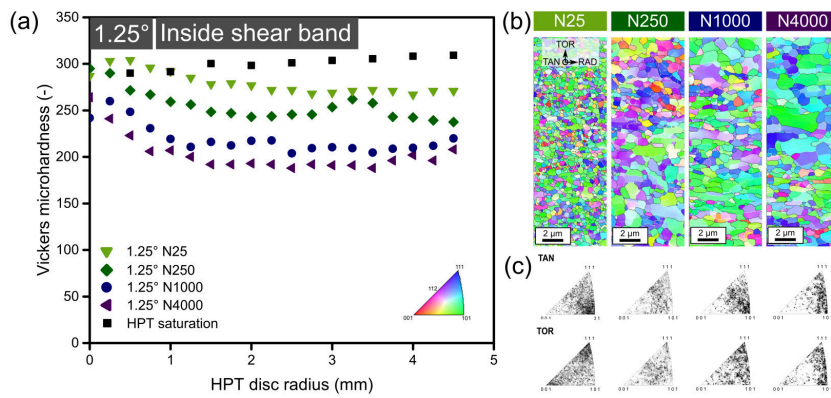


**Figure G.6** Evolution of (a) the microhardness along the HPT disc radius, (b) the grain structure in representative EBSD scans taken at  $r = 4$  mm and (c) the corresponding crystallographic orientations in IPFs calculated for the tangential and torsional direction for UFG samples subjected to CHPT at  $1.25^\circ$  twist angle for 25, 250, 1000 and 4000 times.

lative strains, for instance  $1.25^\circ$  for 4000 cycles and  $5^\circ$  for 1000 cycles, shows that hardness is lower for the smaller strain amplitude. Accordingly the grain and subgrain sizes measured from EBSD scans inside the shear band (Fig. 7a) were a bit larger and about the same outside the shear band (Fig. 7b) for the  $1.25^\circ$  twist angle. The evolution of the IPFs with increasing accumulated strains (Fig. 6c) follows in principal of trend in the 5 samples, with a preference for  $\{111\}$  planes parallel to the shear plane and a scatter between  $\langle 101 \rangle$  and  $\langle 112 \rangle$  for the shear direction. However, the intensities are somewhat smaller as compared to  $5^\circ$  twist angle.

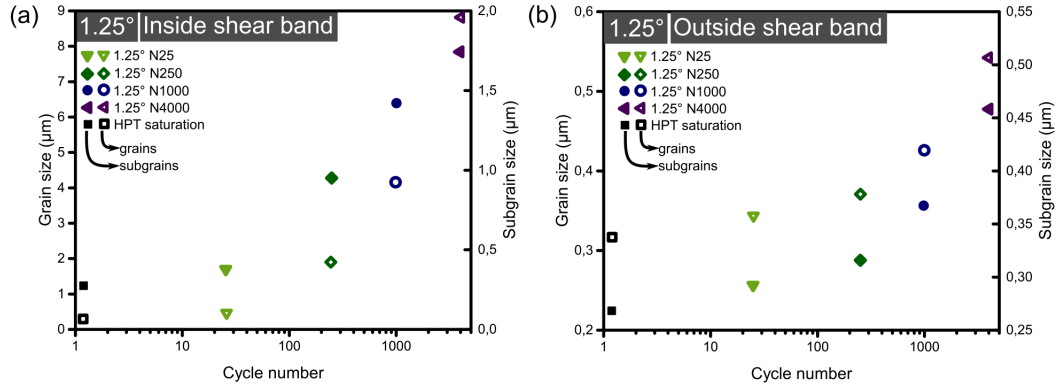


**Figure G.7** Calculations of grain and subgrain sizes (a) inside and (b) outside of the shear band for samples cycled at  $1.25^\circ$  twist angle for cycle numbers of 25, 250, 1000 and 4000 times.

Irrespective of the twist angle the structure does not change significantly along the HPT disc radius, thus, with the nominal strain amplitude. This is clearly visible in the EBSD scans of the sample subjected to only 5 cycles at  $5^\circ$  twist angle (Fig. 8, first row). However, for the sample deformed to 4900 cycles the grain size changes distinctly along the HPT radius (Fig. 8, second row).

Interestingly, the grains are finer at larger radii ( $r = 4$  mm and  $\epsilon_{acc} = 6583$ ) and get coarser towards the disc center ( $r = 1$  mm and  $\epsilon_{acc} = 1646$ ). The gradient-like evolution of the grain and subgrain size measured from the EBSD data is visible in Fig. 9, where the largest grains exceed  $10 \mu\text{m}$  in size at  $r = 1$  mm, while at  $r = 4$  mm the grain size is only around  $1.6 \mu\text{m}$ . Accordingly the microhardness follows a similar but inverse trend, decreasing with increasing HPT disc radius from 184 HV at  $r = 1$  mm to 267 HV at  $r = 4$  mm. At these huge accumulated cyclic strains the IPF maps calculated from the EBSD data have intensified their preferred orientations towards  $\{111\} \langle 101 \rangle$  (Fig. 8). The height of the overview EBSD scans in the background equals the HPT disc thickness (Fig. 9). Still fine scaled regions can only be seen in the disc center ( $r = 1$  mm), whereas the rest of the sample consists of uniformly coarsened regions only, which means that the shear band comprises the entire sample volume for radii  $r > 1$  mm.

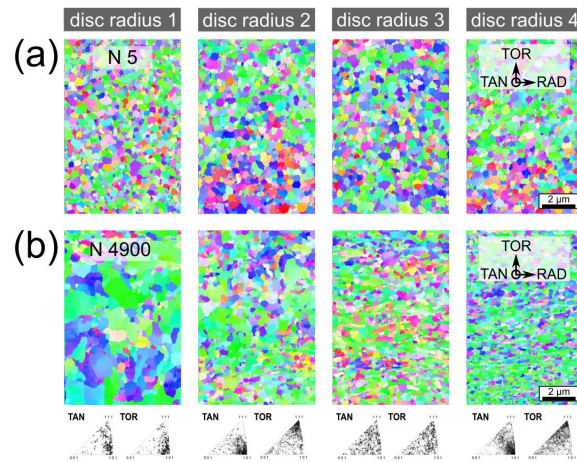


**Figure G.8** IPF color maps and IPFs taken from the shear band region for samples subjected to  $5^\circ$  twist angle show a) a constant grain size along the HPT disc radius after 5 cycles and b) decreasing grain size with increasing HPT disc radius after 4900 cycles.

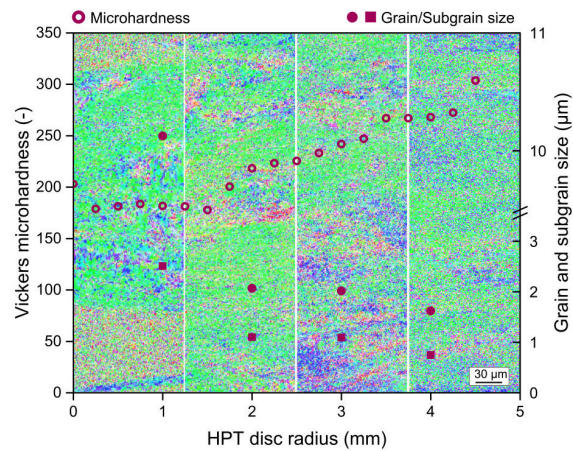


**Figure G.9** Gradient of microhardness, grain and subgrain size along the HPT disc radius after  $N = 5000$  at  $\Theta = 5^\circ$ . EBSD scans in the background span the entire HPT disc height and reveal only coarsened SB regions except for the very center of the HPT disc at  $r = 1$  mm.

### G.3.3 Cyclic high pressure torsion of UFG structures at cryogenic conditions

Similar as for the experiments at room temperature prior to CHPT the UFG structure was processed by monotonic HPT at 77 K. This resulted in a steady state microhardness of 382 HV (Fig. 10), which is distinctively higher than the saturation hardness of 301 HV achieved for deformation at room temperature (Fig. 3a and 5a). The microhardness scattered widely over the HPT disc for both cycle numbers. This is due to the development of shear bands, thus several measurements were taken inside the shear band and some outside (Fig. 10a). Inside the shear band the microhardness values drop down to about 320 HV beyond an HPT disc radius of roughly 3 mm, where the indents were placed inside the shear band. Similar to room temperature experiments the shear band thickness increases from the center towards the edge of the HPT disc exhibiting a wedge-like shape (Fig. 10b). Unlike than at room temperature the shear band thickness did not increase significantly with increasing cycle number, but their number multiplied. EBSD scans taken at an HPT disc radius of 3 mm within the shear band reveal distinct grain growth compared to the cryogenic saturation regime. The calculated grain sizes were 199 nm and 231 nm after 50 and 500 cycles of CHPT, respectively, showing that coarsening proceeds with the accumulated strain.

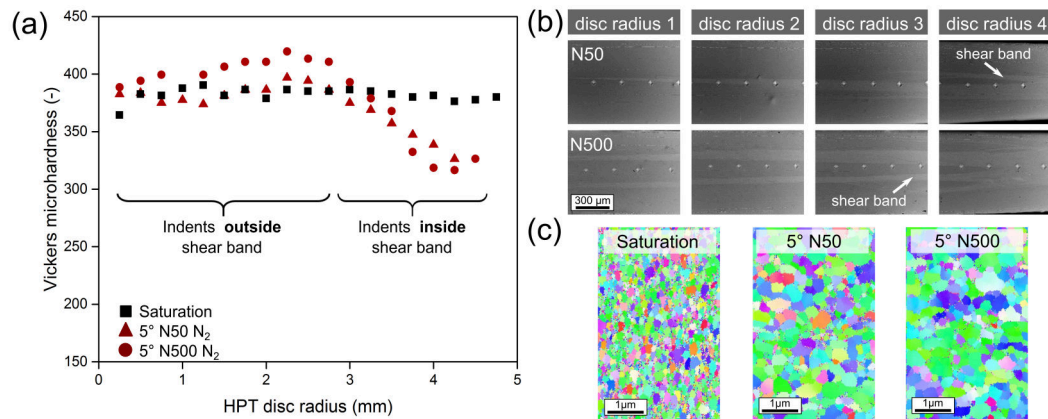


**Figure G.10** a) Microhardness is plotted for the initial UFG structure (black) processed at 77K as well as for the CHPT deformed structures to 50 and 500 cycles at 77K (red). b) BSE images along the HPT disc radii reveal formation of shear bands and c) a coarsening inside of it compared to the starting grain size visible in the IPF color maps.

### G.3.4 Effect of different starting grain sizes

So far the experiments focused on structural changes of UFG nickel subjected to cyclic loading and the effect of deformation temperature. However, also the starting grain size itself may, if varied significantly, influence the occurrence of shear bands

or grain growth. To investigate this in more detail cyclically induced changes of the UFG microstructure were compared to the structural evolution of initially coarse grained and nanocrystalline nickel upon CHPT. EBSD scans of the cycled CG material (Fig. 11b) show a refinement of the structure with increasing HPT disc radius, thus strain amplitude, after 100, 247, 1000 and 5000 cycles.

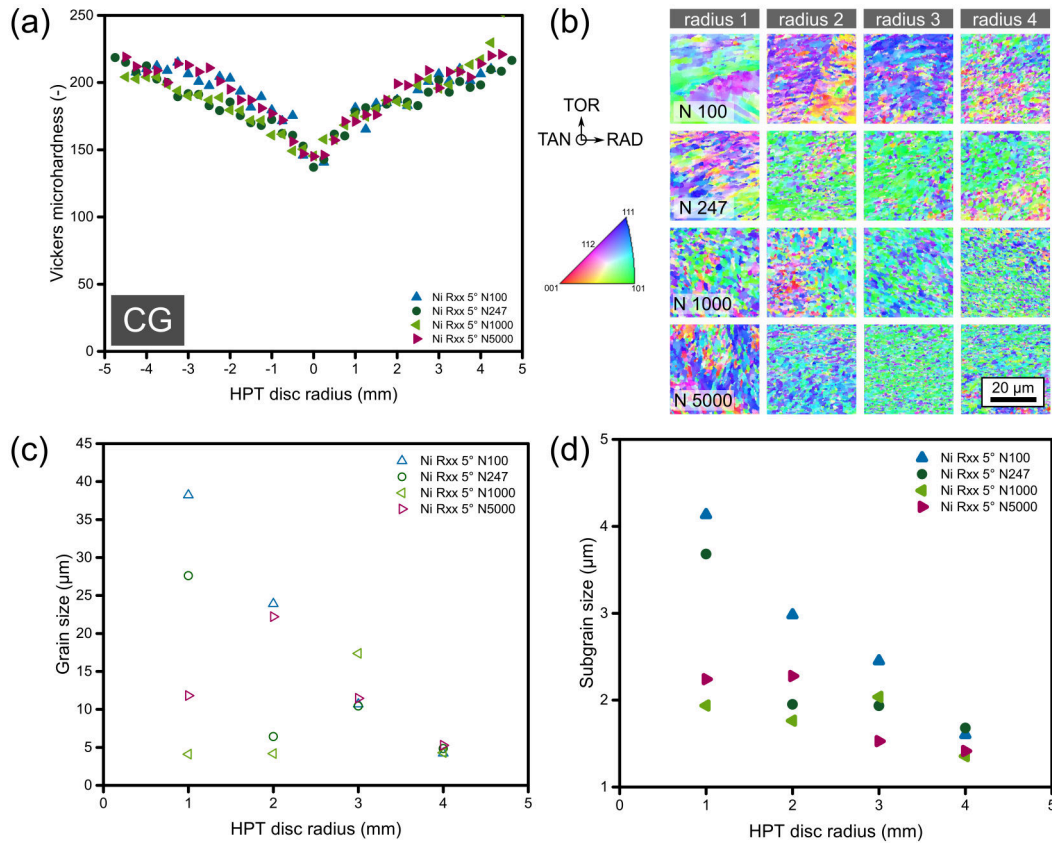


**Figure G.11** a) The microhardness increases with the HPT disc radius after CHPT of the coarse grained nickel in agreement with the refinement of grain and subgrain sizes. After sufficient number of cycles similar crystallographic orientations as observed in the UFG starting structure (Fig. 9) develop.

Most importantly structural modifications, i.e. the refinement of the structure, proceeds homogeneously over the HPT disc height, being not confined or accelerated within a shear band what is a clear difference to the UFG microstructure. The continuous refinement is also reflected in the gradient of the microhardness (Fig. 11a), which increases along the HPT disc radius up to a maximum of about 220 HV. Interestingly, the maximum hardness in CG at  $r = 4$  mm corresponds to the minimum hardness in UFG after 1000 cycles at the same twist angle of  $5^\circ$ . Although the evolution of the grain (Fig. 11c) and subgrain sizes (Fig. 11d) calculated from the EBSD data roughly follows a gradient-like distribution of the microhardness af-

ter 100 cycles, for larger cycle numbers the grain size scatters along the HPT disc radius although for larger radii, independent of the cycle number a relatively constant value can be obtained. Moreover, the microhardness evolution does not differ significantly for the different applied cycles, although the corresponding grain and subgrain sizes vary markedly. The crystallographic orientations obtained from the EBSD scans are comparable to the ones of the cycled UFG structure at large cycle numbers (compare for instance Fig. 9), suggesting the development of a similar crystallographic texture during CHPT irrespective of the starting grain size.

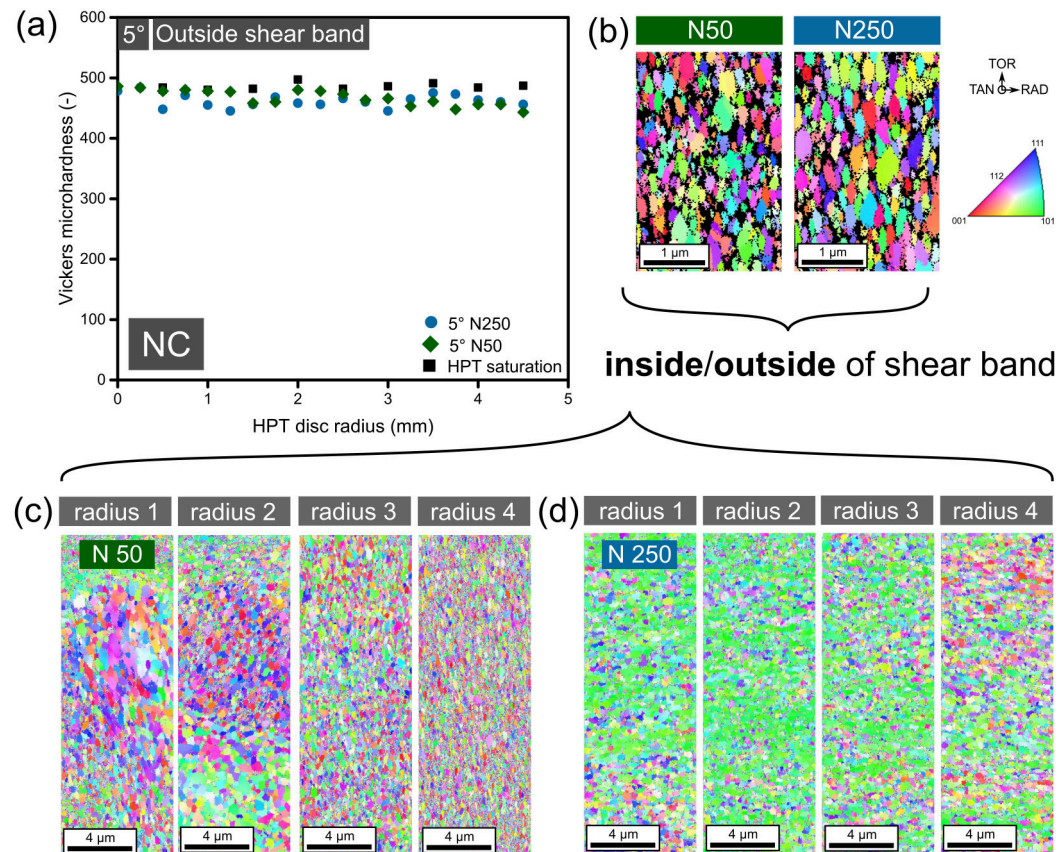


**Figure G.12** a) Microhardness indents taken in the center of the HPT disc show minor cyclic softening. b) As visible from EBSD scans taken at  $r = 2$  mm single grains have grown up to several hundred nanometers after cyclic loading for 50 and 250 cycles at 5° twist angle. c) Within a shear band developing nearby the surface after 50 cycles distinct grain growth occurs and d) gets more pronounced by increasing the cycles to 250.

Microhardness measurements for the NC sample with an initial grain size of about 22 nm and a microhardness of 485 HV prior to cycling (Fig. 12a) showed after 50 cycles at 5° twist angle a small drop by 19 HV down to mean values of 466 HV. This slight reduction of the hardness did not continue with increasing the number

of cycles to 250. Despite the neglecting changes in the microhardness single grains have already grown up to several hundred nanometers (Fig. 12b).

Grain size measurements from the recorded EBSD data are not fully reliable as the resolution of the SEM is insufficient to resolve the still very fine grain sizes assumed in the thin regions between large grains (unindexed points). The microhardness and EBSD scans were located in the middle of the HPT disc height, where for the UFG starting grain size already a pronounced shear band has developed. For the NC starting material no evidence for strain localization is apparent from these data. However, extended analyses revealed a narrow shear band that developed near the surface of the HPT disc already after 50 cycles and similar features could be detected after 250 cycles. The shear bands consist of coarsened grains after 50 (Fig. 12c) and 250 cycles (Fig. 12d), though the structure is very inhomogeneous in size as finer regions can be detected nearby heavily coarsened ones. The effect of grain size increase on the mechanical behavior could not be evaluated as microhardness measurements within the shear band were inhibited by their narrow appearance. The crystallography within the shear band differs significantly from the NC structure in its surrounding but is akin to the cycled UFG structure after 250 cycles. Although also outside the shear band a coarsening was observed (Fig. 12b) the crystallography did not change notably.

## G.4 Discussion

Similar to conventional fatigue experiments CHPT induces structural changes in the UFG structure by the formation of shear bands and coarsening of the structure. CHPT offers the advantage that the hydrostatic pressure under which cyclic torsional deformation takes place suppresses crack initiation which allows a systematic study on these instability mechanisms. This offers the unique possibility to track the evolution of instabilities up to enormous cyclic strains of 6583 in this study. Although in real applications significantly smaller grains are accumulated, monitoring the evolution of structural instabilities over long distances allows to deduce principals under which conditions they are privileged to originate and further spread out. As a consequence profound conclusions about driving forces triggering the formation of shear bands on the one hand and grain coarsening on the other hand are derivable. In the following the impact of strain amplitude, accumulated strain, thermal activation, grain boundary type, crystallography and the initial grain size on the extent of grain growth and shear band formation, as well as on the subsequent cyclic softening can be evaluated.

### G.4.1 Accumulated strain vs. strain amplitude

An amplifying effect of the applied strain or stress amplitude on cyclic softening has frequently been reported for UFG metals [6,10,32] as well as a more homogenous [5] or pronounced coarsening of the structure [15,32]. On the contrary enhanced cyclic softening and grain coarsening was observed for decreasing strain amplitudes,

explained with the concomitant extended lifetime which ensures longer times for diffusion controlled processes assisting grain growth [23]. Along with the enhanced life time higher accumulated strains were imposed to the sample in the case of smaller strain amplitudes. A stimulating effect of the accumulated strain with respect to cyclic softening or grain coarsening was also observed in the current study similar to [5,33]. During the period of shear band thickening from 5 up to 1000 cycles for  $5^\circ$  twist angle and similarly from 25 up to 4000 cycles for  $1.25^\circ$  twist angle cyclic softening but also the coarsening of the grain and subgrain structure progressively increased inside [Fig. 4a, 7a] and outside [Fig. 4b, 7b] of the shear band. The continuous coarsening independent of the local strain amplitude clearly shows that the accumulated strain induces progressive grain boundary migration what is also reflected in the microhardness.

Assuming that most of the strain is concentrated within the shear band and outside of it only micro yielding takes place [15] differences in the nominal strain amplitude along the HPT disc radius in the beginning were balanced by the wedge-like shape of the shear band. Therefore, the local strain amplitude within the shear band becomes more evenly distributed and may account for the roughly constant hardness (Fig. 3a, 6a) and grain size distribution within the shear band (Fig. 8a) along the HPT disc radius.

However, samples subjected to different strain amplitudes ( $\Theta = 1.25^\circ$  and  $\Theta = 5^\circ$ ) but deformed to the same amount of accumulated strain can be compared in order to identify the effect of the strain amplitude. Samples subjected to  $\Theta = 1.25^\circ$  and 4000 cycles ( $\epsilon_{acc} = 1104$  at  $r = 4$  mm) reveal slightly coarser grains than a sample subjected to  $\Theta = 5^\circ$  and 1000 cycles ( $\epsilon_{acc} = 971$  at  $r = 4$  mm) and so a comparable accumulate strain. This is also in agreement with somewhat lower microhardness levels for the smaller strain amplitude. Although from the results a smaller strain amplitude seems to accelerate grain growth one has to be cautious as locally during the growth of the shear band the strain amplitude is changing. This could cause that the difference in the nominal strain amplitude is not exactly represented in the local strain amplitude.

Nevertheless, an influence of the strain amplitude cannot be neglected which is supported by a comparison of the samples cycled for 1000 and 4900 cycles at  $5^\circ$  twist angle. After 4900 cycles, except for the very center of the HPT disc ( $r < 1$  mm), where still UFG regions are visible at the top and the bottom, the shear band comprises the entire sample volume. Therefore, the local strain amplitude equals the nominal one. At this stage the evolution of the coarsened grain size is governed by the nominal strain amplitude rather than the accumulated strain unlike to the period of shear band thickening (e.g. 5-1000 cycles). The grain and subgrain size is with  $1.6 \mu\text{m}$  and  $0.7 \mu\text{m}$  ( $r = 4$  mm) significantly finer as compared to the sample cycled 1000 times with  $6.9 \mu\text{m}$  and  $1.4 \mu\text{m}$  ( $r = 4$  mm), respectively, although the accumulated strain after 1000 cycles is six times smaller. Therefore, despite the further accumulation of strain even a refinement must have taken place once the thickness of the shear band comprises the HPT disc height, i.e. between 1000 and 4900 cycles. Further, the gradient-like distribution of the grain and subgrain sizes

as well as the inverse gradient of the microhardness suggest that the nominal strain amplitude governs the coarsening process and not the accumulated strain. This allows for the conclusion, that cyclically induced grain growth is not an “everlasting” process as most probably the nominal strain amplitude determines the coarsened grain size upon cyclic loading.

#### **G.4.2 Evolution of structural parameters and its effect on cyclic softening**

Inside the shear band not only coarsening of the grains but also of the subgrains was observed with increasing cycle number. These findings are in contrast to earlier in-situ investigations identifying the migration of HAGB as the basic mechanism for cyclic grain growth, while LAGB rather stay unaffected or at most disappear when their neighborhood is altered significantly [24]. However, the nominal strain amplitudes and also the accumulated strain amplitudes were significantly smaller for the presented cyclic micro bending experiments in [24]. Nevertheless, this suggests that the increase of the subgrain size present at higher cyclic strains may occur in a different manner as migration of HAGB. Presumably if the size of the grown grains has become sufficiently large it allows for the accumulation of dislocations in a substructure similar as observed in coarse grained materials during fatigue. The development of typical fatigue substructures within coarsened grains have also been reported in previous studies on UFG materials [4,5,23].

As in CHPT crack initiation is prevented by the hydrostatic pressure, the cyclic softening reflected in the microhardness measurements can exclusively be attributed to the structural changes, i.e. grain and subgrain growth. For both twist angles a progressive drop in the microhardness is observed with increasing accumulated strain accompanied by a continuous increase of the grain and subgrain sizes. As an example 1000 cycles of CHPT at 5° twist angle leads to the reduction of hardness by more than 80 HV from 301 HV to 217 HV. Simultaneously the grain size increases by more than 24 times to 6.5  $\mu\text{m}$ , but the subgrain size only to 1.3  $\mu\text{m}$  in average. As the grain size is too large to account for a hardness of 217 HV in Ni the subgrain boundaries must be decisive for controlling the strength which is in agreement with earlier findings [34].

In a foregoing study [24] the effect of grain coarsening on the mechanical stability was evaluated for the region outside of the shear band upon 50 cycles of CHPT at 5° twist angle. A slight growth of the grains and subgrains from 310 nm and 260 nm to 373 nm and 322 nm was observed, respectively but did not result in a detectable drop of the microhardness. Probably the weak cyclic softening assumed is counterbalanced by alternative processes, causing a hardening of the structure. Considering that in the matrix only minor cyclic strains have to be accommodated, as the majority is concentrated within the shear band, only limited dislocation activity is required in this area. It could be possible that the activation of already existing lattice dislocations would be sufficient for micro yielding. Thus, the absence of cyclic softening at these low cyclic strains could be explained by an exhaustion of lattice

dislocations in this region. Further, the migrated grain boundaries could be already more equilibrated due to their movement what complicates dislocations emission from grain boundaries. The superposition of the thereby induced hardening with the softening due to the slight grain growth may preserve the initial hardness level. This would explain why cyclic softening is negligible unless a certain grain size has been exceeded. Similar findings of cyclic hardening have been observed in fatigue experiments on NC metals [35,36].

### **G.4.3 Driving forces for cyclically induced grain growth in UFG structures**

In principal two types of driving forces for grain growth can be distinguished, which are either thermally or mechanically based. More pronounced grain growth at room temperature compared to lower temperatures of 223 K during LCF experiments on UFG copper revealed enhanced cyclic softening and suggested a critical role of the temperature [23]. From this it could be concluded that in the absence of a thermal activation grain coarsening during cyclic loading should diminish. However, the CHPT experiments performed under cryogenic conditions (Fig. 10) prove this argument to be wrong. Even at 77 K, thus at a diminishing homologues temperature for nickel, the formation of shear bands is observed and inside of it severe grain coarsening is revealed already after 50 and 500 cycles. Thus, also in the absence of significant thermal activation cyclically induced modifications of the structure are present, which are very similar to room temperature experiments. Also the microhardness dropped within the shear band yielding in a softening of 15 % after 50 cycles which is about the same compared to room temperature experiments (16 % of softening after 50 cycles). Therefore it needs to be emphasized that the thermal activation of grain boundaries during cyclic loading cannot be a pre-requisite for their migration. For this reason fatigue induced grain growth can be considered to be mainly mechanically driven, although it can be thermally facilitated.

The cyclic stress or the cyclic strain can be considered as such mechanical driving forces for cyclically induced coarsening of UFG structures. In most cases the coupling of the grain boundary to shear-stress is used to explain mechanically induced migration of grain boundaries [1620], although direct measurements of shear displacement are rare. The concept of stress driven grain boundary migration was originally described for bicrystals, exhibiting grain boundaries completely different from the highly distorted ones after SPD, which were tested at relatively high homologous temperatures [21,22]. However, the importance of the cyclic stresses could not be verified for CHPT deformation of UFG Ni. In the HPT discs the flow stress is evenly distributed over the height at least at the beginning when the structure is still homogeneous and not coarser inside or finer outside of a shear band. Further, no preferred grain boundaries are present in the starting material. Nevertheless, the coarsening process intensifies already after a few cycles within the shear band, thus in regions of high cyclic strain [13,14,37]. Additionally, the coarsening continuously reduces the flow stress and so the maximal shear stresses acting on a grain boundary.

Still coarsening was amplified in these regions of large strain and not where larger stresses are present. Similar observations have been made for static straining experiments, where structural coarsening occurred in the highly strained necking region [38].

The importance of the strain for triggering grain boundary migration is further pointed out by the evolution of torsional texture components favorably oriented for cyclic slip within the heavily coarsened regions [15]. With increasing accumulated strain a preferential growth of  $\{111\} \langle 101 \rangle$  oriented grains occurs inside the shear band (Fig. 3a). This crystallographic orientation enables the cyclic strain to be accommodated by only a single slip system [39]. Outside the shear band crystallographic orientations prevail (Fig. 5b), which necessitate two slip systems to accommodate the shear strain. This could lead to much easier dislocation slip in the favorably oriented grains, which in turn may increase the rate of generated disconnections, which are steps like grain boundary defects but are associated with a grain boundary dislocation and can be formed by the interaction of lattice dislocations with grain boundaries [28]. In-situ TEM work showed that in UFG metals the migration of such disconnections can be considered as the elementary step for grain boundary migration on the mesoscale [27]. Hence, enhanced dislocation interactions with grain boundaries in the  $\{111\} \langle 101 \rangle$  grains could be responsible for the easier migration of grain boundaries leading to a coarsening of the structure. These interactions continuously trigger the migration of boundaries and account for the continuous grain growth procedure with increasing accumulated strain, but also the stop of grain growth when subboundaries form acting as barriers for lattice dislocations. Accordingly, it must be concluded that the grain boundary migration mechanism is strongly triggered by dislocation based plasticity processes and must therefore not be understood as a novel deformation mechanism in UFG metals as often reported [40]. This is also confirmed by the occurrence of texture components after HPT and CHPT, expected for dislocation based plasticity.

#### G.4.4 Growth of cyclically induced shear bands

The sample volume occupied by the shear band depends on the nominal strain amplitude (Fig. 1, Tab. 3). With larger nominal strain amplitudes the shear band gets thicker leading to its wedgelike shape. Additionally, it grows in thickness with increasing cycle numbers. Spreading of such shear bands during LCF has been described earlier as a consequence of the continuous softening due to coarsened and rotated grains keeping cyclic deformation favorable in this softened region [13]. However, this does not reveal the specific driving forces triggering the shear band to grow in thickness instead of maintaining the cyclic strain accommodation in a narrow band.

It was shown, that the IPFs inside (Fig. 3) and outside (Fig. 5) of the shear band exhibit different torsional texture components. This implies if the shear band increases its dimension in the thickness direction by attaching adjacent grains, those would have to rotate from  $\{100\} \langle 101 \rangle$  outside the shear band towards  $\{111\} \langle 101 \rangle$

or  $\{111\}\langle 112\rangle$ . As mentioned earlier, the torsional texture components outside of the shear band facilitate cyclic slip by two non-coplanar slip systems. On the contrary inside the shear band the mostly  $(111)[112]$  and  $(111)[101]$  oriented grains can accommodate the cyclic strain by either coplanar slip on two different slip system. Thus, the rotation of grains towards crystallographic orientations inside of the shear band increases the sample volume of preferable cyclic slip conditions and ensures more efficient accommodation of cyclic strain. This could indeed be understood as a driving force for increasing the shear bands thickness.

However, thickening of the shear band does not necessarily imply that only adjacent grains outside of the shear band are continuously attached to the shear band. The presence of very narrow shear bands which are located in the vicinity of the major one (see also Fig. 3 in [15]) and consist of only one or at least a couple of grains in thickness (Fig. 13) rather suggest that the growth of the shear band occurs by coalescence of this narrow shear band nuclei with the dominant shear band. The evolution of multiple narrower shear bands and their subsequent coalescence with increasing accumulated strain can eventually destroy the entire UFG structure as observed after 4900 cycles.

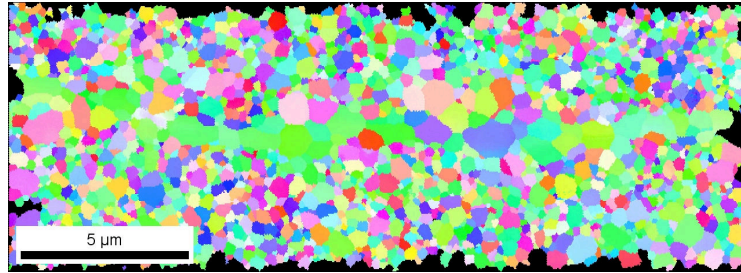


**Figure G.13** Narrow shear band “nucleus“ consisting of a sequence of coarsened grains, found in the vicinity of the major shear band.

#### G.4.5 Effect of the starting grain size on cyclically induced strain localization

Strain localization in shear bands is also possible in NC Ni, though the microhardness in the middle of the HPT disc did not drop notably after 50 cycles (Fig. 12) unlike to the UFG case [15] where the shear band caused significant softening. Nevertheless, a shear band developed which is located in the vicinity of the HPT disc surface. Compared to the structure in the HPT disc center, EBSD scans inside the shear band (Fig. 12) revealed severe coarsening of the structure even after 50 cycles, getting more homogeneous if the accumulated strain is further increased. Interestingly also the crystallography seems to be become akin to the UFG case after 250 cycles, suggesting that a similar coarsening mechanism occurs. A severe softening within the shear band is therefore assumed, although not measurable due to the narrow appearance of the shear band.

The CG Ni responded to the cyclic strain by a refinement of the microstructure with increasing strain amplitude and accumulated strain (Fig. 11). The consecutive formation of a substructure and increase of the boundary misorientation by the continuous accumulation of dislocations cause a hardening instead of a softening as shown by the increase of hardness along the HPT disc radius (Fig. 11). The continuous increase of the hardness prevents the localization of strain within shear bands and enables a homogeneous refinement procedure. This points to the crucial role of strain hardening for preventing shear band formation and maintaining homogeneous plastic deformation [41]. Nevertheless, the crystallography in the cycled CG structure is the same as within the shear bands in the NC and UFG structures, proving that in any case dislocation based plasticity mechanisms are present and in the UFG and NC structures are involved in the coarsening procedure within the shear band.

## G.5 Conclusion

The stability of UFG, CG and NC Ni structures was challenged by applying CHPT, an alternative assessment for LCF experiments. By prohibiting failure of the sample the evolution of microstructural changes was followed up to accumulated strains of more than 6500 and allowed for the following conclusions for the structural instabilities upon cyclic deformation in UFG Ni:

- i) The thickness of cyclically induced shear bands can grow with the nominal strain amplitude, thus along the HPT disc radius, but also with the accumulated strain when the number of cycles is increased.
- ii) Grain growth occurs outside and inside of the shear band, though the localized strain accelerates the grain growth procedure.
- iii) The coarsening of grains and subgrains proceeds continuously with the accumulated strain, thus with the number of cycles applied.
- iv) The steady increase of the subgrain size causes pronounced cyclic softening.
- v) The evolution of torsional texture components requiring only a single slip system, suggest that multiplied dislocation activities and assumed interaction with grain boundaries account for the growth of grains.
- vi) Cyclically induced grain coarsening is not an “everlasting“ phenomenon, as once the shear band comprises the entire sample volume not the accumulated strain, but the nominal strain amplitude governs the grain- and subgrain size and therefore also the cyclic strength.
- vii) Enhanced grain growth within shear bands was also observed under cryogenic conditions and so in the absence of thermal activation.

In summary, these observations allow for the conclusion, that thermal activation is not a prerequisite for cyclically induced grain growth and rather a mechanical activation of the grain boundary accounts for its migration. Furthermore, not the cyclic stress, which is constant over the HPT disc height, but the cyclic strain triggers boundary migration. Finally, as the formation of shear bands is absent in initially CG materials, but distinct grain coarsening is observed within shear bands for the NC structures, the occurrence of cyclic strain localization in shear bands is a result of the disability for strain hardening in fine scaled materials.

### **Acknowledgements**

Financial support by the FWF Austrian Science Fund within project number P24429-N20 and by the European Research Council und ERC Gran Agreement No. 340185 USMS is gratefully acknowledged.

### **References**

- [1] M. Dao, L. Lu, R. Asaro, J. Dehossan, E. Ma, Toward a quantitative understanding of mechanical behavior on nanocrystalline metals, *Acta Mater.* 55 (2007) 4041-4065.
- [2] M.A. Meyers, A. Mishra, D.J. Benson, Mechanical properties of nanocrystalline materials, *Prog. Mater. Sci.* 51 (2006) 427-556.
- [3] H. Mughrabi, Fatigue, an everlasting materials problem - still en vogue, *Proc. Eng.* 2 (2010) 3-26.
- [4] H. Mughrabi, H.W. Höppel, Cyclic deformation and fatigue properties of very fine-grained metals and alloys, *Int. J. Fatigue* 32(9)(2010) 1413-1427.
- [5] S. Agnew, J. Weertman, Cyclic softening of ultrafine grain copper, *Mater. Sci. Eng. A* 244(2) (1998) 145-153.
- [6] S.R. Agnew, A.Y. Vinogradov, S. Hashimoto, J.R. Weertman, Overview of fatigue performance of Cu processed by severe plastic deformation, *J. Electron. Mater.* 28(9) (1999) 1038-1044.
- [7] A. Vinogradov, Y. Kaneko, K. Kitagawa, S. Hashimoto, R.Z. Valiev, On the Cyclic Response of Ultrafine-Grained Copper, *MSF* 269-272 (1998) 987-992.
- [8] S.D. Wu, Z.G. Wang, C.B. Jiang, G.Y. Li, Scanning electron microscopy-electron channelling contrast investigation of recrystallization during cyclic deformation of ultrafine grained copper processed by equal channel angular pressing, *Philos. Mag. Lett.* 82(10) (2002) 559-565.
- [9] S.D. Wu, Z.G. Wang, C.B. Jiang, G.Y. Li, I.V. Alexandrov, R.Z. Valiev, Shear bands in cyclically deformed ultrafine grained copper processed by ECAP, *Mater. Sci. Eng. A* 387-389 (2004) 560-564.
- [10] L. Kunz, P. Lukáš, M. Svoboda, Fatigue strength, microstructural stability and strain localization in ultrafine-grained copper, *Mater. Sci. Eng. A* 424(1-2) (2006) 97-104.

- [11] L. Kunz, P. Lukáš, L. Pantelejev, O. Man, Stability of ultrafine-grained structure of copper under fatigue loading, *Procedia Eng.* 10 (2011) 201-206.
- [12] M. Wong, W. Kao, J. Lui, C. Chang, P. Kao, Cyclic deformation of ultrafine-grained aluminum, *Acta Mater.* 55(2) (2007) 715-725.
- [13] H.W. Höppel, C. Xu, M. Kautz, N. Barta-Schreiber, T.G. Langdon, H. Mughrabi, Cyclic Deformation Behaviour and Possibilities for Enhancing the Fatigue Properties of Ultrafine-Grained Metals, In: Zehetbauer, M., Valiev, R.Z. (eds.) *Nanomaterials by Severe Plastic Deformation* (2004) 677-683.
- [14] S. Malekjanie, P.D. Hodgson, N.E. Stanford, T.B. Hilditch, Shear bands evolution in ultrafine-grained aluminium under cyclic loading, *Scripta Mater.* 68 (2013) 821-824.
- [15] M.W. Kapp, O. Renk, T. Leitner, P. Ghosh, B. Yang, R. Pippan, Cyclically induced grain growth within shear bands investigated in UFG nickel by cyclic high pressure torsion, accepted for publication in *J. Mater. Res.* (2017).
- [16] D.S. Gianola, S. van Petegem, M. Legros, S. Brandstetter, H. van Swygenhoven, K.J. Hemker, Stress-assisted discontinuous grain growth and its effect on the deformation behavior of nanocrystalline aluminum thin films, *Acta Mater.* 54(8) (2006) 2253-2263.
- [17] D.S. Gianola, B.G. Mendis, X.M. Cheng, K.J. Hemker, Grain-size stabilization by impurities and effect on stress-coupled grain growth in nanocrystalline Al thin films, *Mater. Sci. Eng., A* 483-484 (2008) 637-640.
- [18] T.J. Rupert, D.S. Gianola, Y. Gan, K.J. Hemker, Experimental observations of stress-driven grain boundary migration, *Science* 326(5960) (2009) 1686-1690.
- [19] M. Legros, D.S. Gianola, K.J. Hemker, In situ TEM observations of fast grain-boundary motion in stressed nanocrystalline aluminum films, *Acta Mater.* 56(14) (2008) 3380-3393.
- [20] Y. Zhang, J.A. Sharon, G.L. Hu, K.T. Ramesh, K.J. Hemker, Stress-driven grain growth in ultrafine grained Mg thin film, *Scripta Mater.* 68 (2013) 424-427.
- [21] D. Molodov, V. Ivanov, G. Gottstein, Low angle tilt boundary migration coupled to shear deformation, *Acta Mater.* 55 (2007) 1843-1848.
- [22] T. Gorkaya, K.D. Molodov, D.A. Molodov, G. Gottstein, Concurrent grain boundary motion and grain rotation under an applied stress, *Acta Mater.* 59 (2011) 5674-5680.
- [23] H.W. Höppel, Z.M. Zhou, H. Mughrabi, R.Z. Valiev, Microstructural study of the parameters governing coarsening and cyclic softening in fatigued ultrafine-grained copper, *Philos. Mag. A* 82 (2002) 1781-1794.
- [24] M.W. Kapp, T. Kremmer, C. Motz, B. Yang, R. Pippan, Structural instabilities during cyclic loading of ultrafine-grained copper studied with micro bending experiments, *Acta Mater.* 125 (2017) 351-358.
- [25] O. Renk, A. Hohenwarter, S. Wurster, R. Pippan, Direct evidence of grain boundary motion as the dominant restoration mechanism in the steady-state regime of extremely cold-rolled copper, *Acta Mater.* 77 (2014) 401-410.
- [26] P. Ghosh, O. Renk, R. Pippan, Microtexture analysis of restoration mechanisms during high pressure torsion of pure nickel, *Mater. Sci. Eng. A* 684 (2017) 101-109.

- [27] A. Rajabzadeh, M Legros, N. Combe, F. Momprou, D.A. Molodov, Evidence of grain boundary dislocation step motion associated to shear-coupled grain boundary, *Philos. Mag.* 93 (2013) 1299-1316.
- [28] A. Rajabzadeh, F. Momprou, S. Lartigue-Korinek, N. Combe, M. Legros, D.A. Molodov, The role of disconnections in deformation-coupled grain boundary migration, *Acta Mater.* 77 (2014) 223-235.
- [29] R. Pippan, S. Scheriau, A. Hohenwarter, M. Hafok, Advantages and Limitations of HPT: A Review, *Mater Sci. Forum* 1621 (2008) 584-586.
- [30] A. Hohenwarter, A. Bachmaier, B. Gludovatz, S. Scheriau, R. Pippan, Technical parameters affecting grain refinement by high pressure torsion, *Int. J. Mat. Res.* 100 (2009) 16531661.
- [31] B. Yang, H. Vehoff, A. Hohenwarter, M. Hafok, R. Pippan, Strain effects on the coarsening and softening of electrodeposited nanocrystalline Ni subjected to high pressure torsion, *Scripta Mater.* 58 (2008) 790793.
- [32] D. Canadina, T. Niendorf, H.J. Maier, A comprehensive evaluation of parameters governing the cyclic stability of ultrafine-grained FCC alloys, *Mater. Sci. Eng. A* 528 (2011) 6345-6355.
- [33] C.F. Kwan, Z. Wang, A composite nature of cyclic strain accommodation mechanisms of accumulative roll bonding (ARB) processed Cu sheet materials, *Mater. Sci. Eng. A* (2011) 2042-2048.